



Classe di Scienze

Corso di perfezionamento in
Metodi e Modelli per le Scienze Molecolari

XXXVI ciclo

Modeling Atomistic Nanoplasmonics: Classical and Hybrid Quantum Mechanical/Classical Schemes

Supervisor

Prof. Chiara Cappelli

Co-supervisor

Dr. Tommaso Giovannini

Candidato
Pablo Grobas Illobre

Anno accademico 2023–2024

To my family

Contents

Abstract	1
Publications	3
Introduction	5
1 Classical Models for Nanoplasmonics	7
1.1 What is Nanoplasmonics?	7
1.2 Boundary Element Method (BEM)	9
1.3 Frequency-Dependent Fluctuating Charges (ω FQ)	12
2 Surface-Enhanced Spectroscopies	15
2.1 History and Multiscale QM/Classical Modeling	15
2.2 Surface-Enhanced Raman Scattering (SERS)	16
2.3 Surface-Enhanced Fluorescence (SEF)	19
3 Overview of attached publications	23
4 Attached Publications	25
I. Do We Really Need Quantum Mechanics to Describe Plasmonic Properties of Metal Nanostructures?	26
II. Fully atomistic modeling of plasmonic bimetallic nanoparticles: nanoalloys and core-shell systems	38
III. Multiscale Modeling of Surface Enhanced Fluorescence	48
IV. Mixed Atomistic-Implicit Quantum/Classical Approach to Molecular Nanoplasmonics	66
5 Summary, conclusions, and future perspectives	79
Acknowledgments / Agradecementos	81
References	85

Abstract

Nanoplasmonics is characterized by complex physical phenomena that give rise to enhanced optical properties of plasmonic substrates. Furthermore, the interaction of nanoplasmonic devices with molecular systems can significantly influence the molecular response, leading to either enhanced or quenched physicochemical properties, such as their spectroscopic signals. Therefore, understanding the theoretical foundations of nanoplasmonics is essential for the experimental optimization of these devices, prior to their commercialization. In this context, we have developed theoretical approaches grounded in classical physics to evaluate realistic, large-scale nanoplasmonic substrates. These classical approaches retain the atomistic characteristics of the plasmonic profile, which strongly influences the material's response. The results obtained have been benchmarked and validated against *ab initio* and experimental data, thus confirming the robustness of our calculations. Furthermore, we have extended these approaches to evaluate plasmon-mediated molecular properties. With this aim, we have coupled these classical methodologies to analyze nanoplasmonic materials with a Time-Dependent Density Functional Theory description of the molecule. More in detail, we have applied this multiscale framework to evaluate Surface-Enhanced Raman Scattering and Surface-Enhanced Fluorescence spectroscopies. Our findings demonstrate that preserving the atomistic profile of plasmons is crucial, as spectroscopic signals are highly sensitive to the morphology of the plasmonic substrates.

Publications

This thesis is based on the following publications:

- [Paper I] Giovannini, T., Bonatti, L., Lafiosca, P., Nicoli, L., Castagnola, M., **Grobas Illobre, P.**, Corni, S., & Cappelli, C., “Do we really need quantum mechanics to describe plasmonic properties of metal nanostructures?”
ACS Photonics 9 (2022): 3025-3034
<https://doi.org/10.1021/acsphotonics.2c00761>
- [Paper II] Nicoli, L., Lafiosca, P., **Grobas Illobre, P.**, Bonatti, L., Giovannini, T., & Cappelli, C., “Fully atomistic modeling of plasmonic bimetallic nanoparticles: nanoalloys and core-shell systems”
Front. Photon. 4 (2023): 1199598
<https://doi.org/10.3389/fphot.2023.1199598>
- [Paper III] **Grobas Illobre, P.**, Lafiosca, P., Guidone, T., Mazza, F., Giovannini, T., & Cappelli, C., “Multiscale modeling of surface enhanced fluorescence”
Nanoscale Adv. 6 (2024): 3410-3425
<https://doi.org/10.1039/D4NA00080C>
- [Paper IV] **Grobas Illobre, P.**, Lafiosca, P., Bonatti, L., Giovannini, T., & Cappelli, C., “Mixed Atomistic-Implicit Quantum/Classical Approach to Molecular Nanoplasmonics”
J. Chem. Phys. 162 (2025): 044103
<https://doi.org/10.1063/5.0245629>

Introduction

Plasmonic substrates are systems presenting peculiar optical properties due to the coherent oscillation of valence electrons in response to external radiation, giving rise to what is known as plasmons.^{1–4} A wide range of materials exhibit plasmonic properties, such as pure metals,^{5–9} metal alloys,^{10–14} and graphene-based structures,^{15–20} among others.^{21–23}

Interestingly, the type of plasmons formed is strongly influenced by the size of the substrate. On larger substrates, such as thin metallic films, surface plasmons propagate along the surface in a wave-like manner. In contrast, as the substrate is reduced to nanoscale dimensions, plasmons oscillations become highly localized within the structure, resulting in **Localized Surface Plasmons (LSPs)**.^{1,2} LSPs produce a significantly higher enhanced electric field at the substrate's surface than Surface Plasmons. This enhancement is especially pronounced in regions known as “hot spots”, typically found at sharp interfaces within the structure.^{4,24–26} Furthermore, plasmonic materials possess a remarkable ability to confine light within sub-nanometer gaps, where quantum tunneling effects play a significant role.^{26–29} Notably, the effectiveness of a plasmonic substrate for specific applications is primarily determined by the intensity of the electric field enhancement it produces, which in turn depends on its unique optical response upon light irradiation.^{30,31}

In this context, the optical response associated with LSPs can be fine-tuned by adjusting the substrates' size, morphology, and chemical composition.^{10,32–34} This adaptability facilitates the development of **nanoplasmonic devices** precisely tailored for targeted applications. These devices are typically used to analyze the enhanced spectroscopic characteristics of molecules positioned near the substrates, where plasmon-induced perturbations drive the variations in the molecular response. More specifically, these investigations have established the research field of **Surface-Enhanced Spectroscopies**, with Surface-Enhanced Raman Scattering being the first discovered and still the most widely utilized technique.^{31,35–38} Recent advancements have further expanded this area of study to the so-called Tip-Enhanced Spectroscopies, where the intense electric field localized between a plasmonic tip-base setup significantly influences the molecular response.^{39–43} Regardless of the specific substrate configuration, modifications in the molecular spectroscopic signal are dictated by the perturbation experienced by the molecule, which depends jointly on the substrate's response and the molecule-substrate distance.^{30,31,44–46}

Then, how can we engineer substrates to achieve an optimal response that satisfies our needs? This question naturally brings together scientists across diverse fields, engaging physicists, chemists, materials scientists, and many others in the search for a comprehensive solution. In particular, computational scientists play a key role by providing a deep understanding of the physical phenomena governing the plasmonic response of the substrates, as well as their eventual effect in modifying the physicochemical properties of molecular systems. Consequently, the theoretical – *in silico* – design of plasmonic substrates offers valuable insights before their experimental validation and potential commercialization.^{26,47,48}

To this end, several theoretical approaches have been proposed over the years. Quantum Mechanics (QM) offers a highly accurate framework for understanding plasmon-mediated phenomena. However, QM calculations are computationally prohibitive for simulating realistic nanoplasmonic systems, particularly at larger scales.^{49–57} This limitation has led to the extensive development of alternative theoretical methodologies, especially those rooted in classical physics. In particular, the study of plasmon-enhanced molecular properties often employs **QM/Classical multiscale models**. These can be seen as “focused models” in which molecules and substrates are treated as distinct subsystems, each evaluated at different levels of theory. Typically, the molecular spectroscopic signal is calculated at the QM level, while the plasmonic response of the substrate is described classically. This approach reduces the degrees of freedom involved in the overall response, enabling the study of large plasmonic systems and simplifying the analysis of molecule-substrate interactions.^{44,58–62}

During my Ph.D., I have focused on the theoretical aspects of simulating nanoplasmonics. Specifically, I have extended state-of-the-art methodologies, based on classical physics, that retain the atomistic characteristics of the substrate’s LSPs while maintaining optimal computational efficiency. Additionally, I have integrated these methodologies within QM/Classical frameworks. Through this approach, I have evaluated the plasmon-modified spectroscopic signals of molecular systems positioned in close proximity to the substrate. More precisely, I have developed theoretical frameworks to study Surface-Enhanced Raman Scattering and Surface-Enhanced Fluorescence spectroscopies.

This dissertation is organized as follows. Chapter 1 provides an overview of the theoretical modeling of plasmonic substrates. In Chapter 2, the background of QM/Classical methodologies and their application to analyzing Surface-Enhanced Raman Scattering and Surface-Enhanced Fluorescence spectroscopies are reviewed. Chapter 3 summarizes the key aspects of the papers that form the foundation of this thesis, while Chapter 4 includes these manuscripts. Finally, Chapter 5 concludes this dissertation with a summary, conclusions, and future perspectives.

Chapter 1

Classical Models for Nanoplasmonics

This chapter provides the background for the theoretical modeling of nanoplasmonics, which is the cornerstone of this Ph.D. thesis. The first section introduces the field of nanoplasmonics and offers an overview of the theoretical framework commonly used for its theoretical modeling. The following sections focus on the methodologies that are the basis of the research presented in this dissertation. In particular, the Boundary Element Method and the Frequency-Dependent Fluctuating Charges and Fluctuating Dipoles models are revised.

1.1 What is Nanoplasmonics?

As described in the introduction, **plasmonic substrates** exhibit enhanced optical properties due to the coherent oscillation of conductive electrons upon light irradiation, giving rise to Localized Surface Plasmons (LSPs). The field of “nanoplasmonics” specifically focuses on plasmonic materials whose optical response is confined to nanoscale dimensions. A notable example is single metal nanoparticles (NPs). The formation of LSPs in NPs is schematically illustrated in Fig. 1.1.^{1–4}

LSPs characterize the optical response of a NP by creating a large electric transition dipole, which reaches its maximum at the **Plasmon Resonance Frequency (PRF)**. The PRF is highly sensitive to the defining parameters of a given NP, namely its chemical composition, shape, and size.^{10,32–34} For instance, in spherical noble metal NPs, the PRF shifts toward shorter wavelengths (blue shift) as the NP size decreases. Conversely, when the NP is shaped as a nanorod, the PRF shifts toward longer wavelengths (red shift) with an increasing aspect ratio (i.e., the length-to-width ratio of the nanorod). These parameters can be precisely controlled experimentally, with extensive literature available on methodologies for NP synthesis.^{63–67}

In this context, any theoretical methodology aiming to reproduce nanoplasmonic features must consider the subtle factors impacting the optical response. QM methods, particularly through Time-Dependent Density Functional Theory, provide a comprehen-

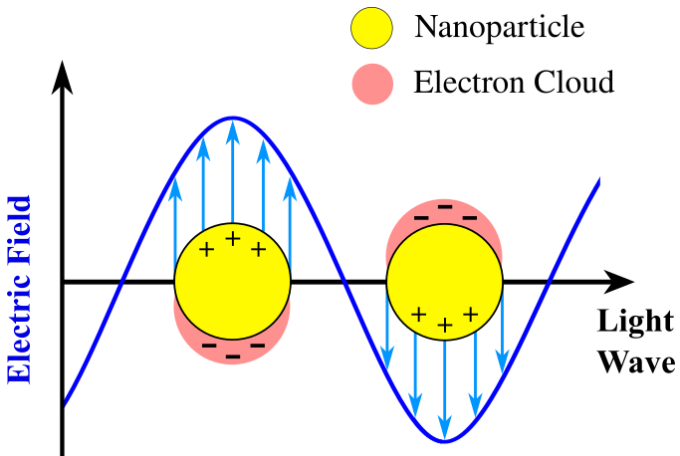


Figure 1.1: Graphical representation of LSP formation.

sive framework for describing plasmon-related phenomena. However, the computational cost of QM calculations, stemming from the large number of degrees of freedom considered, restricts their application to systems constituted by few atoms.^{54,57,58,68}

To address this limitation, methodologies based on **classical electrodynamics** have been developed. These models focus on specific parameters governing the response, aiming to achieve an optimal balance between accuracy and computational efficiency.^{4,27,69–72} In contrast to *ab initio* approaches, classical methodologies require calibration, typically performed against experimental data or QM systems of manageable size.

A widely used family of classical models derives from the solution of Maxwell's equations of electromagnetism. In these models, the NP is treated as a **continuum** entity, with its plasmonic properties governed by the material's permittivity function, which directly determines the response. This framework includes Mie theory,⁷³ the Discrete Dipole Approximation (DDA),⁷⁴ the Finite Difference Time Domain (FDTD) method,^{75–77} and the Boundary Element Method (BEM).^{4,69,70}

Furthermore, two classical frameworks that evaluate the **atomistic** characteristics of NPs exist in the literature. The first approach comprises the family of Discrete Interaction Models (DIMs),^{59,78–89} while the second is the Frequency-Dependent Fluctuating Charges (ω FQ) model.^{26,61,90–97} Notably, preserving the atomistic profile allows a precise evaluation of the huge electric field enhancement generated at the plasmonic **hot spots**, localized at sharp interfaces within the structure.^{24–26,98}

DIM models replicate the plasmonic response of materials by calculating frequency-dependent charges and/or dipoles. Atomic capacitances govern the description of charges while interacting atomic polarizabilities determine the dipoles. These polarizabilities and capacitances are phenomenologically parameterized to follow a Drude-Lorentz trend, ensuring that the model reproduces the plasmonic properties of NPs and captures both intra- and interband transitions globally.^{78,81} However, DIMs' original formulation failed

to account for the size dependency of the plasmonic response, a fundamental characteristic of nanoplasmonics. Addressing this limitation necessitated modifications to the DIM framework, leading to the development of the coordination-dependent Discrete Interaction Model (cd-DIM).⁸³

In contrast, the ω FQ model analyzes the optical response by calculating frequency-dependent atomic charges. The approach is rooted in the Drude model for charge redistribution between atoms and the Fluctuating Charges model. Unlike DIM, the ω FQ model incorporates an intraband description based on well-established textbook principles. Moreover, the model constrains charge transfer to neighboring atoms, emulating the typical profile of quantum tunneling. As a result, ω FQ effectively models the optical response determined by intraband electronic transitions and captures the plasmonic properties related to finite-size effects.⁹⁰

To conclude, several classical models incorporate corrections to capture the modification of the plasmonic features due to quantum effects.^{27,53,71,99–104} For example, the Quantum Corrected BEM was developed to model light confinement at subnanometer junctions, where quantum tunneling plays a major role.^{105,106} The same applies to the cd-DIM framework, whose response based on atomistic coordination dependencies accounts for quantum-related finite-size effects.⁸³ In contrast, ω FQ inherently incorporates quantum tunneling with a straightforward, distance-dependent behavior at the atomic scale, as will be discussed in more detail in the following.⁹⁰

This thesis focuses on modeling the atomistic features of metallic NPs and their significant impact on the plasmonic response. To achieve this, the ω FQ model serves as the cornerstone of the research presented in this dissertation. Additionally, the optical response of NPs has also been analyzed implicitly through BEM, which constitutes one of the most widely employed continuum models for nanoplasmonics.

1.2 Boundary Element Method (BEM)

Over the past 50 years, BEM has been established as a robust and efficient numerical approach for evaluating the interaction of plasmonic materials with electromagnetic fields. Within the Polarization Continuum Model (PCM) framework, BEM serves as a powerful tool for solving the equations describing the systems. In this context, BEM enables a detailed analysis of the resulting plasmonic phenomena, which plays a pivotal role in determining the optical response of plasmonic materials.^{58,60,62,69,70,92,105–125}

Within the BEM approach, a closed continuum surface entity is embedded in a dielectric medium. This surface is tessellated by using a set of triangles (or rectangles), known as *tesserae*, whose size can be effectively adjusted to achieve the optimal computational cost and accuracy. At the geometrical barycenter of each *tessera*, a surface charge (σ) is placed. For a system consisting of T *tesserae*, a total of T surface charges are computed. The charges depend on the frequency(ω)-dependent permittivities of the embedding medium, $\varepsilon_1(\omega)$, and the plasmonic material, $\varepsilon_2(\omega)$. The sum of the charges yields a global surface charge density that encapsulates the physics governing the plasmonic response.^{4,116} Fig. 1.2 illustrates the BEM modeling of a spherical NP.

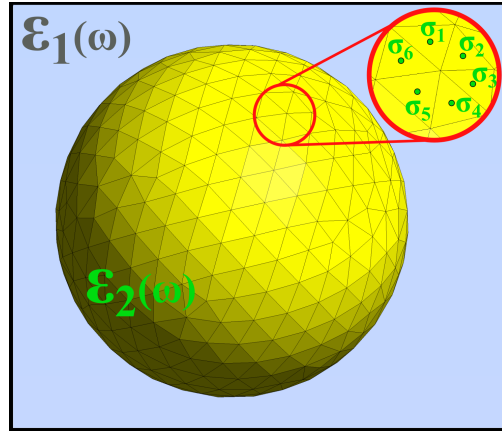


Figure 1.2: Graphical representation of a spherical system modeled using BEM.

The calculation of BEM charges relies on two fundamental components: a **continuum surface** that defines the geometry, and the **permittivities** that describe the material's response in a given medium. The optical properties of plasmonic materials are then evaluated through the computed BEM charges.^{60,69,92,107,121,123,126}

How, then, are BEM charges computed? The answer depends on the methodology chosen to solve Maxwell's equations. Several strategies have been proposed in the literature to address this challenge.^{4,105,116} The original PCM formulation emerged in the 1980s to study solvation effects, receiving later the name of Dielectric Polarizable Continuum Model (DPCM).^{4,108,116} Later, the solution to the electrostatics problem was reformulated exploiting the theory of integral equations, giving rise to the Integral Equation Formalism for the Polarizable Continuum Model (IEFPCM).^{110,116} Both DPCM and IEFPCM equations can be numerically solved through BEM, and their application can be extended to study the optical response of metallic NPs.^{60,92,116}

The research presented in this thesis (see Chapter 3) focuses on NPs whose size is significantly smaller than the wavelength of the interacting incident electric field. In this scenario, the incident electric field can be treated as uniform across the NPs, simplifying the equations by allowing us to neglect retardation effects. This approximation frames the problem in the so-called **quasistatic regime**. Within this regime, we can express the **BEM-DPCM** equation in compact matrix notation as:^{4,116}

$$\left[2\pi \left(\frac{\varepsilon_2(\omega) + \varepsilon_1(\omega)}{\varepsilon_2(\omega) - \varepsilon_1(\omega)} \right) \mathbf{A} + \mathbf{F} \right] \boldsymbol{\sigma}(\omega) = -\mathbf{E}_{\vec{n}}^{\text{ext}}(\omega), \quad (1.1)$$

while the **BEM-IEFPCM** equation reads:^{60,116}

$$\left[2\pi \left(\frac{\varepsilon_2(\omega) + \varepsilon_1(\omega)}{\varepsilon_2(\omega) - \varepsilon_1(\omega)} \right) \mathbf{I} + \mathbf{F} \right] \mathbf{S} \mathbf{A}^{-1} \boldsymbol{\sigma}(\omega) = -(2\pi \mathbf{I} + \mathbf{F}) \mathbf{V}^{\text{ext}}(\omega). \quad (1.2)$$

In Eqs. (1.1) and (1.2), $\sigma(\omega)$ represents the BEM charges calculated at a given frequency ω , while $\varepsilon_2(\omega)$ and $\varepsilon_1(\omega)$ are the frequency-dependent dielectric permittivities of the metal and the surrounding medium, respectively. For a system composed of T *tesserae*, \mathbf{I} is the $T \times T$ identity matrix, \mathbf{A} is a diagonal matrix containing the area of each element, $\mathbf{E}_{\vec{n}}^{\text{ext}}$ is the external electric field projected along the normal of the *tesserae*, and \mathbf{V}^{ext} is the potential generated by this field, evaluated at the barycenter of each *tessera*. Finally the \mathbf{F} and \mathbf{S} matrices depend on the geometrical parameters of the *tesserae*. Their elements are defined as:^{109,116}

$$S_{ij} = \begin{cases} \frac{A_j}{|\mathbf{s}_i - \mathbf{s}_j|}, & \text{if } i \neq j \\ 1.0694\sqrt{4\pi A_i}, & \text{if } i = j \end{cases} \quad F_{ij} = \begin{cases} \frac{(\mathbf{s}_i - \mathbf{s}_j) \cdot \mathbf{n}_j}{|\mathbf{s}_i - \mathbf{s}_j|^3} \cdot A_j, & \text{if } i \neq j \\ 1.0694 \cdot \frac{\sqrt{4\pi A_i}}{2R}, & \text{if } i = j \end{cases}$$

where \mathbf{s}_i , A_i , and \vec{n}_i represent the position, area, and normal vector of the i -th *tessera*, respectively, while R is the radius of the sphere containing the ensemble of *tesserae*.

For more information on the mathematical derivation of the BEM-DPCM and BEM-IEFPCM formalisms, see Refs. 116 and 4.

In conclusion, while both approaches describe the same physical phenomena and yield analogous expressions, their key differences lie in the finer details. Specifically, Eq. (1.2) provides a more general formulation than Eq. (1.1). Additionally, because BEM-IEFPCM charges are driven by a potential, rather than a field, this approach is less prone to numerical instabilities.¹¹⁶ These numerical challenges become more significant as the complexity of the mesh geometry increases.^{4,60} Nevertheless, for simpler BEM systems with regular geometries, both formalisms remain equally effective. To illustrate this, Fig. 1.3 shows the absorption spectrum of a 20 Å radius gold BEM sphere in vacuum, calculated using both methodologies.

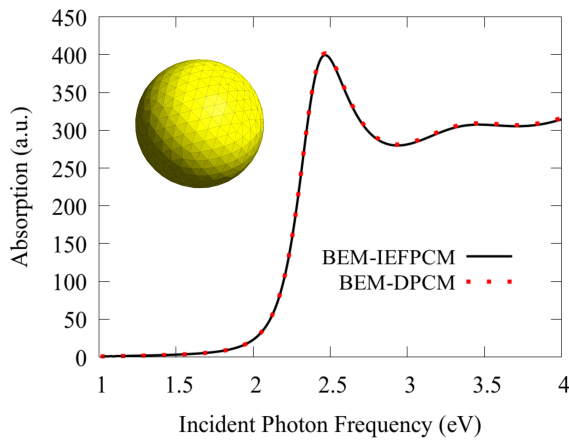


Figure 1.3: Absorption spectrum of a 20 Å radius gold BEM sphere in vacuum. The response is described using the Brendel-Bormann fitting for gold permittivity.¹²⁷

1.3 Frequency-Dependent Fluctuating Charges (ω FQ)

In its initial formulation, the ω FQ approach, introduced by Giovannini *et al.* in 2019, provided an atomistic yet classical framework for calculating the plasmonic response of simple metal NPs, e.g. Sodium NPs.⁹⁰ Since then, ω FQ has been rigorously compared to BEM,⁹² and has been adapted to investigate graphene systems.^{26,61,91,93–95} These developments have established ω FQ as a powerful model for calculating plasmonic features with atomic-level precision. Additionally, the classical nature of ω FQ enables the investigation of large atomistic systems, which would be computationally unfeasible for full QM methods.^{54,58,128–131}

Within ω FQ approach, the plasmonic properties of a system can be analyzed through the computation of frequency-dependent charges, that fluctuate according to an external oscillating electric field. The physics governing the ω FQ charges is grounded on the **Drude conduction model** to describe the electronic charge flow between atoms. According to the Drude framework, the fluctuation of electronic momentum (\mathbf{p}) under the influence of an external electric field (\mathbf{E}) can be expressed in either the time domain (t) or the frequency domain (ω) as:^{90,132}

$$\frac{d\mathbf{p}}{dt} = \mathbf{E}(t) - \frac{\mathbf{p}}{\tau} \quad \xrightarrow{\text{Fourier transform}} \quad -i\omega\mathbf{p}(\omega) = \mathbf{E}(\omega) - \frac{\mathbf{p}(\omega)}{\tau} \quad (1.3)$$

where τ represents the relaxation time, which accounts for the dephasing decay due to intraband scattering processes.

In a closed system, the time-dependent charge fluctuation at each atomic site is governed by the electronic charge flow entering from the surrounding j atoms and exiting through the specific i site, therefore conserving the total charge. In a homogeneous system, the fluctuating atomic charge (q_i) can be expressed as:^{90,92}

$$\frac{dq_i}{dt} = \sum_j A_{ij} \left(n_j \langle \mathbf{p} \rangle \cdot \vec{l}_{ji} - n_i \langle \mathbf{p} \rangle \cdot \vec{l}_{ij} \right) \xrightarrow{n_i=n_j=n} \frac{dq_i}{dt} = \sum_j 2nA_{ij} \langle \mathbf{p} \rangle \cdot \vec{l}_{ji} \quad (1.4)$$

In Eq. (1.4), $\langle \mathbf{p} \rangle$ represents the average electronic momentum over all trajectories between the i -th and j -th atoms, while \vec{l}_{ij} is the unit vector connecting these two atoms. n is the static 3D electron density of each atom within the homogeneous system, and A_{ij} represents the effective area through which the charge transfer occurs. By considering an external monochromatic field oscillating at frequency ω , and substituting $\langle \mathbf{p}(\omega) \rangle$ from Eq. (1.3), the ω FQ charges in the frequency domain can be written as:^{90,92}

$$-i\omega q_i = \sum_j 2nA_{ij} \frac{\langle \mathbf{E}(\omega) \rangle}{1/\tau - i\omega} \cdot \vec{l}_{ji} \quad (1.5)$$

We can then bridge Eq. (1.5) to atomic properties by linking the averaged electric field between a given pair of atoms to their electrochemical potential (μ^{el}) and distance (l_{ij}). This relationship can be approximated as $\langle \mathbf{E}(\omega) \rangle \cdot \vec{l}_{ji} \approx (\mu_j^{el} - \mu_i^{el})/l_{ij}$, leading to

the expression:^{90,92}

$$-\mathrm{i}\omega q_i = \sum_j \frac{2n}{1/\tau - \mathrm{i}\omega} \frac{A_{ij}}{l_{ij}} (\mu_j^{el} - \mu_i^{el}) \quad (1.6)$$

The charge exchange due to the Drude conduction mechanism is restricted to nearest neighboring atoms by introducing a distance-dependent Fermi-like damping function, $f(l_{ij})$. This modifies Eq. (1.6) as:⁹⁰

$$-\mathrm{i}\omega q_i = \sum_j (1 - f(l_{ij})) \frac{2n}{1/\tau - \mathrm{i}\omega} \frac{A_{ij}}{l_{ij}} (\mu_j^{el} - \mu_i^{el}) \quad (1.7)$$

$$f(l_{ij}) = \frac{1}{1 + \exp \left[-d \left(\frac{l_{ij}}{s \cdot l_{ij}^0} - 1 \right) \right]} \quad (1.8)$$

In Eq. (1.8), l_{ij}^0 represents the nearest-neighbor distance in the bulk metal, while d and s control the profile of the damping function. The latter two parameters are adjusted to capture the typical distance dependence of charge transfer for a given atom-atom pair. Notably, this simple $1 - f(l_{ij})$ correction introduces a phenomenological **quantum tunneling regime** at short interatomic distances for the ω FQ charge transfer, while still operating within a classical framework.⁹⁰

The final step is determining an appropriate functional form for the electrochemical potential. To do this, we rely on the **Fluctuating Charges (FQ)** model^{133–135} reformulated to account for the influence of an external frequency-dependent electric potential ($\mathbf{V}^{\text{ext}}(\omega)$) that polarizes the charges. Given that the FQ charges are defined as s-type Gaussian functions, we can express μ_i^{el} from the derivative of the modified FQ energy functional (\mathbf{F}) with respect to the charge q_i :⁹⁰

$$F_{ij} = \sum_i \left(q_i \chi_i + \frac{1}{2} q_i \eta_i q_i + q_i V_i^{\text{ext}}(\omega) + \sum_{j \neq i} q_i T_{ij}^{\text{qq}} q_j \right), \quad (1.9)$$

$$\mu_i^{el} = \frac{\partial F_{ij}}{\partial q_i} = \chi_i + q_i \eta_i + V_i^{\text{ext}}(\omega) + \sum_{j \neq i} T_{ij}^{\text{qq}} q_j, \quad (1.10)$$

where χ_i and η_i are the electronegativity and chemical potential of atom i , respectively, while \mathbf{T}^{qq} is the interaction tensor between two Gaussian charges.^{90,136}

Substituting Eq. (1.10) into Eq. (1.7), we obtain the final ω FQ equation:^{90,92}

$$\sum_j \left[\sum_k K_{ik}(\omega) (T_{jk}^{\text{qq}} - T_{ik}^{\text{qq}}) + \mathrm{i}\omega \delta_{ij} \right] q_j(\omega) = \sum_j (V_i^{\text{ext}} - V_j^{\text{ext}}) K_{ij}(\omega). \quad (1.11)$$

In Eq. (1.11), the diagonal terms of \mathbf{T}^{qq} include the values of η for each atom, while $\mathbf{K}(\omega)$ collects the terms related to the Drude model and the Fermi damping, such that:

$$K_{ij}(\omega) = \begin{cases} (1 - f(l_{ij})) \frac{2n}{1/\tau - i\omega} \frac{A_{ij}}{l_{ij}}, & \text{if } i \neq j, \\ 0, & \text{if } i = j. \end{cases} \quad (1.12)$$

Eq. (1.11) enables the calculation of ω FQ charges fluctuating under the effect of an external monochromatic field. Furthermore, this formulation of ω FQ assumes a homogeneous potential across the plasmonic substrate, neglecting retardation effects, thus framing the **ω FQ response within the quasistatic approximation**.

To conclude this section, I would like to highlight the contributions within this Ph.D. thesis that have extended the capabilities of the ω FQ model. Notably, ω FQ effectively describes the optical response of plasmonic substrates in cases where interband transitions are not involved. In [Paper I], we address this limitation by introducing a further source of polarization in the form of fluctuating dipoles, leading to the development of the Frequency-Dependent Fluctuating Charges and Fluctuating Dipoles (ω FQF μ) model. Additionally, [Paper II] extended ω FQF μ to study Au-Ag alloys, which required a redefinition of the equation governing the response. Finally, in [Paper IV] we proposed a multilevel approach combining the atomistic ω FQF μ formalism with the continuum BEM model to study silver metal NPs. This new model, which we named **ω FQF μ -BEM**, allows for the study of large metal systems by modeling the core of NPs as a spherical BEM geometry while preserving the atomistic details of the plasmonic behavior at the surface. The key features of the ω FQ, ω FQF μ , ω FQF μ -BEM, and BEM models for analyzing plasmonic substrates are summarized and compared in Table 1.1.

	ω FQ	ω FQF μ	ω FQF μ -BEM	BEM
Atomistic	✓	✓	✓*	✗
Interband Transitions	✗	✓	✓	✓
Inter/Intra-band Decouple	✗	✓	✓*	✗
Finite-size effects	✓	✓	✓	✗
Quantum tunnelling	✓	✓	✓*	✗
Defected Geometries	✓	✓	✓*	✗
Large systems	✗	✗	✓	✓

Legend: ✓ = Yes, ✗ = No, ✘ = Corrections/workarounds required
✓* = Yes, in the atomistic part

Table 1.1: Comparison of the key features of ω FQ, ω FQF μ , ω FQF μ -BEM, and BEM models.

Chapter 2

Surface-Enhanced Spectroscopies

This chapter presents the theoretical approaches used in the Ph.D. thesis to investigate the enhanced spectroscopic signals of molecules adsorbed on plasmonic NPs. The first section presents the historical context of surface-enhanced spectroscopies and introduces the fundamental principles of multiscale QM/Classical modeling. The following sections describe the specific QM/Classical strategies I employed to investigate surface-enhanced Raman scattering and surface-enhanced fluorescence.

2.1 History and Multiscale QM/Classical Modeling

The discovery of surface-enhanced spectroscopies can be traced back to the 1970s, when unexpectedly strong Raman signals were observed from molecules adsorbed onto silver electrodes.¹³⁷ Soon after, this discovery was replicated and further explored, paving the path for a rapidly growing area of study.^{5,138,139} These findings laid the foundation for Surface-Enhanced Raman Scattering spectroscopy, which significantly improved the sensitivity of conventional Raman techniques.^{31,130,140–149}

Since the discovery of SERS, other enhanced phenomena have been investigated from both experimental and theoretical perspectives. Some examples include Surface-Enhanced Fluorescence,^{9,46,58,60,66,126,150–154} Plasmon-mediated Electronic Energy Transfer,^{29,44,62,155–159} and Surface-Enhanced Raman Optical Activity,^{160–164} among others.^{31,41,42,165–170} Regardless of the specific property being studied, these enhanced effects can generally be attributed to the complex interaction of molecules with plasmonic substrates. Consequently, analyzing the molecule-substrate interactions requires a profound understanding of the complex physicochemical processes underlying the response.

In this context, theoretical modeling of surface-enhanced properties gained significant attention in numerous research papers. Entering the 21st century, some studies treated the molecule and substrate as a unified system, analyzing them within the framework of quantum mechanics (QM). However, this approach presented the major challenge of accurately representing plasmonic substrates. Due to computational limitations, many full *ab initio* models oversimplified the substrate structure to only a few atoms, which is far smaller than the actual size of substrates used in experiments.^{54,58,128–131} To overcome

this limitation, alternative approaches studied the NPs' response using classical mechanics, while the adsorbed molecules were analyzed at the QM level of theory, resulting in hybrid QM/Classical multiscale methodologies.^{61,80,123,171} These methodologies analyze the NP-molecule system by evaluating three interactions that shape the spectroscopic properties of the molecule: NP-light, molecule-light, and NP-molecule interactions. A graphical representation of these three interconnected interactions is shown in Fig. 2.1.

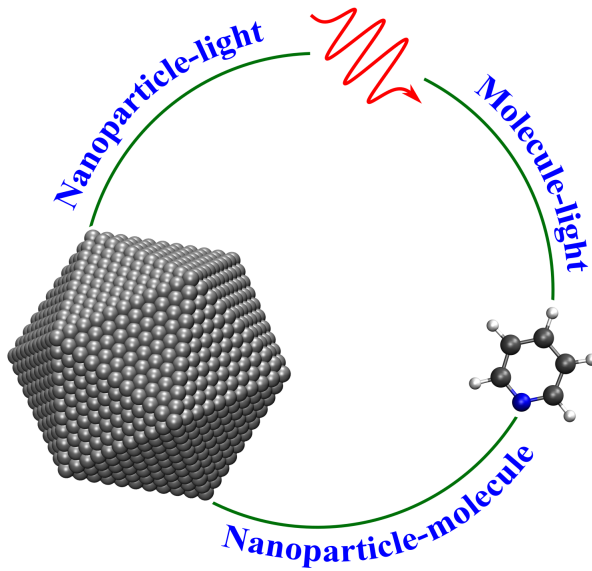


Figure 2.1: Graphical depiction of the multiscale QM/Classical modeling framework.

The NP-light interaction has already been addressed using classical models, as discussed in Chapter 1. In contrast, the molecular response to light irradiation is treated as a well-established textbook concept and will not be derived in detail in this dissertation.^{172,173} The remaining aspect is the **mutual polarization** between the plasmonic substrate and the molecular system.

As stated above, this thesis focused on surface-enhanced Raman scattering and surface-enhanced fluorescence. The two spectroscopies share the conceptual partitioning of the system in Fig. 2.1. In the following, the fundamental physics behind them is presented and discussed.

2.2 Surface-Enhanced Raman Scattering (SERS)

Surface-Enhanced Raman Scattering (SERS) exploits the significant amplification of Raman signals from molecules adsorbed onto plasmonic substrates, effectively overcoming the inherent low sensitivity of conventional Raman spectroscopy.^{30,31,61,148,149,174,175} Since its discovery, this technique has garnered significant interest, leading to a vast body of literature that explores both its experimental and theoretical aspects. Beyond

academic research, SERS has found applications in diverse fields such as medicine, biology, and catalysis, highlighting its versatility and potential for real-world implementations.^{1,30,31,130,141–149,174–182}

The remarkable enhancement of Raman signals observed in SERS, which can reach up to $10^{10–11}$ fold, is largely attributed to two primary mechanisms: electromagnetic enhancement and chemical enhancement. The electromagnetic mechanism, responsible for amplifications of up to $10^{6–7}$, arises from the interaction between the molecules and the intense electric fields generated by plasmonic nanostructures. In contrast, chemical enhancement, contributing an additional $10^{2–3}$ fold increase, arises when the molecules are chemisorbed to the substrate.^{31,148,149,183}

To achieve a deeper understanding of SERS enhancement mechanisms, theoretical modeling has become indispensable, with multiscale hybrid QM/Classical strategies serving as essential tools. Notably, S. Corni and J. Tomasi pioneered the QM/BEM approach, which allowed for the study of SERS spectra for molecules physisorbed onto substrates modeled as a continuum dielectric.^{70,111,112,117,184} Later, Jensen *et al.* expanded on this by introducing a classical atomistic description of plasmonic nanoparticles through the Discrete Interaction Models (DIMs), leading to the development of the QM/DIM formalism for SERS.^{59,80–82,86,185,186} These multiscale models are highly effective in capturing the electromagnetic enhancement mechanism. However, they do not account for chemical enhancement effects. Despite this limitation, the dominant role of electromagnetic enhancement has allowed these models to produce valuable insights, helping to rationalize experimental results.⁶¹

Throughout my Ph.D. research, I have focused on the development of classical models to study the plasmonic response of metal NPs and their integration with a QM formalism to evaluate SERS, focusing on the electromagnetic enhancement mechanism (see [Paper IV]). In this QM/Classical coupling, two key contributions from the NP influence the molecular signal: the **image field** and the **reflected field**. The image field is generated by the polarization of the NP in response to the molecular electronic density, which is perturbed by light irradiation. In contrast, the reflected field results from the NP's interaction with the electromagnetic field scattered by the molecule and subsequently reflected on the NP.^{59,61,70} A graphical representation summarizing this modeling framework is provided in Fig. 2.2

In a QM/Classical framework, the QM response polarized by the classical NP is evaluated within the framework of the Time-Dependent Kohn-Sham equations as:^{61,172,173}

$$\left[\begin{pmatrix} \mathbf{A} & \mathbf{B} \\ \mathbf{B}^* & \mathbf{A}^* \end{pmatrix} - (\omega + i\Gamma) \begin{pmatrix} \mathbf{I} & 0 \\ 0 & -\mathbf{I} \end{pmatrix} \right] \begin{pmatrix} \mathbf{X} \\ \mathbf{Y} \end{pmatrix} = - \begin{pmatrix} \mathbf{Q} \\ \mathbf{Q}^* \end{pmatrix} \quad (2.1)$$

$$\begin{aligned} A_{ai,bj} &= (\varepsilon_a - \varepsilon_i)\delta_{ab}\delta_{ij} + (ai|bj) - c_x(ab|ij) + c_l f_{ai,bj}^{xc} + K_{ai,bj}^{\text{pol}}(\omega) \\ B_{ai,bj} &= (ai|bj) - c_x(aj|ib) + K_{ai,bj}^{\text{pol}}(\omega) \\ Q_{ia} &= \langle \phi_i | V^{\alpha,\text{pert}}(\mathbf{r}, \omega) | \phi_a \rangle \end{aligned} \quad (2.2)$$

In Eq. (2.1), ω denotes the input frequency, while Γ is a phenomenological damping

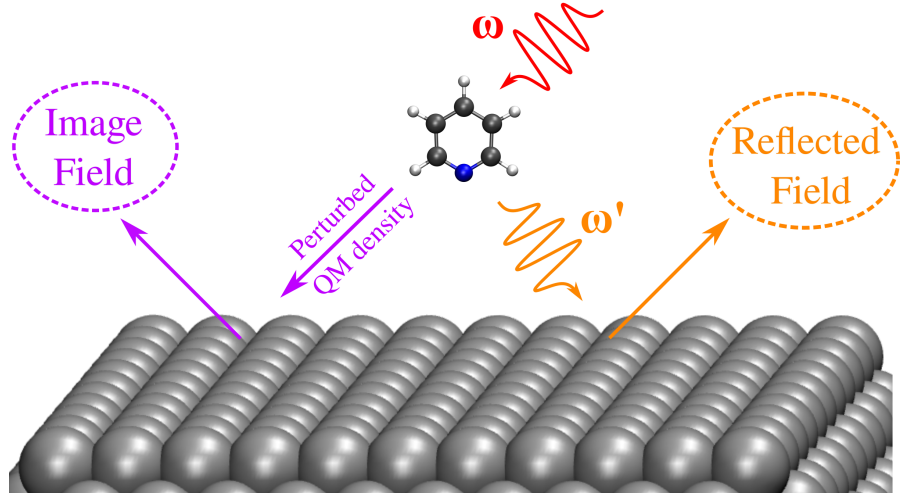


Figure 2.2: Graphical representation of molecule-substrate interactions in SERS.

term accounting for the excited states lifetime. The matrices \mathbf{X} and \mathbf{Y} correspond to the excitation and de-excitation transition densities, respectively. The indices i, j (a, b) refer to occupied (virtual) Kohn-Sham orbitals, $(ai|bj)$ represents two-electron integrals, and ε symbolizes the molecular orbital energy. The terms c_x and c_l vary in form depending on the chosen exchange-correlation DFT functional, and \mathbf{K}^{pol} accounts for the contribution of the image field polarization. Then, the expectation value of the perturbation operator ($V^{\alpha, \text{pert}}$) gathers the effects of the potential arising from the external electric field and the local field operator, which includes the influence of the reflected field.^{59,61,70}

Solving Eq. (2.1) enables the calculation of the polarizability tensor ($\bar{\alpha}$), which encapsulates the QM response to external radiation. The polarizability is computed by contracting the dipole matrix (\mathbf{H}) with the first-order perturbed density matrix (\mathbf{P}). When a monochromatic electric field with frequency ω interacts with the system and scatters at frequency ω' , the polarizability is given by $\bar{\alpha}_{\alpha\beta}(\omega; \omega') = -\text{tr} [\mathbf{H}^\alpha(\omega)\mathbf{P}^\beta(\omega')]$, where the indices α and β represent the Cartesian components of the incident and scattered fields, respectively.^{59,61,70}

Finally, Raman spectra can be computed from $\bar{\alpha}$ using Placzek's theory. This approach evaluates the spectra based on the frequency-dependent polarizability derivatives corresponding to the normal modes of a QM system. Under the assumption that $\omega \approx \omega'$, the intensity of the Raman signal associated with the k -th normal mode (I^k) is given by:^{187–189}

$$I^k \propto \frac{(\omega - \omega_k)^4}{\omega_k} \{ 45[\alpha'_k(\omega - \omega_k; \omega)]^2 + 7[\gamma'_k(\omega - \omega_k; \omega)]^2 \} \quad (2.3)$$

where ω_k is the frequency of the k -th normal mode, and α'_k and γ'_k are its isotropic and anisotropic polarizability derivatives, respectively.

2.3 Surface-Enhanced Fluorescence (SEF)

The relationship between the fluorescence lifetimes of chromophores and their proximity to metal surfaces was first observed in the 1960s.¹⁹⁰ However, it was after the discovery of SERS that Surface-Enhanced Fluorescence (SEF) began to garner significant scientific attention.^{150,151} Since then, SEF has emerged as a valuable tool with applications spanning a variety of fields, including biosensing,^{46,66,191–194} and bioimaging.^{41,60,195,196}

The fluorescence modification of a chromophore near a metal surface is primarily driven by the energy transfer between them, which strongly depends on the distance separating the chromophore and the metal. Notably, very short distances often result in significant or complete fluorescence **quenching**. Conversely, increasing this distance can **enhance** fluorescence signals up to 10^5 folds. The maximum enhancement occurs at an optimal chromophore–NP separation, which can be experimentally adjusted to precise levels.^{8,153,154,197–199}

Understanding the fluorescence enhancement or quenching caused by the metal effect requires a detailed analysis of the underlying physical phenomena. As illustrated in the Jablonski diagram in Fig. 2.3, the fluorescence of a chromophore mediated by a nearby metal NP, assuming only singlet molecular states (S) are involved, typically follows three key steps:^{58,126}

1. **Absorption:** The chromophore undergoes enhanced excitation from its electronic ground state (S_0) to an excited state. This step is described by the **absorption rate** (Γ^{abs}).
2. **Relaxation:** The excited states undergo radiationless internal conversion and further non-radiative relaxation to the lowest vibrational state of the emitting excited electronic state (S_1).
3. **Emission:** The chromophore returns from S_1 to S_0 emitting photons, which generate the fluorescence signal. This is governed by the **radiative decay rate** (Γ^{rad}). In addition, non-radiative relaxation occurs towards S_0 . This is characterized by the **non-radiative decay rate** (Γ^{nonrad}).

In this context, the distances between molecules and NPs typically used in the experiments are sufficiently large to render any chemical effects on the SEF process negligible.^{153,154} Consequently, a purely electrostatic QM/Classical modeling approach can effectively capture the empirical variations observed in SEF signals, particularly by assessing how the NPs influence Γ^{abs} , Γ^{rad} , and Γ^{nonrad} .

During my Ph.D., I extended the ω FQ($F\mu$) model to investigate the impact of atomistic metal NPs on the fluorescence response of nearby chromophores using a QM/Classical strategy. To achieve this, I reformulated the QM/Continuum framework established by Corni *et al.* to a QM/Atomistic perspective, as detailed in [Paper III].^{58,60,62,113–115,126} This theoretical modeling incorporates the metallic polarization to the Time-Dependent Density Functional Theory (TDDFT) equation, which is expressed as:^{113,172,173}

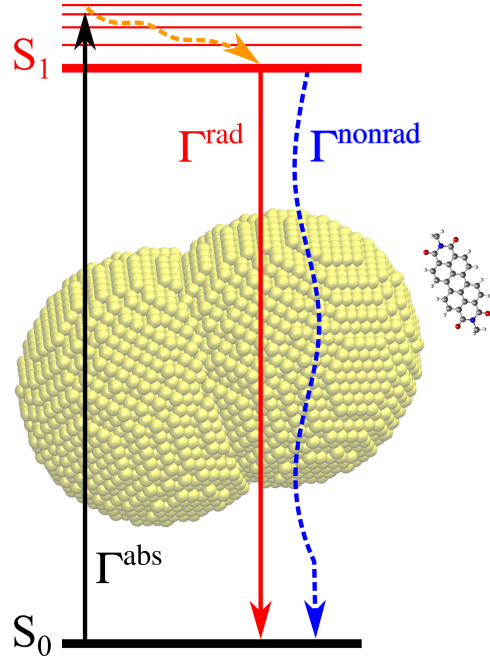


Figure 2.3: Jablonski diagram of a common SEF setup.

$$\left[\begin{pmatrix} \mathbf{A} & \mathbf{B} \\ \mathbf{B}^* & \mathbf{A}^* \end{pmatrix} - \omega \begin{pmatrix} \mathbf{I} & 0 \\ 0 & -\mathbf{I} \end{pmatrix} \right] \begin{pmatrix} \mathbf{X} \\ \mathbf{Y} \end{pmatrix} = 0 \quad (2.4)$$

where the \mathbf{A} and \mathbf{B} matrices are defined in Eq. (2.2), ω represents the frequency, and \mathbf{X} and \mathbf{Y} are the excitation and de-excitation transition densities, respectively.

It is important to note that Eq. (2.4) only includes the NP's polarization arising from the image field. The modified TDDFT equations can be solved to calculate the real and imaginary parts of the excitation frequencies.¹¹³ We can then obtain the fluorescence descriptors using the expressions:^{58,60,114,126}

$$\begin{aligned} \Gamma^{\text{abs}} &= \frac{2\pi}{3\hbar c} |\boldsymbol{\mu}_{\text{tot}}^{0K}|^2 & \Gamma^r &= \frac{4\omega'^3}{3\hbar c^3} |\boldsymbol{\mu}_{\text{tot}}^{K0}|^2 & \Gamma^{\text{nr}} &= -2\omega'' \\ \Phi^{\text{RB}} &= \frac{\Gamma^{\text{abs}}}{\Gamma_{\text{free}}^{\text{abs}}} \left(\frac{\Gamma^r}{\Gamma^r + \Gamma^{\text{nr}}} \right) \end{aligned} \quad (2.5)$$

where $\boldsymbol{\mu}_{\text{tot}}^{0K}$ ($= \boldsymbol{\mu}_{\text{molecule}}^{0K} + \boldsymbol{\mu}_{\text{NP}}^{0K}$) represents the total dipole generated by the $0 \rightarrow K$ transition in the molecule-NP system, \hbar is the reduced Planck constant, and c is the speed of light. ω' and ω'' are the real and imaginary parts of the excitation frequency, respectively. Additionally, $\Gamma_{\text{free}}^{\text{abs}}$ is the absorption rate of the molecule *in vacuo*, while Φ^{RB} indicates the relative brightness.

To conclude this section, I would like to highlight that Φ^{RB} quantifies the modification of the chromophore's fluorescence signal in the presence of the NP. Specifically,

$\Phi^{\text{RB}} = 1$ indicates the fluorescence intensity of the free molecule, $\Phi^{\text{RB}} < 1$ signifies quenching, and $\Phi^{\text{RB}} > 1$ denotes fluorescence enhancement. According to Eq. (2.5), the optimal SEF setup increases Γ^{abs} and Γ^{rad} , while minimizing the value of Γ^{nonrad} . This can be achieved by tuning the plasmon resonance frequency of the metal, therefore regulating the extent to which the NP response influences the absorption and emission processes.^{58,60,126}

Chapter 3

Overview of attached publications

In [Paper I], we developed the Frequency-Dependent Fluctuating Charges and Fluctuating Dipoles ($\omega\text{FQF}\mu$) model by extending the ωFQ framework. $\omega\text{FQF}\mu$ endows each NP atom with a charge and a dipole, which enables the description of the d -shell polarizability. As a result, the approach captures the effect of intraband and interband transitions influencing the optical response of plasmonic NPs. To validate the model, $\omega\text{FQF}\mu$ results on silver and gold NPs were compared to TDDFT simulations. More specifically, we successfully replicated well-known quantum size effects, including the modifications in plasmon resonance direction and magnitude, non-local effects on the response, the gradual disappearance of the plasmon resonance in gold, and the atomistic details in the induced density at the plasmon resonance. Furthermore, we demonstrated the model's ability to describe charge transfer through a quantum tunneling regime, particularly in the context of NPs interacting at subnanometer distances.

CRediT Contributions: Data Curation, Formal Analysis, Investigation, Visualization, Writing - original draft.

[Paper II] extended the $\omega\text{FQF}\mu$ model to analyze the plasmonic properties of bimetallic Au-Ag atomistic NPs. To this end, we modified the governing equations of the model to study chemically heterogeneous systems, effectively capturing modifications in both intraband and interband transitions affecting the optical response. We parametrized the new terms accounting for the Au-Ag interactions against *ab initio* studies. Additionally, we validated our approach by comparing $\omega\text{FQF}\mu$ results with experimental data. In particular, we demonstrated its capability to precisely reproduce the plasmon resonance peaks, their shifts, and the plasmonic transition densities across various Au-Ag alloy NPs, including spheres, nanorods, and spherical core shells. Notably, while our current application focuses on bimetallic systems, the generalization of the formalism allows for the analysis of alloys composed of any atomic types, upon the appropriate parametrization of the particular metal-metal interactions.

CRediT Contributions: Data Curation, Formal Analysis, Investigation, Visualization, Writing – Original Draft.

In [Paper III], we proposed a multiscale QM/ ω FQF μ strategy to simulate Surface-enhanced Fluorescence (SEF) of chromophores near noble metal substrates. We adapted state-of-the-art QM/Continuum methodologies to a QM/atomistic formalism, within the framework of TDDFT. Initially, we validated our model against QM/BEM simulations by successfully replicating the fluorescence signal of a chromophore near spherical Ag and Au NPs. Then, we investigated how gold NPs with complex shapes (icosahedral and cuboctahedral) influence fluorescence compared to simple spherical geometries of the same size. Additionally, we studied the significant variations in SEF due to subtle atomistic modifications in silver nanorods. Finally, we analyzed the fluorescence behavior of chromophores interacting with gold and silver metal dimers, providing insights into the geometric arrangements enhancing SEF performance. Our findings underscore how NP morphology strongly influences fluorescence, while also highlighting the limitations of QM/Continuum models in accurately describing systems featuring sharp interfaces.

CRediT Contributions: Data curation, Formal analysis, Investigation, Methodology, Software, Validation, Visualization, Writing - original draft.

Finally, in [Paper IV] we developed the ω FQF μ -BEM model, which integrates the fully atomistic ω FQF μ approach with a continuum BEM layer. ω FQF μ -BEM describes the NP's surface at the ω FQF μ level, preserving the atomistic details of the surface response, while the NP's core is described as an implicit BEM sphere, which is computationally more efficient. Initially, our investigation focused on spherical silver NPs, analyzing their absorption spectra and transition density at plasmon resonance frequencies. Notably, our findings aligned with theoretical predictions based on the hybridization of individual plasmonic modes of the BEM core and ω FQF μ shell, validating our approach. Next, we refined the parameters governing the response, including the thickness of the atomistic shell, the core-to-shell distance, and the BEM discretization and permittivity function. As a result, the model demonstrated excellent computational performance while preserving the atomistic details of the localized surface plasmons. Furthermore, we extended the model to a multiscale QM/ ω FQF μ -BEM framework for simulating SERS of molecules physisorbed on icosahedral silver NPs. Rigorous testing against QM/ ω FQF μ and QM/BEM values confirmed that our model retains the atomistic details of the plasmonic behavior affecting SERS signals, while greatly improving computational efficiency, especially for larger NPs.

CRediT Contributions: Data curation, Formal analysis, Investigation, Methodology, Software, Validation, Visualization, Writing - original draft.

Chapter 4

Attached Publications

I. Do We Really Need Quantum Mechanics to Describe Plasmonic Properties of Metal Nanostructures?

Do We Really Need Quantum Mechanics to Describe Plasmonic Properties of Metal Nanostructures?

Tommaso Giovannini,* Luca Bonatti, Piero Lafiosca, Luca Nicoli, Matteo Castagnola, Pablo Grobas Illobre, Stefano Corni, and Chiara Cappelli*



Cite This: *ACS Photonics* 2022, 9, 3025–3034



Read Online

ACCESS |

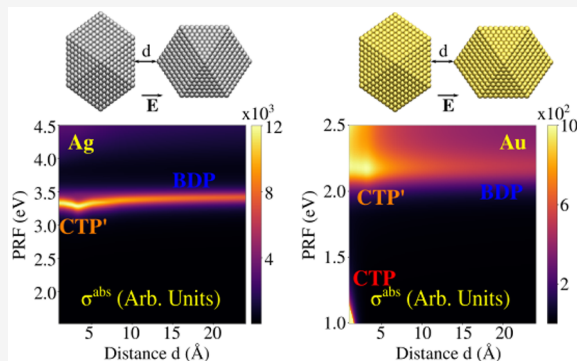
 Metrics & More

 Article Recommendations

 Supporting Information

ABSTRACT: Optical properties of metal nanostructures are the basis of several scientific and technological applications. When the nanostructure characteristic size is of the order of few nm or less, it is generally accepted that only a description that explicitly describes electrons by quantum mechanics can reproduce faithfully its optical response. For example, the plasmon resonance shift upon shrinking the nanostructure size (red-shift for simple metals, blue-shift for *d*-metals such as gold and silver) is universally accepted to originate from the quantum nature of the system. Here we show instead that an atomistic approach based on classical physics, ω FQF μ (frequency dependent fluctuating charges and fluctuating dipoles), is able to reproduce all the typical “quantum” size effects, such as the sign and the magnitude of the plasmon shift, the progressive loss of the plasmon resonance for gold, the atomistically detailed features in the induced electron density, and the non local effects in the nanoparticle response. To support our findings, we compare the ω FQF μ results for Ag and Au with literature time-dependent DFT simulations, showing the capability of fully classical physics to reproduce these TDDFT results. Only electron tunneling between nanostructures emerges as a genuine quantum mechanical effect, that we had to include in the model by an ad hoc term.

KEYWORDS: atomistic, interband, gold, silver, tunneling, field enhancement



1. INTRODUCTION

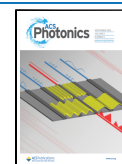
The recent progress in nanoscience has allowed to experimentally reach the atomistic detail in the geometrical arrangement of metal nanoaggregates.^{1–5} This has paved the way for many technological applications, including the creation of local hot-spots featuring enormously enhanced electric field, that has allowed single molecule detection, and even submolecular resolutions, when coupled to surface enhanced spectral techniques.^{6–13} A deep understanding of the peculiarities of these structures may benefit of an unavoidable interplaying between theory and experiments. At subnanometric scales such as for atomistically defined needles/tips, quantum effects play an important role in the plasmonic response and therefore need to be considered.^{14–23} As a result, a unified theoretical approach to describe the plasmonic properties of metal nanoaggregates under different regimes needs to consistently take into account the physical phenomena underlying the quantum and classical response.^{19,24,25}

Large-size nanoparticles are typically described by means of classical electrodynamics, such as the Mie theory,²⁶ the Discrete Dipole Approximation (DDA),²⁷ the electromagnetic Finite Difference Time Domain (FDTD),²⁸ or the Boundary Element Method (BEM).^{29–34}

Nonlocal corrections can be considered by exploiting spatially dependent dielectric function based models³⁵ or hydrodynamic models,^{36–38} which are also able to account for the electron spill-out effect that determines the near-field generated in plasmonic hot-spots of *d*-metals.^{39–41} However, these models substantially discard atomistic details, which could become relevant when studying surface-assisted spectroscopic properties.⁴² It is also worth noting that electron spill-out and nonlocal effects can effectively be treated by means of surface response functions, which would need to be specified for different surface planes.^{43,44} Limitations of these approaches for nanoparticles have recently been discussed.⁴⁵ In this context, ab initio modeling, at the Time-Dependent Density Functional Theory (TDDFT) level, is still considered the most accurate approach to deal with these effects;^{46–50} however, it can only treat relatively small metal nanoparticles (NP; with diameter < 5 nm); therefore, real-size systems

Received: May 20, 2022

Published: September 1, 2022



cannot be afforded due to the prohibitively large computational cost. Such a situation naturally leads to the conclusion that an explicit quantum mechanical treatment of electrons, such as DFT and TDDFT, is mandatory to provide a realistic picture of plasmonic phenomena in this size regime. Such a conclusion is not really challenged by the existing classical atomistic approaches to nanoplasmatics,^{51–57} that, while delivering accurate results, are based on fitting very general classical response expressions on TDDFT calculations, retaining therefore the physical basis of the latter.

In this paper, we explore whether a classical atomistic method based on essentially classical ingredients (Drude conduction mechanism and classical polarizabilities to reproduce interband polarization) can reproduce the optical response of complex plasmonic nanostructures. To this goal, we propose a physically robust approach to describe the plasmonic properties of sizable metal nanoaggregates characterized by the presence of interband transitions. Together with collective electronic excitations, they determine the plasmonic response of noble metal nanoparticles. The model is based on the recently developed ω FQ method,^{32,58–61} in which each metal atom is endowed with a net charge, which varies as a response of the external electric field. The charge-exchange between atoms is governed by the Drude mechanism. As an element of mere quantum mechanical origin that we found essential to add to our classical atomistic picture, the Drude charge exchange is modulated by quantum tunneling, which guarantees a correct description of the optical response for subnanometric junctions.^{15,16,18,20,22,58,62,63} Although the method has been successfully applied to sodium nanostructures and graphene-based materials,^{58,59} the basic formulation of ω FQ overlooks interband contributions, thus, it is unsuitable to describe the plasmonic properties of nanostructures based on *d*-metals.^{64–68} Here, we substantially extend ω FQ so to assign each metal atom with an atomic complex-valued polarizability (i.e., a complex-valued dipole moment), appropriately tuned to model interband effects. The resulting approach is called ω FQF μ (frequency-dependent fluctuating charges and fluctuating dipoles) by analogy with a parent polarizable approach, which has been proposed by some of the present authors to treat completely different chemical systems.^{69–71} The theoretical basis of the approach stems from the evidence that *d*-states can efficiently be treated as polarizable shells placed at lattice positions.⁶⁷

Notice that ω FQF μ was developed from a different perspective compared to other classical atomistic approaches.^{51–54} Indeed, ω FQF μ is built from textbook bulk metal physics rather than fitting of generic polarizability and capacity frequency-dependent expressions. This provides practical benefits as well. In fact, Drude-tunneling and interband regimes are perfectly decoupled in the two terms that depend on ω FQs⁵⁸ and ω F μ s, thus allowing for a fine, physically guided, tuning of the plasmonic response. In the following, we show that ω FQF μ is able to correctly reproduce the plasmonic properties of Ag and Au nanostructures as a function of size and shape, and also their plasmonic response when forming subnanometer junctions. Remarkably, the favorable scaling of the method permits to afford large systems (more than 10^4 atoms), which cannot be treated at the quantum-mechanical level. Also, the ability of ω FQF μ to fully retain the atomistic detail is crucial to reproduce not only the plasmonic response but also near-field enhancements, which play a key-role in near-field enhanced spectroscopies.^{72,73}

2. THEORETICAL MODEL

ω FQF μ is a fully atomistic, classical approach which substantially extends ω FQ, which assigns to each metal atom a time dependent charge. Under the action of a time dependent external electric field, metal atoms exchange charge via the Drude conduction mechanism, which is further assisted by quantum tunneling, which limits the charge transfer among nearest neighboring atoms and makes the interaction decrease with the typical exponential decay.⁵⁸ In particular, ω FQ charge equation of motion in the frequency domain (ω) reads:⁵⁸

$$\begin{aligned} -i\omega q_i(\omega) &= \frac{2n_0\tau}{1-i\omega\tau} \sum_j [1-f(l_{ij})] \frac{\mathcal{A}_{ij}}{l_{ij}} (\phi_j^{\text{el}} - \phi_i^{\text{el}}) \\ &= \sum_j K_{ij} (\phi_j^{\text{el}} - \phi_i^{\text{el}}) \end{aligned} \quad (1)$$

where $q_i(\omega)$, a complex-valued quantity, is the Fourier component at the frequency ω of the oscillating atomic charge on atom *i*. n_0 is the metal density, τ the friction time, \mathcal{A}_{ij} is the effective area connecting *i*th and *j*th atoms, and l_{ij} is their distance. ϕ^{el} is the electrochemical potential acting on each metal atom, which takes into account the interactions between the different atoms and their interaction with the external electric field, which oscillates at frequency ω . $f(l_{ij})$ is a Fermi-like function mimicking quantum tunneling:⁵⁸

$$f(l_{ij}) = \frac{1}{1 + \exp\left[-d\left(\frac{l_{ij}}{s \cdot l_{ij}^0} - 1\right)\right]} \quad (2)$$

where l_{ij}^0 is the equilibrium atom–atom distance, whereas d and s are dimensionless parameters that determine the sharpness and the center of the Fermi function $f(l_{ij})$, respectively. Their values can be determined by comparing computed results with reference ab initio data (see also Section S1 in the Supporting Information (SI)). In eq 1, Drude and tunneling terms are collected in the K matrix. The parameters entering ω FQ all have a clear microscopic physical meaning. Therefore, their values can be either chosen by an independent experiment or fitted to reproduce higher level results, and then the soundness of their values can be judged. We took the latter perspective, as discussed in the SI.

Due to its physical foundations, ω FQ cannot describe the specificity of metals featuring *d*-electrons, which contribute to interband transitions and that substantially affect the plasmon response.^{64–68} Therefore, we here extend ω FQ into a novel method, ω FQF μ , in which each atom is assigned a charge and an additional source of polarization, that is, an atomic polarizability (to which an induced dipole moment is associated). The presence of the dipole moments is included in eq 1 by taking into account the interaction between charges and dipoles in the electrochemical potential. The induced dipole moments μ_i are instead obtained by solving the following set of linear equations:

$$\mu_i = \alpha_i^\omega (\mathbf{E}_i^{\text{ext}} + \mathbf{E}_i^\mu + \mathbf{E}_i^q) \quad (3)$$

where, \mathbf{E}^{ext} , \mathbf{E}^μ , and \mathbf{E}^q are the external electric field and those generated by the other dipole moments and charges, respectively. α^ω is the atomic complex polarizability, which is introduced to describe interband transitions. Remarkably, α^ω can easily be obtained by extracting interband contributions

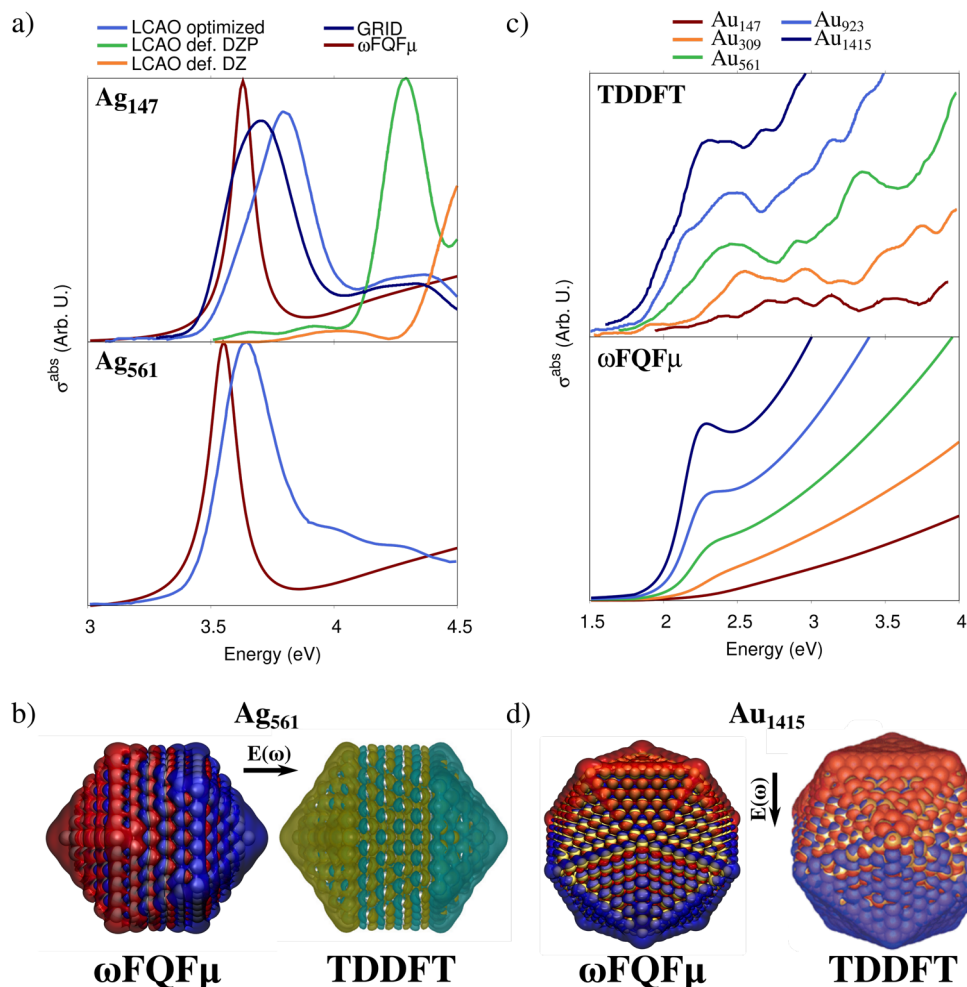


Figure 1. (a) Computed $\omega\text{FQF}\mu$ and TDDFT σ^{abs} for Ag₁₄₇ (~ 0.8 nm radius) and Ag₅₆₁ (~ 1.4 nm radius). TDDFT results are reproduced from ref 87 and obtained by exploiting different basis sets (LCAO optimized, def. DZ (double- ζ), def. DZP (double- ζ polarized)) and on a real-space grid (GRID). (b) $\omega\text{FQF}\mu$ and TDDFT⁸⁷ plasmon densities for Ag₅₆₁. TDDFT plasmon densities adapted with permission from ref 87. Copyright 2015 APS Publications. (c) $\omega\text{FQF}\mu$ and TDDFT⁸⁸ σ^{abs} for Au₁₄₇–Au₁₄₁₅ (~ 1.9 nm radius). (d) $\omega\text{FQF}\mu$ and TDDFT⁸⁸ plasmon densities for Au₁₄₁₅. TDDFT plasmon densities adapted with permission from ref 88. Copyright 2014 ACS Publications. $\omega\text{FQF}\mu$ isovalue are set to 0.002 and 0.0005 au for Ag and Au, respectively.

from the experimental permittivity function (see *Section S1* in the *SI*), with no need to introduce a posteriori adjustable parameters.

To effectively couple charges and dipoles, that is, to simultaneously account for Drude and interband transitions, *eqs 1* and *3* need to be solved simultaneously. By explicitly indicating all terms, the problem can be recast as the following set of linear equations:

$$\begin{aligned} & \sum_{j=1}^N \left(\sum_{k=1}^N K_{ik} (T_{kj}^{qq} - T_{ij}^{qq}) + i\omega\delta_{ij} \right) q_j \\ & + \sum_{j=1}^N \left(\sum_{k=1}^N K_{ik} (T_{kj}^{q\mu} - T_{ij}^{q\mu}) \right) \mu_j \\ & = \sum_{k=1}^N K_{ik} (V_i^{\text{ext}} - V_k^{\text{ext}}) \end{aligned} \quad (4)$$

$$\sum_{j \neq i} T_{ij}^{\mu q} q_j + \sum_{j \neq i} T_{ij}^{\mu\mu} \mu_j + \frac{1}{\alpha_i^\omega} \mu_i = \mathbf{E}_i^{\text{ext}} \quad (5)$$

where T^{qq} , $T^{q\mu}$, and $T^{\mu\mu}$ define charge–charge, charge–dipole, dipole–dipole interactions, respectively. By imposing $T^{\mu\mu}$ diagonal elements to correspond to $1/\alpha_i^\omega$, *eqs 4* and *5* can be written in a compact matrix formulation as

$$\begin{pmatrix} \mathbf{A}^{qq} & \mathbf{A}^{q\mu} \\ \mathbf{T}^{\mu q} & \mathbf{T}^{\mu\mu} \end{pmatrix} \begin{pmatrix} \mathbf{q} \\ \boldsymbol{\mu} \end{pmatrix} = \begin{pmatrix} \mathbf{f}^q \\ \mathbf{f}^\mu \end{pmatrix} \quad (6)$$

where the complex \mathbf{A} matrices include interaction kernels and the K_{ij} terms (see *Section S1* in the *SI* for more details). The right-hand side of *eq 6* accounts for external polarization sources, that is, the electric potential and field calculated at atomic positions:

$$\begin{aligned} f_i^q &= \sum_j K_{ij} (V_i^{\text{ext}} - V_j^{\text{ext}}) \\ \mathbf{f}_i^\mu &= \mathbf{E}_i^{\text{ext}} \end{aligned}$$

Notably, any kind of plasmonic materials can be modeled by $\omega\text{FQF}\mu$ because it integrates all relevant physical ingredients (i.e., Drude conduction, electrostatics, quantum tunneling and interband transition) via *eq 1* and *eq 3*. Also, once complex-

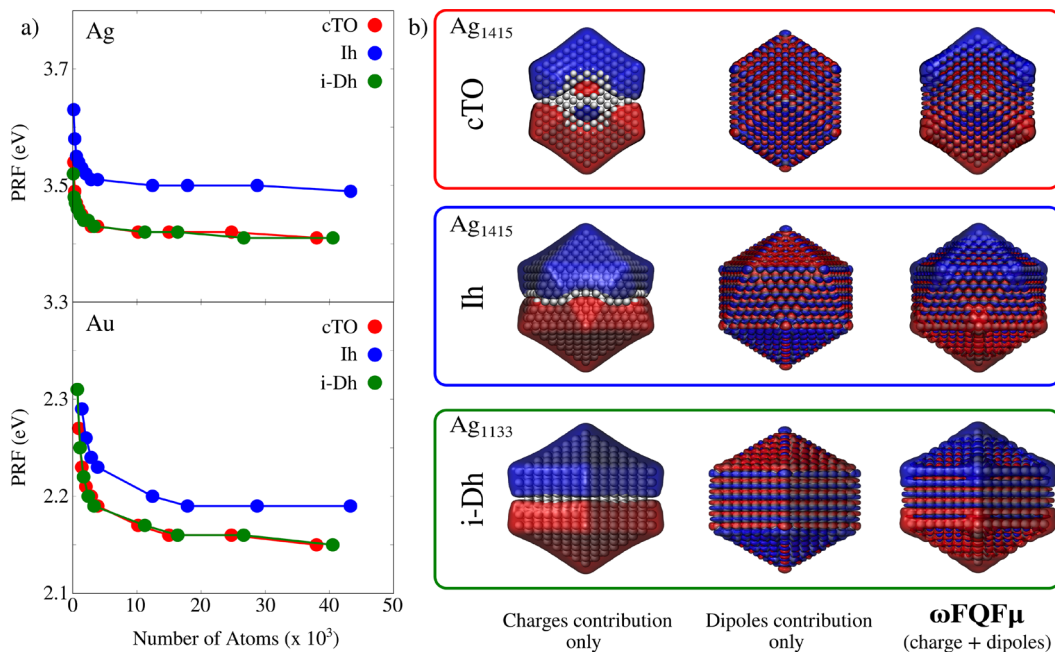


Figure 2. (a) Ag and Au PRF for cTO, Ih, and i-Dh NPs as a function of the number of atoms. (b) Ag densities calculated at the PRF for cTO (top), Ih (middle), and i-Dh (bottom) geometries. Charge and dipole contributions are plotted together with $\omega\text{FQF}\mu$ plasmon densities. Isovalues are 0.002 and 0.0005 au for Ag and Au, respectively.

valued charges and dipoles are computed, the absorption cross section σ^{abs} and the induced electric field can easily be calculated (see Section S1 in the SI for more details).

To conclude this section, it is worth noting that other atomistic, classical models, belonging to the Discrete Interaction Model (DIM) class, have been proposed to describe the plasmonic response of noble-metal nanoparticles.^{54,74} Among them, the coordination-dependent–Discrete Interaction Model (cd-DIM)⁷⁴ is able to properly describe the size dependency of the Plasmon Resonance Frequency (PRF) for Ag NPs and the plasmonic response of Ag dimers, which is governed by quantum tunneling. Within this model, both effects arise from a modification of the coordination of surface atoms and the consequent modification of the atomic polarizability that is considered to be a parametrized function of the coordination number. In our approach the first effect genuinely originates from the screening effect of d -electrons, which is physically modeled by the presence of the α^ω term. A correct description of the plasmonic response of dimers arises from the phenomenological introduction of the quantum tunneling via the Fermi function in eq 2.

3. RESULTS AND DISCUSSION

3.1. Optical Response of Metal Nanoparticles: $\omega\text{FQF}\mu$ versus TDDFT Results. Here the capability of $\omega\text{FQF}\mu$ in describing typical plasmonic response properties of single metal nanoparticles is discussed.⁷⁵ Although the model is completely general, it is here applied to Ag and Au nanoparticles (NP), for which α^ω values are obtained from the permittivity functions reported by Etchegoin et al. in ref 76 and fitted in ref 77 (see also Section S1 in the SI). For both metals, we first consider NPs with three different geometrical arrangements, namely, truncated cuboctahedron (cTO), icosahedral (Ih), and ino-decahedron (i-Dh), which are all characterized by atomistically defined edges.⁵⁴ Their plasmonic

properties are studied as a function of the size (from a minimum of 85 atoms, ~ 5 Å radius, to a maximum of 43287 atoms, ~ 65 Å radius).^{78–80} Note that geometry relaxation is not considered, because it only slightly affects optical responses.^{23,81–86}

Although sizable NPs cannot be afforded by ab initio methods, they can indeed be treated by $\omega\text{FQF}\mu$,⁶⁰ at a reasonable computational time (on average, 59 min on Intel(R) Xeon(R) Gold 5120 CPU @ 2.20 GHz, 28 processors, for each frequency given in input for the structure composed of 43287 atoms). As an example of the performance of $\omega\text{FQF}\mu$, Kuiska et al.⁸⁷ have reported that the calculation of the optical spectrum of Ag₅₆₁ (~ 1.4 nm radius) in Ih geometry with the time-propagation (TP) approach to TDDFT requires a wall time of 42.0 h with 512 cores.⁸⁷ For the same system, $\omega\text{FQF}\mu$ only requires 25 s on the aforementioned platform. Remarkably, $\omega\text{FQF}\mu$ and reference TDDFT data are very similar (see Figure 1a, bottom panel). Slight discrepancies in the PRF and band broadening among the two models can be justified by considering that TDDFT results substantially vary as a function of the basis set; this is demonstrated by the data shown in Figure 1a (top panel), which are taken from ref 87. Clearly, reference ab initio data display large variability of almost 1 eV when moving from linear combinations of atomic orbitals (LCAO) with different basis sets to real space grid calculation (GRID) results. We also remark that the width of peaks is chosen arbitrarily in TDDFT calculations.

A similar comparison can be performed for Au Ih NPs. TDDFT absorption cross sections reproduced from ref 88 and calculated at the $\omega\text{FQF}\mu$ level are reported in Figure 1c,d. Also, in this case, $\omega\text{FQF}\mu$ can correctly reproduce PRF trends as a function of the NP size and the relative intensities of the bands for the different NPs.

One of the most peculiar features of noble metal NPs and, in general, of d -metals is that the PRF blue shifts as the size of the

system decreases, in contrast to what happens for simple metals (and correctly reproduced by $\omega\text{FQ}\mu$ ⁵⁸). The physical origin of this blue-shift has been studied in the past.⁶⁷ The screening of the Coulomb interaction among conduction electrons (that determines the plasmon frequency) by the localized *d*-electron core interplays with conduction electrons spill-out at the cluster surface. In short, the *d*-electron core screens electron–electron repulsion, thus decreasing the *d*-metal plasmon frequency compared to what is expected on the basis of the free-electron density of the metal. At the surface, conduction electrons spill out of the structure; in ωFQ and $\omega\text{FQ}\mu$, the finite size of each atomic distribution accounts for this effect. In parallel, the *d*-electron core, which is localized on the metal atom (described by a point dipole in $\omega\text{FQ}\mu$) cannot effectively screen the electron–electron repulsion. As a result, the plasmon frequency moves back to the nonscreened, free-electron value. Remarkably, $\omega\text{FQ}\mu$ can indeed describe this mechanism because it provides the right result for the right reason. In fact, if the *d*-electron core response is artificially switched-off (i.e., $\alpha^o \rightarrow 0$ in eq 3), the plasmon frequency (which is overall increased), red shifts for metal nanoparticles, as it is expected based on spill-out effects only.^{58,87} This is demonstrated by the plots reported in Figure S3 in the SI.

The dependence of computed PRFs on the number of atoms is reported in Figure 2a for different geometries; the plots clearly demonstrate that $\omega\text{FQ}\mu$ can indeed correctly reproduce the previously reported trends. Also, the linear fit of Ag Ih PRFs as a function of the inverse of the NP diameter permits to linearly extrapolate PRF = 3.47 eV for an infinite diameter. This value is in almost perfect agreement with the mesoscopic limit of 3.43 eV, as obtained at the quasi-static FDTD (QSFDTD) level,⁸⁷ and in excellent agreement with the extrapolated ab initio value of 3.35 eV (see also Figure S4 in the SI).⁸⁷

The investigation of plasmon densities (i.e., the imaginary part of the charge density induced by a monochromatic electromagnetic field oscillating at the PRF) is of fundamental importance for correctly characterizing the plasmon resonance. Computed densities at the PRF for the largest structures in each geometrical arrangement are depicted in Figure 2b. In all cases, they represent a dipolar plasmon. Our result can be compared with reference ab initio data for Ag₅₆₁ (~1.4 nm radius, see Figure 1b) and Au₁₄₁₅ (~1.9 nm radius, see Figure 1d). In both cases, the agreement is almost perfect.

For the purpose of a deeper theoretical analysis, $\omega\text{FQ}\mu$ can also be used to decouple the contributions of Drude and interband transitions to the total plasmon density. Charge and dipole contributions are graphically depicted in Figure 2b for selected Ag NPs (see Figure S5 in the SI for Au NPs). Clearly, the two plasmon densities are associated with dipole moments in opposite directions. This finding remarks the screening role of the *d*-electrons response.^{41,67} As explained above, this results in the typical blue shift observed for *d*-metals.

To further demonstrate the ability of $\omega\text{FQ}\mu$ to correctly take into account screening effects in *d*-metal NPs, we can compare density distributions in inner regions. Computed $\omega\text{FQ}\mu$ and TDDFT densities for Au₁₄₁₅ Ih NP (~1.9 nm radius), in the central region of the cluster (defined for $-2 < z < 2$ Å), are depicted in Figure 3. Notice that densities are computed at the corresponding PRFs, which only differ by 0.01 eV. Coherently with the results reported in Figure 1d, positive and negative charges are located at the top and bottom surface regions, respectively. However, $\omega\text{FQ}\mu$ and TDDFT

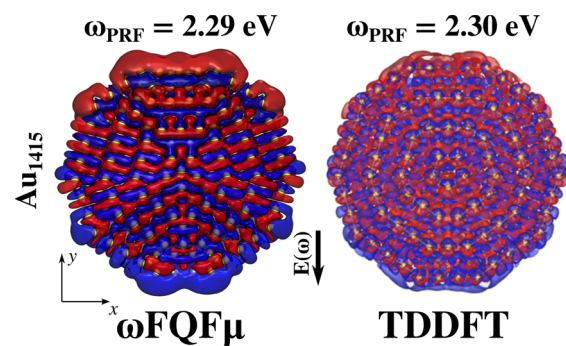


Figure 3. $\omega\text{FQ}\mu$ and TDDFT⁸⁸ Au₁₄₁₅ (~1.9 nm radius) plasmon densities in the central region of the cluster ($-2 < z < 2$ Å). TDDFT plasmon densities adapted with permission from ref 88. Copyright 2014 ACS Publications.

densities are mainly characterized by a local charge distribution around each Au atom, which is polarized along an opposite direction with respect to the polarization of the surface density. Such a behavior is related to screening effects, which are correctly taken into account by our atomistic, yet classical model.

In Figure 4a,b the total enhanced electric field ($|E|/|E_0|$, where E_0 is the external electric field intensity) at the PRF is reported. Such quantity (elevated to the fourth power) is related to field enhancement factors that are measured in SERS experiments.¹⁰ The dependence of $|E|/|E_0|$ factors as a function of the number of atoms and the NPs radius is reported in Figure 4a and b, respectively. Notice that enhancement factors are computed at a distance of 3 Å from the tip of each structure; according to many previous reports, it corresponds to the typical adsorption distance of molecular systems.⁸⁹ $|E|/|E_0|$ color maps at the PRF for each geometrical arrangement are graphically displayed in Figures 4c. As expected, $|E|/|E_0|$ maximum values correspond to tips, and are reported for cTO geometries (for both gold and silver), where edges are the sharpest. Interestingly, for all arrangements, $|E|/|E_0|$ follows a $\sqrt[3]{N}$ trend (N being the number of atoms) and, thus, a linear trend with respect to NP radius, because the difference in the electric potential linearly increases with the NP intrinsic size. Remarkably, $\omega\text{FQ}\mu$ is also able to quantify the differences between Ag and Au NPs, being the latter associated with much lower enhancement factors as compared to the former, as expected in this frequency range.

As a final comment, it is remarkable that $\omega\text{FQ}\mu$ is able to describe nonlocal effects. To demonstrate that, we artificially changed the total electric potential and field acting on a specific atom placed at the surface or at the centroid of Ag₁₄₇ (~0.8 nm radius) and Ag₃₈₇₁ (~2.7 nm radius) structures in the Ih configuration. As a result, independently of the atom position, not only charge and the dipole of the perturbed atom are modified, but also those of other atoms (see Figure S6 in the SI).

3.2. Subnanometer Junctions. In this section we will show that $\omega\text{FQ}\mu$ has the potential to describe hot-spots in subnanometer junctions in a physically consistent manner. This is possible due to the account for quantum tunneling (eq 1), which dominates the plasmon response in these systems. To showcase $\omega\text{FQ}\mu$ performances, we study Ag₂₈₆₉/Au₂₈₆₉ (~2.6 nm radius) cTO dimers. In particular, we select two different morphologies obtained by approaching two NPs so to obtain surface–tip or surface–surface geometrical arrange-

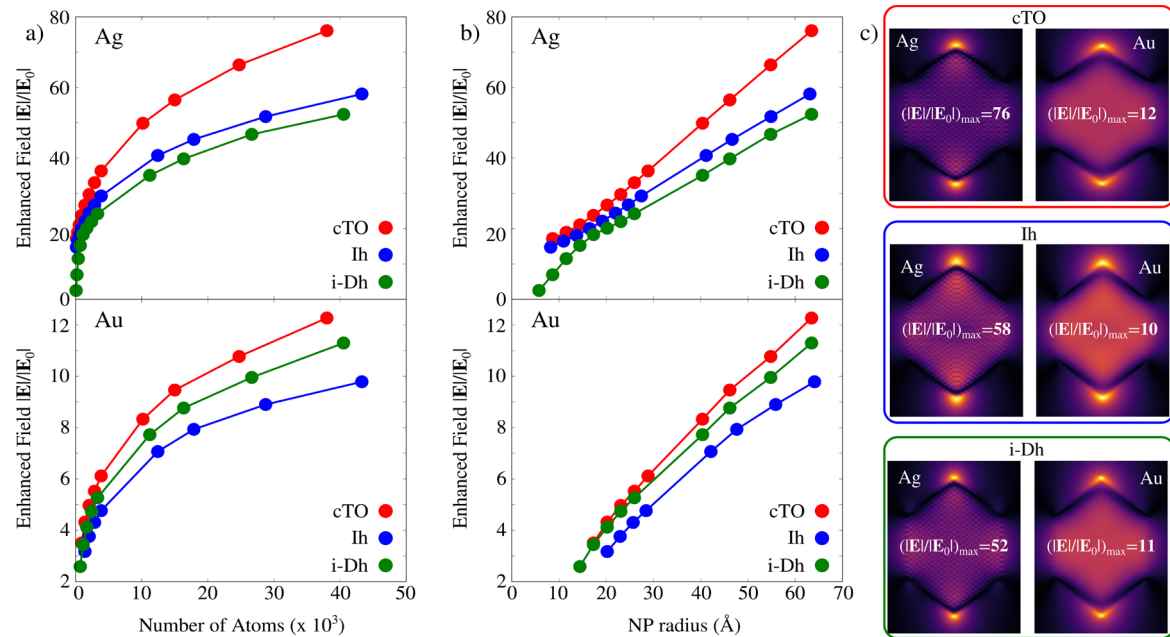


Figure 4. Ag and Au enhanced electric field $|E|/|E_0|$ calculated at 3 Å from the tips for cTO, Ih, and i-Dh NPs as a function of the number of atoms (a) and NP radius (b). (c) Ag and Au $|E|/|E_0|$ color maps for cTO (top), Ih (middle), and i-Dh (bottom) geometries.

ments (see Figures 5 and 6).⁹⁰ Note that for both structures the structural relaxation effects are not taken into account,

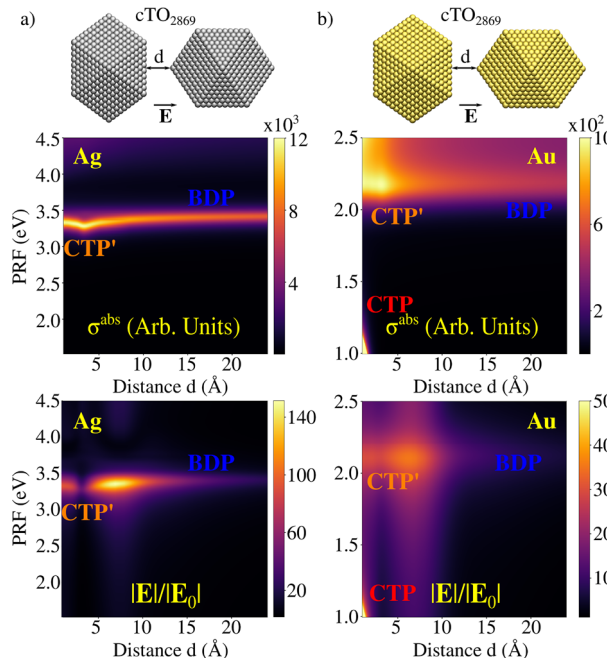


Figure 5. Ag (a) and Au (b) cTO₂₈₆₉ dimers in surface–tip geometrical arrangement. Color maps of σ^{abs} and $|E|/|E_0|$ as a function of the PRF and the distance between the two NPs are reported in the middle and bottom panels, respectively.

similarly to previous studies.⁸¹ However, to study the effects of structural relaxation we have modeled surface roughness as derived from an atomic adjustment on the surface of one of the two cTO NPs in the surface–surface arrangement (see Figure S7 in the SI).

For the ideal cTO dimers, we investigate both σ^{abs} and $|E|/|E_0|$ calculated at the gap's center as a function of the distance d

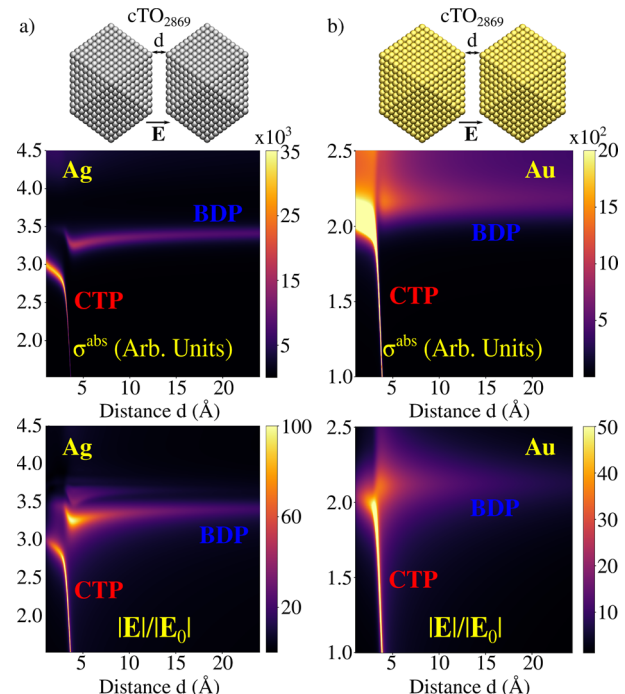


Figure 6. Ag (a) and Au (b) cTO₂₈₆₉ dimers in surface–surface geometrical arrangement. Color maps of σ^{abs} and $|E|/|E_0|$ as a function of the PRF and the distance between the two NPs are reported in middle and bottom panels, respectively.

between the two monomers, in the range 1–24 Å. Computed spectra (Figure 5a,b) are characterized by a high energy peak (~3.5 eV for Ag and ~2.2 eV for Au), which red-shifts as d decreases. However, a clear discontinuity occurs at around 4 Å, where quantum tunneling plays a relevant role; in fact, such a distance is close to the Ag–Ag and Au–Au equilibrium distances.

For Au dimers, a second peak at lower energies is visible ($d < 2 \text{ \AA}$, PRF $< 1.5 \text{ eV}$), which blue-shifts as d decreases (see Figure 5b). This band is not present for Ag, because its PRF falls below the investigated frequency range. Highest energy PRF corresponds to the typical Boundary Dipolar Plasmon, BDP, whereas the low-energy peak is associated with a Charge Transfer Plasmon, CTP, where a dipole moment arises in the whole structure (see Figures S8 and S9 in the SI). Note that for distances at which the CT mechanism takes place (for $d < 4 \text{ \AA}$), the high energy peak is associated with a high-order charge transfer plasmon, usually called CTP'. The clear discontinuity highlighted in σ^{abs} plots is also evident in the case of the computed $|E|/|E_0|$ values, which are reported as a color map as a function of the distance in Figure 5, bottom panels. For Ag, the maximum $|E|/|E_0|$ is depicted before the two NPs enter in the CT regime, whereas the opposite holds for the Au dimer, for which it corresponds to the CTP peak.

The surface–surface arrangements show similar plasmonic features, independently of the metal nature (see Figure 6a,b). In fact, both spectra are characterized by the presence of two bands when $d < 4 \text{ \AA}$: a CTP and a CTP' peak (very low in intensity for Ag and fused with CTP for Au), which blue-shift or red-shift as d decreases, respectively. For $d > 4 \text{ \AA}$ spectra are instead dominated by the BDP mode. The associated $|E|/|E_0|$ factors are plotted as a function of the distance in Figure 6, bottom panels. The computed values are of the same order of magnitude as for the previous case. Also, the maximum enhancement for Ag is shown at about 3.3 eV, for a distance of about 4 \AA , that is, when CT effects start to dominate the plasmonic response. For Au, the maximum $|E|/|E_0|$ occurs at lower distances ($d \sim 3 \text{ \AA}$), however it is associated with the CTP' plasmonic mode, differently from the tip–substrate arrangement. Interestingly, in case of Ag, a clear additional region of enhancement is displayed at energies larger than 3.5 eV, for $d > 4 \text{ \AA}$. This region is associated with a high-order plasmon, which is indeed dark in the σ^{abs} .

Finally, note that, for both studied geometries, the maximum $|E|/|E_0|$ is 3–5 times larger than the corresponding factor obtained for the Ag monomer and even 10 times for Au.

4. SUMMARY AND CONCLUSIONS

We have discussed the prediction of a classical physics based model for nanoplasmonics, $\omega\text{FQF}\mu$. $\omega\text{FQF}\mu$ is a general atomistic approach to describe the plasmonic features of complex metal nanostructures characterized by interband transitions. In the model, which is formulated in the frequency domain, each atom of the structure is endowed with both a complex-valued charge and dipole, which are determined by solving response equations to an external monochromatic electric field. The two polarization sources conceptually describe the two fundamental mechanisms occurring in d -metals, that is, Drude conduction (charges) and d -electrons polarization (dipoles). Remarkably, charges and dipoles mutually interact; therefore, all physical features of metal nanostructures are considered. $\omega\text{FQF}\mu$ is fully classical, therefore nanostructures of realistic size can be computed with accuracy comparable to full ab initio calculations, but with enormously lower computational cost. Note that the interband polarizability in eq 3 arises from the quantum nature of the system; however, in our approach it is modeled without explicitly considering the quantum nature of the constituting atoms.

From a conceptual point of view, demonstrating that $\omega\text{FQF}\mu$ is able to reproduce the findings of a fully quantum description of the system is clearly questioning the notion that an explicit quantum mechanical treatment is needed to describe the change in plasmonic properties upon shrinking of the nanostructure size. From the results presented in this work, it turns out that only quantum tunneling (relevant for nanoaggregates and nanojunction) is inaccessible by such classical physics, and we had in fact to phenomenologically include the tunneling in $\omega\text{FQF}\mu$. It is finally worth noting that another relevant quantum effect, Landau damping, is not included in this classical modeling and would in principle require adding a phenomenological correction to $\omega\text{FQF}\mu$.

From a computational perspective, the developed method paves the way for an investigation of the plasmonic properties of realistic metal nanoparticles, characterized by complex shapes that require an atomistic detail.

■ ASSOCIATED CONTENT

SI Supporting Information

The Supporting Information is available free of charge at <https://pubs.acs.org/doi/10.1021/acsphtronics.2c00761>.

Details on $\omega\text{FQF}\mu$ equations and parametrization; Computational details; Ag and Au single NPs absorption cross sections and comparison with reference data; Demonstration of $\omega\text{FQF}\mu$ nonlocality; Plasmon densities for Ag/Au cTO₂₈₆₉ dimers (PDF)

■ AUTHOR INFORMATION

Corresponding Authors

Tommaso Giovannini – Scuola Normale Superiore, 56126 Pisa, Italy; orcid.org/0000-0002-5637-2853; Email: tommaso.giovannini@sns.it

Chiara Cappelli – Scuola Normale Superiore, 56126 Pisa, Italy; orcid.org/0000-0002-4872-4505; Email: chiara.cappelli@sns.it

Authors

Luca Bonatti – Scuola Normale Superiore, 56126 Pisa, Italy
Piero Lafiosca – Scuola Normale Superiore, 56126 Pisa, Italy

Luca Nicoli – Scuola Normale Superiore, 56126 Pisa, Italy
Matteo Castagnola – Scuola Normale Superiore, 56126 Pisa, Italy

Pablo Grobas Illobre – Scuola Normale Superiore, 56126 Pisa, Italy; orcid.org/0000-0003-2544-9712

Stefano Corni – Dipartimento di Scienze Chimiche, Università di Padova, 35131 Padova, Italy; Istituto di Nanoscienze del Consiglio Nazionale delle Ricerche CNR-NANO, 41125 Modena, Italy; orcid.org/0000-0001-6707-108X

Complete contact information is available at:
<https://pubs.acs.org/doi/10.1021/acsphtronics.2c00761>

Funding

This work has received funding from the European Research Council (ERC) under the European Union's Horizon 2020 Research and Innovation Program (Grant Agreement No. 818064). S.C. gratefully acknowledge the European Union's Horizon 2020 FET Project ProID (No. 964363) for funding.

Notes

The authors declare no competing financial interest.

ACKNOWLEDGMENTS

We gratefully acknowledge the Center for High Performance Computing (CHPC) at SNS for providing the computational infrastructure.

REFERENCES

- (1) Junno, T.; Deppert, K.; Montelius, L.; Samuelson, L. Controlled manipulation of nanoparticles with an atomic force microscope. *Appl. Phys. Lett.* **1995**, *66*, 3627–3629.
- (2) Ishida, T.; Murayama, T.; Taketoshi, A.; Haruta, M. Importance of size and contact structure of gold nanoparticles for the genesis of unique catalytic processes. *Chem. Rev.* **2020**, *120*, 464–525.
- (3) Sau, T. K.; Rogach, A. L. Nonspherical noble metal nanoparticles: colloid-chemical synthesis and morphology control. *Adv. Mater.* **2010**, *22*, 1781–1804.
- (4) Liz-Marzán, L. M. Tailoring surface plasmons through the morphology and assembly of metal nanoparticles. *Langmuir* **2006**, *22*, 32–41.
- (5) Grzelczak, M.; Pérez-Juste, J.; Mulvaney, P.; Liz-Marzán, L. M. Shape control in gold nanoparticle synthesis. *Chem. Soc. Rev.* **2008**, *37*, 1783–1791.
- (6) Willets, K. A.; Van Duyne, R. P. Localized surface plasmon resonance spectroscopy and sensing. *Annu. Rev. Phys. Chem.* **2007**, *58*, 267–297.
- (7) Zhang, R.; Zhang, Y.; Dong, Z.; Jiang, S.; Zhang, C.; Chen, L.; Zhang, L.; Liao, Y.; Aizpurua, J.; Luo, Y.; Yang, J. L.; Hou, J. G. Chemical mapping of a single molecule by plasmon-enhanced Raman scattering. *Nature* **2013**, *498*, 82–86.
- (8) Jiang, S.; Zhang, Y.; Zhang, R.; Hu, C.; Liao, M.; Luo, Y.; Yang, J.; Dong, Z.; Hou, J. Distinguishing adjacent molecules on a surface using plasmon-enhanced Raman scattering. *Nat. Nanotechnol.* **2015**, *10*, 865–869.
- (9) Chiang, N.; Chen, X.; Goubert, G.; Chulhai, D. V.; Chen, X.; Pozzi, E. A.; Jiang, N.; Hersam, M. C.; Seideman, T.; Jensen, L.; Van Duyne, R. P. Conformational contrast of surface-mediated molecular switches yields Ångstrom-scale spatial resolution in ultrahigh vacuum tip-enhanced Raman spectroscopy. *Nano Lett.* **2016**, *16*, 7774–7778.
- (10) Langer, J.; et al. Present and Future of Surface-Enhanced Raman Scattering. *ACS Nano* **2020**, *14*, 28–117.
- (11) Benz, F.; Schmidt, M. K.; Dreismann, A.; Chikkaraddy, R.; Zhang, Y.; Demetriadou, A.; Carnegie, C.; Ohadi, H.; De Nijs, B.; Esteban, R.; et al. Single-molecule optomechanics in “picocavities”. *Science* **2016**, *354*, 726–729.
- (12) Yang, B.; Chen, G.; Ghafoor, A.; Zhang, Y.; Zhang, Y.; Zhang, Y.; Luo, Y.; Yang, J.; Sandoghdar, V.; Aizpurua, J.; et al. Subnanometre resolution in single-molecule photoluminescence imaging. *Nat. Photonics* **2020**, *14*, 693–699.
- (13) Liu, P.; Chulhai, D. V.; Jensen, L. Single-Molecule Imaging Using Atomistic Near-Field Tip-Enhanced Raman Spectroscopy. *ACS Nano* **2017**, *11*, 5094–5102.
- (14) Teperik, T. V.; Nordlander, P.; Aizpurua, J.; Borisov, A. G. Quantum effects and nonlocality in strongly coupled plasmonic nanowire dimers. *Opt. Express* **2013**, *21*, 27306–27325.
- (15) Zhu, W.; Esteban, R.; Borisov, A. G.; Baumberg, J. J.; Nordlander, P.; Lezec, H. J.; Aizpurua, J.; Crozier, K. B. Quantum mechanical effects in plasmonic structures with subnanometre gaps. *Nat. Commun.* **2016**, *7*, 11495.
- (16) Urbieto, M.; Barbry, M.; Zhang, Y.; Koval, P.; Sánchez-Portal, D.; Zabala, N.; Aizpurua, J. Atomic-Scale Lightning Rod Effect in Plasmonic Picocavities: A Classical View to a Quantum Effect. *ACS Nano* **2018**, *12*, 585–595.
- (17) Savage, K. J.; Hawkeye, M. M.; Esteban, R.; Borisov, A. G.; Aizpurua, J.; Baumberg, J. J. Revealing the quantum regime in tunnelling plasmonics. *Nature* **2012**, *491*, 574–577.
- (18) Marinica, D.; Kazansky, A.; Nordlander, P.; Aizpurua, J.; Borisov, A. G. Quantum plasmonics: nonlinear effects in the field enhancement of a plasmonic nanoparticle dimer. *Nano Lett.* **2012**, *12*, 1333–1339.
- (19) Esteban, R.; Borisov, A. G.; Nordlander, P.; Aizpurua, J. Bridging quantum and classical plasmonics with a quantum-corrected model. *Nat. Commun.* **2012**, *3*, 825.
- (20) Esteban, R.; Zugarramurdi, A.; Zhang, P.; Nordlander, P.; García-Vidal, F. J.; Borisov, A. G.; Aizpurua, J. A classical treatment of optical tunneling in plasmonic gaps: extending the quantum corrected model to practical situations. *Faraday Discuss.* **2015**, *178*, 151–183.
- (21) Campos, A.; Troc, N.; Cottancin, E.; Pellarin, M.; Weissker, H.-C.; Lermé, J.; Kociak, M.; Hillenkamp, M. Plasmonic quantum size effects in silver nanoparticles are dominated by interfaces and local environments. *Nat. Phys.* **2019**, *15*, 275–280.
- (22) Scholl, J. A.; García-Etxarri, A.; Koh, A. L.; Dionne, J. A. Observation of quantum tunneling between two plasmonic nanoparticles. *Nano Lett.* **2013**, *13*, 564–569.
- (23) Barbry, M.; Koval, P.; Marchesin, F.; Esteban, R.; Borisov, A.; Aizpurua, J.; Sánchez-Portal, D. Atomistic near-field nanoplasmatics: reaching atomic-scale resolution in nano optics. *Nano Lett.* **2015**, *15*, 3410–3419.
- (24) Baumberg, J. J.; Aizpurua, J.; Mikkelsen, M. H.; Smith, D. R. Extreme nanophotonics from ultrathin metallic gaps. *Nat. Mater.* **2019**, *18*, 668–678.
- (25) Chen, X.; Liu, P.; Jensen, L. Atomistic electrodynamics simulations of plasmonic nanoparticles. *J. Phys. D Appl. Phys.* **2019**, *52*, 363002.
- (26) Mie, G. Beiträge zur Optik trüber Medien, speziell kolloidaler Metallösungen. *Ann. Phys.-Berlin* **1908**, *330*, 377–445.
- (27) Draine, B. T.; Flatau, P. J. Discrete-dipole approximation for scattering calculations. *J. Opt. Soc. Am. A* **1994**, *11*, 1491–1499.
- (28) Tafove, A.; Hagness, S. C.; Piket-May, M. *Computational Electromagnetics: The Finite-Difference Time-Domain Method*; Elsevier: Amsterdam, The Netherlands, 2005.
- (29) Myroshnychenko, V.; Carbó-Argibay, E.; Pastoriza-Santos, I.; Pérez-Juste, J.; Liz-Marzán, L. M.; García de Abajo, F. J. Modeling the optical response of highly faceted metal nanoparticles with a fully 3D boundary element method. *Adv. Mater.* **2008**, *20*, 4288–4293.
- (30) García de Abajo, F. J.; Howie, A. Retarded field calculation of electron energy loss in inhomogeneous dielectrics. *Phys. Rev. B* **2002**, *65*, 115418.
- (31) Mennucci, B.; Corni, S. Multiscale modelling of photoinduced processes in composite systems. *Nat. Rev. Chem.* **2019**, *3*, 315–330.
- (32) Bonatti, L.; Gil, G.; Giovannini, T.; Corni, S.; Cappelli, C. Plasmonic Resonances of Metal Nanoparticles: Atomistic vs Continuum Approaches. *Front. Chem.* **2020**, *8*, 340.
- (33) Marcheselli, J.; Chateau, D.; Lerouge, F.; Baldeck, P.; Andraud, C.; Parola, S.; Baroni, S.; Corni, S.; Garavelli, M.; Rivalta, I. Simulating Plasmon Resonances of Gold Nanoparticles with Bipyrudal Shapes by Boundary Element Methods. *J. Chem. Theory Comput.* **2020**, *16*, 3807–3815.
- (34) Coccia, E.; Fregoni, J.; Guido, C.; Marsili, M.; Pipolo, S.; Corni, S. Hybrid theoretical models for molecular nanoplasmonics. *J. Chem. Phys.* **2020**, *153*, 200901.
- (35) Luo, Y.; Fernandez-Dominguez, A.; Wiener, A.; Maier, S. A.; Pendry, J. Surface plasmons and nonlocality: a simple model. *Phys. Rev. Lett.* **2013**, *111*, 093901.
- (36) Ciraci, C.; Pendry, J. B.; Smith, D. R. Hydrodynamic model for plasmonics: a macroscopic approach to a microscopic problem. *ChemPhysChem* **2013**, *14*, 1109–1116.
- (37) Raza, S.; Bozhevolnyi, S. I.; Wubs, M.; Mortensen, N. A. Nonlocal optical response in metallic nanostructures. *J. Phys.: Condens. Matter* **2015**, *27*, 183204.
- (38) Ciraci, C.; Della Sala, F. Quantum hydrodynamic theory for plasmonics: Impact of the electron density tail. *Phys. Rev. B* **2016**, *93*, 205405.
- (39) Toscano, G.; Raza, S.; Jauho, A.-P.; Mortensen, N. A.; Wubs, M. Modified field enhancement and extinction by plasmonic nanowire dimers due to nonlocal response. *Opt. Express* **2012**, *20*, 4176–4188.
- (40) David, C.; García de Abajo, F. J. Surface plasmon dependence on the electron density profile at metal surfaces. *ACS Nano* **2014**, *8*, 9558–9566.

- (41) Toscano, G.; Straubel, J.; Kwiatkowski, A.; Rockstuhl, C.; Evers, F.; Xu, H.; Asger Mortensen, N.; Wubs, M. Resonance shifts and spill-out effects in self-consistent hydrodynamic nanoplasmonics. *Nat. Commun.* **2015**, *6*, 1–11.
- (42) Bonatti, L.; Nicoli, L.; Giovannini, T.; Cappelli, C. In silico design of graphene plasmonic hot-spots. *Nanoscale Adv.* **2022**, *4*, 2294–2302.
- (43) Gonçalves, P.; Christensen, T.; Rivera, N.; Jauho, A.-P.; Mortensen, N. A.; Soljačić, M. Plasmon–emitter interactions at the nanoscale. *Nat. Commun.* **2020**, *11*, 1–13.
- (44) Echarri, A. R.; Gonçalves, P.; Tserkezis, C.; de Abajo, F. J. G.; Mortensen, N. A.; Cox, J. D. Optical response of noble metal nanostructures: quantum surface effects in crystallographic facets. *Optica* **2021**, *8*, 710–721.
- (45) Babaze, A.; Ogando, E.; Stamatopoulou, P. E.; Tserkezis, C.; Mortensen, N. A.; Aizpurua, J.; Borisov, A. G.; Esteban, R. Quantum surface effects in the electromagnetic coupling between a quantum emitter and a plasmonic nanoantenna: time-dependent density functional theory vs. semiclassical Feibelman approach. *Opt. Express* **2022**, *30*, 21159–21183.
- (46) Zhu, M.; Aikens, C. M.; Hollander, F. J.; Schatz, G. C.; Jin, R. Correlating the crystal structure of a thiol-protected Au25 cluster and optical properties. *J. Am. Chem. Soc.* **2008**, *130*, 5883–5885.
- (47) Rossi, T. P.; Zugarramurdi, A.; Puska, M. J.; Nieminen, R. M. Quantized evolution of the plasmonic response in a stretched nanorod. *Phys. Rev. Lett.* **2015**, *115*, 236804.
- (48) Weissker, H.-C.; Mottet, C. Optical properties of pure and core-shell noble-metal nanoclusters from TDDFT: The influence of the atomic structure. *Phys. Rev. B* **2011**, *84*, 165443.
- (49) Marchesin, F.; Koval, P.; Barbry, M.; Aizpurua, J.; Sánchez-Portal, D. Plasmonic response of metallic nanojunctions driven by single atom motion: quantum transport revealed in optics. *ACS Photonics* **2016**, *3*, 269–277.
- (50) Sinha-Roy, R.; Garcia-Gonzalez, P.; Weissker, H.-C.; Rabilloud, F.; Fernandez-Domínguez, A. I. Classical and ab Initio Plasmonics Meet at Sub-nanometric Noble Metal Rods. *ACS Photonics* **2017**, *4*, 1484–1493.
- (51) Morton, S. M.; Jensen, L. A discrete interaction model/quantum mechanical method for describing response properties of molecules adsorbed on metal nanoparticles. *J. Chem. Phys.* **2010**, *133*, 074103.
- (52) Morton, S. M.; Jensen, L. A discrete interaction model/quantum mechanical method to describe the interaction of metal nanoparticles and molecular absorption. *J. Chem. Phys.* **2011**, *135*, 134103.
- (53) Jensen, L. L.; Jensen, L. Electrostatic interaction model for the calculation of the polarizability of large noble metal nanoclusters. *J. Phys. Chem. C* **2008**, *112*, 15697–15703.
- (54) Jensen, L. L.; Jensen, L. Atomistic electrodynamics model for optical properties of silver nanoclusters. *J. Phys. Chem. C* **2009**, *113*, 15182–15190.
- (55) Zakomirnyi, V. I.; Rinkevicius, Z.; Baryshnikov, G. V.; Sørensen, L. K.; Ågren, H. Extended discrete interaction model: plasmonic excitations of silver nanoparticles. *J. Phys. Chem. C* **2019**, *123*, 28867–28880.
- (56) Rinkevicius, Z.; Li, X.; Sandberg, J. A.; Mikkelsen, K. V.; Ågren, H. A hybrid density functional theory/molecular mechanics approach for linear response properties in heterogeneous environments. *J. Chem. Theory Comput.* **2014**, *10*, 989–1003.
- (57) Zakomirnyi, V. I.; Rasskazov, I. L.; Sørensen, L. K.; Carney, P. S.; Rinkevicius, Z.; Ågren, H. Plasmonic nano-shells: atomistic discrete interaction versus classic electrodynamics models. *Phys. Chem. Chem. Phys.* **2020**, *22*, 13467–13473.
- (58) Giovannini, T.; Rosa, M.; Corni, S.; Cappelli, C. A classical picture of subnanometer junctions: an atomistic Drude approach to nanoplasmonics. *Nanoscale* **2019**, *11*, 6004–6015.
- (59) Giovannini, T.; Bonatti, L.; Polini, M.; Cappelli, C. Graphene plasmonics: Fully atomistic approach for realistic structures. *J. Phys. Chem. Lett.* **2020**, *11*, 7595–7602.
- (60) Lafiosca, P.; Giovannini, T.; Benzi, M.; Cappelli, C. Going Beyond the Limits of Classical Atomistic Modeling of Plasmonic Nanostructures. *J. Phys. Chem. C* **2021**, *125*, 23848–23863.
- (61) Yamada, A. Classical electronic and molecular dynamics simulation for optical response of metal system. *J. Chem. Phys.* **2021**, *155*, 174118.
- (62) Duan, H.; Fernández-Domínguez, A. I.; Bosman, M.; Maier, S. A.; Yang, J. K. Nanoplasmonics: classical down to the nanometer scale. *Nano Lett.* **2012**, *12*, 1683–1689.
- (63) Scholl, J. A.; Koh, A. L.; Dionne, J. A. Quantum plasmon resonances of individual metallic nanoparticles. *Nature* **2012**, *483*, 421–427.
- (64) Pinchuk, A.; Kreibig, U.; Hilger, A. Optical properties of metallic nanoparticles: influence of interface effects and interband transitions. *Surf. Sci.* **2004**, *557*, 269–280.
- (65) Pinchuk, A.; Von Plessen, G.; Kreibig, U. Influence of interband electronic transitions on the optical absorption in metallic nanoparticles. *J. Phys. D: Appl. Phys.* **2004**, *37*, 3133.
- (66) Balamurugan, B.; Maruyama, T. Evidence of an enhanced interband absorption in Au nanoparticles: size-dependent electronic structure and optical properties. *Appl. Phys. Lett.* **2005**, *87*, 143105.
- (67) Liebsch, A. Surface-plasmon dispersion and size dependence of Mie resonance: silver versus simple metals. *Phys. Rev. B* **1993**, *48*, 11317.
- (68) Santiago, E. Y.; Besteiro, L. V.; Kong, X.-T.; Correa-Duarte, M. A.; Wang, Z.; Govorov, A. O. Efficiency of hot-electron generation in plasmonic nanocrystals with complex shapes: surface-induced scattering, hot spots, and interband transitions. *ACS Photonics* **2020**, *7*, 2807–2824.
- (69) Giovannini, T.; Puglisi, A.; Ambrosetti, M.; Cappelli, C. Polarizable QM/MM approach with fluctuating charges and fluctuating dipoles: the QM/FQFμ model. *J. Chem. Theory Comput.* **2019**, *15*, 2233–2245.
- (70) Giovannini, T.; Riso, R. R.; Ambrosetti, M.; Puglisi, A.; Cappelli, C. Electronic transitions for a fully polarizable qm/mm approach based on fluctuating charges and fluctuating dipoles: linear and corrected linear response regimes. *J. Chem. Phys.* **2019**, *151*, 174104.
- (71) Giovannini, T.; Egidi, F.; Cappelli, C. Molecular spectroscopy of aqueous solutions: a theoretical perspective. *Chem. Soc. Rev.* **2020**, *49*, 5664–5677.
- (72) Verma, P. Tip-enhanced Raman spectroscopy: technique and recent advances. *Chem. Rev.* **2017**, *117*, 6447–6466.
- (73) Zhang, W.; Yeo, B. S.; Schmid, T.; Zenobi, R. Single molecule tip-enhanced Raman spectroscopy with silver tips. *J. Phys. Chem. C* **2007**, *111*, 1733–1738.
- (74) Chen, X.; Moore, J. E.; Zekarias, M.; Jensen, L. Atomistic electrodynamics simulations of bare and ligand-coated nanoparticles in the quantum size regime. *Nat. Commun.* **2015**, *6*, 8921.
- (75) Ringe, E.; McMahon, J. M.; Sohn, K.; Cobley, C.; Xia, Y.; Huang, J.; Schatz, G. C.; Marks, L. D.; Van Duyne, R. P. Unraveling the effects of size, composition, and substrate on the localized surface plasmon resonance frequencies of gold and silver nanocubes: a systematic single-particle approach. *J. Phys. Chem. C* **2010**, *114*, 12511–12516.
- (76) Etchegoin, P. G.; Le Ru, E.; Meyer, M. An analytic model for the optical properties of gold. *J. Chem. Phys.* **2006**, *125*, 164705.
- (77) Johnson, P. B.; Christy, R.-W. Optical constants of the noble metals. *Phys. Rev. B* **1972**, *6*, 4370.
- (78) Johnson, H. E.; Aikens, C. M. Electronic structure and TDDFT optical absorption spectra of silver nanorods. *J. Phys. Chem. A* **2009**, *113*, 4445–4450.
- (79) Bae, G.-T.; Aikens, C. M. Time-dependent density functional theory studies of optical properties of Ag nanoparticles: octahedra, truncated octahedra, and icosahedra. *J. Phys. Chem. C* **2012**, *116*, 10356–10367.
- (80) Cottancin, E.; Celep, G.; Lermé, J.; Pellarin, M.; Huntzinger, J.; Vialle, J.; Broyer, M. Optical properties of noble metal clusters as a

function of the size: comparison between experiments and a semi-quantal theory. *Theor. Chem. Acc.* **2006**, *116*, 514–523.

(81) Chen, X.; Jensen, L. Morphology dependent near-field response in atomistic plasmonic nanocavities. *Nanoscale* **2018**, *10*, 11410–11417.

(82) Kreibig, U.; Vollmer, M. *Optical Properties of Metal Clusters*; Springer Science & Business Media, 2013; Vol. 25.

(83) Novo, C.; Gomez, D.; Perez-Juste, J.; Zhang, Z.; Petrova, H.; Reismann, M.; Mulvaney, P.; Hartland, G. V. Contributions from radiation damping and surface scattering to the linewidth of the longitudinal plasmon band of gold nanorods: a single particle study. *Phys. chem. Chem. Phys.* **2006**, *8*, 3540–3546.

(84) Juvé, V.; Cardinal, M. F.; Lombardi, A.; Crut, A.; Maioli, P.; Pérez-Juste, J.; Liz-Marzán, L. M.; Del Fatti, N.; Vallée, F. Size-dependent surface plasmon resonance broadening in nonspherical nanoparticles: single gold nanorods. *Nano Lett.* **2013**, *13*, 2234–2240.

(85) Foerster, B.; Joplin, A.; Kaefer, K.; Celiksoy, S.; Link, S.; Sönnichsen, C. Chemical interface damping depends on electrons reaching the surface. *ACS Nano* **2017**, *11*, 2886–2893.

(86) Douglas-Gallardo, O. A.; Soldano, G. J.; Mariscal, M. M.; Sánchez, C. G. Effects of oxidation on the plasmonic properties of aluminum nanoclusters. *Nanoscale* **2017**, *9*, 17471–17480.

(87) Kuusma, M.; Säkko, A.; Rossi, T. P.; Larsen, A. H.; Enkovaara, J.; Lehtovaara, L.; Rantala, T. T. Localized surface plasmon resonance in silver nanoparticles: Atomistic first-principles time-dependent density-functional theory calculations. *Phys. Rev. B* **2015**, *91*, 115431.

(88) Iida, K.; Noda, M.; Ishimura, K.; Nobusada, K. First-principles computational visualization of localized surface plasmon resonance in gold nanoclusters. *J. Phys. Chem. A* **2014**, *118*, 11317–11322.

(89) Payton, J. L.; Morton, S. M.; Moore, J. E.; Jensen, L. A hybrid atomistic electrodynamics–quantum mechanical approach for simulating surface-enhanced raman scattering. *Acc. Chem. Res.* **2014**, *47*, 88–99.

(90) Kim, M.; Kwon, H.; Lee, S.; Yoon, S. Effect of nanogap morphology on plasmon coupling. *ACS Nano* **2019**, *13*, 12100–12108.

□ Recommended by ACS

Broadband Transient Response and Wavelength-Tunable Photoacoustics in Plasmonic Hetero-nanoparticles

Anton Yu. Bykov, Anatoly V. Zayats, *et al.*

MARCH 16, 2023

NANO LETTERS

READ

Effect of Material and Shape of Nanoparticles on Hot Carrier Generation

Ly Thi Minh Huynh, Sangwoon Yoon, *et al.*

SEPTEMBER 23, 2022

ACS PHOTONICS

READ

Plasmon-Mediated Energy Transfer between Two Systems out of Equilibrium

Camilo R. Pérez de la Vega, Valentina Krachmalnicoff, *et al.*

APRIL 10, 2023

ACS PHOTONICS

READ

Lattice Resonances for Thermoplasmonics

Lauren Zundel, Alejandro Manjavacas, *et al.*

DECEMBER 27, 2022

ACS PHOTONICS

READ

Get More Suggestions >

II. Fully atomistic modeling of plasmonic bimetallic nanoparticles: nanoalloys and core-shell systems



OPEN ACCESS

EDITED BY

Stefania D'Agostino,
National Research Council (CNR), Italy

REVIEWED BY

Cristian Ciraci,
Italian Institute of Technology (IIT), Italy
Maxim A. Yurkin,
Institute of Chemical Kinetics and
Combustion (RAS), Russia

*CORRESPONDENCE

Tommaso Giovannini,
✉ tommaso.giovannini@sns.it
Chiara Cappelli,
✉ chiara.cappelli@sns.it

RECEIVED 03 April 2023

ACCEPTED 07 June 2023

PUBLISHED 16 June 2023

CITATION

Nicoli L, Lafiosca P, Grobas Illobre P, Bonatti L, Giovannini T and Cappelli C (2023). Fully atomistic modeling of plasmonic bimetallic nanoparticles: nanoalloys and core-shell systems. *Front. Photonics* 4:1199598.
doi: 10.3389/fphot.2023.1199598

COPYRIGHT

© 2023 Nicoli, Lafiosca, Grobas Illobre, Bonatti, Giovannini and Cappelli. This is an open-access article distributed under the terms of the [Creative Commons Attribution License \(CC BY\)](#). The use, distribution or reproduction in other forums is permitted, provided the original author(s) and the copyright owner(s) are credited and that the original publication in this journal is cited, in accordance with accepted academic practice. No use, distribution or reproduction is permitted which does not comply with these terms.

Fully atomistic modeling of plasmonic bimetallic nanoparticles: nanoalloys and core-shell systems

Luca Nicoli¹, Piero Lafiosca¹, Pablo Grobas Illobre¹, Luca Bonatti¹, Tommaso Giovannini^{1*} and Chiara Cappelli^{1,2*}

¹Classe di Scienze, Scuola Normale Superiore, Pisa, Italy, ²European Laboratory for Non-Linear Spectroscopy (LENS), Florence, Italy

The recently developed ω FQF μ model (*ACS Photonics*, 9, 3,025–3,034) is extended to bimetallic nanoparticles, such as nanoalloys and core-shell systems. The method finds its grounds in basic physical concepts, such as Drude conduction theory, electrostatics, interband transitions, and quantum tunneling. The approach, which is parametrized on *ab initio* simulations of Ag-Au nanoalloys, is challenged against complex Ag-Au nanostructures (spheres, nanorods, and core-shell nanoparticles). Remarkable agreement with available experimental data is found, thus demonstrating the reliability of the newly developed approach.

KEYWORDS

atomistic, alloys, core-shell, plasmonics, gold, silver, bimetallic

1 Introduction

Metal nanoparticles (NPs) exhibit unique optical properties, which are mainly due to the formation of surface plasmons, i.e., collective excitations of conductive electrons. (Moskovits, 1985; Nie and Emory, 1997; Maier, 2007; Anker et al., 2008; Atwater and Polman, 2010; Santhosh et al., 2016). At the plasmon resonance frequency (PRF) such surface plasmons exhibit a resonant behavior, which gives rise to a huge enhancement of the electric field in the proximity of the NP surface. This phenomenon is exploited to increase the detection limit of common analytical techniques. (Kneipp et al., 1997; Maier et al., 2003; Muehlschlegel et al., 2005; Lim et al., 2010; Giannini et al., 2011; Neuman et al., 2018). PRF can be tuned by varying the NP shape, dimension, and chemical composition (Ag, Au, Al, ...). As an alternative, bimetallic nanoalloys or core-shell NPs can be used. Such systems are constituted by two different metal elements, e.g., Ag-Au, Au-Cu, Cu-Ag (Xiang et al., 2008; Wang et al., 2009; Huang et al., 2015; Gong and Leite, 2016; Cao et al., 2018; Ma et al., 2020; Awada et al., 2021). In this case, the PRF can be tuned not only by modifying the aforementioned variables (size, shape, ...) but also the relative concentration of the two metals.

Many theoretical approaches have been developed to describe the plasmonic properties of single metal NPs (Corni and Tomasi, 2001; 2002a; Aizpurua et al., 2003; Myroshnychenko et al., 2008; Hohenester and Trügler, 2012; Ciraci et al., 2013; Ciraci and Della Sala, 2016; Giovannini et al., 2019b; Bonatti et al., 2020; Coccia et al., 2020; Baghramyan et al., 2021; Giannone et al., 2021; Della Sala, 2022; Della Sala et al., 2022), among which is worth mentioning quantum hydrodynamic models, which are able to describe both nonlocal and

electron spill-out effects (Ciraci et al., 2013; Raza et al., 2015; Ciraci and Della Sala, 2016). However, the most widely exploited methods are based on classical physics, (Corni and Tomasi, 2002b; Hao et al., 2007; Jensen and Jensen, 2008; Jensen and Jensen, 2009; Pérez-González et al., 2010; Halas et al., 2011; Ciraci et al., 2012; Chen et al., 2015), such as the Mie Theory (Mie, 1908), the finite difference time domain (FDTD) (Shuford et al., 2006), the Discrete Dipole Approximation (DDA) (Draine and Flatau, 1994) or exploit a continuum representation of the NP by means of the Boundary Element Method (BEM) (Corni and Tomasi, 2001; García de Abajo and Howie, 2002; Hohenester and Trügler, 2012; Hohenester, 2015). All the classical approaches mentioned above rely on defining a suitable permittivity function ϵ . Clearly, in the case of bimetallic systems, ϵ -dependent methods are not flexible enough to treat *a priori* any chemical composition and need to resort to experimentally measured ϵ values for specific alloy concentrations or to approximations, which may not be physically justified (such as a linear combination of the ϵ values of the two metals) (Peña-Rodríguez and Pal, 2011a; Verbruggen et al., 2013; Ma et al., 2015; Putra et al., 2017; Kuddah et al., 2020; Newmai et al., 2022).

Atomistic approaches appear as the most natural choice to overcome this problem. Full *ab initio* methods can be exploited, however, their prohibitive computational cost limits their application to relatively small systems (Barcaro et al., 2011; López Lozano et al., 2013; Barcaro et al., 2014; Barcaro et al., 2015; Olobardi et al., 2019; Asadi-Aghbolaghi et al., 2020; Danielis et al., 2021). For this reason, classical atomistic approaches have been developed, (Jensen and Jensen, 2008; Jensen and Jensen, 2009; Chen et al., 2015; Zakomirnyi et al., 2019; Zakomirnyi et al., 2020), however they have only marginally been applied to the description of bimetallic NPs (Sørensen et al., 2021).

In this work, we extend ω FQF μ (Giovannini et al., 2022) to simulate the optical properties of bimetallic NPs, with special emphasis on Ag-Au nanoalloys and core-shell systems. ω FQF μ is a fully atomistic, classical, approach, which assigns each atom of the metal nanoalloy with an electric charge and an electric dipole moment, which vary as a response to an externally applied electric field. The theoretical foundations of ω FQF μ lay in Drude's theory of conduction, classical electrodynamics, interband transitions, and quantum tunneling. In fact, the Drude mechanism of charge exchange is modeled through the equation of motion of the electric charges (Giovannini et al., 2019b; Bonatti et al., 2020; Giovannini et al., 2020; Lafiosca et al., 2021; Bonatti et al., 2022), while interband contributions are taken into account by means of effective interband polarizability (Giovannini et al., 2022) introduced to mimic d-shell polarizability (Liebsch, 1993). Also, quantum tunneling effects, which play a crucial role in nanojunctions and nanoaggregates (Esteban et al., 2012; Giovannini et al., 2019b), are described by tuning charge exchange through a phenomenological function. Therefore, ω FQF μ conceptually differs from other approaches which are based on classical physics only.

The manuscript is organized as follows. In the next section, the formulation of ω FQF μ for bimetallic systems is presented. After a brief section presenting the computational details, the method is tested against the reproduction of the plasmonic properties of alloyed spherical NPs, alloyed nanorods, and spherical core-shell

systems. Conclusions and a sketch of the future perspectives of the approach end the manuscript.

2 Materials and methods

2.1 Theoretical model

In this section, we extend ω FQF μ (Giovannini et al., 2022) to describe the optical properties of bimetallic systems. To this end, we follow the derivation reported in (Giovannini et al., 2019b) and (Giovannini et al., 2022). In ω FQF μ , the fluctuations of the electronic density of a plasmonic substrate composed of N atoms emerging as a response to the external electric field are represented by a set of N discrete fluctuating complex-valued charges q_i and N fluctuating complex-valued dipoles μ_i , which are located at atomic positions. The equation of motion of charges q originates from the continuity equation (Giovannini et al., 2019b) (atomic units are used throughout the paper):

$$\frac{dq_i}{dt} = \sum_{ij} A_{ij} (n_j \langle \mathbf{p}_j \rangle_i \cdot \hat{\mathbf{l}}_{ji} - n_i \langle \mathbf{p}_i \rangle_j \cdot \hat{\mathbf{l}}_{ij}) \\ = \sum_{ij} (A_j n_j \langle \mathbf{p}_j \rangle_i \cdot \hat{\mathbf{l}}_{ji} - A_i n_i \langle \mathbf{p}_i \rangle_j \cdot \hat{\mathbf{l}}_{ij}) \quad (1)$$

where n_i is the electron density on atom i , $\langle \mathbf{p}_i \rangle_j$ is the momentum of the electron associated with atom i averaged over all the trajectories towards atom j . $\hat{\mathbf{l}}_{ij} = -\hat{\mathbf{l}}_{ji}$ is the unit vector connecting i and j . A_{ij} is the effective area dividing i th and j th atoms, and its value modulates the charge exchange between each atom pair. By following (Giovannini et al., 2019b; Giovannini et al., 2020; Giovannini et al., 2022), A_{ij} is approximated as an atomic parameter (A_i). The electron momentum \mathbf{p}_i can be estimated by means of the Drude model of conductance (Bade, 1957) as follows:

$$\frac{d\mathbf{p}_i}{dt} = \mathbf{E}_i(t) - \frac{\mathbf{p}_i}{\tau_i} \quad (2)$$

where $\mathbf{E}_i(t)$ is the electric field acting on the i th atom and τ_i is the relaxation time associated with scattering events. Assuming the external uniform monochromatic electric field $\mathbf{E}^{\text{ext}}(t) = \mathbf{E}^{\text{ext}}(\omega) \exp(-i\omega t)$ oscillates at frequency ω , we can reformulate Eqs 1, 2 in the frequency domain, i.e.:

$$-i\omega q_i = \sum_j \left(A_j n_j \frac{\langle \mathbf{E}_j(\omega) \rangle_i \cdot \hat{\mathbf{l}}_{ji}}{1/\tau_j - i\omega} - A_i n_i \frac{\langle \mathbf{E}_i(\omega) \rangle_j \cdot \hat{\mathbf{l}}_{ij}}{1/\tau_i - i\omega} \right) \quad (3)$$

Following the original derivation reported in (Giovannini et al., 2019b), we can write:

$$\langle \mathbf{E}_i(\omega) \rangle_j \cdot \hat{\mathbf{l}}_{ij} \approx \frac{\phi_j - \phi_i}{l_{ij}} \quad (4)$$

where ϕ_i is the chemical potential of atom i and $l_{ij} = l_{ji}$ is the distance between i th and j th atoms. By this, Eq. 3 becomes:

$$-i\omega q_i = \sum_j \left(\frac{A_j n_j (1 - f_{ji}(l_{ij}))}{1/\tau_j - i\omega} + \frac{A_i n_i (1 - f_{ij}(l_{ij}))}{1/\tau_i - i\omega} \right) \frac{\phi_i - \phi_j}{l_{ij}} \quad (5)$$

where quantum tunneling effects are expressed in terms of a Fermi-like function f_{ij} (l_{ij}), which reads:

$$f_{ij}(l_{ij}) = \frac{1}{1 + \exp\left[-d_{ij}\left(\frac{l_{ij}}{s_{ij}l_{ij}^0} - 1\right)\right]} \quad (6)$$

where l_{ij}^0 is the equilibrium distance between atoms i and j , and the parameters d_{ij} and s_{ij} determine the shape of the damping function. Notice that the inclusion of a phenomenological description of quantum tunneling is needed to correctly describe the optical response of plasmonic subnanometer junctions and hot-spots (Esteban et al., 2012; Esteban et al., 2015; Scholl et al., 2013; Giovannini et al., 2019b; Bonatti et al., 2022; Giovannini et al., 2022). Indeed, in the case of plasmonic nanoaggregates, charge transfer plasmons (CT) may occur. In ω FQF μ , the charge exchange among different NPs is governed by Drude and tunneling mechanisms, and the total system charge is conserved (see Eq. 5), allowing for a physically consistent description of such plasmonic modes. To make the notation more compact, the following terms are introduced (Lafiosca et al., 2021):

$$w_i(\omega) = \frac{2n_i}{1/\tau_i - i\omega} \quad (7)$$

$$K_{ij} = A_i \frac{1 - f_{ij}(l_{ij})}{l_{ij}} \quad (8)$$

$$z_i(\omega) = -\frac{i\omega}{w_i(\omega)} \quad (9)$$

Dividing Eq. 5 by $w_i(\omega)$, we obtain:

$$z_i(\omega)q_i = \frac{1}{2} \sum_j \left(K_{ij} + \frac{w_j(\omega)}{w_i(\omega)} K_{ji} \right) (\phi_i - \phi_j) \quad (10)$$

where the chemical potential ϕ_i can be written as:

$$\phi_i = \sum_k T_{ik}^{qq} q_k + \sum_k T_{ik}^{qu} \boldsymbol{\mu}_k + V_i^{\text{ext}} \quad (11)$$

The first and the second terms in Eq. 11 are the electric potential generated by the charges and the dipoles of the system, mediated by the interaction tensors T^{qq} and T^{qu} (see (Giovannini et al., 2019a) for their definitions). V_i^{ext} is the electric potential associated with the external electric field. By plugging Eq. 11 into Eq. 10, the linear equations ruling charge evolution are obtained, i.e.:

$$\begin{aligned} \mathbf{Z}(\omega)\mathbf{q} &= \frac{1}{2} (\bar{\mathbf{K}} + \bar{\mathbf{H}}(\omega)) \mathbf{T}^{qq} \mathbf{q} + \frac{1}{2} (\bar{\mathbf{K}} + \bar{\mathbf{H}}(\omega)) \mathbf{T}^{qu} \boldsymbol{\mu} \\ &\quad + \frac{1}{2} (\bar{\mathbf{K}} + \bar{\mathbf{H}}(\omega)) \mathbf{V} \end{aligned} \quad (12)$$

where the following matrices are introduced:

$$H_{ij}(\omega) = \frac{w_j(\omega)}{w_i(\omega)} K_{ji} \quad (13)$$

$$\bar{K}_{ij} = K_{ij} - \sum_k K_{ik} \delta_{ij} \quad (14)$$

$$Z_{ij} = z_i \delta_{ij} \quad (15)$$

$$\bar{H}_{ij} = H_{ij} - \sum_k H_{ik} \delta_{ij} \quad (16)$$

The electric dipoles $\boldsymbol{\mu}_i$, which are introduced to properly model interband contributions, are obtained by solving the following set of linear equations:

$$\boldsymbol{\mu}_i = \alpha_i(\omega) [\mathbf{E}_i^{\text{ext}}(\omega) + \mathbf{E}_i^q(\omega) + \mathbf{E}_i^\mu(\omega)] \quad (17)$$

where $\alpha_i(\omega)$ is the frequency-dependent polarizability of the i th atom, related to interband terms, which multiplies the total electric field acting on the i th dipole, composed by the external field $\mathbf{E}_i^{\text{ext}}$, the field generated by the fluctuating charges, \mathbf{E}_i^q , and the field generated by the fluctuating dipoles, \mathbf{E}_i^μ . If the system is homogeneous, α_i is calculated as reported in (Giovannini et al., 2022):

$$\alpha_i(\omega) \equiv \alpha_A^{\text{IB}}(\omega) = \frac{\varepsilon_A^{\text{IB}}(\omega)}{4\pi n_A} \quad (18)$$

where $\varepsilon_A^{\text{IB}}$ is the interband contribution to the frequency-dependent permittivity function and n_A is the number density of atoms of the chemical element A . ε^{IB} is calculated by subtracting the Drude term from the frequency-dependent permittivity.

If the system is heterogeneous, the link between the macroscopic, bulk dynamical permittivity $\varepsilon^{\text{IB}}(\omega)$ and the microscopic, atomistic frequency-dependent interband polarizability $\alpha_i(\omega)$ is not straightforward. Let us focus on bimetallic systems, composed of two chemical elements A and B . We assume the interband polarizability of the i th atom belonging to the A moiety to be a function of the local composition of the system, i.e., $\alpha_{A,i}^{\text{IB,alloy}}(N_{A,i}, N_{B,i})$, where $N_{A,i}$ and $N_{B,i}$ are the number of nearest neighbors of A and B type, respectively. The simplest approach is to model $\alpha_{A,i}^{\text{IB,alloy}}$ as the weighted average of α_A^{IB} and α_B^{IB} . Therefore, the interband frequency-dependent polarizability of the i th atom of species A in the alloy composed by materials A and B is defined as follows:

$$\alpha_i(\omega) \equiv \alpha_{A,i}^{\text{IB,alloy}}(\omega) = \left(\frac{\frac{N_{A,i}+1}{\alpha_A^{\text{IB}}(\omega)} + \frac{N_{B,i}}{\alpha_B^{\text{IB}}(\omega)}}{N_{A,i} + N_{B,i} + 1} \right)^{-1} \quad (19)$$

Notice that, possible alternative approaches, e.g., to resort to arithmetic averages have been investigated. However, the weighted harmonic mean indeed gives the best numerical results (see Supplementary Figure S1 and Sec. S1 in the Supplementary Materials – SM).

Starting from Eq. 17, the final expression for the electric dipoles becomes (Giovannini et al., 2022):

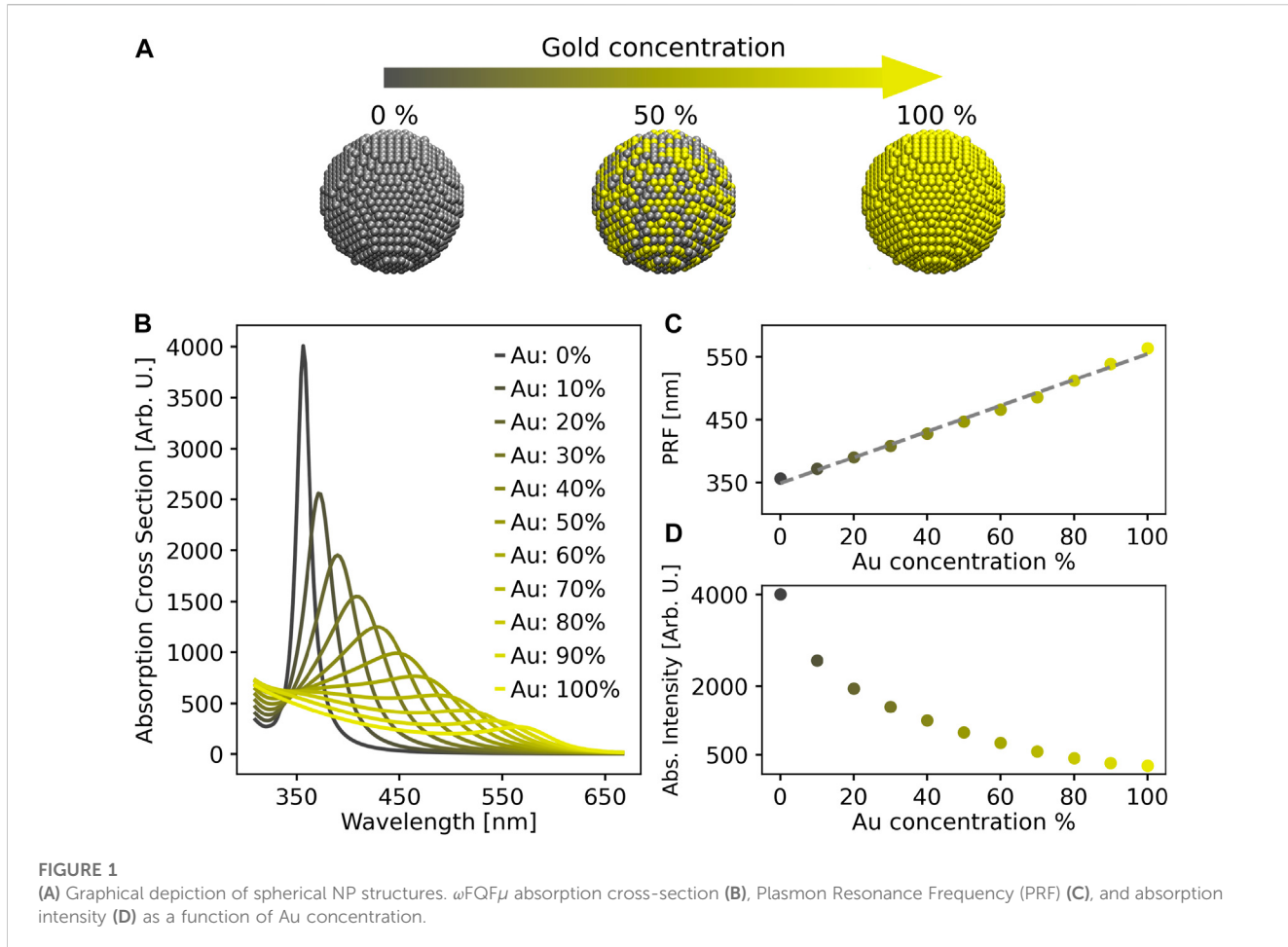
$$\boldsymbol{\mu}_i = \alpha_i(\omega) \left[\mathbf{E}_i^{\text{ext}} + \sum_k \mathbf{T}_{ik}^{qu} q_k + \sum_k \mathbf{T}_{ik}^{uu} \boldsymbol{\mu}_k \right] \quad (20)$$

where the field generated by the multipoles is mediated by the interaction tensors \mathbf{T}^{qu} and \mathbf{T}^{uu} , defined according to (Giovannini et al., 2019a).

The coupled charge-dipole equations can finally be written in a compact notation as follows:

$$\begin{aligned} &\left[\begin{array}{cc} \frac{1}{2} (\bar{\mathbf{K}} + \bar{\mathbf{H}}(\omega)) \mathbf{T}^{qq} - \mathbf{Z}(\omega) & \frac{1}{2} (\bar{\mathbf{K}} + \bar{\mathbf{H}}(\omega)) \mathbf{T}^{qu} \\ \mathbf{T}^{qu} & \mathbf{T}^{uu} - \mathbf{Z}^{\text{IB}}(\omega) \end{array} \right] \begin{bmatrix} \mathbf{q} \\ \boldsymbol{\mu} \end{bmatrix} \\ &= \begin{bmatrix} \frac{1}{2} (\bar{\mathbf{K}} + \bar{\mathbf{H}}(\omega)) \mathbf{V}^{\text{ext}} \\ -\mathbf{E}^{\text{ext}} \end{bmatrix} \end{aligned} \quad (21)$$

where \mathbf{Z}^{IB} is a diagonal matrix, of which the elements $Z_i^{\text{IB}}(\omega) = -1/\alpha_i(\omega)$ are defined according to Eq. 19. Notice that in the case of homogenous systems, i.e., $A = B$, the standard ω FQF μ equations presented by Giovannini et al. (2022) are recovered. From the values of charges and dipoles, the complex polarizability $\bar{\alpha}$ can be



computed, from which the absorption cross section σ^{abs} can be calculated:

$$\bar{\alpha}(\omega)_{kl} = \frac{\partial \bar{d}_k(\omega)}{\partial E_l(\omega)} = \sum_i q_{i,k}(\omega) \cdot \frac{k_i}{E_l(\omega)} - \sum_i \mu_{i,k}(\omega) \quad (22)$$

$$\sigma^{\text{abs}} = \frac{4\pi}{3c} \omega \text{ tr}(\text{Im}(\bar{\alpha}(\omega))) \quad (23)$$

In the previous equations \mathbf{d} is the total complex dipole moment, i runs over NP atoms, k represents x, y, z positions of the i th atom, and l runs over x, y, z directions of the external electric field. c is the speed of light and $\text{Im}(\bar{\alpha})$ is the imaginary part of the complex polarizability $\bar{\alpha}$.

2.2 Computational details

The developed ω FQF μ approach is challenged to reproduce the optical response of several Ag-Au nanostructures. In particular, we first consider Ag-Au spherical nanoalloys with diameter $D = 5.2$ nm (4,347 atoms) and Ag-Au nanorods with $D = 2.5$ nm and length $L = 10$ nm (2,560 atoms), which are generated by using Atomic Simulation Environment (ASE) Python module v. 3.17 (Larsen et al., 2017). A lattice constant of 4.08 Å (Haynes, 2014) and a Face-Centered Cubic (FCC) packing are exploited. For both spheres and nanorods, ten alloy compositions are considered by starting from pure Ag structures and increasing the percentage of Au atoms, which

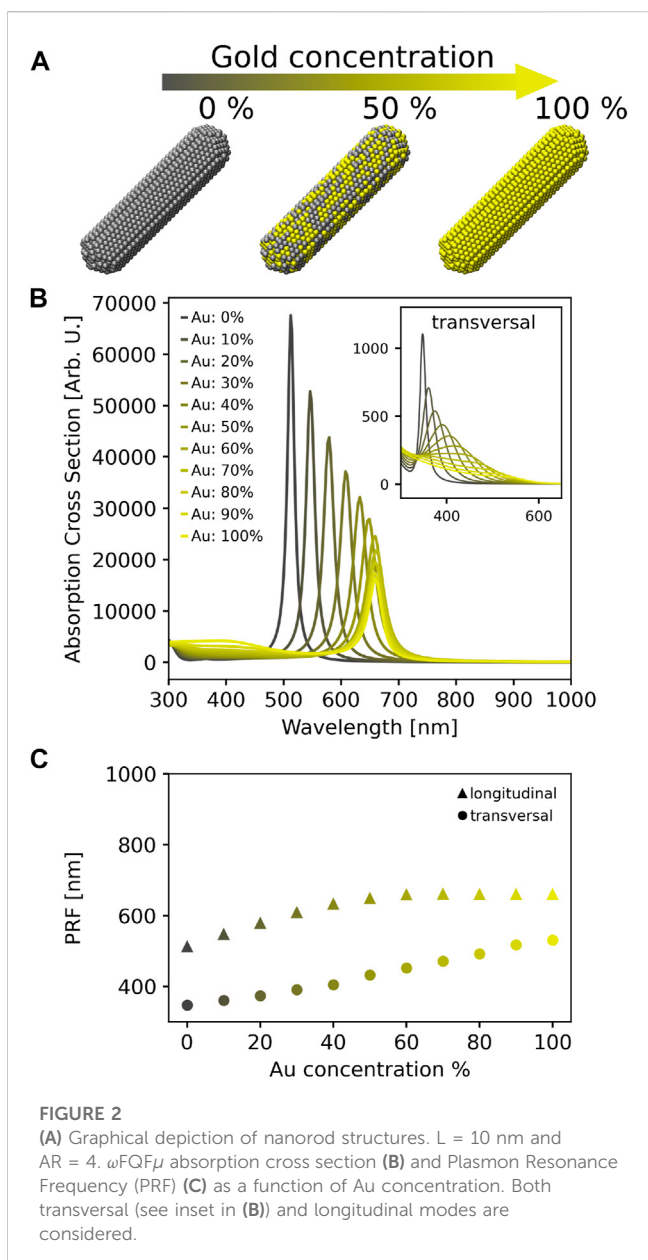
randomly replace Ag atoms (from 0% to 100%, with a constant step of 10%). To gain statistical significance, for each Au percentage, ten nanoalloy structures are generated by randomly replacing the proper fraction of Ag with Au, similarly to the strategy followed in previous studies (Sørensen et al., 2021). As a further example, core-shell spherical systems, which are constituted by an inner Au sphere ($D = 5.0$ nm, 3,851 atoms) surrounded by an outer Ag shell ($D = 6.25$ nm, 3,698 atoms), are investigated.

ω FQF μ equations are solved by using a stand-alone Fortran 95 package. ω FQF μ parameters (see Eqs 5, 6, 18) for Ag and Au atoms are taken from (Giovannini et al., 2022). In particular, Drude and interband parameters are recovered from Ag and Au experimental permittivity functions (Etchegoin et al., 2006). The parameters $d_{ij} = 12.0$ and $s_{ij} = 0.95$ entering Eq. 6 are obtained by fitting ω FQF μ results for $i = \text{Ag}$ and $j = \text{Au}$ (and vice versa) on reference time-dependent density functional theory + tight binding (TD-DFT + TB) (Asadi-Aghbolaghi et al., 2020) absorption spectra of Ag-Au clusters (see Sec. S2 in the SM).

3 Results and discussion

3.1 Spherical nanoparticles and nanorods

The modeling of the dependence of the absorption cross-section σ^{abs} of a spherical NP on the Au concentration has received much



attention in the literature (Papavassiliou, 1976; Link et al., 1999; Rioux et al., 2014; Ristig et al., 2015). In particular, a simple linear combination of Ag and Au permittivity functions combined with the Mie theory cannot reproduce the linear behavior of the plasmon redshift upon increasing Au concentration which is experimentally observed (Link et al., 1999). This issue can be solved by following the strategy proposed by Rioux et al. (2014), who have developed an analytical and rigorous model to predict a composition-dependent complex dielectric function of Ag-Au alloys, based on critical point analysis of the band-structure of Ag and Au. By coupling such modeling to the Mie theory, the correct trend is followed for spherical nanoalloys. It is worth noting that such a strategy might be exploited within the more refined, yet continuum, BEM method, thus overcoming the limitations of this approach in describing the plasmonic properties of nanoalloys. However, while the methodology proposed by Rioux et al. (2014) is

rigorous from the theoretical point of view, its extension to different alloy compositions, and to alloys of different chemical nature rather than Au and Ag is far from trivial, due to the high (about 30) number of parameters that would need to be fitted to obtain the composition dependent dielectric function.

Computed ω FQ μ values for σ^{abs} of a spherical NP with different Au concentrations are reported in (see Figure 1). In all cases, spectra are characterized by a main peak (associated with the dipolar mode, see Supplementary Figure S2 in the SM), which redshifts and lowers in intensity as the Au concentration increases. By plotting the PRF (in nm) as a function of the percentage of Au (see Figure 1C), a linear trend is observed ($R^2 \sim 1.00$). This behavior perfectly follows Vegard's law, which reads:

$$\lambda^{\text{Vegard}}(x) = (1 - x)\lambda_{\text{Ag}} + x\lambda_{\text{Au}} \quad (24)$$

where x is the percentage of Au atoms. Such a linear dependence of the absorption wavelength on Au percentage is reported by many experimental works (Papavassiliou, 1976; Link et al., 1999; Rioux et al., 2014; Ristig et al., 2015). The slope (2.06 nm/% Au) of the line fitted on ω FQ μ results is in good agreement with experimental data (Link et al., 1999) (~ 1.35 nm/% Au). Furthermore, by moving from pure Ag to pure Au NPs, the intensity of the plasmon band exponentially decreases ($R^2 = 0.99$, see Figure 1D), thus perfectly reproducing experimental findings (Link et al., 1999).

We note that, remarkably, other classical atomistic approaches may fail at reproducing the experimentally reported linear trend in wavelength and the exponentially decreasing intensity (Sørensen et al., 2021). Differently, ω FQ μ can correctly reproduce all the plasmonic properties of these structures, which is a key result of this paper.

We now move to discuss the plasmonic properties of Ag-Au alloy nanorods. Also in this case, we study the dependence of the absorption frequency on the Au concentration, which varies from 0% (pure Ag nanorod) to 100% (pure Au nanorod), with a constant step of 10%. ω FQ μ absorption cross sections, which are reported in Figure 2B, are clearly dominated by an intense peak which redshifts and decreases in intensity as the gold concentration increases. This peak is associated with the longitudinal dipolar mode (see also Supplementary Figure S3 in the SM). From a comparison with spherical NPs (see Figure 1B), we note that the dipolar peak moves to lower energies, independently of the chemical composition of the alloy nanorod. Also, in this case, additional bands can be appreciated in the region between 350 and 500 nm. There, octupolar plasmons arise (Bonatti et al., 2020), together with transversal dipolar modes. The associated bands associated are graphically depicted as an inset in Figure 2B, and redshift and lower in intensity as the Au concentration increases.

The PRFs (in nm) of both the longitudinal and transversal dipolar modes as a function of the Au percentage are graphically depicted in Figure 2C. The transversal mode follows the linear trend ($R^2 = 0.99$) predicted by Vegard's law (see Eq. 24), while for the longitudinal plasmon, an evident deviation from the linear regime is observed, especially for Au concentrations larger than 40%. Our findings are in agreement with the experimental measurements reported by Bok et al. (2009), where for the transversal peak a linear trend is measured. Also, the experimental slope (1.47 nm/%Au) correlates significantly well with our calculations (1.92 nm/%Au). Differently, the longitudinal absorption wavelength is reported to be rather independent of the chemical composition for Au percentages > 40%, while a slight

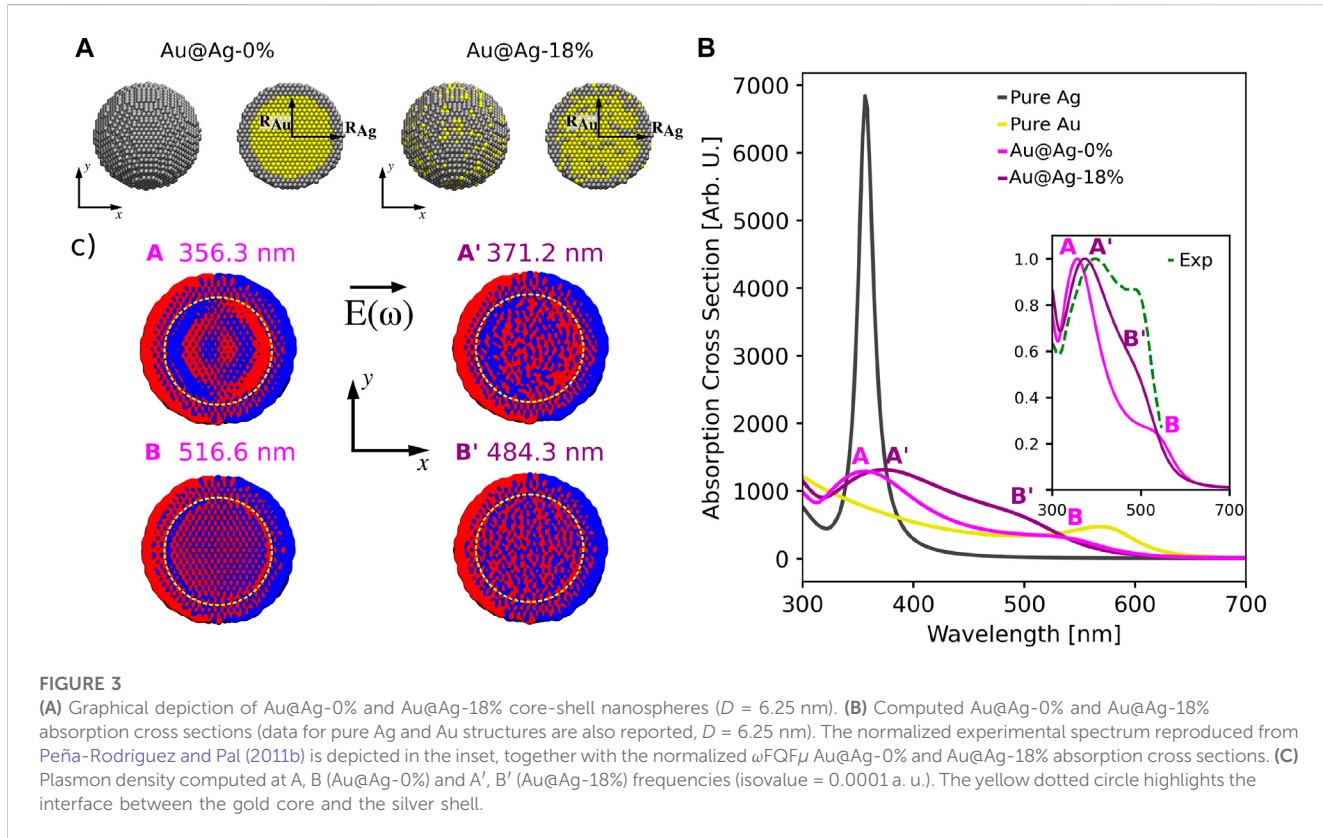


FIGURE 3

(A) Graphical depiction of Au@Ag-0% and Au@Ag-18% core-shell nanospheres ($D = 6.25$ nm). (B) Computed Au@Ag-0% and Au@Ag-18% absorption cross sections (data for pure Ag and Au structures are also reported, $D = 6.25$ nm). The normalized experimental spectrum reproduced from Peña-Rodríguez and Pal (2011b) is depicted in the inset, together with the normalized ω FQF μ Au@Ag-0% and Au@Ag-18% absorption cross sections. (C) Plasmon density computed at A, B (Au@Ag-0%) and A', B' (Au@Ag-18%) frequencies (isovalue = 0.0001 a. u.). The yellow dotted circle highlights the interface between the gold core and the silver shell.

blueshift is expected by increasing the Ag concentration Bok et al. (2009). Note that a DDA description is able to reproduce the composition dependence of the longitudinal mode but fails at describing the linear trend of the transversal peak (Bok et al., 2009). This is probably related to the exploited linear combination of Ag and Au permittivity functions. Remarkably, ω FQF μ correctly models both behaviors.

These findings can be explained by considering that the longitudinal dipolar mode falls at energies that are reasonably far from interband transition regions of both Ag and Au. In this regime, Drude free electrons play a dominant role (Link et al., 1999; Bok et al., 2009) and the good agreement with experiments reported by both DDA (Bok et al., 2009) and ω FQF μ show that the permittivity function in this region can be reasonably approximated as a linear combination of Ag and Au Drude contributions. Differently, the transversal plasmon mode absorbs at much higher energies, where interband effects cannot be neglected (Kreibig et al., 1995). This proves the reliability of ω FQF μ , which, differently from other models (Draine and Flatau, 1994), describes the plasmonic resonance by means of both electric charges and dipoles, modeling the intraband and interband mechanisms, respectively.

3.2 Au@Ag core-shell NPs

ω FQF μ is not limited to the description of nanoalloys, but can generally describe bimetallic nanostructures. To showcase its applicability, we consider pure core-shell (Au@Ag-0%) spherical NPs with a diameter D of 6.25 nm (3,698 atoms, see Figure 3A), constituted

by a Au core ($D_{Au} = 5$ nm), and an external Ag shell (external $D_{Ag} = 6.25$ nm, $D_{Au}/D_{Ag} = 0.8$). In addition, to show the flexibility of ω FQF μ , the effect of alloying such structures, which has been experimentally realized (Ristig et al., 2015; Blommaerts et al., 2019), is also taken into account, by randomly replacing 18% of the core Au atoms with Ag, and viceversa for the Ag shell (Au@Ag-18%, see Figure 3A).

Computed ω FQF μ absorption cross sections in the visible range for both core-shell systems are reported in Figure 3B, together with reference spectra for Ag and Au spherical NPs with $D = 6.25$ nm. Similarly to Figure 1B, Ag and Au reference absorption spectra are characterized by a main peak, located at about 360 nm and 570 nm for Ag and Au, respectively. The spectrum of the pure Au@Ag-0% core-shell is instead dominated by two peaks A and B, in agreement with (Peña-Rodríguez and Pal, 2011a; Chen et al., 2012; Gao et al., 2014), which fall at about 356 nm (A) and 517 nm (B). To deeply investigate the nature of the plasmons associated with these two bands, we graphically report in Figure 3C, left panel, the electron densities at the excitation energies for pure Au@Ag-0% core-shell (on a slice in the xy plane). As it can be appreciated, both peaks are associated with a global dipolar plasmon. However, they differ for the electron distribution in both the Au core and the interface between the two regions (see yellow dashed line in Figure 3C). Indeed, for peak A a huge charge accumulation at the interface is reported, while for peak B, the boundary between the Ag shell and the Au core is only partially marked. This is due to the fact that our model allows for charge exchange between the two layers, which is for instance not accounted for by other classical descriptions (Szántó et al., 2021). However, such a charge transfer is limited by the different tunneling barriers between the two metals, as introduced in Eq. 6, and by the different chemical nature

(chemical hardness, polarizability, Drude parameters, ...). As a consequence, charge accumulation at the Ag-Au interface is expected.

Similarly, the Au@Ag-18% absorption cross section (see Figure 3B) is characterized by two main peaks A' and B', which are blue- and red-shifted as compared to their counterparts in Au@Ag-0% system. Such a behavior can be justified by considering that by increasing the alloying degree up to 50%, a fully alloyed Ag-Au spherical NP is obtained. Therefore, in this situation, a single band is expected at about 450 nm (see also Figure 1B). The plasmonic nature of the electron densities computed at the A' and B' frequencies is graphically reported in Figure 3C, right panel. A global dipolar plasmon is observed. However, by also comparing with Au@Ag-0%, charge accumulation at the core-shell boundary is still present, but less pronounced, in particular for B'. This confirms the above speculation: indeed, by increasing the alloying degree, a decrease in the potential barrier at the interface is obtained.

To conclude the discussion on Au@Ag core-shell systems, we compare our results with experimental absorption cross sections reported by Peña-Rodríguez and Pal (2011b) (see inset in Figure 3B), who studied the plasmonic response of Au@Ag core-shell spherical NPs with $D = 44.2$ nm and characterized by $D_{Au}/D_{Ag} = 0.81$ (comparable with our simulations). As it can be noticed, the experimental spectrum is characterized by two main peaks at about 400 nm and 497 nm. This is in very good agreement with our calculations, thus further demonstrating the reliability of our model. In fact, only a slight discrepancy in relative intensities, probably due to different experimental conditions (size of the NP, solvent, ...), is observed.

4 Conclusion

ω FQF μ has been extended to the description of bimetallic metal nanoalloys and core-shell NPs, and has been applied to spherical alloyed NPs and nanorods, for which alternative methods proposed in the literature fail, due to incorrect modeling of interband contributions. Remarkably, ω FQF μ correctly reproduces experimental trends, also in the case of core-shell systems; this is a direct consequence of the atomistic nature of the approach, which permits a physically consistent picture of the local environment of each specific atom.

ω FQF μ is general enough to describe any kind of bimetallic system; for instance, it can be applied to complex geometrical arrangements, such as subnanometer junctions, which form when two NPs approach each other. Such complex nanostructures require appropriate treatment of interband transitions and reliable modeling of quantum tunneling effects. The effect of alloying in subnanometer junctions has been only marginally investigated, due to the lack of theoretical approaches to correctly describe the plasmonic properties of alloys and generic bimetallic systems. ω FQF μ can indeed be applied to these systems and this investigation will be the topic of future studies. Also, ω FQF μ can be extended to generic multi-metallic nanostructures, through the generalization of Eq. 19 followed by a specification of the quantities entering Eq. 6.

As a final technological perspective, relevant for instance in sensing applications, the approach can be potentially applied to compute spectral properties of molecules adsorbed on bimetallic systems, by generalizing previous studies on homogenous substrates (Payton et al., 2013; Lafiosca et al., 2023). In this way, Surface-Enhanced spectroscopic signals can be simulated by retaining an

atomistic description of the plasmonic substrate, which plays a crucial role in bimetallic systems, as it is demonstrated in this work.

Data availability statement

The raw data supporting the conclusion of this article will be made available by the authors, without undue reservation.

Author contributions

LN, PL, and TG developed the theoretical methodology. LN, PL, and PG ran ω FQF μ calculations. TG, LN, and PL implemented the method into the stand-alone Fortran95 code for ω FQF μ calculations. LN, PL, PG, LB, and TG analyzed data and wrote the original draft manuscript. TG and CC discussed and supervised the whole project. CC acquired the funding and finalized the manuscript (final version). All authors contributed to the article and approved the submitted version.

Funding

This work has received funding from the European Research Council (ERC) under the European Union's Horizon 2020 research and innovation program (grant agreement N. 818064). CC acknowledges funding from PNRR MUR project PE0000023-NQSTI.

Acknowledgments

We gratefully acknowledge the Center for High-Performance Computing (CHPC) at SNS for providing the computational infrastructure.

Conflict of interest

The authors declare that the research was conducted in the absence of any commercial or financial relationships that could be construed as a potential conflict of interest.

Publisher's note

All claims expressed in this article are solely those of the authors and do not necessarily represent those of their affiliated organizations, or those of the publisher, the editors and the reviewers. Any product that may be evaluated in this article, or claim that may be made by its manufacturer, is not guaranteed or endorsed by the publisher.

Supplementary material

The Supplementary Material for this article can be found online at: <https://www.frontiersin.org/articles/10.3389/fphot.2023.1199598/full#supplementary-material>

References

- Aizpurua, J., Hanarp, P., Sutherland, D., Käll, M., Bryant, G. W., and García de Abajo, F. J. (2003). Optical properties of gold nanorings. *Phys. Rev. Lett.* 90, 057401. doi:10.1103/physrevlett.90.057401
- Anker, J. N., Hall, W. P., Lyandres, O., Shah, N. C., Zhao, J., and Van Duyne, R. P. (2008). Biosensing with plasmonic nanosensors. *Nat. Mater.* 7, 442–453. doi:10.1038/nmat2162
- Asadi-Aghbolaghi, N., Ruger, R., Jamshidi, Z., and Visscher, L. (2020). Td-dft+ tb: An efficient and fast approach for quantum plasmonic excitations. *J. Phys. Chem. C* 124, 7946–7955. doi:10.1021/acs.jpcc.0c00979
- Atwater, H. A., and Polman, A. (2010). Plasmonics for improved photovoltaic devices. *Nat. Mater.* 9, 205–213. doi:10.1038/nmat2629
- Awada, C., Dab, C., Grimaldi, M. G., Alshoabi, A., and Ruffino, F. (2021). High optical enhancement in au/ag alloys and porous au using surface-enhanced Raman spectroscopy technique. *Sci. Rep.* 11, 4714. doi:10.1038/s41598-021-84093-0
- Bade, W. (1957). Drude-model calculation of dispersion forces. i. general theory. *J. Chem. Phys.* 27, 1280–1284. doi:10.1063/1.1743991
- Baghramyan, H. M., Della Sala, F., and Ciraci, C. (2021). Laplacian-level quantum hydrodynamic theory for plasmonics. *Phys. Rev. X* 11, 011049. doi:10.1103/physrevx.11.011049
- Barcaro, G., Broyer, M., Durante, N., Fortunelli, A., and Stener, M. (2011). Alloying effects on the optical properties of ag–au nanoclusters from tddft calculations. *J. Phys. Chem. C* 115, 24085–24091. doi:10.1021/jp2087219
- Barcaro, G., Sementa, L., Fortunelli, A., and Stener, M. (2014). Optical properties of pt and ag–pt nanoclusters from tddft calculations: Plasmon suppression by pt poisoning. *J. Phys. Chem. C* 118, 28101–28108. doi:10.1021/jp508824w
- Barcaro, G., Sementa, L., Fortunelli, A., and Stener, M. (2015). Optical properties of nanoalloys. *Phys. Chem. Chem. Phys.* 17, 27952–27967. doi:10.1039/c5cp00498e
- Blommaerts, N., Vanrompay, H., Nuti, S., Lenaerts, S., Bals, S., and Verbruggen, S. W. (2019). Unraveling structural information of turkevich synthesized plasmonic gold–silver bimetallic nanoparticles. *Small* 15, 1902791. doi:10.1002/smll.201902791
- Bok, H.-M., Shuford, K. L., Kim, S., Kim, S. K., and Park, S. (2009). Multiple surface plasmon modes for gold/silver alloy nanorods. *Langmuir* 25, 5266–5270. doi:10.1021/la803900w
- Bonatti, L., Gil, G., Giovannini, T., Corni, S., and Cappelli, C. (2020). Plasmonic resonances of metal nanoparticles: Atomistic vs. continuum approaches. *Front. Chem.* 8, 340. doi:10.3389/fchem.2020.00340
- Bonatti, L., Nicoli, L., Giovannini, T., and Cappelli, C. (2022). *In silico* design of graphene plasmonic hot-spots. *Nanoscale Adv.* 4, 2294–2302. doi:10.1039/d2na00088a
- Cao, M., Liu, Q., Chen, M., Chen, L., Yang, D., Hu, H., et al. (2018). Fully alloying au/ag nanorods in a photothermal nano-oven: Superior plasmonic property and enhanced chemical stability. *ACS Omega* 3, 18623–18629. doi:10.1021/acsomega.8b03020
- Chen, Y., Wu, H., Li, Z., Wang, P., Yang, L., and Fang, Y. (2012). The study of surface plasmon in au/ag core/shell compound nanoparticles. *Plasmonics* 7, 509–513. doi:10.1007/s11468-012-9336-6
- Chen, X., Moore, J. E., Zekarias, M., and Jensen, L. (2015). Atomistic electrodynamics simulations of bare and ligand-coated nanoparticles in the quantum size regime. *Nat. Commun.* 6, 8921. doi:10.1038/ncomms9921
- Ciraci, C., and Della Sala, F. (2016). Quantum hydrodynamic theory for plasmonics: Impact of the electron density tail. *Phys. Rev. B* 93, 205405. doi:10.1103/physrevb.93.205405
- Ciraci, C., Hill, R., Mock, J., Urzhumov, Y., Fernández-Domínguez, A., Maier, S., et al. (2012). Probing the ultimate limits of plasmonic enhancement. *Science* 337, 1072–1074. doi:10.1126/science.1224823
- Ciraci, C., Pendry, J. B., and Smith, D. R. (2013). Hydrodynamic model for plasmonics: A macroscopic approach to a microscopic problem. *ChemPhysChem* 14, 1109–1116. doi:10.1002/cphc.201200992
- Coccia, E., Fregoni, J., Guido, C., Marsili, M., Pipolo, S., and Corni, S. (2020). Hybrid theoretical models for molecular nanoplasmonics. *J. Chem. Phys.* 153, 200901. doi:10.1063/5.0027935
- Corni, S., and Tomasi, J. (2001). Enhanced response properties of a chromophore physisorbed on a metal particle. *J. Chem. Phys.* 114, 3739–3751. doi:10.1063/1.1342241
- Corni, S., and Tomasi, J. (2002a). Excitation energies of a molecule close to a metal surface. *J. Chem. Phys.* 117, 7266–7278. doi:10.1063/1.1507579
- Corni, S., and Tomasi, J. (2002b). Surface enhanced Raman scattering from a single molecule adsorbed on a metal particle aggregate: A theoretical study. *J. Chem. Phys.* 116, 1156–1164. doi:10.1063/1.1428349
- Danielis, N., Vega, L., Fronzoni, G., Stener, M., Bruix, A., and Neyman, K. M. (2021). Agpd, aupd, and aupt nanoalloys with ag-or au-rich compositions: Modeling chemical ordering and optical properties. *J. Phys. Chem. C* 125, 17372–17384. doi:10.1021/acs.jpcc.1c04222
- Della Sala, F., Pachter, R., and Sukharev, M. (2022). Advances in modeling plasmonic systems. *J. Chem. Phys.* 157, 190401. doi:10.1063/5.0130790
- Della Sala, F. (2022). Orbital-free methods for plasmonics: Linear response. *J. Chem. Phys.* 157, 104101. doi:10.1063/5.0100797
- Draine, B. T., and Flatau, P. J. (1994). Discrete-dipole approximation for scattering calculations. *J. Opt. Soc. Am. A* 11, 1491–1499. doi:10.1364/josaa.11.001491
- Esteban, R., Borisov, A. G., Nordlander, P., and Aizpurua, J. (2012). Bridging quantum and classical plasmonics with a quantum-corrected model. *Nat. Commun.* 3, 825. doi:10.1038/ncomms1806
- Esteban, R., Zugarramurdi, A., Zhang, P., Nordlander, P., García-Vidal, F. J., Borisov, A. G., et al. (2015). A classical treatment of optical tunneling in plasmonic gaps: Extending the quantum corrected model to practical situations. *Faraday Discuss.* 178, 151–183. doi:10.1039/c4fd00196f
- Etchegoin, P. G., Le Ru, E., and Meyer, M. (2006). An analytic model for the optical properties of gold. *J. Chem. Phys.* 125, 164705. doi:10.1063/1.2360270
- Gao, C., Hu, Y., Wang, M., Chi, M., and Yin, Y. (2014). Fully alloyed ag/au nanospheres: Combining the plasmonic property of ag with the stability of au. *J. Am. Chem. Soc.* 136, 7474–7479. doi:10.1021/ja502890c
- García de Abajo, F. J., and Howie, A. (2002). Retarded field calculation of electron energy loss in inhomogeneous dielectrics. *Phys. Rev. B* 65, 115418. doi:10.1103/physrevb.65.115418
- Giannini, V., Fernández-Domínguez, A. I., Heck, S. C., and Maier, S. A. (2011). Plasmonic nanoantennas: Fundamentals and their use in controlling the radiative properties of nanoemitters. *Chem. Rev.* 111, 3888–3912. doi:10.1021/cr1002672
- Giannone, G., Smiga, S., D'Agostino, S., Fabiano, E., and Della Sala, F. (2021). Plasmon couplings from subsystem time-dependent density functional theory. *J. Phys. Chem. A* 125, 7246–7259. doi:10.1021/acs.jpca.1c05384
- Giovannini, T., Puglisi, A., Ambrosetti, M., and Cappelli, C. (2019a). Polarizable qm/mm approach with fluctuating charges and fluctuating dipoles: The qm/qffμ model. *J. Chem. Theory Comput.* 15, 2233–2245. doi:10.1021/acs.jctc.8b01149
- Giovannini, T., Rosa, M., Corni, S., and Cappelli, C. (2019b). A classical picture of subnanometer junctions: An atomistic drude approach to nanoplasmonics. *Nanoscale* 11, 6004–6015. doi:10.1039/c8nr09134j
- Giovannini, T., Bonatti, L., Polini, M., and Cappelli, C. (2020). Graphene plasmonics: Fully atomistic approach for realistic structures. *J. Phys. Chem. Lett.* 11, 7595–7602. doi:10.1021/acs.jpclett.0c02051
- Giovannini, T., Bonatti, L., Lafiosca, P., Nicoli, L., Castagnola, M., Illobre, P. G., et al. (2022). Do we really need quantum mechanics to describe plasmonic properties of metal nanostructures? *ACS Photonics* 9, 3025–3034. doi:10.1021/acsphotonics.2c00761
- Gong, C., and Leite, M. S. (2016). Noble metal alloys for plasmonics. *ACS Photonics* 3, 507–513. doi:10.1021/acsphtnics.5b00586
- Halas, N. J., Lal, S., Chang, W.-S., Link, S., and Nordlander, P. (2011). Plasmons in strongly coupled metallic nanostructures. *Chem. Rev.* 111, 3913–3961. doi:10.1021/cr200061k
- Hao, F., Nehl, C. L., Hafner, J. H., and Nordlander, P. (2007). Plasmon resonances of a gold nanostar. *Nano Lett.* 7, 729–732. doi:10.1021/nl062969c
- Haynes, W. (2014). *CRC handbook of chemistry and physics*. Boca Raton: CRC Press.
- Hohenester, U., and Trügler, A. (2012). MNPBEM – a Matlab toolbox for the simulation of plasmonic nanoparticles. *Comput. Phys. Commun.* 183, 370–381. doi:10.1016/j.cpc.2011.09.009
- Hohenester, U. (2015). Quantum corrected model for plasmonic nanoparticles: A boundary element method implementation. *Phys. Rev. B* 91, 205436. doi:10.1103/physrevb.91.205436
- Huang, J., Zhu, Y., Liu, C., Zhao, Y., Liu, Z., Hedhili, M. N., et al. (2015). Fabricating a homogeneously alloyed au/ag shell on au nanorods to achieve strong, stable, and tunable surface plasmon resonances. *Small* 11, 5214–5221. doi:10.1002/smll.201501220
- Jensen, L. L., and Jensen, L. (2008). Electrostatic interaction model for the calculation of the polarizability of large noble metal nanoclusters. *J. Phys. Chem. C* 112, 15697–15703. doi:10.1021/jp804116z
- Jensen, L. L., and Jensen, L. (2009). Atomistic electrodynamics model for optical properties of silver nanoclusters. *J. Phys. Chem. C* 113, 15182–15190. doi:10.1021/jp904956f
- Kneipp, K., Wang, Y., Kneipp, H., Perelman, L. T., Itzkan, I., Dasari, R. R., et al. (1997). Single molecule detection using surface-enhanced Raman scattering (sers). *Phys. Rev. Lett.* 78, 1667–1670. doi:10.1103/physrevlett.78.1667
- Kreibig, U., Vollmer, M., Kreibig, U., and Vollmer, M. (1995). “Theoretical considerations,” in *Optical properties of metal clusters*, 13–201.
- Kuddah, M., Putra, M., and Djuhana, D. (2020). “The incident electrical field angle effect in localized surface plasmon resonance (lspr) of bimetallic ag–au nanorod using mnpbem simulation,” in IOP Conference Series: Materials Science and Engineering (IOP Publishing), 012058.
- Lafiosca, P., Giovannini, T., Benzi, M., and Cappelli, C. (2021). Going beyond the limits of classical atomistic modeling of plasmonic nanostructures. *J. Phys. Chem. C* 125, 23848–23863. doi:10.1021/acs.jpcc.1c04716

- Lafiosca, P., Nicoli, L., Bonatti, L., Giovannini, T., Corni, S., and Cappelli, C. (2023). Qm/classical modeling of surface enhanced Raman scattering based on atomistic electromagnetic models. *J. Chem. Theory Comput.* doi:10.1021/acs.jctc.3c00177
- Larsen, A. H., Mortensen, J. J., Blomqvist, J., Castelli, I. E., Christensen, R., Dulak, M., et al. (2017). The atomic simulation environment—A python library for working with atoms. *J. Phys. Condens. Matter* 29, 273002. doi:10.1088/1361-648x/aa680e
- Liebsch, A. (1993). Surface-plasmon dispersion and size dependence of mie resonance: Silver versus simple metals. *Phys. Rev. B* 48, 11317–11328. doi:10.1103/physrevb.48.11317
- Lim, D.-K., Jeon, K.-S., Kim, H. M., Nam, J.-M., and Suh, Y. D. (2010). Nanogap-engineerable Raman-active nanodumbbells for single-molecule detection. *Nat. Mater.* 9, 60–67. doi:10.1038/nmat2596
- Link, S., Wang, Z. L., and El-Sayed, M. (1999). Alloy formation of gold-silver nanoparticles and the dependence of the plasmon absorption on their composition. *J. Phys. Chem. B* 103, 3529–3533. doi:10.1021/jp990387w
- López Lozano, X., Mottet, C., and Weissker, H.-C. (2013). Effect of alloying on the optical properties of ag-*au* nanoparticles. *J. Phys. Chem. C* 117, 3062–3068. doi:10.1021/jp309957y
- Ma, Y.-W., Zhang, L.-H., Wu, Z.-W., Yi, M.-F., Zhang, J., and Jian, G.-S. (2015). The study of tunable local surface plasmon resonances on au-ag and ag-*au* core-shell alloy nanostructure particles with dda method. *Plasmonics* 10, 1791–1800. doi:10.1007/s11468-015-9997-z
- Ma, J., Liu, X., Wang, R., Zhang, J., Jiang, P., Wang, Y., et al. (2020). Bimetallic core-shell nanostars with tunable surface plasmon resonance for surface-enhanced Raman scattering. *ACS Appl. Nano Mater.* 3, 10885–10894. doi:10.1021/acsnano.0c02144
- Maier, S. A., Kik, P. G., Atwater, H. A., Meltzer, S., Harel, E., Koel, B. E., et al. (2003). Local detection of electromagnetic energy transport below the diffraction limit in metal nanoparticle plasmon waveguides. *Nat. Mater.* 2, 229–232. doi:10.1038/nmat852
- Maier, S. A. (2007). *Plasmonics: Fundamentals and applications*. Springer Science & Business Media.
- Mie, G. (1908). Beiträge zur optik trüber medien, speziell kolloidaler metallösungen. *Ann. Phys.-Berlin* 330, 377–445. doi:10.1002/andp.19083300302
- Moskovits, M. (1985). Surface-enhanced spectroscopy. *Rev. Mod. Phys.* 57, 783–826. doi:10.1103/revmodphys.57.783
- Muehlschlegel, P., Eisler, H.-J., Martin, O. J., Hecht, B., and Pohl, D. (2005). Resonant optical antennas. *Science* 308, 1607–1609. doi:10.1126/science.1111886
- Myroshnychenko, V., Rodríguez-Fernández, J., Pastoriza-Santos, I., Funston, A. M., Novo, C., Mulvaney, P., et al. (2008). Modelling the optical response of gold nanoparticles. *Chem. Soc. Rev.* 37, 1792–1805. doi:10.1039/b711486a
- Neuman, T., Esteban, R., Casanova, D., García-Vidal, F. J., and Aizpurua, J. (2018). Coupling of molecular emitters and plasmonic cavities beyond the point-dipole approximation. *Nano Lett.* 18, 2358–2364. doi:10.1021/acs.nanolett.7b05297
- Newmai, M. B., Verma, M., Dahiya, A., and Kumar, P. S. (2022). Monomer driven growth of catalytically active ag-*au* plasmonic nanoalloys. *J. Phys. Chem. Solids* 161, 110371. doi:10.1016/j.jpcs.2021.110371
- Nie, S., and Emory, S. R. (1997). Probing single molecules and single nanoparticles by surface-enhanced Raman scattering. *Science* 275, 1102–1106. doi:10.1126/science.275.5303.1102
- Olobardi, S., Vega, L., Fortunelli, A., Stener, M., Vines, F., and Neyman, K. M. (2019). Optical properties and chemical ordering of ag-pt nanoalloys: A computational study. *J. Phys. Chem. C* 123, 25482–25491. doi:10.1021/acs.jpcc.9b07382
- Papavassiliou, G. C. (1976). Surface plasmons in small au-ag alloy particles. *J. Phys. F. Met. Phys.* 6, L103–L105. doi:10.1088/0305-4608/6/4/004
- Payton, J. L., Morton, S. M., Moore, J. E., and Jensen, L. (2013). A hybrid atomistic electrodynamics–quantum mechanical approach for simulating surface-enhanced Raman scattering. *Acc. Chem. Res.* 47, 88–99. doi:10.1021/ar400075r
- Peña-Rodríguez, O., and Pal, U. (2011a). Au@ ag core–shell nanoparticles: Efficient all-plasmonic fano-resonance generators. *Nanoscale* 3, 3609–3612. doi:10.1039/c1nr10625b
- Peña-Rodríguez, O., and Pal, U. (2011b). Enhanced plasmonic behavior of bimetallic (ag-*au*) multilayered spheres. *Nanoscale Res. Lett.* 6, 279. doi:10.1186/1556-276X-6-279
- Pérez-González, O., Zabala, N., Borisov, A., Halas, N., Nordlander, P., and Aizpurua, J. (2010). Optical spectroscopy of conductive junctions in plasmonic cavities. *Nano Lett.* 10, 3090–3095. doi:10.1021/nl1017173
- Putra, M., Djuhana, D., Fauzia, V., Harmoko, A., and Imawan, C. (2017). “A numerical study of the sensitivity of surface plasmon resonance bimetallic silver-gold alloys using boundary element method,” in IOP Conference Series: Materials Science and Engineering (IOP Publishing), 012016.
- Raza, S., Bozhevolnyi, S. I., Wubs, M., and Mortensen, N. A. (2015). Nonlocal optical response in metallic nanostructures. *J. Phys. Condens. Matter* 27, 183204. doi:10.1088/0953-8984/27/18/183204
- Rioux, D., Vallières, S., Besner, S., Muñoz, P., Mazur, E., and Meunier, M. (2014). An analytic model for the dielectric function of au, ag, and their alloys. *Adv. Opt. Mater.* 2, 176–182. doi:10.1002/adom.201300457
- Ristig, S., Prymak, O., Loza, K., Gocyla, M., Meyer-Zaika, W., Heggen, M., et al. (2015). Nanostructure of wet-chemically prepared, polymer-stabilized silver-gold nanoalloys (6 nm) over the entire composition range. *J. Mater. Chem. B* 3, 4654–4662. doi:10.1039/c5tb00644a
- Santhosh, K., Bitton, O., Chuntonov, L., and Haran, G. (2016). Vacuum rabi splitting in a plasmonic cavity at the single quantum emitter limit. *Nat. Commun.* 7, 11823. doi:10.1038/ncomms11823
- Scholl, J. A., García-Etxarri, A., Koh, A. L., and Dionne, J. A. (2013). Observation of quantum tunneling between two plasmonic nanoparticles. *Nano Lett.* 13, 564–569. doi:10.1021/nl304078v
- Shuford, K. L., Ratner, M. A., Gray, S. K., and Schatz, G. C. (2006). Finite-difference time-domain studies of light transmission through nanohole structures. *Appl. Phys. B* 84, 11–18. doi:10.1007/s00340-006-2218-x
- Sørensen, L. K., Utyshev, A. D., Zakomirnyi, V. I., and Ågren, H. (2021). Atomistic description of plasmonic generation in alloys and core shell nanoparticles. *Phys. Chem. Chem. Phys.* 23, 173–185. doi:10.1039/d0cp04854b
- Szántó, G., Csarnovics, I., and Bonyár, A. (2021). Numerical investigation of the refractive index sensitivity of au/ag core–shell nanostructures for sensing applications. *Sens. Bio-Sens.* 32, 100414. doi:10.1016/j.sbsr.2021.100414
- Verbruggen, S. W., Keulemans, M., Martens, J. A., and Lenaerts, S. (2013). Predicting the surface plasmon resonance wavelength of gold–silver alloy nanoparticles. *J. Phys. Chem. C* 117, 19142–19145. doi:10.1021/jp4070856
- Wang, C., Peng, S., Chan, R., and Sun, S. (2009). Synthesis of auag alloy nanoparticles from core/shell-structured ag/au. *Small* 5, 567–570. doi:10.1002/smll.200801169
- Xiang, Y., Wu, X., Liu, D., Li, Z., Chu, W., Feng, L., et al. (2008). Gold nanorod-seeded growth of silver nanostructures: From homogeneous coating to anisotropic coating. *Langmuir* 24, 3465–3470. doi:10.1021/la702999c
- Zakomirnyi, V. I., Rinkevicius, Z., Baryshnikov, G. V., Sørensen, L. K., and Ågren, H. (2019). Extended discrete interaction model: Plasmonic excitations of silver nanoparticles. *J. Phys. Chem. C* 123, 28867–28880. doi:10.1021/acs.jpcc.9b07410
- Zakomirnyi, V. I., Rasskazov, I. L., Sørensen, L. K., Carney, P. S., Rinkevicius, Z., and Ågren, H. (2020). Plasmonic nano-shells: Atomistic discrete interaction versus classic electrodynamics models. *Phys. Chem. Chem. Phys.* 22, 13467–13473. doi:10.1039/d0cp02248a

III. Multiscale Modeling of Surface Enhanced Fluorescence



Cite this: DOI: 10.1039/d4na00080c

Received 26th January 2024
Accepted 20th May 2024

DOI: 10.1039/d4na00080c
rsc.li/nanoscale-advances

1 Introduction

Under the action of an external electric field, metal nanoparticles (NPs) can exhibit localized surface plasmons (LSPs), which are collective excitations of conductive electrons. LSPs are associated with a significant enhancement of the induced electric field, up to several orders of magnitude. When a molecular system is posed in the NP proximity, its photo-physical and spectral properties can be substantially affected, yielding the so-called surface-enhanced spectroscopies.^{1–15} Among them, Surface-Enhanced Fluorescence (SEF) exploits the enhancement of the fluorescence signal, which can be useful to study biological matrices interacting with plasmonic nanostructures for biosensing applications.^{16–20} Remarkably, precise control of the NP structure and the resulting plasmonic response has enabled the mapping of single molecules, achieving submolecular resolution, within the so-called Tip-Enhanced Photoluminescence (TEPL) experiments.^{21–24} The interplay of the complex physical phenomena underlying SEF and related techniques, such as the optical response of plasmonic substrates and their interaction with the electronic structure of the chromophore, are still not fully understood, thus challenging the rationalization of the measured results. In this context, reliable computational approaches capable of accurately describing how the NP structure affects SEF signals

are needed, especially those models featuring a fully atomistic, realistic description of the nanosystem.^{18,22,25–30}

In this work, the first fully atomistic multiscale approach to SEF is developed. The model can be used to describe realistic nanostructures with atomistic details, substantially overcoming common issues related to the huge computational cost of full QM treatments of the system, which only allows the description of systems (molecule + nanostructure) composed of a few atoms.^{28,31,32} Our approach is based on the coupling of quantum mechanics (QM), defined at the density functional theory (DFT) level to determine the molecular electronic structure, with a novel fully atomistic electrodynamical approach to describe the plasmonic response of complex-shaped nanostructures, namely the frequency-dependent fluctuating charges and fluctuating dipoles (ω FQF μ) method.^{33,34} ω FQF μ is physically grounded on the Drude conduction model, electrostatics, and interband transitions and includes corrections to describe quantum tunneling effects, which can be crucial to reliably model nanoaggregates. In ω FQF μ , each metal atom is endowed with a fluctuating charge, accounting for intraband transitions (Drude regime), and a fluctuating dipole, describing interband transitions. The method can remarkably capture plasmonic properties of systems featuring subnanometer junctions^{35–37} and defects.^{38–40} Recent extensions have also permitted the calculation of the plasmonic response of bimetallic systems.⁴¹ Notably, ω FQF μ reproduces *ab initio* results, questioning the common notion that an explicit QM treatment is needed for describing plasmonic response upon shrinking the nanostructure size.³³ Furthermore, the coupling of ω FQF μ to a QM formalism (QM/ ω FQF μ) to evaluate surface-enhanced Raman scattering (SERS) signals of molecules in the vicinity of complex-shaped nanostructures, has recently been proposed.³⁴

Scuola Normale Superiore, Piazza dei Cavalieri 7, 56126 Pisa, Italy. E-mail: tommaso.giovannini@sns.it; chiara.cappelli@sns.it

† Electronic supplementary information (ESI) available: Details on the BEM model. Geometrical parameters and computed plasmon resonance frequencies. Atomistic vs. Continuum for Ag structures. Fluorescence Dependence on NP size and morphology. PDI interacting with Ag Nanorods. PDI interacting with NP dimers. See DOI: <https://doi.org/10.1039/d4na00080c>



In this paper, QM/ ω FQF μ is extended to the calculation of SEF signals. The modeling of fluorescence processes presents significant challenges compared to SERS. Specifically, the electronic structure of both the molecular Ground State (GS) and the emitting Excited State (ES) needs to be accurately described. This is achieved in terms of a Time-Dependent Density Functional Theory (TD-DFT)/ ω FQF μ formalism, which is specified by reformulating at the fully atomistic level the methodology proposed for implicit, non-atomistic, descriptions of the nanostructure.^{27–29,42–45} The latter describe the nanostructure as a continuum dielectric whose response is determined by the permittivity functions. Due to their implicit nature, atomistic features and their effect on the molecular response are neglected.

The manuscript is organized as follows. In Section 2, the theoretical foundations of ω FQF μ are recalled, and its coupling to a TDDFT formalism to study the SEF response is presented. After highlighting the computational details, in Section 4, TDDFT/ ω FQF μ is challenged to simulate SEF of a well-studied chromophore (*N,N'*-dimethylperylene 3,4,9,10-dicarboximide – PDI) near metal NPs of increasing complexity. Conclusions and future perspectives end the manuscript.

2 Theory

2.1 ω FQF μ

ω FQF μ is a fully atomistic model specifically developed for studying plasmonic responses of metal NPs.^{33,35} It combines the Drude model for intraband transitions with an effective polarizability, which mimics core electrons and interband transitions.^{46–49} To physically consistently model both mechanisms, each atom is endowed with a charge (ω FQ) and a dipole (ω F μ). Under the action of a monochromatic external electric field, the atoms exchange charge *via* the Drude conduction mechanism, which is further assisted by quantum tunneling, thus limiting charge transfer among the nearest neighboring atoms and making the interaction decrease with the typical exponential decay. In particular, ω FQ charge equation of motion in the frequency domain (ω) reads:^{33,35,37}

$$-i\omega q_i(\omega) = \frac{2n_0\tau}{1-i\omega\tau} \sum_j [1 - f(r_{ij})] \frac{\mathcal{A}_{ij}}{r_{ij}} (\phi_j^{\text{el}} - \phi_i^{\text{el}}) \quad (1)$$

where q_i is the electric charge on the i -th atom, n_0 is the 3D density, τ the scattering time, and \mathcal{A}_{ij} denotes the effective area connecting atoms i and j . The Fermi damping function $f(r_{ij})$ describes quantum tunneling effects³⁵ in terms of the interatomic distance $r_{ij} = |r_i - r_j|$ (r_i is the position of atom i). ϕ_i^{el} accounts for the electrochemical potential of the i -th atom, and takes into account charge–charge and charge–dipole interactions, and the external electric field.

To introduce interband effects, each atom is assigned an additional source of polarization, *i.e.*, atomic polarizability, to which an induced dipole moment is associated. The induced dipole moments μ_i are obtained by solving the following linear equation:³³

$$\mu_i = \alpha_i^\omega (\mathbf{E}_i^{\text{ext}} + \mathbf{E}_i^{\text{u}} + \mathbf{E}_i^{\text{q}}) \quad (2)$$

where $\mathbf{E}_i^{\text{ext}}$, \mathbf{E}_i^{u} and \mathbf{E}_i^{q} are the external electric field and the electric fields on atom i generated by the other dipoles and charges, respectively. Additionally, α_i^ω is the atomic complex polarizability, which mimics interband transitions.^{33,41} Remarkably, α_i^ω can be easily obtained by extracting interband contributions from the experimental permittivity function without introducing *a posteriori* any adjustable parameters.^{33,41}

To effectively couple charges and dipoles, eqn (1) and (2) are simultaneously solved using the following set of linear equations:³³

$$\left[\begin{pmatrix} \mathbf{D}^{\text{q}} & \mathbf{D}^{\text{qu}} \\ \mathbf{T}^{\text{uq}} & \mathbf{T}^{\text{uu}} \end{pmatrix} - \begin{pmatrix} z(\omega)\mathbf{I}_N & 0 \\ 0 & z'(\omega)\mathbf{I}_{3N} \end{pmatrix} \right] \begin{pmatrix} \mathbf{q} \\ \boldsymbol{\mu} \end{pmatrix} = \begin{pmatrix} \mathbf{R} \\ -\mathbf{E}^{\text{ext}} \end{pmatrix} \quad (3)$$

where \mathbf{D}^{q} gathers the interaction between charges, \mathbf{D}^{qu} accounts for the charge–dipole terms, and $\mathbf{T}^{\{\text{u}\}\text{q}}$ and \mathbf{T}^{uu} matrices represent the charge–dipole and dipole–dipole interaction kernels, respectively.⁵⁰ \mathbf{I}_N is the $N \times N$ identity matrix, where N is the number of atoms. z and z' functions are the complex frequency-dependent diagonal shifts associated with charges and dipoles, respectively (see ref. 33 for their definitions). In the right-hand side, \mathbf{R} and \mathbf{E}^{ext} enclose the effect of the external potential and field acting on each charge and dipole.

2.2 QM/classical coupling (QM/ ω FQF μ) and fluorescence descriptors

To evaluate the fluorescence response of a chromophore when it is influenced by the plasmonic response of a nearby metallic NP, ω FQF μ is coupled with a QM treatment of the molecule, in a multiscale fashion. Through the developed method, the effect of NP atomistic features on the fluorescence response of the nearby molecular system is evaluated, thus overcoming the limitations of QM/continuum methodologies previously proposed.^{27–29,42,43,45}

Molecular fluorescence response originates from the following subsequent processes: (a) initially, the molecule absorbs a photon from the incident electric field, being promoted to an ES; (b) the molecule undergoes internal relaxation, reaching the minimum of the emitting ES; (c) the chromophore decays to the GS, either radiatively, emitting a photon, or non-radiatively.^{27–29,43,45}

We exploit the time-dependent formulation of density functional theory (TD-DFT)^{42,44,51} and we modify it to take into account the effects of the plasmonic NP. Within a QM/ ω FQF μ formalism, Casida's equations read:³⁴

$$\left[\begin{pmatrix} \mathbf{A}(\omega) & \mathbf{B}(\omega) \\ \mathbf{B}^*(-\omega^*) & \mathbf{A}^*(-\omega^*) \end{pmatrix} - \omega \begin{pmatrix} \mathbf{I} & 0 \\ 0 & -\mathbf{I} \end{pmatrix} \right] \begin{pmatrix} \mathbf{X}_\omega \\ \mathbf{Y}_\omega \end{pmatrix} = 0 \quad (4)$$

$$A_{ai,bj}(\omega) = (\varepsilon_a - \varepsilon_b)\delta_{ab}\delta_{ij} + K_{ai,bj}^0 + K_{ai,bj}^{\text{pol}}(\omega) \quad (5a)$$

$$B_{ai,bj}(\omega) = K_{ai,jb}^0 + K_{ai,jb}^{\text{pol}}(\omega) \quad (5b)$$

where ω is the excitation frequency while \mathbf{X}_ω and \mathbf{Y}_ω are the excitation and de-excitation transition densities, respectively. Eqn (4) contains \mathbf{AB} TD-DFT matrices defined in eqn (5a) and



(5b), whose elements ($i, j/a, b$ indices run over occupied/virtual orbitals) are defined in terms of the molecular orbital energies ε . $K_{ai,bj}^0$ is the exchange-correlation contribution, while \mathbf{K}^{pol} is a frequency-dependent term that includes the polarization arising from the NP, which is expressed as:

$$K_{ai,bj}^{pol}(\omega) = \sum_v \mathbf{q}(\omega)(r_v, [\Psi_a^* \Psi_i]) \mathbf{V}(r_v, [\Psi_b^* \Psi_j]) - \sum_v \mu(\omega)(r_v, [\Psi_a^* \Psi_i]) \mathbf{E}(r_v, [\Psi_b^* \Psi_j]) \quad (6)$$

where $\mathbf{q}(\omega)(r_v, [\Psi_a^* \Psi_i])$ and $\mu(\omega)(r_v, [\Psi_a^* \Psi_i])$ represent the frequency-dependent charges and dipoles at the atomic position r_v , induced by the $\Psi_a^* \Psi_i$ distribution. They interact with the potential $\mathbf{V}(r_v, [\Psi_j^* \Psi_b])$ and field $\mathbf{E}(r_v, [\Psi_j^* \Psi_b])$ generated by the $\Psi_j^* \Psi_b$ distribution, respectively.

From the mathematical point of view, \mathbf{q} and μ are complex quantities, making \mathbf{K}^{pol} complex. By following ref. 42, the modified TD-DFT problem is solved by treating the imaginary parts as a perturbation to the first order. In particular, excitation energies and transition densities are computed from the real part of the poles (eqn (4)) as follows (' indicates real quantities):⁴²

$$\left[\begin{pmatrix} \mathbf{A}'(\omega') & \mathbf{B}'(\omega') \\ \mathbf{B}'(-\omega') & \mathbf{A}'(-\omega') \end{pmatrix} - \omega' \begin{pmatrix} \mathbf{I} & 0 \\ 0 & -\mathbf{I} \end{pmatrix} \right] \begin{pmatrix} \mathbf{X}'_\omega \\ \mathbf{Y}'_\omega \end{pmatrix} = 0 \quad (7)$$

The imaginary excitation frequency can be computed by exploiting the perturbative treatment as: (" marks imaginary parts):⁴²

$$\omega'' = \left[(\mathbf{X}'_\omega^\dagger \quad \mathbf{Y}'_\omega^\dagger) \begin{pmatrix} \mathbf{A}''(\omega') & \mathbf{B}''(\omega') \\ -\mathbf{B}''(-\omega') & -\mathbf{A}''(-\omega') \end{pmatrix} \begin{pmatrix} \mathbf{X}'_\omega \\ \mathbf{Y}'_\omega \end{pmatrix} \right] \quad (8)$$

The response imaginary component is associated with the molecular non-radiative lifetime (τ^{nr}) through the inverse of the non-radiative decay rate (Γ^{nr}). The latter is given by:⁴⁴

$$\Gamma^{nr} = \frac{1}{\tau^{nr}} = -2\omega_{Im} \quad (9)$$

The molecular radiative energy dissipation instead generates the fluorescence signal from the emitting ES to GS. This is generally characterized by the radiative lifetime (τ^r), which can be expressed as the inverse of the radiative decay rate (Γ^r). Furthermore, the emission probability is defined by the absorption coefficient (A), which is related to the population of the emitting ES. Within QM/ ω FQF μ , A and Γ^r are calculated (in a.u.) as follows:

$$A = \frac{2\pi}{3c} |\mathbf{d}_{tot}^{0K}|^2 \quad (10)$$

$$\Gamma^r = \frac{4\omega^3}{3c^3} |\mathbf{d}_{tot}^{0K}|^2 \quad (11)$$

where c is the speed of light, whereas \mathbf{d}_{tot}^{0K} is the total transition dipole from the molecular GS to the K-th ES. This takes into account both the molecular transition dipole moment (\mathbf{d}_{mol}^{0K} , calculated by solving eqn (7)) and the dipole moment induced on the plasmonic NP by the molecular transition (\mathbf{d}_{plas}^{0K}).²⁹ Thus, they can be defined as:

$$\mathbf{d}_{tot}^{0K} = \mathbf{d}_{mol}^{0K} + \mathbf{d}_{plas}^{0K} \quad (12)$$

$$\mathbf{d}_{plas}^{0K} = \sum_i q_i^{0K} \mathbf{r}_i + \sum_i \mu_i^{0K} \quad (13)$$

where q^{0K} and μ^{0K} are ω FQF μ charges and dipoles induced by the molecular transition $0 \rightarrow K$. As stated above, the efficiency of fluorescence response arises from the interplay of the discussed processes. To account for both the absorption and emission mechanisms, the relative brightness (Φ^{RB}) is computed in the following way:

$$\Phi^{RB} = \frac{A}{A^{free}} \left(\frac{\Gamma^r}{\Gamma^r + \Gamma^{nr}} \right) = \frac{A}{A^{free}} \Phi^{FQY} \quad (14)$$

where A/A^{free} is the absorption ratio in the presence or absence of the NP. The absorption ratio is multiplied by the number of emitted photons against the total number of absorbed photons. Such ratio is generally called fluorescence quantum yield (Φ^{FQY}), which is lower or equal to one by definition. Φ^{RB} quantifies fluorescence enhancement or quenching of the chromophore signal as a result of the interaction with the plasmonic NP.²⁷⁻²⁹

3 Computational details

The method is applied to studying the fluorescence response of *N,N'*-dimethylperylene 3,4,9,10-dicarboximide (PDI) chromophore as interacting with metal nanostructures of different shapes and dimensions. Both a longitudinal (L) and transversal (T) orientation of PDI relative to the NPs are considered. The fluorescence response is then investigated as a function of the PDI-NP distance (from 3 to 200 Å compared to the closest PDI hydrogen atom). In all calculations, PDI is treated at the QM level, while the metal nanostructure is classically described by using ω FQF μ . The latter is compared to the implicit description of the plasmonic systems to validate the novel approach, as provided by the BEM method. Following ref. 27, the NP response is computed at the experimental absorption (515 nm) and emission (525 nm) frequencies of PDI dissolved in *n*-heptane. The absorption coefficient (eqn (10)) is computed from the GS optimized geometry of PDI, while the non radiative decay and radiative decay rates (eqn (9) and (11)) are evaluated using the first ES optimized geometry.

Atomistic NPs are built with the Atomic Simulation Environment (ASE) Python module v. 3.17.⁵² A face-centered cubic (FCC) arrangement and a lattice parameter of 4.08 Å are exploited, for both Ag and Au NPs. The geometrical relaxation of NPs is not considered because it slightly affects their optical response, as reported in ref. 33.⁵³⁻⁵⁹ Four morphologies are analyzed: spherical, cuboctahedral (cTO), icosahedral (Ih), and cylindrical rods. The optical response of such NPs is simulated



employing ω FQF μ , using the parameters reported in ref. 33 (see also Table S3 in the ESI \dagger). ω FQF μ charges and dipoles are calculated by solving eqn (3) by direct matrix inversion for the single rods and spherical, Ih, and cTO structures with radius ≤ 30 Å. For all other studied systems (Tables S1 and S2 of the ESI \dagger), the Generalized Minimal RESidual method (GMRES) is used (RMSD threshold = 1.0×10^{-11}).³⁷

Spherical continuum structures are created using GMSH code,⁶⁰ with 5890 tesserae for each NP. Their optical properties are studied at the BEM level, using the Dielectric Polarizable Continuum Model (DPCM) formalism (see Sec. S1.1 of the ESI \dagger for more details).^{61–63} For both Ag and Au NPs, the frequency-dependent permittivity function of Etchegoin *et al.*⁶⁴ as fitted by Johnson and Christy^{65,66} is used. The permittivity function is corrected to account for the dependence of the mean free path of the electrons on the sphere radius, as described in ref. 27. BEM equations are solved by matrix inversion (see eqn (1) of the ESI \dagger). More details about the geometries and the associated Plasmon Resonance Frequencies (PRFs) are given in Tables S1 and S2 in the ESI \dagger .

In all calculations, the PDI is described at the (TD-) DFT level by using the B3LYP functional combined with a double- ζ -polarized DZP basis set.²⁷ All QM/ ω FQF μ and QM/BEM calculations are performed by using a locally modified version of the Amsterdam Modelling Suite (AMS).⁶⁷

4 Results and discussion

In this section, ω FQF μ is applied to compute the fluorescence response of PDI placed near noble metal NPs. First, QM/ ω FQF μ and QM/BEM implementations are validated on spherical NPs. Then, QM/ ω FQF μ is used to investigate the effect of different geometrical arrangements/parameters on the PDI fluorescence response.

4.1 Atomistic vs. continuum descriptions of spherical NPs

The fluorescence response of PDI as adsorbed in L or T orientation on a spherical NP (see Fig. 1a) is studied. In particular,

the attention is focused on the first bright excitation (HOMO-LUMO), which is associated with a $\pi \rightarrow \pi^*$ transition with the transition dipole moment aligned with the principal axis of the chromophore (see Fig. 1b).

In Fig. 2, calculated QM/ ω FQF μ and QM/BEM Γ^r and Γ^{nr} are reported (in logarithmic scale) as a function of the PDI-Au NP distance and Au NP radius for both L and T orientations (panels a and b, respectively). The results for Ag NPs are similar and are reported in Fig. S1 and S2 of the ESI \dagger .

Let us first focus on Γ^r . For the L orientation (see Fig. 2a, both QM/ ω FQF μ and QM/BEM Γ^r decrease as the PDI-NP distance increases, converging at large distances to the gas-phase Γ^r value. This is because, in such a configuration, the PDI transition dipole moment and the plasmon dipole moment are parallel. As a result, the plasmon-induced Γ^r is larger than its gas-phase counterpart and decreases as a function of the PDI-NP distance because the interaction between the two parts vanishes at large separations ($d_{\text{plas}}^{\text{KO}} \rightarrow 0$). For the same reasons, by enlarging the NP size, Γ^r increases because the associated $d_{\text{plas}}^{\text{KO}}$ increases. It is worth remarking that QM/ ω FQF μ and QM/BEM results are in almost perfect agreement, also from the quantitative point of view.

In contrast, for the T configuration (Fig. 2b), different trends are observed depending on the NP size. In fact, for small NPs (radius ≤ 10 Å), QM/ ω FQF μ and QM/BEM Γ^r increase as the PDI-NP distance increases. For larger NPs (radius > 10 Å), QM/ ω FQF μ and QM/BEM Γ^r decrease at small distances (<25 Å) and then increase at larger distances, displaying a minimum. In particular, by increasing the NP radius, the minimum shifts towards larger distances. In all cases, at large distances, the gas-phase Γ^r is recovered. These findings can be explained by considering that in T configuration the NP plasmon dipole moment and PDI transition dipole moment are anti-parallel. As a consequence, when $|d_{\text{plas}}^{\text{KO}}| > |d_{\text{mol}}^{\text{KO}}|$ Γ^r decreases (small distances), while when $|d_{\text{plas}}^{\text{KO}}| < |d_{\text{mol}}^{\text{KO}}|$ Γ^r increases (large distances). Γ^r minimum is displayed when $|d_{\text{plas}}^{\text{KO}}| \approx |d_{\text{mol}}^{\text{KO}}|$. By increasing the NP radius, a larger induced NP dipole is obtained, shifting the Γ^r minimum to larger distances. In this

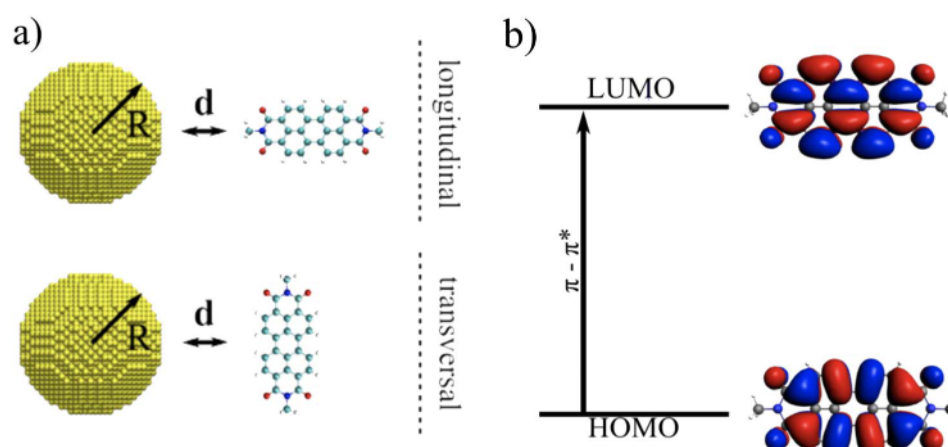


Fig. 1 (a) Graphical depiction of PDI interacting with a spherical NP of radius R. PDI is placed at a distance d from the NP in longitudinal (top) and transversal (bottom) configurations. (b) PDI molecular orbitals involved in the electronic transition under study.



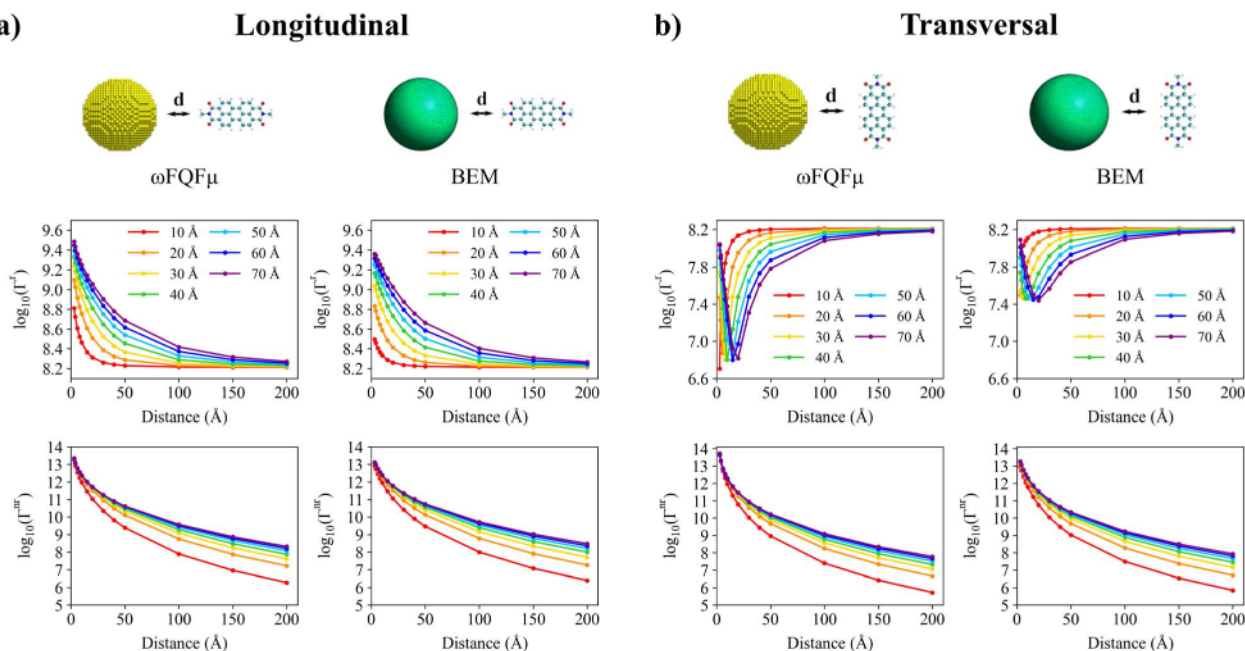


Fig. 2 Longitudinal (a) and transversal (b) orientations of PDI interacting with a spherical Au NP studied at the QM/ ω FQF μ (left) and QM/BEM (right) levels (see top panel). Radiative (middle) and nonradiative (bottom) decay rates (logarithmic scale) as a function of the PDI-NP distance as obtained by varying the NP radius (from 10 Å to 70 Å).

case, QM/ ω FQF μ and QM/BEM agreement is only qualitative. This can be related to the different plasmonic properties provided by the two approaches, *i.e.* different PRFs and different absorption profiles (see Fig. S3 of the ESI†). To investigate how the atomistic features of the NP surface affect the computed QM/ ω FQF μ Γ^r , in Fig. S4 of the ESI† we report a scan over the NP-PDI angle (from 0 to 180°, with a step of 20°) for T disposition. Specifically, for NPs with a radius of 20 Å and 70 Å, PDI is positioned at the distance corresponding to the minimum of Γ^r (6 and 20 Å, respectively). Our findings reveal small and periodic fluctuations of Γ^r as a function of the angle, which are reduced as the NP size increases, highlighting the weaker impact of atomistic details as the structure approximates that of a perfect sphere. Thus, the numerical discrepancies between QM/ ω FQF μ and QM/BEM reported in Fig. 2b mostly arise from the diverse modeling of the optical response of the NPs, rather than the atomistic features of the NP surface.

Remarkably, computed results are in agreement with experimental findings,^{18,68–70} and are consistent with similar analysis performed at the semi-empirical ZINDO/BEM level,²⁷ thus demonstrating the reliability of ω FQF μ .

QM/ ω FQF μ and QM/BEM Γ^{nr} display a similar behavior for both L and T configurations (see Fig. 2a and b). In particular, Γ^{nr} decreases as the PDI-NP distance increases for all considered NPs and approaches zero. Indeed, PDI non-radiative decay channels are neglected; thus, Γ^{nr} vanishes in the gas phase limit. At small distances, Γ^{nr} assumes almost the same value for all NP radii because the NP can be approximated as an infinite plane surface. At larger distances, Γ^{nr} increases for large NP sizes because a large dipole moment is induced on the NP (see eqn (6)). Remarkably, at large distances, and for all NP size, Γ^{nr} follows a distance⁻⁶ trend, following the Förster limit. These

findings are again in agreement with previous computational investigations.²⁷

To conclude this section, the relative brightness Φ^{RB} is evaluated. In Fig. 3, Φ^{RB} of PDI adsorbed in L configuration on Au (a) and Ag (b) spherical NPs are reported, as calculated at the QM/ ω FQF μ (left) and QM/BEM (right) levels. In particular, Φ^{RB} dependence on the NP radius and PDI-NP distance is studied and graphically depicted as a 3D plot. It can be noticed that, for Au NPs, Φ^{RB} decreases by increasing the radius for a specific PDI-NP distance. For a fixed radius, Φ^{RB} shows the opposite trend, *i.e.*, it increases by increasing the PDI-NP separation. Thus, for Au NPs, a general quenching effect is obtained at both QM/ ω FQF μ and QM/BEM levels. For Ag NPs, an increment in Φ^{RB} is observed by enlarging the PDI-NP distance, similarly to Au NPs. In contrast, Φ^{RB} behavior as a function of the NP radius is more complex and displays a minimum, which is shifted at larger radii as the PDI-NP distance increases. The different Ag-Au trends can be ascribed to the diverse plasmonic properties of the two materials. In fact, the absorption/emission PDI frequencies are close to Au PRF and fall in the pre-resonant region for Ag NPs. Consequently, the non-radiative decay channels are facilitated by Au NPs, thus yielding larger Γ^{nr} than Γ^r and A (see eqn (14)), finally resulting in Φ^{RB} reduction.^{27,28} A similar investigation for the T orientation is reported in Fig. S5 of the ESI† for which a less pronounced quenching effect is observed, in agreement with experimental findings.^{18,68–70}

4.2 QM/ ω FQF μ for complex-shaped nanostructures

4.2.1 Effect of the NP morphology. In this section, QM/ ω FQF μ is applied to the study of the fluorescence response of PDI induced by complex-shaped Au NPs. Ih and cTO



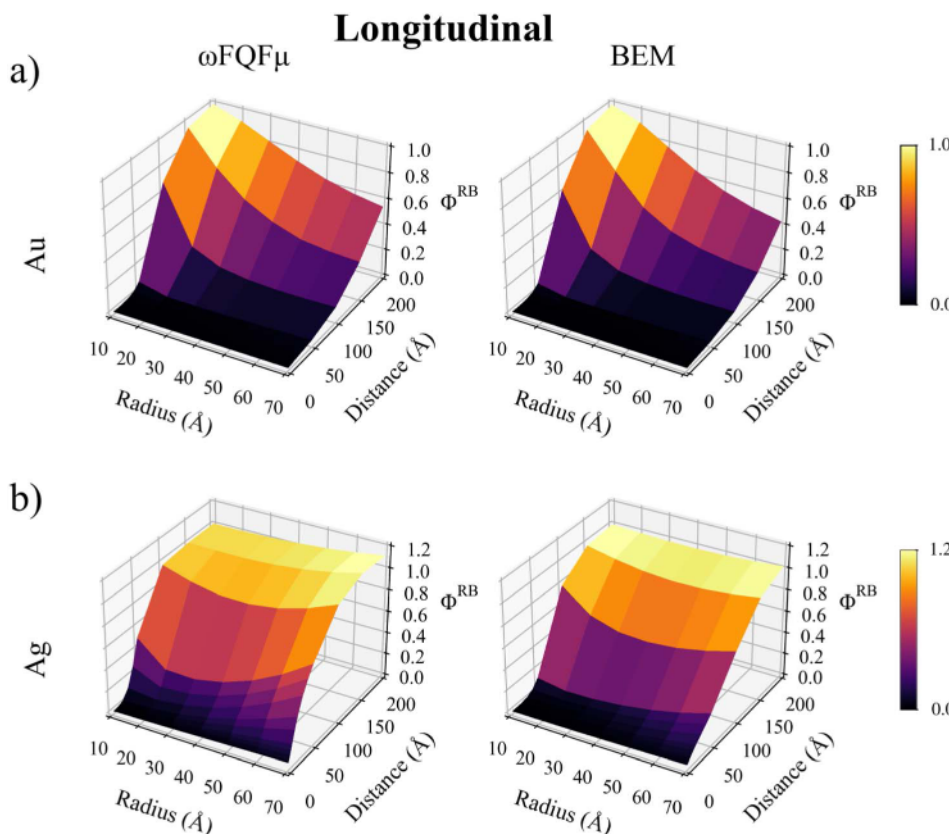


Fig. 3 QM/ωFQF μ (left) and QM/BEM (right) Φ^{RB} as a function of PDI-NP distance and NP radius for PDI in L orientation interacting with a spherical Au (a) and Ag (b) NP.

morphologies are considered; they feature sharp edges and atomistically defined tips, which require fully atomistic descriptions to be appropriately modeled. In fact, continuum BEM descriptions can lead to large numerical instabilities for these morphologies.^{29,71}

In Fig. 4(i and j), QM/ωFQF μ Γ^r , Γ^{nr} , and Φ^{RB} values are reported as a function of the PDI-NP distance. A values are not given, because their trend is similar to Γ^r . PDI lays in the L orientation in the vicinity of spherical, Ih and cTO NPs with a radius of 30 Å. To highlight how different morphologies affect the fluorescence parameters, the differences between Γ^r , Γ^{nr} , and Φ^{RB} values for the various morphologies and the data for the spherical case are computed as follows:

$$\%X = \left(\frac{X_{\text{Ih/cTO}} - X_{\text{sph}}}{X_{\text{sph}}} - 1 \right) \times 100, \quad X = \{\Gamma^r, \Gamma^{nr}, \Phi^{RB}\} \quad (15)$$

where $X_{\text{Ih/cTO}}$ and X_{sph} indicate Γ^r , Γ^{nr} , Φ^{RB} values computed for Ih or cTO, and spherical NPs, respectively.

$\% \Gamma^{nr}$ maximum value occurs when PDI is close to Ih/cTO NPs and rapidly decreases until it reaches a plateau. In fact, for large distances, both $\Gamma_{\text{Ih/cTO}}^{nr}$ and Γ_{sph}^{nr} values follow a Förster-like behavior (\propto distance⁻⁶), and thus $\% \Gamma^{nr}$ converges to a finite value (see eqn (15)). $\% \Gamma_{\text{Ih/cTO}}^r$ instead presents lower values than the spherical reference, smoothly converging towards zero as the PDI-NP distance increases. The combination of Γ^r and Γ^{nr} variation profiles as a function of the distance determines the $\% \Phi^{RB}$ function, which exhibits a maximum in the distance region

between 50 and 100 Å. Indeed, $\% \Phi^{RB}$ profile is related to the intersection point of $\% \Gamma^r$ and $\% \Gamma^{nr}$ curves. Furthermore, Fig. 4(i and j) shows a substantial $\% \Phi^{RB}$ reduction at short distances (<30 Å) for both Ih and cTO morphologies. In this region, $\% \Gamma^r$ displays its lowest values while $\% \Gamma^{nr}$ reaches its maximum, overall favoring the quenching of the fluorescence signal. This behavior is due to the significant enhancement of the electric field near the sharp tips of cTO and Ih NPs.^{33,35} Although these results show the same general behavior for Ih and cTO NPs, some subtle differences are worth discussing. Specifically, $\% \Gamma^{nr}$ is smaller for cTO than for Ih, and consequently, cTO $\% \Phi^{RB}$ is slightly larger.

To deepen the analysis, how a variation in the NP size affects the fluorescence response is investigated. To this end, Ih, cTO and spherical NPs with radii ranging from 10 to 70 Å are studied (see Fig. 4(c-h), and S6 and S7 in the ESI†). First, the NP size highly affects both $\% \Gamma^{nr}$ and $\% \Gamma^r$. In fact, for short PDI-NP distances, $\% \Gamma^{nr}$ increases, while the opposite holds for $\% \Gamma^r$. This results in a substantial decrease in $\% \Phi^{RB}$ in this distance region. At larger distances (50–100 Å), both morphologies display fluorescence responses that largely exceed that obtained for the reference spherical NPs, reaching a maximum that shifts toward larger distances and decreases in intensity by increasing NP size. Fig. 4(g and h) clearly shows that the discrepancies between the cTO and Ih become more pronounced for small NP radii. In fact, within this size range, the atomistic differences in Ih/cTO morphologies are more significant. The radius dependence of the $\% \Phi^{RB}$ maxima originates from a slight mismatch



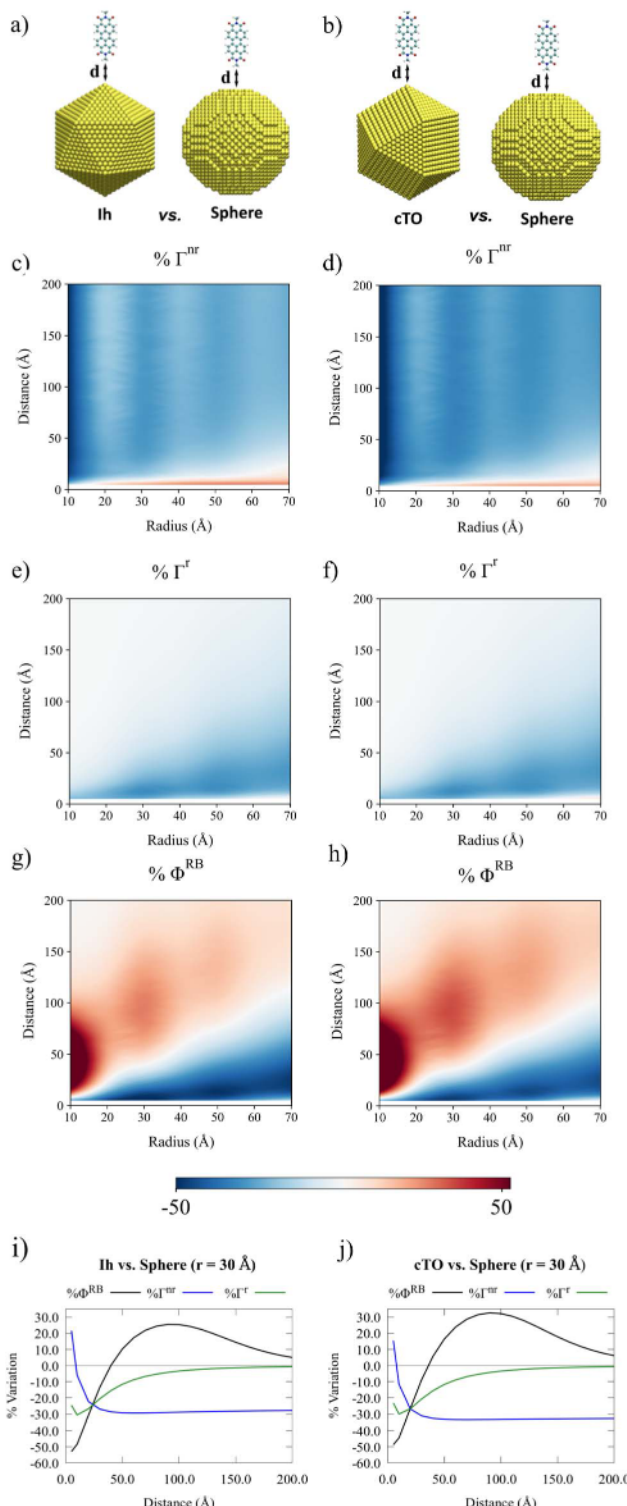


Fig. 4 Graphical representation of PDI interacting with Au Ih (a) and cTO (b) NPs, compared with spherical NPs. QM/ωFQFμ % Γ^{nr} (c and d), % Γ^r (e and f), and % Φ^{RB} (g and h) 2D color plots as a function of the PDI-NP distance and NP radius for Ih vs. sphere and cTO vs. sphere systems, respectively. QM/ωFQFμ % Γ^{nr} , % Γ^r , and % Φ^{RB} values for systems of 30 Å radius are displayed in panels (i) (Ih vs. sphere) and (j) (cTO vs. sphere).

in the effective sphere-cTO/Ih size due to the atomistically defined structures (see Tables S1 and S2 of the ESI † for the effective size of the studied structures). To avoid the maxima fluctuations reported in Fig. 4(g and h), we have performed the same study by relying on a linear interpolation of the Φ^{RB} values on the effective radius of the spherical NPs corresponding to the effective radius of cTO NPs (see Fig. S8 in the ESI†).

4.2.2 Dependence of fluorescence response on the chromophore-NP configuration. To further demonstrate the versatility of QM/ωFQFμ, how the relative configuration of the molecule-NP system affects the fluorescence response is here evaluated. The possibility of performing this kind of investigation is a remarkable feature of the fully atomistic nature of the method.

In Fig. 5, Φ^{RB} and % Φ^{RB} as a function of PDI-NP distance and the PDI-NP configuration are graphically depicted. In particular, the PDI moiety is adsorbed in L orientation on the tip (T), side (S), and face (F) of both Ih (a) and cTO (b) NPs of 30 Å radius. As a comparison, the PDI adsorbed on a spherical NP of equal size (30 Å radius) is also reported. QM/ωFQFμ results show that, for both Ih and cTO, the highest deviation in the fluorescence response compared to the spherical reference is obtained for the T configuration. This is not unexpected, and it is due to the largely inhomogeneous electric field near the sharp interfaces of the metal structures.³⁴ The fully atomistic nature of the model can also capture the smaller differences, that are instead reported for S and F configurations. In particular, such differences become more pronounced when moving from Ih to cTO NPs (see % Φ^{RB} in Fig. 5, bottom). This is due to the alternating triangular and squared faces in the cTO structure, which accentuates the inhomogeneity of the near-field.

4.2.3 PDI interacting with Ag nanorods. The previous sections have focused on the capacity of Au NPs to quench the fluorescence signal emitted by a nearby chromophore. Several strategies can be exploited to enhance the fluorescence response, *i.e.* the relative brightness Φ^{RB} . For instance, fluorescence enhancement can be obtained by increasing the size of the nanostructures, which makes Γ^r to be dominant over Γ^{nr} (see eqn (14)) due to the increased NP dipole moment.^{27,72} Another possibility is to consider NPs exhibiting a PRF close (in energy) to an electronic absorption of the chromophore.^{27–29} This results in a more efficient absorption process, leading to a higher population of the excited states and, consequently, a higher emission probability.

To investigate this aspect, the fluorescence response of PDI in the proximity of silver nanorods (SNRs) is studied. Indeed nanorods have been amply exploited experimentally to enhance fluorescence signals. In fact, their PRF can be easily tuned by varying their aspect ratio.^{73–76} Notably, ωFQFμ can accurately reproduce nanorod's PRF values.³³

In Fig. 6(b), absorption cross-section are reported for two SNRs with fixed radius ($r = 18.5$ Å) and two lengths ($L = 149.5$ Å and $L = 154$ Å; see Fig. 6(a)). The absorption spectrum is dominated by a main plasmonic peak, associated with the dipolar plasmon. As expected, by increasing the SNR length, the PRF redshifts of about 0.04 eV. The plasmonic response sensitivity as a function of the SNR length can be exploited to match absorption (ω_{abs}) or emission (ω_{em}) PDI frequencies.

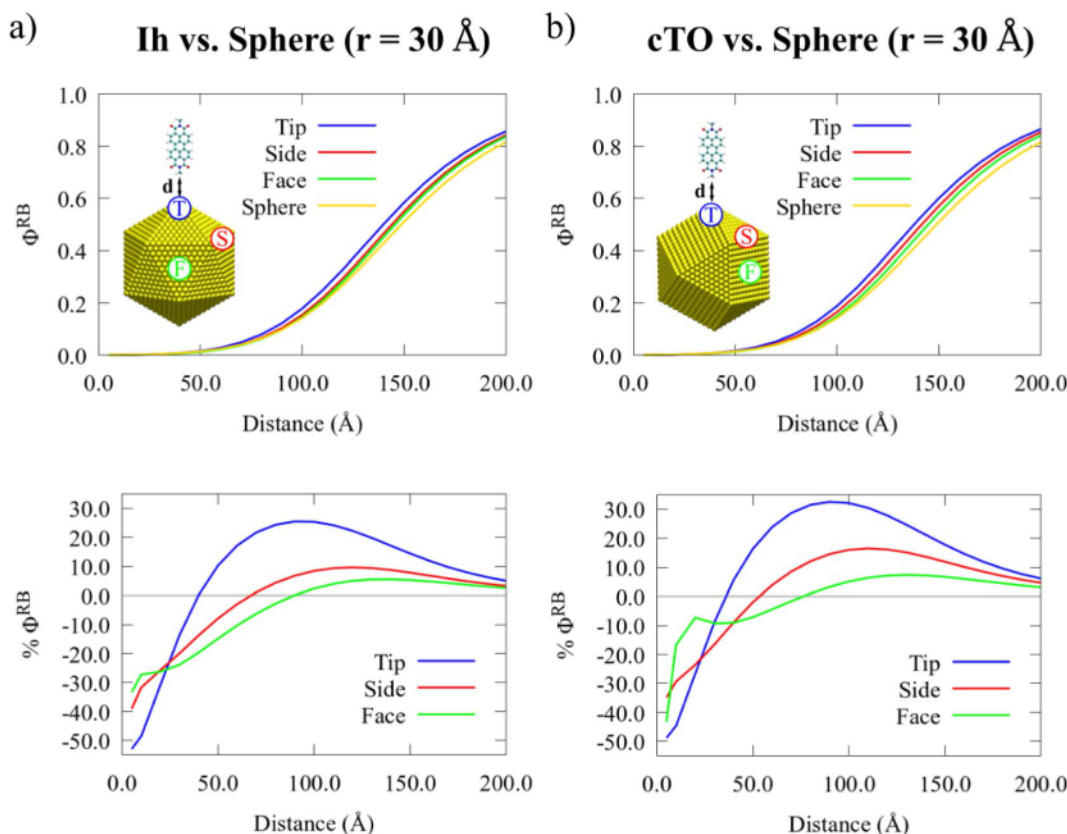


Fig. 5 QM/ωFQFμ Φ^{RB} (top) and % Φ^{RB} (bottom) as a function of the PDI-NP distance for tip, side, and face PDI adsorption geometries. Ih (a) and cTO (b) NP morphologies are studied and compared to spherical NPs.

PDI Φ^{RB} values as a function of the SNR-PDI distance are also given in Fig. 6(c) for both nanorods. As expected, the highest fluorescence enhancement is reported when the PRF coincides with ω_{abs} . However, a large fluorescence enhancement is also

obtained when PRF aligns with ω_{em} . Although Φ^{FQY} values computed in the two cases are almost identical (see eqn (14)), the energy similarity of ω_{abs} and ω_{em} and the large SNR dipole moment lead to enhanced A values.

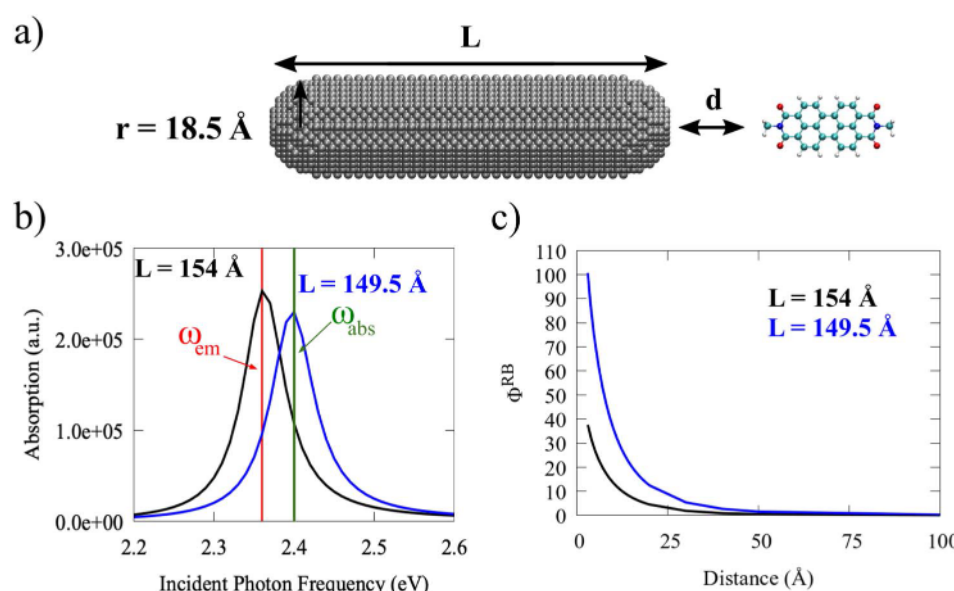


Fig. 6 (a) Geometrical representation of the studied SNRs interacting with PDI. (b) PRF of a SNRs with 18.5 \AA radius (r) as function of the length (L). PDI emission (ω_{em}) and absorption (ω_{abs}) frequencies are marked with vertical red and green lines, respectively. (c) PDI Φ^{RB} as a function of PDI-SNR distance for $L = 149.5 \text{ \AA}$ and $L = 154 \text{ \AA}$.



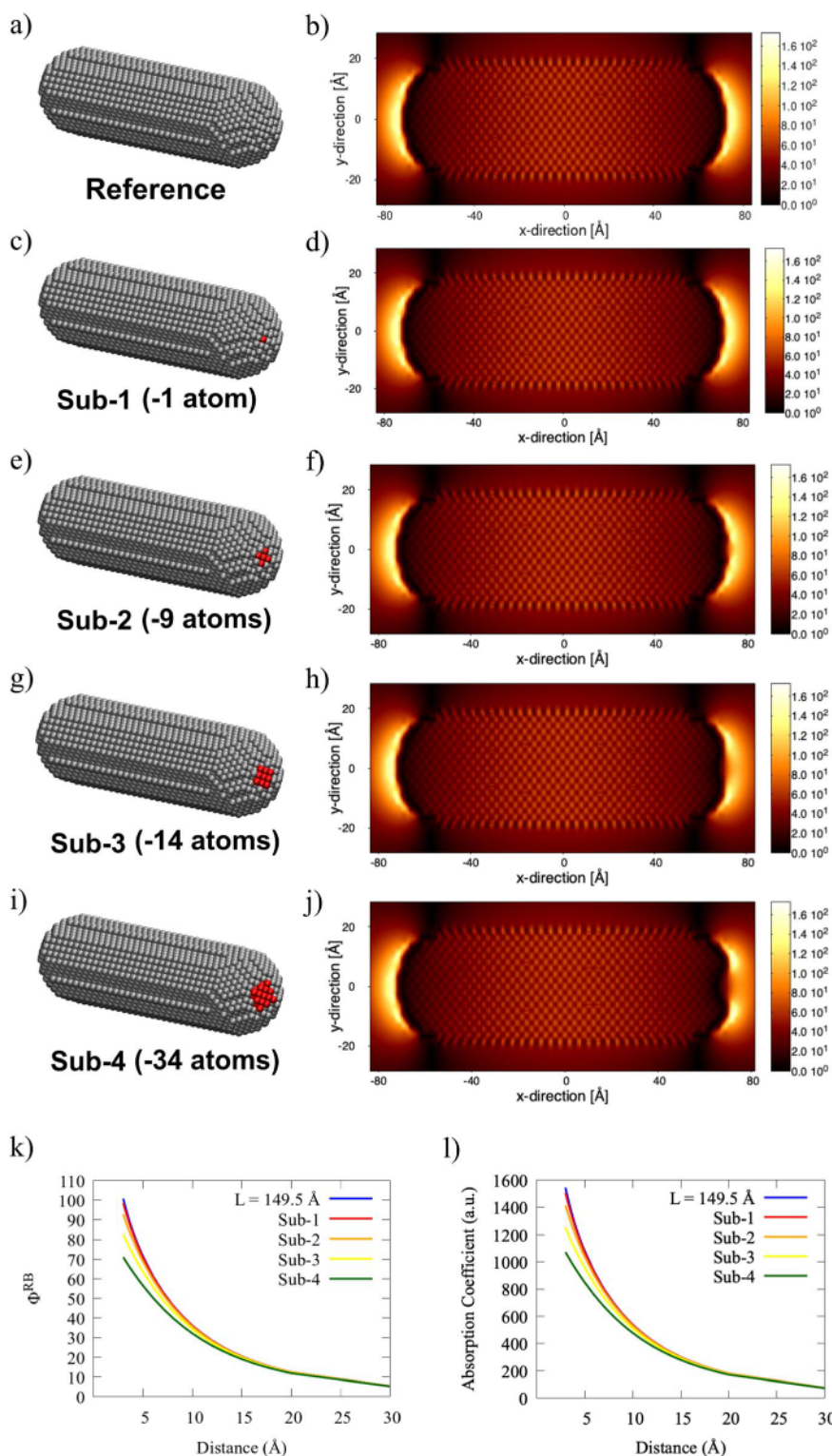


Fig. 7 (a) Graphical depiction of SNR pristine (a), $r = 18.5 \text{ \AA}$; $L = 149.5 \text{ \AA}$ and defected structures (c, e, g and i), as obtained by atomistic deletions at the SNR end (see red regions). The number of removed atoms is also reported for each structure. The associated $\omega FQF\mu$ electric field enhancement 2D color maps, obtained at the PRF for a field polarization along the principal axis, are given in panels (b, d, f, h and j). (k) QM/ $\omega FQF\mu$ Φ^{RB} and A (l) values as a function of the PDI-SNR distance.

Let's focus on how SNR atomistic structure close to PDI affects the molecular Φ^{RB} . Fig. 7 provides a graphical representation of such structure modifications, which are obtained

by digging the SNR end close to PDI with a concentric (with nanorod axis) sphere with increasing radius. This results in the removal of SNR atoms within the volumes spanned by the

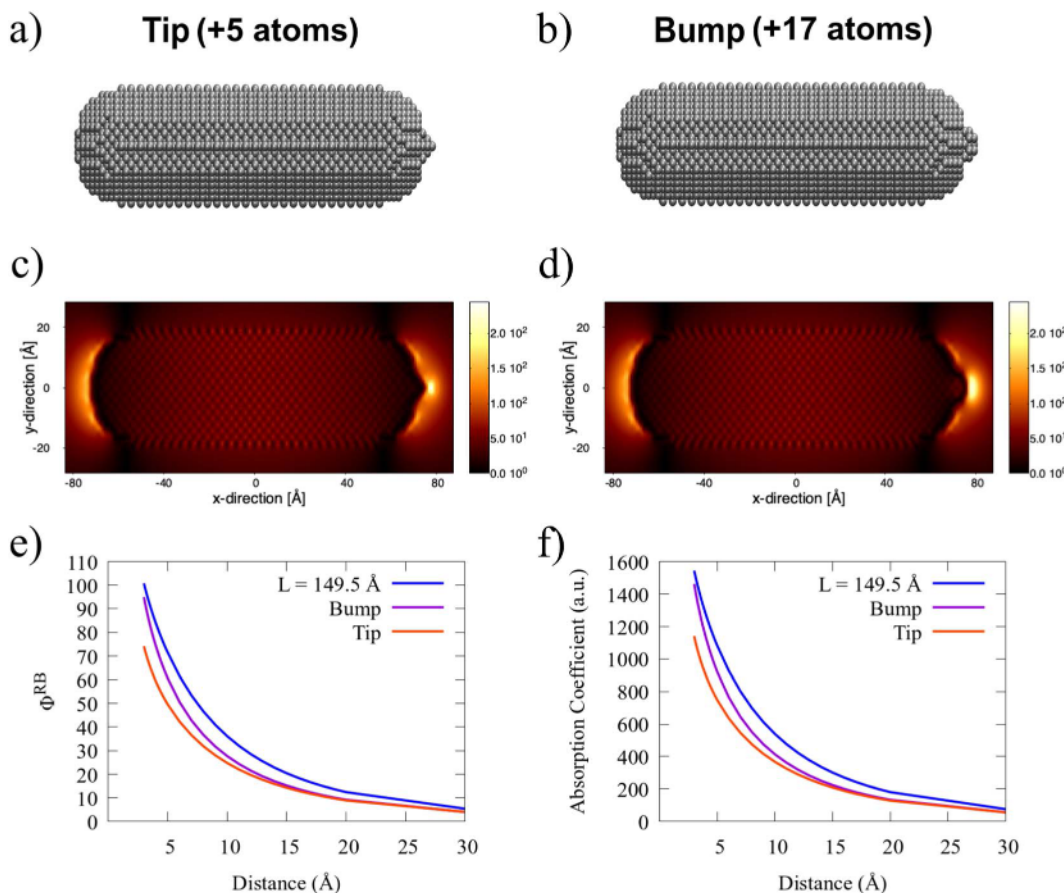


Fig. 8 (a) Graphical depiction of SNRs featuring an atomistic tip (a) and a bump (b). The number of added atoms compared to the pristine SNR ($r = 18.5 \text{ \AA}$; $L = 149.5 \text{ \AA}$) is also reported for each structure. The associated $\omega\text{FQF}\mu$ electric field enhancement 2D color maps, obtained at the PRF for a field polarization along the principal axis, are given in panels (c and d). (e) QM/ $\omega\text{FQF}\mu$ Φ^{RB} and (f) values as a function of the PDI-SNR distance.

selected spheres. In particular, the number of the removed atoms for the four studied geometrical modifications (Sub-1–Sub-4) are given in Fig. 7(c, e, g and i), where they are also highlighted in red. The electric field enhancement color maps associated with each SNR are also reported. Following ref. 33, the latter are calculated as the ratio between the magnitude of the induced and the incident electric fields. The external field is polarized along the SNR principal axis and oscillates at the dipolar PRF of each structure ($\omega = 2.40 \text{ eV}$). Color maps clearly show that the maximum field enhancement is obtained at the two SNR ends. By digging the SNR right end, a substantial reduction of the electric field enhancement in the deletion region is reported.

Fig. 7(k) shows the impact of these atomistic modifications on Φ^{RB} as a function of the PDI-SNR distance as compared to the reference SNR ($L = 149.5 \text{ \AA}$). Clearly, the largest discrepancies emerge at small PDI-SNR distances. In particular, the structures characterized by the highest atomistic deletions (Sub-3 and Sub-4) feature a substantial reduction in Φ^{RB} values. This is expected and is related to the modifications in the local field enhancement (see Fig. 7(h and j)). Indeed, Γ^r and Γ^{nr} variations as a function of PDI-SNR distance have small effect on Φ^{FQY} . Thus, the reported differences primarily originate

from the changes in A as a function of the PDI-NP distance (see eqn (14) and Fig. 7(l)).

An opposite structural modification is also possible, *i.e.*, the increasing of the SNR end close to the PDI with a small sharp tip – +5 atoms – or a spherical bump – +17 atoms (see Fig. 8(a and b)). Both systems feature a larger and more localized enhanced field than the pristine SNR (see Fig. 8(c and d) and 7(b)). In particular, the most localized enhanced field is obtained for the tip-SNR due to its sharp profile. Fig. 8(e) shows Φ^{RB} values of PDI placed at the proximity of both systems as a function of the PDI-SNR distance, taking the full SNR ($L = 149.5 \text{ \AA}$) as a reference. Tip-SNR and bump-SNR are both associated with a significant Φ^{RB} reduction, especially for small PDI-SNR distances. In particular, the largest discrepancy with the reference is given by Tip-SNR, for which the computed fluorescence response is comparable with the Sub-4 system (see Fig. 7(k)). For both geometrical modifications, the overall quenching of the fluorescence signal is due to the smaller SNR dipole compared to the reference, which results in a lower absorption coefficient A (see eqn (14) and Fig. 8(f)). It is worth mentioning that the structural modifications of the SNR only modify their electrical properties but not their absorption profile compared to the pristine structure (see Fig. S9 in the ESI†).



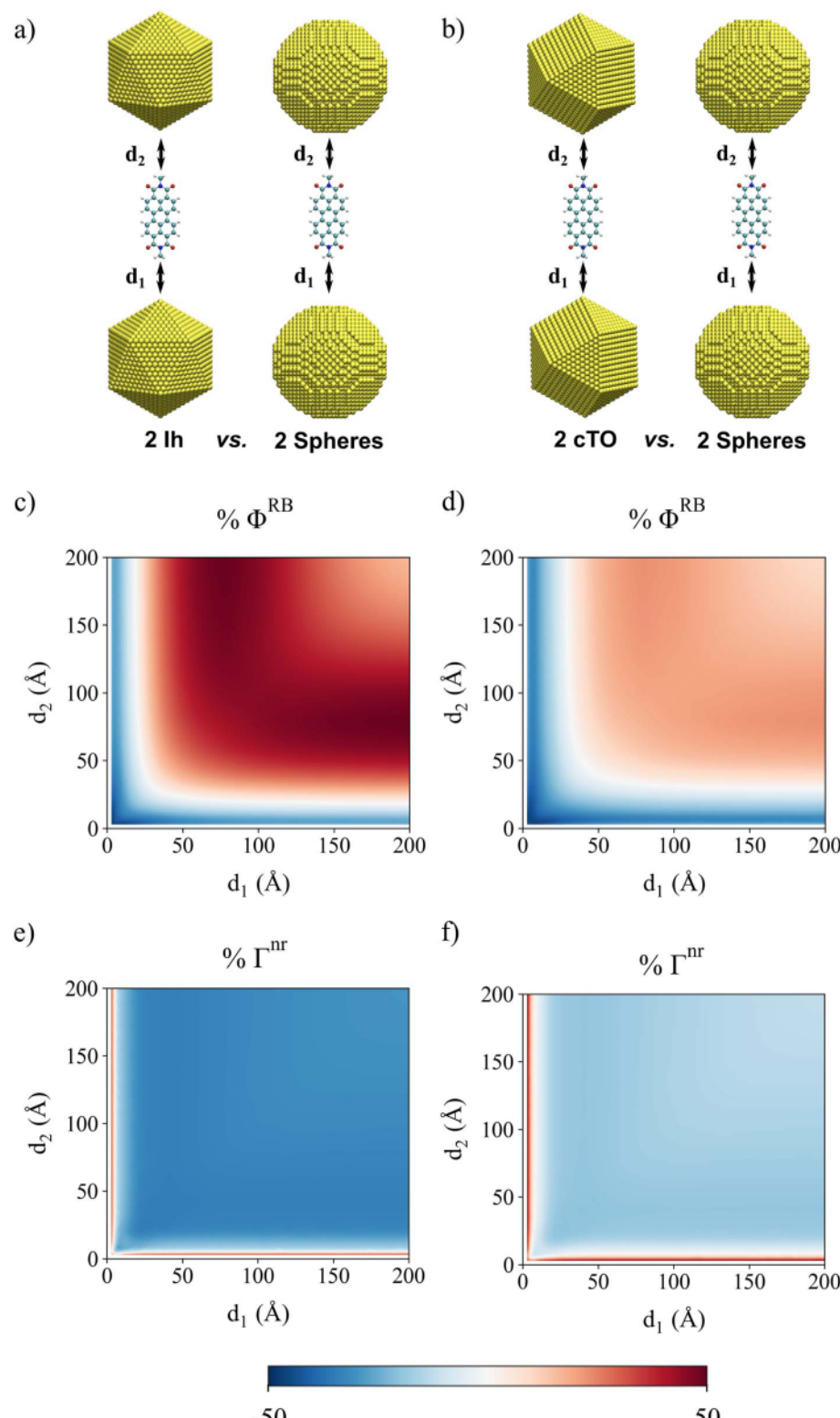


Fig. 9 Graphical representation of PDI interacting with Au Ih (a) and cTO (b) dimers, as compared with spherical NP dimers (radius 30 Å). QM/ωFQFμ % Φ^{RB} (c and d), % Γ^{nr} (e and f) 2D color plots as a function of the distances between PDI and the two NPs, for Ih vs. sphere and cTO vs. sphere systems, respectively.

To underscore the importance of a fully atomistic modeling of the substrate, in Fig. S10 in the ESI† we replicate the simulations reported in Fig. 7 and 8 by exploiting the continuum

QM/BEM approach. Specifically, we study the longitudinal absorption, Φ^{RB} , and Φ^{FQY} of pristine SNR ($\mathbf{r} = 18.5 \text{ \AA}$; $\mathbf{L} = 149.5 \text{ \AA}$), as well as those featuring a tip, bump, and the Sub-4 cavity.



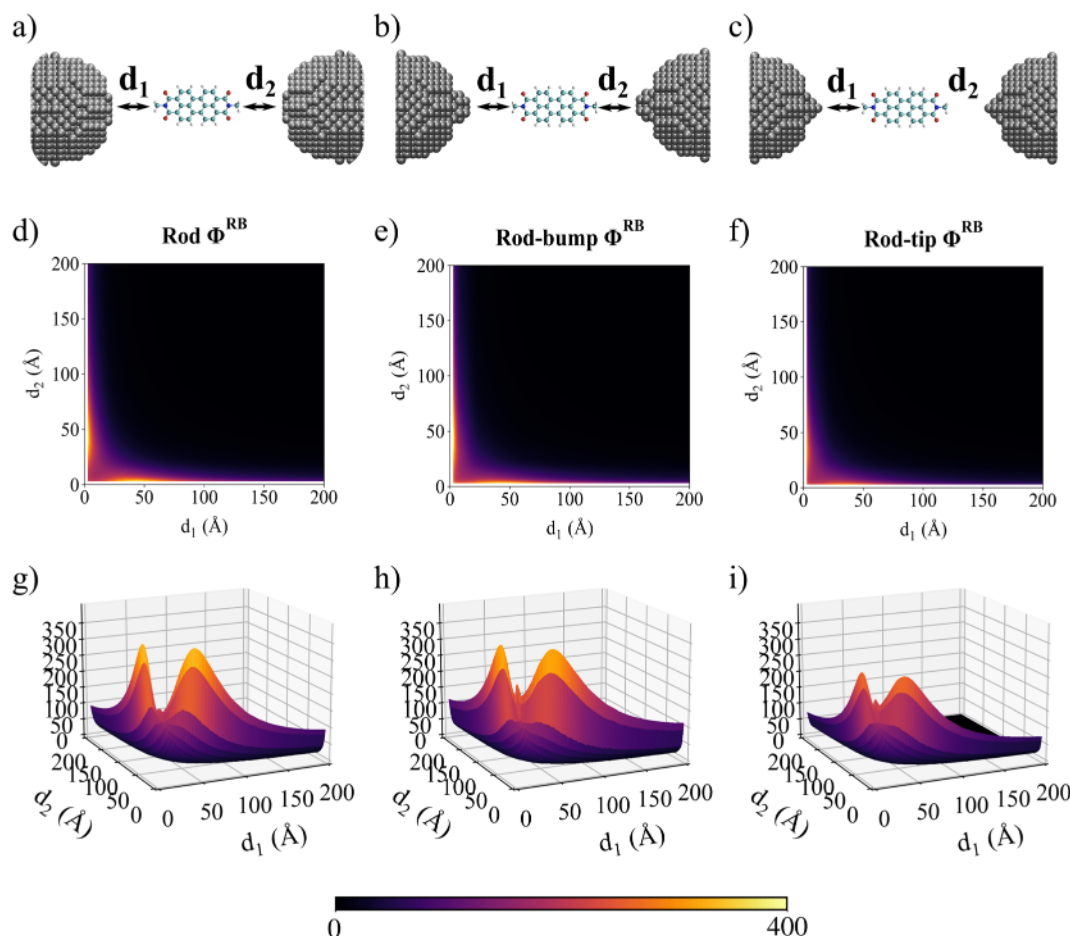


Fig. 10 Graphical depiction of PDI interacting with two pristine Ag SNRs (a), two Ag SNRs featuring bumps (b) and tips (c). QM/ ω FQF μ Φ^{RB} (d–f) and Φ^{RB} (g–i) 2D and 3D color maps as a function of the distances between PDI and the two SNRs.

Additionally, we evaluate three different discretizations of the surfaces ($\sim 10\,000$, ~ 5000 , ~ 1000 tesserae) for each system. Our findings reveal a strong dependence on the number of tesserae used to describe the BEM surface. In particular, while the longitudinal PRFs tend to converge after 5000 tesserae, computed Φ^{RB} and Φ^{FQY} with 5000 and 10 000 tesserae show a mismatch as a function of the SNR-PDI distance. Focusing on the structure presenting the Sub-4 cavity, results suggest strong numerical instabilities when increasing the number of tesserae. This is evidenced by the lower-energy band emerging in the longitudinal absorption plots, along with the Φ^{FQY} trend which presents an anomalous peak instead of the expected gradual decrease with increasing the SNR-PDI separation.

4.2.4 PDI interacting with NP dimers. This section finally focuses on the fluorescence response of PDI interacting with two NPs. As a first case study, PDI in L configuration is sandwiched between two spherical, Ih, or cTO Au NPs with a radius equal to 30 Å (see Fig. 9(a and b)). The fluorescence response is investigated in terms of the Φ^{RB} percentage variation (see eqn (15)) of Ih/cTO NPs compared to spherical NP, as a function of PDI distance from each NP (d_1 and d_2). The results are graphically depicted in Fig. 9(c and d) (see Fig. S11 in the ESI† for the same representation in 3D) for both cTO and Ih NPs. First, %

Φ^{RB} values computed for Ih or cTO NPs follow the same trend. In fact, for small d_1 and d_2 , $\% \Phi^{RB}$ reaches a minimum while at larger distances (≥ 50 Å), both morphologies display fluorescence responses that largely exceed that obtained for the reference spherical NP. In fact, $\% \Phi^{RB}$ reaches a maximum (~ 40 for Ih and ~ 20 for cTO) that decreases in intensity by increasing d_1 and d_2 . Notably, larger $\% \Phi^{RB}$ values are observed for Ih than cTO. These findings are opposite from what is reported for a single NP (see Fig. 4(i and j)). This is due to the lower Γ^{nr} reported for Ih dimer (Fig. 9(e and f)), which reduces the quenching efficiency (absolute values of Φ^{RB} are always lower than 1).

A similar study can be performed by considering PDI interacting with SNR dimers, composed of two reference cylindrical pristine SNRs ($r = 18.5$ Å; $L = 149.5$ Å), two tip-SNRs, and two bump-SNRs (see Fig. 10(a–c)). PDI Φ^{RB} as a function of the distances compared to the two SNRs is studied (see Fig. 10(d–i)). For all shapes, the maximum Φ^{RB} values are obtained when d_1 and d_2 differ (anti-symmetrical displacement). Significant discrepancies compared to the pristine SNR emerge when the bump and the tip are introduced. Specifically, for the bump-SNR, the maximum Φ^{RB} values are similar to the pristine SNR, while a large Φ^{RB} increase is obtained at $d_1 = d_2 = 3$ Å. This



is also observed for the tip-SNR dimer. However, consistently smaller Φ^{RB} values compared to the reference structure are reported in this case. Remarkably, these findings are in agreement with the results already discussed for single SNR NPs.

To conclude this section, it is worth highlighting that the Φ^{RB} observed profiles for Au and Ag dimers are related to the different physicochemical mechanisms governing the fluorescence process. In the Au dimer setup, the fluorescence response is primarily driven by the relative variation of decay rates Φ^{FQY} , whose trend perfectly matches Φ^{RB} behavior (see Fig. S12 in the ESI†). In fact, the maximum fluorescence signal is obtained when a symmetrical arrangement ($d_1 = d_2$) is considered. A fluorescence enhancement can potentially be achieved at small distances by increasing the size of the NP, until reaching the critical point where Γ^r dominates over Γ^{nr} .²⁷ On the contrary, the influence of SNRs on Φ^{RB} is primarily determined by the variations of A as a function d_1 and d_2 (see Fig. S13 of the ESI†), which provide a one-to-one correspondence with Φ^{RB} trends reported in Fig. 10(d–i). Thus, in this case, SNR anti-symmetrical arrangements ($d_1 \neq d_2$) are crucial in enhancing the fluorescence signal.

5 Conclusions

In the present work, the QM/ ω FQFμ formalism has been extended for the first time to study the fluorescence signal of molecular systems close to plasmonic substrates. The approach fully retains the atomistic structure of both the chromophore and the nanostructure, thus allowing the description of how NP atomistic features affect the molecular response.

To demonstrate the reliability of the novel methodology, the fluorescence response of a well-studied fluorophore, PDI, in the presence of plasmonic Ag and Au NPs, is investigated. In particular, diverse NP morphologies are considered, ranging from spherical NPs to complex-shaped NPs, such as Ih and cTO NPs, atomistically defected nanorods and NP dimers. The reported findings show that sharp edges, associated with highly localized induced electric fields, play a crucial role in determining the molecular fluorescence response. Remarkably, this can be accurately described by only exploiting a fully atomistic approach as the one proposed in the present work. As a result, QM/ ω FQFμ is here presented as an effective methodology to rationalize the fluorescence signals in atomistic-defined setups, such as for TEPL or picocavity-controlled SEF,^{22,77,78} pending the development of a reliable computational protocol for the simulation of realistic nanostructures.

Finally, it is worth highlighting how significant fluorescence signal enhancement can be obtained by matching the PRF with the molecular absorption energy achieved by structural deformations on the NP. The findings of the present study underscore the fundamental role of a fully atomistic description for an in-depth understanding of the fluorescence response in the vicinity of complex-shaped nanostructures. Indeed, this work paves the way for the rational design and optimization of plasmonic devices to enhance the fluorescence response of target chromophores.

Conflicts of interest

There are no conflicts to declare.

Acknowledgements

The authors acknowledge Prof. Stefano Corni (Università di Padova) for useful discussion. The authors gratefully acknowledge the Center for High-Performance Computing (CHPC) at SNS for providing the computational infrastructure. CC acknowledges funding from MUR-FARE Ricerca in Italia: Framework per l'attrazione ed il rafforzamento delle eccellenze per la Ricerca in Italia - III edizione. Prot. R20YTA2BKZ, and from PNRR MUR project PE0000023-NQSTI.

References

- M. Li, S. K. Cushing and N. Wu, Plasmon-enhanced optical sensors: a review, *Analyst*, 2015, **140**, 386–406.
- M. Sharifi, F. Attar, A. A. Saboury, K. Akhtari, N. Hooshmand, A. Hasan, M. A. El-Sayed and M. Falahati, Plasmonic gold nanoparticles: Optical manipulation, imaging, drug delivery and therapy, *J. Controlled Release*, 2019, **311–312**, 170–189.
- M. T. Yaraki and Y. N. Tan, Metal nanoparticles-enhanced biosensors: synthesis, design and applications in fluorescence enhancement and surface-enhanced Raman scattering, *Chem.-Asian J.*, 2020, **15**, 3180–3208.
- M. G. Albrecht and J. A. Creighton, Anomalously intense Raman spectra of pyridine at a silver electrode, *J. Am. Chem. Soc.*, 1977, **99**, 5215–5217.
- D. L. Jeanmaire and R. P. Van Duyne, Surface Raman spectroelectrochemistry: Part I. Heterocyclic, aromatic, and aliphatic amines adsorbed on the anodized silver electrode, *J. Electroanal. Chem. Interfacial Electrochem.*, 1977, **84**, 1–20.
- A. Campion and P. Kambhampati, Surface-enhanced Raman scattering, *Chem. Soc. Rev.*, 1998, **27**, 241–250.
- K. A. Willets and R. P. Van Duyne, Localized surface plasmon resonance spectroscopy and sensing, *Annu. Rev. Phys. Chem.*, 2007, **58**, 267–297.
- R. Alvarez-Puebla, L. M. Liz-Marzán and F. J. García de Abajo, Light concentration at the nanometer scale, *J. Phys. Chem. Lett.*, 2010, **1**, 2428–2434.
- E. Le Ru and P. Etchegoin, *Principles of Surface-Enhanced Raman Spectroscopy: and Related Plasmonic Effects*, Elsevier, 2008.
- S. A. Maier, *Plasmonics: Fundamentals and Applications*, Springer Science & Business Media, 2007.
- J. Langer, D. Jimenez de Aberasturi, J. Aizpurua, R. A. Alvarez-Puebla, B. Auguié, J. J. Baumberg, G. C. Bazan, S. E. J. Bell, A. Boisen, A. G. Brolo, J. Choo, D. Cialla-May, V. Deckert, L. Fabris, K. Faulds, E. C. García de Abajo, R. Goodacre, D. Graham, A. J. Haes, C. L. Haynes, C. Huck, T. Itoh, M. Käll, J. Kneipp, N. A. Kotov, H. Kuang, Le Ru, H. K. Lee, J.-F. Li, X. Y. Ling, S. A. Maier, T. Mayerhöfer, M. Moskovits, K. Murakoshi,



- J.-M. Nam, S. Nie, Y. Ozaki, I. Pastoriza-Santos, J. Perez-Juste, J. Popp, A. Pucci, S. Reich, B. Ren, G. C. Schatz, T. Shegai, S. Schlücker, L.-L. Tay, K. G. Thomas, Z.-Q. Tian, R. P. Van Duyne, T. Vo-Dinh, Y. Wang, K. A. Willets, C. Xu, H. Xu, Y. Xu, Y. S. Yamamoto, B. Zhao and L. M. Liz-Marzán, Present and future of surface-enhanced Raman scattering, *ACS Nano*, 2019, **14**, 28–117.
- 12 J. L. Payton, S. M. Morton, J. E. Moore and L. Jensen, A discrete interaction model/quantum mechanical method for simulating surface-enhanced Raman spectroscopy, *J. Chem. Phys.*, 2012, **136**, 214103.
- 13 J. L. Payton, S. M. Morton, J. E. Moore and L. Jensen, A hybrid atomistic electrodynamics–quantum mechanical approach for simulating surface-enhanced Raman scattering, *Acc. Chem. Res.*, 2014, **47**, 88–99.
- 14 Z. Hu, D. V. Chulhai and L. Jensen, Simulating surface-enhanced hyper-Raman scattering using atomistic electrodynamics–quantum mechanical models, *J. Chem. Theory Comput.*, 2016, **12**, 5968–5978.
- 15 D. V. Chulhai, X. Chen and L. Jensen, Simulating ensemble-averaged surface-enhanced Raman scattering, *J. Phys. Chem. C*, 2016, **120**, 20833–20842.
- 16 R. R. Chance, A. Prock and R. Silbey, *Advances in Chemical Physics*, John Wiley & Sons, Ltd, 1978, pp. 1–65.
- 17 S. Garoff, D. A. Weitz, M. S. Alvarez and J. I. Gersten, Electrodynamics at rough metal surfaces: Photochemistry and luminescence of adsorbates near metal-island films, *J. Chem. Phys.*, 1984, **81**, 5189–5200.
- 18 B. Fu, J. D. Flynn, B. P. Isaacoff, D. J. Rowland and J. S. Biteen, Super-Resolving the Distance-Dependent Plasmon-Enhanced Fluorescence of Single Dye and Fluorescent Protein Molecules, *J. Phys. Chem. C*, 2015, **119**, 19350–19358.
- 19 J. Zheng, X. Cheng, H. Zhang, X. Bai, R. Ai, L. Shao and J. Wang, Gold Nanorods: The Most Versatile Plasmonic Nanoparticles, *Chem. Rev.*, 2021, **121**, 13342–13453.
- 20 Y. Jung, J. Kim, N. H. Kim and H. G. Kim, Ag-ZnO Nanocomposites as a 3D Metal-Enhanced Fluorescence Substrate for the Fluorescence Detection of DNA, *ACS Appl. Nano Mater.*, 2023, **6**, 976–985.
- 21 K.-Q. Lin, J. Yi, J.-H. Zhong, S. Hu, B.-J. Liu, J.-Y. Liu, C. Zong, Z.-C. Lei, X. Wang, J. Aizpurua, R. Esteban and B. Ren, Plasmonic photoluminescence for recovering native chemical information from surface-enhanced Raman scattering, *Nat. Commun.*, 2017, **8**, 14891.
- 22 B. Yang, G. Chen, A. Ghafoor, Y. Zhang, Y. Zhang, Y. Luo, J. Yang, V. Sandoghdar, J. Aizpurua, Z. Dong and J. G. Hou, Sub-nanometre resolution in single-molecule photoluminescence imaging, *Nat. Photonics*, 2020, **14**, 693–699.
- 23 H. Lee, D. Y. Lee, M. G. Kang, Y. Koo, T. Kim and K.-D. Park, Tip-enhanced photoluminescence nano-spectroscopy and nano-imaging, *Nanophotonics*, 2020, **9**, 3089–3110.
- 24 W. Peeters, S. Toyouchi, Y. Fujita, M. Wolf, B. Fortuni, E. Fron, T. Inose, J. Hofkens, T. Endo, Y. Miyata and H. Uji-i, Remote Excitation of Tip-Enhanced Photoluminescence with a Parallel AgNW Coupler, *ACS Omega*, 2023, **8**, 38386–38393.
- 25 S. Khatua, P. M. R. Paulo, H. Yuan, A. Gupta, P. Zijlstra and M. Orrit, Resonant Plasmonic Enhancement of Single-Molecule Fluorescence by Individual Gold Nanorods, *ACS Nano*, 2014, **8**, 4440–4449.
- 26 A. Rose, T. B. Hoang, F. McGuire, J. J. Mock, C. Ciraci, D. R. Smith and M. H. Mikkelsen, Control of Radiative Processes Using Tunable Plasmonic Nanopatch Antennas, *Nano Lett.*, 2014, **14**, 4797–4802.
- 27 S. Vukovic, S. Corni and B. Mennucci, Fluorescence enhancement of chromophores close to metal nanoparticles. Optimal setup revealed by the polarizable continuum model, *J. Phys. Chem. C*, 2009, **113**, 121–133.
- 28 A. Sanchez-Gonzalez, S. Corni and B. Mennucci, Surface-Enhanced Fluorescence within a Metal Nanoparticle Array: The Role of Solvent and Plasmon Couplings, *J. Phys. Chem. C*, 2011, **115**, 5450–5460.
- 29 M. Romanelli, G. Dall’Osto and S. Corni, Role of metal-nanostructure features on tip-enhanced photoluminescence of single molecules, *J. Chem. Phys.*, 2021, **155**, 214304.
- 30 S. D. Catingan and A. Moores, Recent Progress in Surface-Enhanced Fluorescence Using Gold Nanorods, *ACS Appl. Nano Mater.*, 2024, DOI: [10.1021/acsanm.3c04756](https://doi.org/10.1021/acsanm.3c04756).
- 31 L. L. Jensen and L. Jensen, Electrostatic Interaction Model for the Calculation of the Polarizability of Large Noble Metal Nanoclusters, *J. Phys. Chem. C*, 2008, **112**, 15697–15703.
- 32 N. Asadi-Aghbolaghi, R. Rüger, Z. Jamshidi and L. Visscher, TD-DFT+TB: An Efficient and Fast Approach for Quantum Plasmonic Excitations, *J. Phys. Chem. C*, 2020, **124**, 7946–7955.
- 33 T. Giovannini, L. Bonatti, P. Lafiosca, L. Nicoli, M. Castagnola, P. G. Illobre, S. Corni and C. Cappelli, Do We Really Need Quantum Mechanics to Describe Plasmonic Properties of Metal Nanostructures?, *ACS Photonics*, 2022, **9**, 3025–3034.
- 34 P. Lafiosca, L. Nicoli, L. Bonatti, T. Giovannini, S. Corni and C. Cappelli, QM/Classical Modeling of Surface Enhanced Raman Scattering Based on Atomistic Electromagnetic Models, *J. Chem. Theory Comput.*, 2023, **19**, 3616–3633.
- 35 T. Giovannini, M. Rosa, S. Corni and C. Cappelli, A classical picture of subnanometer junctions: an atomistic Drude approach to nanoplasmonics, *Nanoscale*, 2019, **11**, 6004–6015.
- 36 L. Bonatti, G. Gil, T. Giovannini, S. Corni and C. Cappelli, Plasmonic resonances of metal nanoparticles: atomistic vs. Continuum approaches, *Front. Chem.*, 2020, **8**, 340.
- 37 P. Lafiosca, T. Giovannini, M. Benzi and C. Cappelli, Going Beyond the Limits of Classical Atomistic Modeling of Plasmonic Nanostructures, *J. Phys. Chem. C*, 2021, **125**, 23848–23863.
- 38 T. Giovannini, L. Bonatti, M. Polini and C. Cappelli, Graphene plasmonics: Fully atomistic approach for realistic structures, *J. Phys. Chem. Lett.*, 2020, **11**, 7595–7602.



- 39 L. Bonatti, L. Nicoli, T. Giovannini and C. Cappelli, In silico design of graphene plasmonic hot-spots, *Nanoscale Adv.*, 2022, **4**, 2294–2302.
- 40 S. Zanotto, L. Bonatti, M. F. Pantano, V. Mišekis, G. Speranza, T. Giovannini, C. Coletti, C. Cappelli, A. Tredicucci and A. Toncelli, Strain-Induced Plasmon Confinement in Polycrystalline Graphene, *ACS Photonics*, 2023, **10**, 394–400.
- 41 L. Nicoli, P. Lafiosca, P. Grobas Illobre, L. Bonatti, T. Giovannini and C. Cappelli, Fully atomistic modeling of plasmonic bimetallic nanoparticles: nanoalloys and core-shell systems, *Front. Photon.*, 2023, **4**, 2673–6853.
- 42 S. Corni and J. Tomasi, Excitation energies of a molecule close to a metal surface, *J. Chem. Phys.*, 2002, **117**, 7266–7278.
- 43 S. Corni and J. Tomasi, Lifetimes of electronic excited states of a molecule close to a metal surface, *J. Chem. Phys.*, 2003, **118**, 6481–6494.
- 44 O. Andreussi, S. Corni, B. Mennucci and J. Tomasi, Radiative and nonradiative decay rates of a molecule close to a metal particle of complex shape, *J. Chem. Phys.*, 2004, **121**, 10190–10202.
- 45 M. Caricato, O. Andreussi and S. Corni, Semiempirical (ZINDO-PCM) Approach to Predict the Radiative and Nonradiative Decay Rates of a Molecule Close to Metal Particles, *J. Phys. Chem. B*, 2006, **110**, 16652–16659.
- 46 A. Pinchuk, G. Von Plessen and U. Kreibig, Influence of interband electronic transitions on the optical absorption in metallic nanoparticles, *J. Phys. D: Appl. Phys.*, 2004, **37**, 3133.
- 47 A. Pinchuk, U. Kreibig and A. Hilger, Optical properties of metallic nanoparticles: influence of interface effects and interband transitions, *Surf. Sci.*, 2004, **557**, 269–280.
- 48 B. Balamurugan and T. Maruyama, Evidence of an enhanced interband absorption in Au nanoparticles: size-dependent electronic structure and optical properties, *Appl. Phys. Lett.*, 2005, **87**, 143105.
- 49 A. Liebsch, Surface-plasmon dispersion and size dependence of Mie resonance: silver versus simple metals, *Phys. Rev. B*, 1993, **48**, 11317.
- 50 T. Giovannini, A. Puglisi, M. Ambrosetti and C. Cappelli, Polarizable QM/MM approach with fluctuating charges and fluctuating dipoles: the QM/FQF μ model, *J. Chem. Theory Comput.*, 2019, **15**, 2233–2245.
- 51 A. Dreuw and M. Head-Gordon, Single-Reference ab Initio Methods for the Calculation of Excited States of Large Molecules, *Chem. Rev.*, 2005, **105**, 4009–4037.
- 52 A. H. Larsen, et al., The atomic simulation environment—a Python library for working with atoms, *J. Phys.: Condens. Matter*, 2017, **29**, 273002.
- 53 M. Barbry, P. Koval, F. Marchesin, R. Esteban, A. Borisov, J. Aizpurua and D. Sánchez-Portal, Atomistic near-field nanoplasmatics: reaching atomic-scale resolution in nanooptics, *Nano Lett.*, 2015, **15**, 3410–3419.
- 54 X. Chen and L. Jensen, Morphology dependent near-field response in atomistic plasmonic nanocavities, *Nanoscale*, 2018, **10**, 11410–11417.
- 55 U. Kreibig and M. Vollmer, *Optical properties of metal clusters*, Springer Science & Business Media, 2013, vol. 25.
- 56 C. Novo, D. Gomez, J. Perez-Juste, Z. Zhang, H. Petrova, M. Reismann, P. Mulvaney and G. V. Hartland, Contributions from radiation damping and surface scattering to the linewidth of the longitudinal plasmon band of gold nanorods: a single particle study, *Phys. Chem. Chem. Phys.*, 2006, **8**, 3540–3546.
- 57 V. Juvé, M. F. Cardinal, A. Lombardi, A. Crut, P. Maioli, J. Pérez-Juste, L. M. Liz-Marzán, N. Del Fatti and F. Vallée, Size-dependent surface plasmon resonance broadening in nonspherical nanoparticles: single gold nanorods, *Nano Lett.*, 2013, **13**, 2234–2240.
- 58 B. Foerster, A. Joplin, K. Kaefer, S. Celiksoy, S. Link and C. Sönnichsen, Chemical interface damping depends on electrons reaching the surface, *ACS Nano*, 2017, **11**, 2886–2893.
- 59 O. A. Douglas-Gallardo, G. J. Soldano, M. M. Mariscal and C. G. Sánchez, Effects of oxidation on the plasmonic properties of aluminum nanoclusters, *Nanoscale*, 2017, **9**, 17471–17480.
- 60 C. Geuzaine and J.-F. G. Remacle, A 3-D finite element mesh generator with built-in pre- and post-processing facilities, *Int. J. Numer. Methods Eng.*, 2009, **79**, 1309–1331.
- 61 S. Corni and J. Tomasi, Surface enhanced Raman scattering from a single molecule adsorbed on a metal particle aggregate: A theoretical study, *J. Chem. Phys.*, 2002, **116**, 1156–1164.
- 62 R. Cammi and J. Tomasi, Remarks on the use of the apparent surface charges (ASC) methods in solvation problems: Iterative versus matrix-inversion procedures and the renormalization of the apparent charges, *J. Comput. Chem.*, 1995, **16**, 1449–1458.
- 63 J. Tomasi, B. Mennucci and R. Cammi, Quantum Mechanical Continuum Solvation Models, *Chem. Rev.*, 2005, **105**, 2999–3094.
- 64 P. G. Etchegoin, E. Le Ru and M. Meyer, An analytic model for the optical properties of gold, *J. Chem. Phys.*, 2006, **125**, 164705.
- 65 M. G. Blaber, A.-I. Henry, J. M. Bingham, G. C. Schatz and R. P. Van Duyne, LSPR Imaging of Silver Triangular Nanoprisms: Correlating Scattering with Structure Using Electrodynamics for Plasmon Lifetime Analysis, *J. Phys. Chem. C*, 2012, **116**, 393–403.
- 66 P. B. Johnson and R.-W. Christy, Optical constants of the noble metals, *Phys. Rev. B*, 1972, **6**, 4370.
- 67 E. Baerends, et al., *ADF (Version 2020.X); Theoretical Chemistry*, Vrije Universiteit, Amsterdam, The Netherlands, 2020, <http://www.scm.com>.
- 68 E. Dulkeith, M. Ringler, T. A. Klar, J. Feldmann, A. Muñoz Javier and W. J. Parak, Gold Nanoparticles Quench Fluorescence by Phase Induced Radiative Rate Suppression, *Nano Lett.*, 2005, **5**, 585–589.
- 69 P. Reineck, D. Gómez, S. H. Ng, M. Karg, T. Bell, P. Mulvaney and U. Bach, Distance and Wavelength Dependent Quenching of Molecular Fluorescence by Au@SiO₂ Core-Shell Nanoparticles, *ACS Nano*, 2013, **7**, 6636–6648.



- 70 J. D. Pajović, R. J. Dojčilović, S. Kaščáková, M. Réfrégiers, D. K. Božanić and V. Djoković, Enhanced resonance energy transfer in gold nanoparticles bifunctionalized by tryptophan and riboflavin and its application in fluorescence bioimaging, *Colloids Surf., B*, 2023, **227**, 113340.
- 71 A. Trügler, *Optical Properties of Metallic Nanoparticles*, Springer International Publishing, 2016.
- 72 P. Anger, P. Bharadwaj and L. Novotny, Enhancement and Quenching of Single-Molecule Fluorescence, *Phys. Rev. Lett.*, 2006, **96**, 113002.
- 73 H. Yuan, S. Khatua, P. Zijlstra, M. Yorulmaz and M. Orrit, Thousand-fold Enhancement of Single-Molecule Fluorescence Near a Single Gold Nanorod, *Angew. Chem., Int. Ed.*, 2013, **52**, 1217–1221.
- 74 E. Wientjes, J. Renger, A. G. Curto, R. Cogdell and N. F. van Hulst, Strong antenna-enhanced fluorescence of a single light-harvesting complex shows photon antibunching, *Nat. Commun.*, 2014, **5**, 4236.
- 75 Z. Mei and L. Tang, Surface-Plasmon-Coupled Fluorescence Enhancement Based on Ordered Gold Nanorod Array Biochip for Ultrasensitive DNA Analysis, *Anal. Chem.*, 2017, **89**, 633–639.
- 76 J.-F. Li, C.-Y. Li and R. F. Aroca, Plasmon-enhanced fluorescence spectroscopy, *Chem. Soc. Rev.*, 2017, **46**, 3962–3979.
- 77 A. Rosławska, T. c. v. Neuman, B. Doppagne, A. G. Borisov, M. Romeo, F. Scheurer, J. Aizpurua and G. Schull, Mapping Lamb, Stark, and Purcell Effects at a Chromophore-Picocavity Junction with Hyper-Resolved Fluorescence Microscopy, *Phys. Rev. X*, 2022, **12**, 011012.
- 78 J. Doležal, A. Sagwal, R. C. de Campos Ferreira and M. Švec, Single-Molecule Time-Resolved Spectroscopy in a Tunable STM Nanocavity, *Nano Lett.*, 2024, **24**, 1629–1634.



IV. Mixed Atomistic-Implicit Quantum/Classical Approach to Molecular Nanoplasmonics

Mixed atomistic-implicit quantum/classical approach to molecular nanoplasmatics

Cite as: J. Chem. Phys. 162, 044103 (2025); doi: 10.1063/5.0245629

Submitted: 28 October 2024 • Accepted: 3 January 2025 •

Published Online: 22 January 2025



View Online



Export Citation



CrossMark

Pablo Grobas Illobre,¹ Piero Lafiosca,¹ Luca Bonatti,¹ Tommaso Giovannini,^{2,a)} and Chiara Cappelli^{1,3,a)}

AFFILIATIONS

¹ Scuola Normale Superiore, Piazza dei Cavalieri 7, 56126 Pisa, Italy

² Department of Physics, University of Rome Tor Vergata, Via della Ricerca Scientifica 1, 00133 Rome, Italy

³ IMT School for Advanced Studies Lucca, Piazza San Francesco 19, Lucca 55100, Italy

^{a)} Authors to whom correspondence should be addressed: tommaso.giovannini@uniroma2.it and chiara.cappelli@sns.it

ABSTRACT

A multiscale quantum mechanical (QM)/classical approach is presented that is able to model the optical properties of complex nanostructures composed of a molecular system adsorbed on metal nanoparticles. The latter is described by a combined atomistic–continuum model, where the core is described using the implicit boundary element method (BEM) and the surface retains a fully atomistic picture and is treated employing the frequency-dependent fluctuating charge and fluctuating dipole (ω FQF μ) approach. The integrated QM/ ω FQF μ -BEM model is numerically compared with state-of-the-art fully atomistic approaches, and the quality of the continuum/core partition is evaluated. The method is then extended to compute surface-enhanced Raman scattering within a time-dependent density functional theory framework.

© 2025 Author(s). All article content, except where otherwise noted, is licensed under a Creative Commons Attribution-NonCommercial-NoDerivs 4.0 International (CC BY-NC-ND) license (<https://creativecommons.org/licenses/by-nc-nd/4.0/>). <https://doi.org/10.1063/5.0245629>

22 January 2025 11:20:58

I. INTRODUCTION

When metal nanoparticles (NPs) are irradiated with external radiation, coherent oscillations of conduction electrons, also named localized surface plasmons (LSPs), can be excited.^{1–3} Most NP optical properties are related to LSP peculiar properties, which can be tuned by varying the NP's size, shape, and chemical composition.⁴ Plasmonic nanostructures can enhance, control, or suppress properties of molecules interacting with light: these features are exploited in molecular nanoplasmatics.^{5–10} A deep understanding of the phenomena that occur at the molecular and nanoscale in the presence of light can be achieved by exploiting multiscale hybrid techniques, which use different levels of description for molecules and plasmonic nanosystems.^{5,11} With these methods, a reliable representation of both atomistic details and collective features, such as plasmons, in these complex systems can be achieved.

In principle, the ideal theoretical approach to molecular nanoplasmatics should rely on a quantum mechanical (QM) description of the whole system (molecule + nanostructured substrate). However, due to their unfavorable computational scaling,

full *ab initio* methods are currently limited to small model systems (generally, <100 atoms), in contrast to the large size of plasmonic substrates, which typically comprise thousands or millions of atoms.^{12–16} To address these limitations, hybrid multiscale QM/classical approaches have been developed,^{11,17,18} where the molecular adsorbate is treated at the QM level, while the substrate's plasmonic response is calculated by using classical electrodynamical methods, substantially reducing the computational cost. The most crude classical description of the plasmonic response of a metal NP is given by continuum implicit approaches, such as the Mie theory,¹⁹ the Finite Difference Time Domain (FDTD),²⁰ or the Boundary Element Method (BEM),^{21–24} which completely disregard the NP atomistic nature. To overcome this limitation, fully atomistic approaches have been developed, such as Discrete Interaction Models (DIMs)^{17,18,25–30} and the Frequency-Dependent Fluctuating Charges and Fluctuating Dipoles (ω FQF μ) approach.^{11,24,31–39} ω FQF μ can correctly reproduce QM results for metal NPs even below the quantum limit (<5 nm),³⁵ capture the plasmonic properties of systems featuring subnanometer junctions,³¹ defects,^{34,36} treat bimetallic particles,³⁷ and colloidal nanostructures.³⁹ In

addition, it describes noble metal NPs³⁵ and graphene-based structures under the same theoretical framework.³² Both families (implicit and atomistic) have pros and cons. Continuum models feature a favorable computational cost, which scales with the size of the NP surface, facilitating the description of large systems.^{23,40–46} However, their implicit, non-atomistic nature fails at capturing the NP plasmonic response in specific configurations characterized by atomistic defects, sub-nanometer junctions, and sharp interfaces,^{45,47} which are associated with huge enhancements of the electric field (the so-called hot-spots). Conversely, while atomistic approaches appropriately capture these features, they become computationally less efficient as the size of the system increases, because their computational cost scales with the number of atoms, i.e., the NP volume.³³

This work proposes a novel multiscale approach specifically designed to overcome the limitations associated with atomistic and continuum approaches. The method, which is here specified for noble metal NPs, describes the core with an implicit approach, by using the BEM method, while the NP surface is treated at the fully atomistic approach, by means of ω FQF μ . The resulting ω FQF μ -BEM approach constitutes, to the best of our knowledge, the first hybrid atomistic–continuum methodology to evaluate the optical response of plasmonic substrates within classical electrodynamics. Furthermore, ω FQF μ -BEM is coupled to a QM description of a molecular adsorbate described at the Time-Dependent Density Functional Theory (TDDFT) level, allowing for the calculation of molecular properties and signals in the vicinity of plasmonic nanostructures.^{11,42,48}

One of the most interesting aspects of molecular nanoplasmatics is the huge enhancement of the induced electric field in the NP surface proximity, which can drastically affect the electronic properties of molecular adsorbates. As a result, molecular spectral signals can be significantly enhanced, providing an invaluable platform for molecular sensing. The most diffuse technique that exploits this effect is Surface Enhanced Raman Scattering (SERS),^{2,6,10,14,49–57} where the molecular Raman signals are enhanced by several orders of magnitude, allowing single molecule detection. SERS is at present used in various applicative fields, such as catalysis, chemical biology, biophysics, and biomedicine.^{58–65} For this reason, in this paper, QM/ ω FQF μ -BEM is extended to compute SERS signals.

This paper is organized as follows: In Sec. II, ω FQF μ and BEM methods are briefly recalled, and the novel ω FQF μ -BEM and QM/ ω FQF μ -BEM models are presented. After a brief section reporting on the computational details, the methods are validated by computing NPs optical properties and SERS spectra of pyridine with the novel approaches or employing reference fully atomistic methods (ω FQF μ and QM/ ω FQF μ). Conclusions and future perspectives end the paper.

II. THEORY

This section gives an overview of the theoretical background leading to the formulation of the QM/ ω FQF μ -BEM approach. First, the integration of the ω FQF μ and BEM models is discussed, and the ω FQF μ -BEM equations are presented to replicate the plasmonic response of fully atomistic NPs as built by a continuum BEM core within an atomistic ω FQF μ shell (see Fig. 1). Then, the QM/ ω FQF μ -BEM coupling is developed and specified to describe the SERS of a

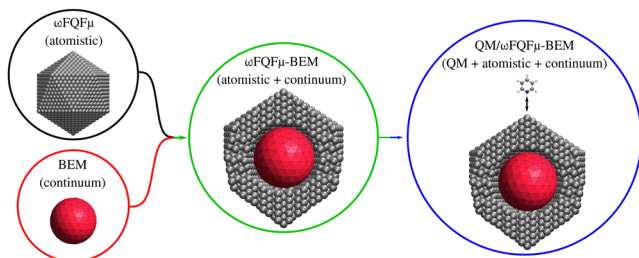


FIG. 1. Graphical representation of ω FQF μ , BEM, ω FQF μ -BEM, and QM/ ω FQF μ -BEM approaches.

molecule, studied at the TDDFT level, placed in the vicinity of the plasmonic NP.

A. Classical models for plasmonics

1. Frequency-dependent fluctuating charges and fluctuating dipoles (ω FQF μ) for plasmonic metal nanoparticles

ω FQF μ is a classical, fully atomistic model that accurately reproduces the plasmonic behavior of noble metal nanostructures.^{31,35} In ω FQF μ , each atom is endowed with a complex electric charge (q) describing intraband transitions^{24,31–34} and a complex dipole (μ) capturing the interband contributions to the optical response.^{11,35,37} Both charges and dipoles are formulated within the quasistatic regime; therefore, retardation effects are neglected.^{31,35,37} Combining the description of the time-dependent charge fluctuation on atom i with the Drude model for evaluating the momentum derivative, the following equation, in the frequency domain, holds:³¹

$$-i\omega q_i(\omega) = \sum_j 2n_0 \mathcal{A}_{ij} \frac{\langle \mathbf{E}(\omega) \rangle}{1/\tau - i\omega} \cdot \vec{l}_{ji}, \quad (1)$$

where $q_i(\omega)$ is the charge lying on atom i and oscillating at frequency ω , n_0 is the atomic density, and τ is the scattering time. \mathcal{A}_{ij} is the effective area ruling charge exchange between atoms i and j , \vec{l}_{ji} is the unit vector that connects both atoms, and $\langle \mathbf{E}(\omega) \rangle$ is the electric field averaged over all trajectories.

Equation (1) can be linked to atomic properties through the electrochemical potential (ϕ^{el}) by approximating $\langle \mathbf{E}(\omega) \rangle \cdot \vec{l}_{ji} \approx (\phi_j^{el} - \phi_i^{el})/l_{ij}$, yielding the following expression:³¹

$$-i\omega q_i(\omega) = \frac{2n_0 \tau}{1 - i\omega \tau} \sum_j^N [1 - f(r_{ij})] \frac{\mathcal{A}_{ij}}{r_{ij}} (\phi_j^{el} - \phi_i^{el}), \quad (2)$$

where $f(r_{ij})$ serves as a phenomenological Fermi damping function designed to limit charge transfer to neighboring atoms. This function also mimics the characteristic profile of quantum tunneling, which is dependent on the distance between atoms (r_{ij}), and it has been parameterized against *ab initio* data.^{31,35,37} ϕ_i^{el} is the electrochemical potential acting on the i -th atom, which includes the potential generated by the external electric field, the charges, and the dipoles.

ω FQF μ dipoles add a further source of polarization, which is crucial for modeling the physics of d -electrons.^{66–68} This is achieved by incorporating a complex frequency-dependent atomic polarizability α_i^ω , extracted from the experimental permittivity, which encloses the effect of interband transitions. The atomic dipoles can then be computed as follows:³⁵

$$\boldsymbol{\mu}_i(\omega) = \alpha_i^\omega \mathbf{E}_i^{\text{tot}}, \quad (3)$$

where $\boldsymbol{\mu}_i(\omega)$ is the complex frequency-dependent atomic dipole on atom i . $\mathbf{E}_i^{\text{tot}}$ represents the total electric field acting on the i -th atomic position and is the superposition of the external electric field and the electric field generated by the dipoles and charges.

Equations (2) and (3) can be reformulated into the following set of linear equations:³⁵

$$\begin{aligned} \sum_{j=1}^N \left(\sum_{k=1}^N \bar{K}_{ik} (\mathbf{T}_{kj}^{qq} - \mathbf{T}_{ij}^{qq}) + i \frac{\omega}{w(\omega)} \delta_{ij} \right) q_j \\ + \sum_{j=1}^N \left(\sum_{k=1}^N \bar{K}_{ik} (\mathbf{T}_{kj}^{q\mu} - \mathbf{T}_{ij}^{q\mu}) \right) \boldsymbol{\mu}_j = \sum_{k=1}^N \bar{K}_{ik} (\mathbf{V}_i^{\text{ext}} - \mathbf{V}_k^{\text{ext}}), \end{aligned} \quad (4)$$

$$\sum_{j \neq i}^N \mathbf{T}_{ij}^{\mu q} q_j + \sum_{j \neq i}^N \mathbf{T}_{ij}^{\mu\mu} \boldsymbol{\mu}_j + \frac{1}{\alpha_i^\omega} \boldsymbol{\mu}_i = \mathbf{E}_i^{\text{ext}}, \quad (5)$$

where \mathbf{T}^{qq} , $\mathbf{T}^{q\mu}$, and $\mathbf{T}^{\mu\mu}$ are the charge-charge, charge-dipole, and dipole-dipole interaction kernels, respectively,^{31,35,69} and $\mathbf{V}_i^{\text{ext}}$ and $\mathbf{E}_i^{\text{ext}}$ are the potential and the electric field generated by the external radiation at each of the i -th atomic positions, respectively. In ω FQF μ , the charges and dipoles are associated with a Gaussian-type density distribution; thus, the interaction kernels are obtained as first proposed by Mayer.⁷⁰ Finally, $w(\omega)$ and \bar{K}_{ij} are defined as follows:^{33,35}

$$w(\omega) = \frac{2n_0}{1/\tau - i\omega}, \quad (6)$$

$$\bar{K}_{ij} = (1 - f(r_{ij})) \frac{\mathcal{A}_{ij}}{r_{ij}}. \quad (7)$$

By defining $\mathbf{T}_{ii}^{\mu\mu} = 1/\alpha^\omega$, Eqs. (4) and (5) can be recast as follows:³⁵

$$\left[\begin{pmatrix} \mathbf{A}^q & \mathbf{A}^{q\mu} \\ \mathbf{T}^{q\mu} & \mathbf{T}^{\mu\mu} \end{pmatrix} - \begin{pmatrix} z(\omega) \mathbf{I}_N & 0 \\ 0 & z'(\omega) \mathbf{I}_{3N} \end{pmatrix} \right] \begin{pmatrix} \mathbf{q} \\ \boldsymbol{\mu} \end{pmatrix} = \begin{pmatrix} \mathbf{R} \\ -\mathbf{E}^{\text{ext}} \end{pmatrix}, \quad (8)$$

where \mathbf{A}^q represents the charge-charge terms and $\mathbf{A}^{q\mu}$ collects the charge-dipole interactions. The frequency dependence is gathered in the z and z' terms, and \mathbf{I}_N is the $N \times N$ identity matrix. Finally, the external potential and external field effects are included in the right-hand-side matrices \mathbf{R} and \mathbf{E}^{ext} . The reader is referred to Sec. S1 of the supplementary material for the description of each term in Eq. (8).

2. Boundary element method (BEM)

The Boundary Element Method (BEM) constitutes a reliable approach for solving the Polarizable Continuum Model equations applied to the study of plasmonic nanoparticles (PCM-NPs).⁴¹ There, the NP is treated as a homogeneous continuum dielectric by exploiting a classical electrodynamics formalism. Plasmonics is

then governed by the frequency-dependent permittivity function chosen to describe the material and that of the media in which it is embedded.^{23,24,45,47,71} BEM involves the calculation of surface charges, which yield a global surface charge density that encapsulates the optical response of the system. BEM charges are calculated upon applying the model on a triangular-discretized mesh delimiting the NP surface. At each triangular centroid, a complex point charge that describes the optical response of the material is calculated. This enables the exploration of the plasmonic properties of the analyzed structures, which is influenced by the geometric features of the discretized mesh and by the material's permittivity function.

Here, we rely on the quasistatic PCM-NP framework formulated in the integral equation formalism and numerically solved using BEM. The computation of the BEM charges (σ) is described as follows:^{16,40,45,72,73}

$$\left(2\pi \frac{\varepsilon_2(\omega) + \varepsilon_1(\omega)}{\varepsilon_2(\omega) - \varepsilon_1(\omega)} \mathbf{I}_P + \mathbf{F} \right) \mathbf{S} \mathbf{A}^{-1} \boldsymbol{\sigma} = -(2\pi \mathbf{I}_P + \mathbf{F}) \mathbf{V}, \quad (9)$$

where $\varepsilon_1(\omega)$ is the complex dielectric function of the environment [for vacuum $\varepsilon_1(\omega) = 1$] and $\varepsilon_2(\omega)$ that of the NP. \mathbf{A} is a diagonal matrix collecting the area of each triangle or *tesserae*. \mathbf{I}_P is the $P \times P$ identity matrix, where P is the number of *tesserae*. The matrices \mathbf{S} and \mathbf{F} are defined based on the geometrical characteristics of the mesh. \mathbf{V} collects the values of the electrostatic potential generated by the external electric field at each triangular centroid. For details on the derivation of Eq. (9), the reader is encouraged to refer to Ref. 72.

We can isolate the frequency-dependent terms of Eq. (9) and reformulate them as follows:

$$(\mathbf{B}^\sigma - \xi(\omega)) \boldsymbol{\sigma} = \mathbf{R}_B. \quad (10)$$

In Sec. S1 of the supplementary material, further details on the \mathbf{F} and \mathbf{S} matrices are given, along with the description of each term in Eq. (10).

3. ω FQF μ -BEM for plasmonic metal nanoparticles

The idea of integrating ω FQF μ and BEM, giving rise to a model that is named ω FQF μ -BEM, arises from their close similarities. In particular, both formalisms are grounded in classical electrodynamics and rely on complex frequency-dependent quantities (charges/dipoles) to describe the optical response of metal NPs. However, these models present notable differences. First, the BEM response is rooted in the permittivity chosen to describe the material and lacks any atomistic description. Conversely, ω FQF μ is based on textbook concepts, such as the Drude model of conduction for describing intraband transitions in terms of fluctuating charges. Interband transitions are recovered through a set of fluctuating dipoles that are defined in terms of the experimental interband polarizability. By this, ω FQF μ can effectively decouple the physical processes influencing the optical response of the plasmonic substrate while also retaining its atomistic nature. However, ω FQF μ encounters scalability challenges, eventually leading to the exploration of alternative strategies to solve Eq. (8).^{33,74} Remarkably, ω FQF μ -BEM can alleviate these limitations by representing NPs as built of an internal continuum BEM core and an external atomistic ω FQF μ shell, with substantial computational savings.

The ω FQF μ -BEM coupling is formulated by including the potential and electric field generated by the BEM charges in the ω FQF μ equations, specifically in ϕ^{el} [Eq. (2)] and \mathbf{E}^{tot} [Eq. (3)], respectively. In addition, the potential generated by the ω FQF μ charges and dipoles needs to be included in the BEM \mathbf{V} matrix [Eq. (9)]. As a result of these modifications, Eqs. (4), (5), and (9) are modified as follows:

$$\begin{aligned} & \sum_{j=1}^N \left(\sum_{k=1}^N \bar{K}_{ik} (\mathbf{T}_{kj}^{\text{qq}} - \mathbf{T}_{ij}^{\text{qq}}) + i \frac{\omega}{w(\omega)} \delta_{ij} \right) q_j \\ & + \sum_{j=1}^N \left(\sum_{k=1}^N \bar{K}_{ik} (\mathbf{T}_{kj}^{\text{q}\mu} - \mathbf{T}_{ij}^{\text{q}\mu}) \right) \mu_j \\ & + \sum_{v=1}^P \left(\sum_{k=1}^N \bar{K}_{ik} (\mathbf{T}_{kv}^{\text{q}\sigma} - \mathbf{T}_{iv}^{\text{q}\sigma}) \right) \sigma_v = \sum_{k=1}^N \bar{K}_{ik} (\mathbf{V}_i^{\text{ext}} - \mathbf{V}_k^{\text{ext}}), \end{aligned} \quad (11)$$

$$\sum_{j \neq i}^N \mathbf{T}_{ij}^{\text{q}\mu} q_j + \sum_{v=1}^P \mathbf{T}_{iv}^{\text{q}\sigma} \sigma_v + \sum_{j \neq i}^N \mathbf{T}_{ij}^{\text{q}\mu} \mu_j + \frac{1}{\alpha_i^\omega} \mu_i = \mathbf{E}_i^{\text{ext}}, \quad (12)$$

$$\begin{aligned} & \left(2\pi \frac{\varepsilon_2(\omega) + \varepsilon_1(\omega)}{\varepsilon_2(\omega) - \varepsilon_1(\omega)} \mathbf{I}_P + \mathbf{F} \right) (\mathbf{S} \mathbf{A}^{-1}) \sigma \\ & = -(2\pi \mathbf{I}_P + \mathbf{F}) (\mathbf{V}^{\text{ext}} + \mathbf{V}^{\omega\text{FQ}} + \mathbf{V}^{\omega\text{F}\mu}), \end{aligned} \quad (13)$$

where Eqs. (11) and (12) include the effect of the BEM charges (σ) in the calculation of the ω FQF μ charges (\mathbf{q}) and dipoles (μ), respectively. Equation (13) extends BEM, including the potential generated by the ω FQF μ charges $\mathbf{V}^{\omega\text{FQ}} = \mathbf{T}_{vi}^{\text{qq}} q_i$ and dipoles $\mathbf{V}^{\omega\text{F}\mu} = \mathbf{T}_{vi}^{\text{q}\mu} \mu_i$. \mathbf{T}^{qq} and $\mathbf{T}^{\text{q}\mu}$ are the interaction kernels of BEM point charges with ω FQF μ charges and dipoles described by Gaussian functions, respectively (see Sec. S1 of the supplementary material for more details).^{31,35,75}

Finally, the linear problem represented by equations Eqs. (11)–(13) can be expressed in compact matrix notation as follows:

$$\begin{pmatrix} \mathbf{A}^q & \mathbf{A}^{q\mu} & \mathbf{A}^{q\sigma} \\ \mathbf{T}^{q\mu} & \mathbf{T}^{\mu\mu} & \mathbf{T}^{\mu\sigma} \\ \mathbf{B}^{\sigma q} & \mathbf{B}^{\sigma\mu} & \mathbf{B}^\sigma \end{pmatrix} - \begin{pmatrix} z(\omega) \mathbf{I}_N & 0 & 0 \\ 0 & z'(\omega) \mathbf{I}_N & 0 \\ 0 & 0 & \xi(\omega) \end{pmatrix} \begin{pmatrix} \mathbf{q} \\ \mu \\ \sigma \end{pmatrix} = \begin{pmatrix} \mathbf{R} \\ -\mathbf{E}^{\text{ext}} \\ \mathbf{R}_B \end{pmatrix}. \quad (14)$$

The terms in Eq. (14) are detailed in Sec. S1 of the supplementary material.

B. QM/ ω FQF μ -BEM model and its extension to SERS

Once ω FQF μ -BEM has been formulated, it can be coupled to a QM description of a molecular system in a QM/Classical fashion,^{5,17,23,76–80} giving rise to the QM/ ω FQF μ -BEM model. ω FQF μ -BEM describes the system's response to external oscillating electric fields; therefore, it can be naturally translated into a linear response formalism. The coupling is done by following the same strategy that was exploited to formulate the two-layer QM/ ω FQF μ approach.¹¹

In this scenario, considering the Kohn–Sham operators generated in a grid of points exploiting a numerical integration

strategy,⁸¹ the ω FQF μ -BEM perturbation operator (V^{pert}) modifying the electronic density has the following expression:

$$\begin{aligned} V^{\text{pert}}(\mathbf{r}, \omega) &= V^{\text{ext}}(\mathbf{r}, \omega) + V^{\text{loc}}(\mathbf{r}, \omega), \\ V^{\text{loc}}(\mathbf{r}, \omega) &= \sum_{l=1}^N q_l^{\text{ext}}(\omega) \mathbf{T}^{(0)}(d_l) + \sum_{l=1}^N \boldsymbol{\mu}_l^{\text{ext}}(\omega) \cdot \mathbf{T}^{(1)}(d_l) \\ &+ \sum_{l=1}^P \sigma_l^{\text{ext}}(\omega) \mathbf{T}^{(0)}(d_l), \end{aligned}$$

where $q^{\text{ext}}(\omega)$, $\boldsymbol{\mu}^{\text{ext}}(\omega)$, and $\sigma^{\text{ext}}(\omega)$ are calculated using Eq. (14), where V^{ext} is the potential originating them. Furthermore, d_l is the distance between the l -th atom or *tessera* centroid and a generic grid point, while $\mathbf{T}^{(0)}$ and $\mathbf{T}^{(1)}$ are the charge-to-grid and dipole-to-grid interaction kernels, respectively.^{11,82}

Considering the notation that the $(i,j)/(a,b)$ indices run over occupied/virtual Kohn–Sham molecular orbitals, the first-order density with respect to the external field component α [$\rho^\alpha(\mathbf{r}, \omega)$] is expressed as follows:

$$\rho^\alpha(\mathbf{r}, \omega) = \sum_{ia} P_{ia}^\alpha(\omega) \Psi_i(\mathbf{r}) \Psi_a^*(\mathbf{r}) + P_{ai}^\alpha \Psi_a(\mathbf{r}) \Psi_i^*(\mathbf{r}), \quad (15)$$

where $\Psi(\mathbf{r})$ represents Kohn–Sham orbitals and $P^\alpha(\omega)$ is the first-order density matrix considering the α component of the external field.

The matrix elements of $\mathbf{P}^\alpha(\omega)$ can be obtained from the solution of the linear response equations within the Time-Dependent Kohn–Sham (TDKS) framework,^{42,48,83}

$$\left[\begin{pmatrix} \mathbf{A} & \mathbf{B} \\ \mathbf{B}^* & \mathbf{A}^* \end{pmatrix} - (\omega + i\Gamma) \begin{pmatrix} \mathbf{I} & 0 \\ 0 & -\mathbf{I} \end{pmatrix} \right] \begin{pmatrix} \mathbf{X} \\ \mathbf{Y} \end{pmatrix} = - \begin{pmatrix} \mathbf{Q} \\ \mathbf{Q}^* \end{pmatrix}. \quad (16)$$

In the QM/ ω FQF μ -BEM approach, the terms entering the linear system in Eq. (16) are modified to account for the presence of the ω FQF μ and BEM layers, i.e.,

$$\begin{aligned} A_{ai,bj} &= (\varepsilon_a - \varepsilon_i) \delta_{ab} \delta_{ij} + (ai|bj) - c_x(ab|ij) \\ &+ c_l f_{ai,bj}^{xc} + C_{ai,bj}^{\text{QM}/\omega\text{FQF}\mu-\text{BEM}}, \\ B_{ai,bj} &= (ai|bj) - c_x(aj|ib) + C_{ai,bj}^{\text{QM}/\omega\text{FQF}\mu-\text{BEM}}, \\ Q_{ia} &= \langle \phi_i | V^{\alpha,\text{pert}}(\mathbf{r}, \omega) | \phi_a \rangle. \end{aligned} \quad (17)$$

In Eq. (16), \mathbf{X} and \mathbf{Y} are the excitation and de-excitation transition densities, respectively, while Γ is a phenomenological damping factor. ε is the molecular orbital energy, $(ai|bj)$ denotes two-electron integrals, and the c_x, c_l parameters vary depending on the DFT functional employed. In addition, $C^{\text{QM}/\omega\text{FQF}\mu-\text{BEM}}$ describes the polarization induced by the ω FQF μ -BEM charges and dipoles, which respond to the perturbed TDKS density.^{11,17,84} On the right-hand-side, $Q_{ia} = \langle \phi_i | V^{\alpha,\text{pert}}(\mathbf{r}, \omega) | \phi_a \rangle$ represents the expectation value of the perturbation operator polarized along α .

QM/ ω FQF μ -BEM can be extended to compute SERS spectra of molecular systems in the vicinity of metal NPs. To this end, the complex polarizability tensor $\tilde{\alpha}_{\alpha\beta}$ needs to be computed,^{11,85} where α/β represent the Cartesian components (x, y, z). After solving Eq. (16), $\tilde{\alpha}_{\alpha\beta}$ can be calculated as follows:

$$\tilde{\alpha}_{\alpha\beta}(\omega; \omega') = -\text{tr} [\mathbf{Q}^\alpha(\omega) \mathbf{P}^\beta(\omega')], \quad (18)$$

where $\mathbf{Q}^\alpha(\omega)$ is calculated as shown in Eq. (17) and includes the QM dipole and the ω FQF μ -BEM local field operators polarized along α .^{11,18,40,86}

According to Placzek's theory of Raman scattering,⁸⁷ the Raman signal can be modeled from the frequency-dependent polarizability tensor. Assuming the frequency of the incident and scattered fields to coincide, the Raman intensity related to the k -th normal mode I^k of the QM molecule is given by^{11,44,87–89}

$$I^k \propto \frac{(\omega - \omega_k)^4}{\omega_k} 45[\alpha'_k(\omega - \omega_k; \omega)]^2 + 7[\gamma'_k(\omega - \omega_k; \omega)]^2, \quad (19)$$

where ω is the incident frequency, while ω_k and α'_k/γ'_k are the frequency and the isotropic/anisotropic polarizability derivatives associated with the k -th normal mode (Q_k), respectively. They are expressed as follows:¹¹

$$\begin{aligned} [\alpha'_k(\omega; \omega')]^2 &= \frac{1}{9} \left| \sum_{i=x,y,z} \frac{\partial \bar{\alpha}_{ii}(\omega; \omega')}{\partial Q_k} \right|^2, \\ [\gamma'_k(\omega; \omega')]^2 &= \frac{1}{2} \left(\frac{3}{4} \sum_{ij=x,y,z} \left| \frac{\partial \bar{\alpha}_{ij}(\omega; \omega')}{\partial Q_k} + \frac{\partial \bar{\alpha}_{ji}(\omega; \omega')}{\partial Q_k} \right|^2 \right. \\ &\quad \left. - 9[\alpha'_k(\omega; \omega')]^2 \right). \end{aligned}$$

III. COMPUTATIONAL DETAILS

Ag structures are created by using the Atomic Simulation Environment (ASE) Python module v. 3.17.⁹⁰ In particular, Ag atoms are disposed in a Face-Centered Cubic (FCC) arrangement defined by a lattice parameter of 4.08 Å. Two morphologies are studied: spherical and icosahedral (Ih) NPs. For ω FQF μ calculations, the parameters defined in Ref. 35 are exploited. Detailed information regarding the geometrical characteristics of all atomistic structures is reported in Tables S2–S5 of the [supplementary material](#).

The continuum BEM meshes representing the surfaces of both spherical and Ih NPs are constructed by using the GMSH software.⁹¹ The frequency-dependent permittivities proposed by Palik,⁹² Brendel-Bormann,⁹³ and Johnson and Christy⁹⁴ are exploited in BEM calculations.

ω FQF μ -BEM spherical and Ih structures are built as a core, described as an implicit spherical NP and treated at the BEM level, surrounded by an atomistic shell, treated at the ω FQF μ level. To validate the novel approach, we investigate the variation of the optical response of a spherical Ag nanostructure (radius 4 nm) as a function of the method parameters, namely, the core-to-shell distance, the thickness of the atomistic shell, the BEM *tessellation*, and the dielectric function to describe BEM response.

In particular, we study the optical response as a function of the minimum core-to-shell distance, which varies from 2.88 to 5.76 Å, corresponding to integer multiples of the nearest neighbor distance (2.88 Å) in the studied FCC lattices. For Ag Ih structures, the atomistic shell is defined, ensuring a minimum thickness of three atomic layers in the thinner region.

In ω FQF μ -BEM, the total complex dipole of the NP ($\tilde{\zeta}$) is computed as follows:

$$\tilde{\zeta}(\omega) = \sum_i^N q_i(\omega) \mathbf{r}_i + \sum_i^N \boldsymbol{\mu}_i(\omega) + \sum_v^P \sigma_v(\omega) \mathbf{s}_v,$$

where \mathbf{r}_i and \mathbf{s}_v are the positions of the i -th atom and of the v -th *tessera* centroid, respectively. From $\tilde{\zeta}$, the NP complex frequency-dependent polarizability ($\tilde{\xi}$) and the absorption cross section (σ^{abs}) can be calculated as follows:

$$\tilde{\xi}(\omega)_{\alpha\beta} = \frac{\tilde{\zeta}_\alpha}{E_{0,\beta}} \implies \sigma^{\text{abs}}(\omega) = \frac{4\pi\omega}{3c} \text{Tr}(\tilde{\xi}), \quad (20)$$

where $\alpha\beta$ indicates the polarization of the incident electric field (E_0), and c is the speed of light.

After validating ω FQF μ -BEM, we exploit the multiscale QM/ ω FQF μ -BEM to calculate SERS signals of pyridine adsorbed on Ag Ih NPs (with radius varying from 1.9 to 3.8 nm). SERS spectra are computed by representing the Ag Ih NP at the fully atomistic ω FQF μ , implicit BEM, and hybrid ω FQF μ -BEM levels, thus allowing for validating the novel method by a robust comparison with state-of-the-art methods. In all cases, pyridine is placed longitudinally at a distance of 3 Å from the NP surface. Such distance is calculated from the nitrogen atom to the nearest NP atom/*tessera* centroid defining the tip of the atomistic/continuum surface of Ag Ih structures.

In all calculations, pyridine is described at the QM level utilizing the BP86 functional and a double- ζ -polarized DZP basis set, in agreement with previous studies.^{11,86} TDDFT equations are solved by imposing a damping factor $\Gamma = 0.01$ eV.^{11,86,95,96} α'_k and γ'_k [see Eq. (19)] are calculated by a numerical differentiation scheme, with a constant step size of 0.001 Å.^{11,97–99} Normal modes' displacements of pyridine are evaluated *in vacuo*, without explicitly considering NP effects, which are expected to be small for the considered system.^{11,86} The influence of the plasmon resonance on SERS signals is assessed by matching the incident light frequency for Raman with the Plasmon Resonance Frequency (PRF) of the NP, whose values are collected in Tables S5 and S6 in the [supplementary material](#). Finally, SERS spectra are plotted using Lorentzian band-shapes characterized by a full width at half maximum (FWHM) of 4 cm⁻¹. QM/ ω FQF μ -BEM, QM/ ω FQF μ , and QM/BEM calculations are performed by using a locally modified version of the Amsterdam Modeling Suite (AMS).⁸¹

The NP effect on Raman signals is evaluated through the definition of three observables: the Enhancement Factor (EF), the Maximum Enhancement Factor (MEF), and the Averaged Enhancement Factor (AEF), which are defined as follows:

$$\text{EF}^k(\omega) = \frac{I_{\text{NP}}^k(\omega)}{I_{\text{vac}}^k(\omega)}, \quad (21)$$

$$\text{MEF}(\omega) = \max_k \text{EF}^k(\omega), \quad (22)$$

$$\text{AEF}(\omega) = \frac{\sum_k I_{\text{NP}}^k(\omega)}{\sum_l I_{\text{vac}}^l(\omega)}, \quad (23)$$

where I_{NP}^k and I_{vac}^k are the molecular Raman intensities associated with the k -th normal mode [see Eq. (19)] in the presence of NP and *in vacuo*, respectively. In Eq. (23), k and l indices run over the set of studied molecular normal modes.

A summary of the parameters involved in ω FQF μ , BEM, ω FQF μ -BEM, and SERS calculations is given in Sec. S2.1 of the *supplementary material*.

IV. RESULTS AND DISCUSSION

In this section, the ω FQF μ -BEM and QM/ ω FQF μ -BEM methods are validated by comparison with the reference ω FQF μ and QM/ ω FQF μ approaches. In particular, ω FQF μ -BEM is first challenged to reproduce the plasmonic features of spherical NPs by analyzing how a variation of the model parameters affects the optical response. Then, QM/ ω FQF μ -BEM is applied to compute SERS of pyridine adsorbed on complex-shaped Ih nanostructures.

A. The ω FQF μ -BEM method for plasmonics

1. Plasmonic features of single nanoparticles

In Fig. 2(a), we show a graphical representation of a spherical NP described at the ω FQF μ -BEM level, constructed by integrating a continuum BEM spherical core within an atomistic ω FQF μ spherical shell. ω FQF μ -BEM spherical NP geometries are defined by four parameters: the radius of the inner BEM core (r_{BEM}), the radii of the outer ω FQF μ shell (R), the BEM core- ω FQF μ shell distance (d), and the difference between the radii of the inner and outer shells (Δr). The computed optical response depends on the proper definition of such parameters, the dielectric function exploited to model the BEM portion, and the number of *tesserae* exploited to mesh the BEM region. It is worth noting that our approach is general, and the full BEM ($r_{BEM} = R$) or the full ω FQF μ ($\Delta r = R$) description can be easily recovered.

Let us first focus on the computed response for a specific geometry, i.e., a spherical NP with $R = 40.00$ Å, $r_{BEM} = 20.26$ Å, $\Delta r = 13.98$ Å, and $d = 5.76$ Å. 11 470 atoms constitute the atomistic shell, while the BEM core is defined by 2972 *tesserae*. The Brendel-Bormann frequency-dependent permittivity⁹³ is exploited to describe the BEM part.

Figure 2(b) compares normalized absorption spectra calculated for ω FQF μ -BEM and the reference, fully atomistic ω FQF μ (hereafter referred to as full- ω FQF μ). The normalization is performed with respect to the full- ω FQF μ PRF absorption. The full- ω FQF μ approach predicts a single absorption peak at 3.47 eV, whereas the ω FQF μ -BEM spectrum features two peaks centered at 2.50 and 3.45 eV. To analyze the physical origin of such a discrepancy, in Fig. 2(c), normalized absorption spectra of the selected spherical NP calculated at the ω FQF μ -BEM level are reported, together with the absorption spectrum of the BEM core and ω FQF μ shell. Spectra are normalized with respect to the maximum absorption of the ω FQF μ shell. The spherical shell spectrum shows a high-intensity peak centered at 3.24 eV and a low-intensity peak at 3.68 eV. These two peaks can be assigned to the bonding ($|\omega_{s+}\rangle$) and anti-bonding ($|\omega_{s-}\rangle$) plasmonic modes, respectively [see Fig. 2(d)], which are typical of plasmonic nanoshells.^{24,100–102} A single plasmonic peak at about 3.43 eV ($|\omega_c\rangle$) is instead present in the spectrum of the

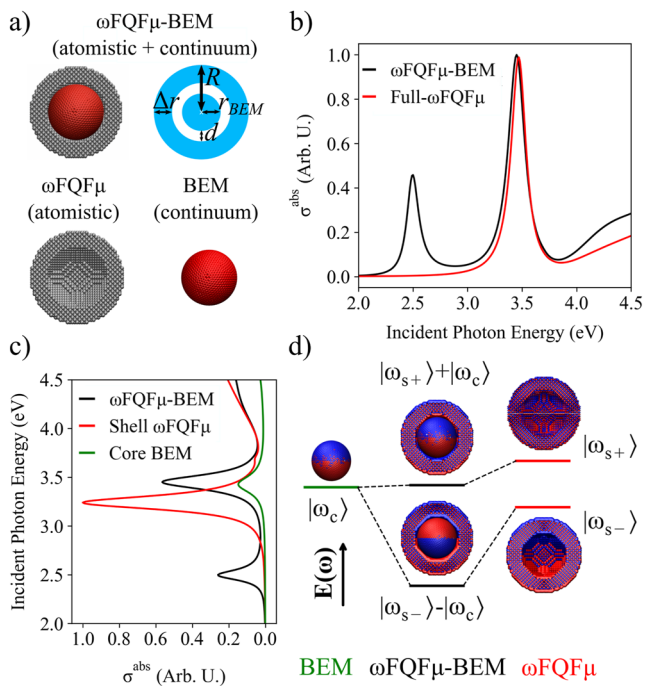


FIG. 2. (a) Graphical representation and geometrical parameters of a spherical NP described by ω FQF μ -BEM. (b) Normalized absorption cross sections σ^{abs} of a spherical Ag NP (radius = 40 Å) computed at the ω FQF μ -BEM and full- ω FQF μ levels. (c) Normalized absorption spectra of the selected spherical NP calculated at the ω FQF μ -BEM level, together with the absorption spectra of the BEM core and ω FQF μ shell. See panel (a). (d) Schematic picture of the hybridization of BEM charge distribution (left) and ω FQF μ densities (right), leading to ω FQF μ -BEM charges and densities (center) calculated at the corresponding PRFs.

BEM core. Such a band corresponds to the dipolar plasmonic excitation [see Fig. 2(d)].

The two peaks reported in the ω FQF μ -BEM spectrum of the spherical NP are thus due to the hybridization of isolated plasmonic modes from the core and shell, similar to what has been reported for other nanostructures.^{102–106} More specifically, the ω FQF μ -BEM peak at 2.50 eV is associated with the hybrid $|\omega_{s-}\rangle - |\omega_c\rangle$ mode, while the band centered at 3.45 eV corresponds to the $|\omega_{s+}\rangle + |\omega_c\rangle$ mode combination [see Fig. 2(d)]. The presence of the low-energy peak is not unexpected because the approach discards any charge transfer between the two classical regions. This peak thus arises as an artifact of our model. However, it can be easily identified because it will always be the lowest energy peak computed in the spectrum (without the need for any benchmarking with a reference calculation), as predicted by hybridization theory.^{102,105} In the following, the focus will thus shift to the $|\omega_{s+}\rangle + |\omega_c\rangle$ band, whose PRF remarkably aligns with that predicted at the full- ω FQF μ level. For clarity, Fig. S1 of the *supplementary material* presents a comparison between the densities computed from the charges + dipoles distribution of the ω FQF μ -BEM $|\omega_{s+}\rangle + |\omega_c\rangle$ band and the full- ω FQF μ PRF, illustrating a clear one-to-one correspondence.

As a final remark, a third $|\omega_{s+}\rangle - |\omega_c\rangle$ mode arises from the hybridization of plasmonic modes. However, the small dipole moment associated with this mode makes it undetectable in the

spectra.^{102,105} Moreover, the relative intensities of the $|\omega_{s-}\rangle - |\omega_c\rangle$ and $|\omega_{s+}\rangle + |\omega_c\rangle$ modes are consistent with the expected hybridization behavior. In particular, the stronger intensity of the $|\omega_{s+}\rangle + |\omega_c\rangle$ mode is expected due to the in-phase oscillation of the core and shell dipole moments.^{102,105}

2. Plasmonic response dependence on the thickness of the atomistic shell

This section first examines how a variation in the shell thickness and core–shell distance d influences the optical response of the metal NPs. In particular, the shell thickness Δr varies from 13.98 to 7.93 Å, with a constant step of ~2.0 Å. Two core-to-shell distances are considered: $d = 2.88$ Å and $d = 5.76$ Å, corresponding to integer multiples of the nearest neighbor distance (2.88 Å) in the studied FCC lattice. In all cases, the BEM matrix is described by the Brendel–Bormann dielectric function.⁹³

Figures 3(a)–3(c) reports absorption cross sections of the spherical NP as a function of shell thickness Δr for $d = 2.88$ and $d = 5.76$ Å, respectively. Data are normalized with respect to the full- ω FQF μ PRF absorption. As a reference, the normalized absorption spectrum computed at the full- ω FQF μ level is reported in all panels. All ω FQF μ -BEM spectra feature an intense peak in the region 3.0–4.5 eV. Such a peak is associated with a dipolar plasmon, as commented in Sec. IV A 1. ω FQF μ -BEM computed PRFs remain almost constant as a function of the shell thickness and only present slight shifts of 0.02–0.04 eV with respect to ω FQF μ PRF (3.47 eV), regardless of the value of d . Differently, reducing

the shell thickness systematically increases the absorption intensity mismatch at the PRF between ω FQF μ -BEM and the reference ω FQF μ data. Notably, the mismatch becomes more pronounced for structures with $d = 2.88$ Å. This behavior is probably due to numerical instabilities occurring when solving the ω FQF μ -BEM linear equation [see Eq. (14)] for the smaller d values, associated with the so-called polarization catastrophe raising for the increase of electrostatic/polarization interactions.¹⁰⁷

To further analyze the plasmonic response as a function of d , Figs. 3(b) and 3(d) graphically illustrate the differences in the computed charges + dipoles density at the ω FQF μ -BEM and full- ω FQF μ levels. In all cases, densities are computed at the PRF for $d = 2.88$ Å and $d = 5.76$ Å, respectively. This qualitative analysis permits us to evaluate the charges + dipoles density deviation near the NP surface of ω FQF μ -BEM with respect to the full- ω FQF μ atomistic structure, whose surface is graphically represented by green dots. The most remarkable differences are observed at the core region, and in particular at the BEM- ω FQF μ interface. This is expected and is due to the artificial boundary that is introduced in our multi-scale method. However, since we are dealing with localized surface plasmons, we are particularly interested in a proper description of surface properties. Note that the differences at the NP surface are negligible for all methods, thus validating the novel methodology. The agreement between the two methods worsens by reducing the atomistic shell thickness, especially for $d = 2.88$ Å. This is again related to numerical instabilities in solving the ω FQF μ -BEM linear equation.

For a more quantitative analysis of the plasmonic density differences close to the NP, in Table I, computed relative errors (ρ^{error}) between integrated densities of ω FQF μ -BEM and full- ω FQF μ are collected. Values are calculated at their corresponding PRFs. ρ^{error} is evaluated within a volume V close to the NP surface, defined as a three-dimensional parallelogram constrained by the coordinate ranges $x, z \in [-10, 10]$ Å and $y \in [40, 50]$ Å (see Fig. S2 of

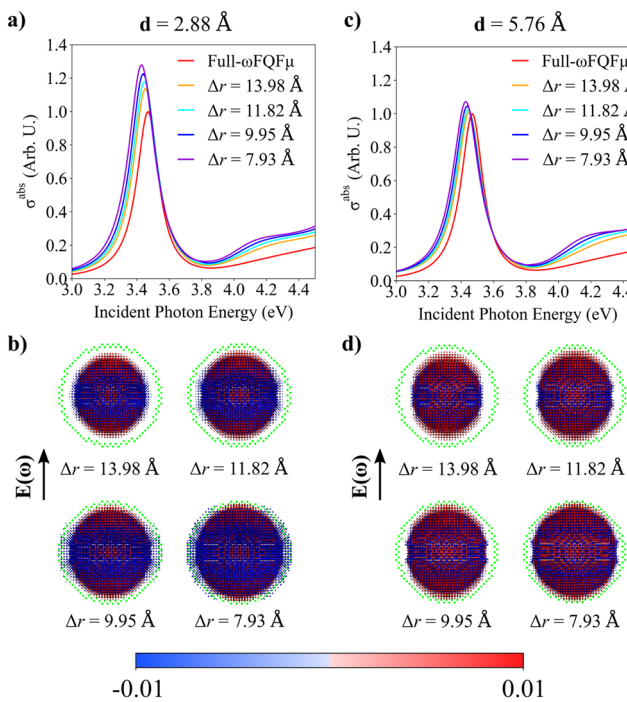


FIG. 3. Normalized absorption spectra of a spherical NP (a) and (c) and absolute density differences plots calculated at the PRFs [(b) and (d)] green dots represent surface NP atoms] as a function of Δr . The NP is described at the full- ω FQF μ and ω FQF μ -BEM levels, setting $d = 2.88$ Å (a) and (b) and $d = 5.76$ Å (c) and (d).

TABLE I. PRFs of the studied spherical NP ($R = 40$ Å) calculated at the ω FQF μ -BEM level ($d = 2.88$ Å and $d = 5.76$ Å) as a function of geometrical parameters (Δr , N_{Atoms} , r_{BEM}). ω FQF μ -BEM computational % speed-up and ρ^{error} with respect to full- ω FQF μ reference are also given.

Δr (Å)	N_{Atoms}	r_{BEM} (Å)	PRF (eV)	Speed-up (%)	ρ^{error} (%)
$d = 2.88$ Å					
13.98	11 470	23.14	3.45	44.35	11.74
11.82	10 258	25.30	3.45	56.87	14.36
9.95	9 080	27.17	3.44	66.01	19.34
7.93	7 676	29.19	3.43	77.32	21.25
$d = 5.76$ Å					
13.98	11 470	20.26	3.45	42.56	3.49
11.82	10 258	22.42	3.44	53.55	5.45
9.95	9 080	24.29	3.44	65.20	6.77
7.93	7 676	26.31	3.43	75.81	10.42
Full- ω FQF μ	15 683	—	3.47	—	—

the [supplementary material](#) for a graphical representation). ρ^{error} is calculated as follows:

$$\rho^{\text{error}} = \frac{\int_V |\rho_{\text{PRF}}^{\omega\text{FQF}\mu-\text{BEM}}(\mathbf{r}) - \rho_{\text{PRF}}^{\text{Full-}\omega\text{FQF}\mu}(\mathbf{r})| d\mathbf{r}^3}{\int_V |\rho_{\text{PRF}}^{\text{Full-}\omega\text{FQF}\mu}(\mathbf{r})| d\mathbf{r}} \cdot 100, \quad (24)$$

where $\rho_{\text{PRF}}^{\omega\text{FQF}\mu-\text{BEM}}$ and $\rho_{\text{PRF}}^{\text{Full-}\omega\text{FQF}\mu}$ are the $\omega\text{FQF}\mu$ -BEM and full- $\omega\text{FQF}\mu$ densities calculated at their PRF, respectively. The results reported in [Table I](#) confirm the qualitative behavior depicted in [Fig. 3](#). In fact, by decreasing the shell thickness, the computed ρ^{error} values increase for both $d = 2.88 \text{ \AA}$ (ranging from about 12% to about 21%) and $d = 5.76 \text{ \AA}$ (ranging from about 3% to about 10%). In addition, this quantitative analysis confirms the better numerical performance of the $\omega\text{FQF}\mu$ -BEM structures with $d = 5.76 \text{ \AA}$, which are consistently associated with the lowest relative errors. Remarkably, for the largest Δr , $\omega\text{FQF}\mu$ -BEM is associated with a relative error of about 3%, thus validating our novel approach as compared to a full atomistic description.

To conclude this section, we investigate the computational savings associated with the multiscale $\omega\text{FQF}\mu$ -BEM as compared to a full $\omega\text{FQF}\mu$ description of the spherical NP. To this end, the relative computational speed-up (in percentage) for single-frequency calculations (at the PRF of the systems) is reported in [Table I](#) as a function of d and Δr . We remark that all calculations exploit a constant number of *tesserae* to mesh the BEM core (~ 2980 *tesserae*). The data reported in [Table I](#) clearly show a substantial computational saving, ranging from about 43% to about 77%, independent of d for a given value of Δr . This is expected because the number of atoms in the $\omega\text{FQF}\mu$ shell decreases while the number of *tesserae* representing the BEM core remains constant. It is worth remarking that for the most accurate $\omega\text{FQF}\mu$ -BEM partitioning ($\Delta r = 13.98 \text{ \AA}$, $d = 5.76 \text{ \AA}$), the speed-up of $\omega\text{FQF}\mu$ -BEM is considerable, without losing accuracy as compared to a full $\omega\text{FQF}\mu$ description. Therefore, the above model parameters represent the best compromise between accuracy and computational cost for $\omega\text{FQF}\mu$ -BEM applications.

3. Plasmonic response dependence on the BEM dielectric functions

We now move to analyze the model parameters affecting the BEM core response, namely, the dielectric function and the number of *tesserae*. To this end, we consider three dielectric functions that are commonly exploited to describe Ag response, recovered from Brendel-Bormann (BB),⁹³ Palik,⁹² and Johnson and Christy (J & C).⁹⁴ Computed absorption cross sections for the selected spherical NP exploiting the three permittivity functions are normalized with respect to the full- $\omega\text{FQF}\mu$ reference and graphically depicted in [Figs. 4\(a\)-4\(c\)](#), for $d = 5.76 \text{ \AA}$ (see [Fig. S3](#) of the [supplementary material](#) for additional values obtained with $d = 2.88 \text{ \AA}$). Absorption properties are reported as a function of the shell thickness Δr . The normalized full atomistic $\omega\text{FQF}\mu$ absorption spectrum is also shown as a reference.

All computed spectra are characterized by a main plasmonic peak, which is associated with a dipolar localized surface plasmon. $\omega\text{FQF}\mu$ -BEM computed PRFs (see also [Table II](#)) remain constant as a function of the shell thickness by exploiting Palik and J & C permittivity functions (3.48 eV), and remarkably the computed PRF is shifted by only 0.01 eV with respect to the reference $\omega\text{FQF}\mu$ PRF (3.47 eV). As commented in [Sec. IV A 2](#), by using the BB $\epsilon(\omega)$, the PRF slightly shifts by decreasing the shell thickness (from 3.45 eV- $\Delta r = 13.98 \text{ \AA}$ to 3.43 eV- $\Delta r = 7.93 \text{ \AA}$). However, also in this case, all data agree with the reference $\omega\text{FQF}\mu$ PRF within the chemical accuracy (0.04 eV to 0.9 kcal/mol).

The absorption cross section at the PRF varies significantly depending on the chosen dielectric function. Notably, absorption intensities in very good agreement with the reference $\omega\text{FQF}\mu$ model are obtained by employing BB and Palik dielectric functions. The $\omega\text{FQF}\mu$ -BEM spectrum computed by using the Palik dielectric function presents a small shoulder at about 3.3 eV, which is also observed at the full BEM level (see [Fig. S4](#) in the [supplementary material](#)) and is thus related to the use of this specific permittivity function. In contrast, a pronounced intensity mismatch as compared to the full- $\omega\text{FQF}\mu$ absorption curve is observed if the J & C dielectric function is employed. Remarkably, such a discrepancy increases as the shell thickness decreases.

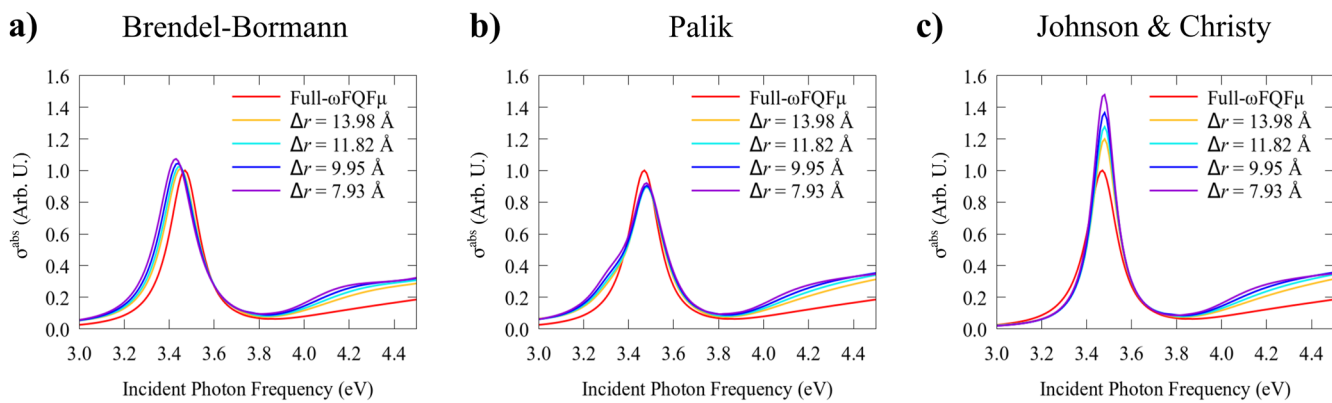


FIG. 4. Normalized absorption spectra of a spherical Ag NP ($R = 40 \text{ \AA}$) treated at the $\omega\text{FQF}\mu$ -BEM ($d = 5.76 \text{ \AA}$) levels as a function of Δr and BEM dielectric function [Brendel-Bormann (a), Palik (b), and Johnson and Christy (c)]. Full- $\omega\text{FQF}\mu$ spectra are also depicted as a reference.

TABLE II. PRFs and ρ^{error} computed for the studied spherical Ag NP ($R = 40 \text{ \AA}$) at the full- $\omega\text{FQF}\mu$ and $\omega\text{FQF}\mu\text{-BEM}$ ($d = 5.76 \text{ \AA}$) levels, as a function of $\omega\text{FQF}\mu\text{-BEM}$ geometrical parameter Δr and BEM dielectric function [Brendel–Bormann (BB), Palik, and Johnson and Christy (J & C)].

$\Delta r (\text{\AA})$	Dielectric function	PRF (eV)	$\rho^{\text{error}} (\%)$
13.98	BB	3.45	3.49
	Palik	3.48	8.21
	J & C	3.48	22.21
11.82	BB	3.44	5.45
	Palik	3.48	9.26
	J & C	3.48	28.30
9.95	BB	3.44	6.77
	Palik	3.48	10.70
	J & C	3.48	31.82
7.93	BB	3.43	10.42
	Palik	3.48	9.22
	J & C	3.48	44.45
Full- $\omega\text{FQF}\mu$	—	3.47	—

To quantitatively analyze surface-related near-field properties, ρ^{error} values as a function of the permittivity function and Δr are reported in Table II. Computed relative errors using BB and J & C permittivities consistently increase by reducing the atomistic shell thickness, unlike those obtained by exploiting the Palik dielectric function, which remains almost constant (about 9%). Notably, the best results (i.e., lowest errors) are obtained by employing BB, with the exception of the case $\Delta r = 7.93 \text{ \AA}$ for which Palik gives the best results. J & C data substantially deviate from reference $\omega\text{FQF}\mu$ values. On the other hand, BB emerges as the most robust permittivity function model to exploit in $\omega\text{FQF}\mu\text{-BEM}$ applications.

As a final validation, we investigate the dependence of absorption spectra on the number of *tesserae* used to mesh the BEM core. In particular, we consider four different tessellations of the spherical BEM core (2990, 1948, 1018, and 390 *tesserae*), while keeping the other model parameters fixed to the best set resulting from the previous analysis ($d = 5.76 \text{ \AA}$, $\Delta r = 13.98 \text{ \AA}$, BB permittivity function). Numerical results are reported in Fig. S5 and Table S3 of the supplementary material. Interestingly, the discretization of the core only minimally affects the plasmonic response (spectra, density-differences plots, and ρ^{error}), while yielding substantial computational % speed-ups, up to 56.68% for 390 *tesserae*. To conclude, the best parameter set, which guarantees the best compromise between computational cost and accuracy, is defined by $d = 5.76 \text{ \AA}$, $\Delta r = 13.98 \text{ \AA}$, the BB permittivity function, and 390 *tesserae*.

B. Molecular plasmonics: QM/ $\omega\text{FQF}\mu\text{-BEM}$ for SERS

As mentioned in Sec. I and specified in Sec. II B, $\omega\text{FQF}\mu\text{-BEM}$ can be coupled to a QM Hamiltonian in a QM/Classical fashion and extended to compute SERS spectra. This section showcases the potentialities of the method to compute SERS spectra of pyridine

near the tip of complex-shaped NPs. To this end, Ag icosahedral (Ih) NPs of increasing size (from 1.9 to 3.8 nm) are selected, and additional calculations modeling the molecule–NP system at the fully atomistic (QM/ $\omega\text{FQF}\mu$) and fully implicit (QM/BEM) levels are discussed. A graphical representation highlighting the structural differences between the various methods is given in Fig. 5, panel (a), whereas geometrical parameters are shown in Table S4 in the supplementary material. To fully characterize $\omega\text{FQF}\mu\text{-BEM}$ Ih systems and, similarly, spherical NPs, four parameters are exploited (the BEM radius r_{BEM} , the BEM- $\omega\text{FQF}\mu$ distance d , the average thickness of the $\omega\text{FQF}\mu$ shell Δr , and the NP radius R), while the equivalent full- $\omega\text{FQF}\mu$ and full-BEM structures are described by a single radius parameter (R). Detailed data on the geometrical features and PRFs of the systems are gathered in Tables S4–S6 of the supplementary material.

In Fig. 5, the SERS signal of pyridine on Ag Ih NPs is studied as a function of the NP radius. Pyridine is adsorbed perpendicularly to the NP surface at a distance of 3 \AA , with the N atom lying closest to the NP. In agreement with the preliminary analysis in Sec. IV A, the BB dielectric function is employed, and d is set to 5.76 \AA . Figure 5(b) illustrates SERS intensities as a function of the NP radius, normalized with respect to the largest signal exhibited by each model. In all cases, this corresponds to the SERS signal of pyridine interacting with the largest Ih NP. Notably, for all models, only the signals associated with specific normal modes are enhanced (see Fig. S7 in the supplementary material for their graphical depiction). This is due to the fact that such vibrations are related to an orthogonal movement of pyridine atoms with respect to the NP surface. As a consequence, they experience the largest field gradient variation and are, therefore, preferentially enhanced, as has recently been shown by some of us.¹¹ The analysis of the results reveals significant similarities between the QM/ $\omega\text{FQF}\mu\text{-BEM}$ and QM/ $\omega\text{FQF}\mu$ approaches while also highlighting substantial discrepancies by using QM/BEM. In particular, the observed Raman peaks are consistent across all models when pyridine is adsorbed on the largest NPs (radius $> 2.7 \text{ nm}$). On the contrary, the smallest full-BEM structures (radius $< 2.5 \text{ nm}$) substantially deviate from the full atomistic picture [see Fig. 5(b)]. To better compare the three approaches, Fig. 5(c) presents normalized Raman spectra for the largest NP studied using each theoretical framework. The spectra depicted in Fig. 5(c) show an almost perfect alignment of the relative Raman intensities between $\omega\text{FQF}\mu\text{-BEM}$ and full- $\omega\text{FQF}\mu$ NPs. In contrast, substantial discrepancies are evident for full-BEM structures, particularly for the Raman peaks centered at 1024, 1207, 1460, and 1568 cm^{-1} .

To comprehensively analyze the performance of the various models, Fig. 5(d) collects AEF and MEF descriptors calculated as a function of the NP radius. For all methods, such indices are monotonically increasing. The reference QM/ $\omega\text{FQF}\mu$ approach predicts a maximum AEF and MEF of about 5000 and 12 000, respectively, thus displaying an overall enhancement of about 10^3 . QM/BEM shows a substantial quantitative mismatch, providing AEF and MEF that are completely overestimated by several orders of magnitude (about 10^8). Conversely, QM/ $\omega\text{FQF}\mu\text{-BEM}$ presents a clear trend of quantitative similarity with the reference fully atomistic results, predicts AEF and MEF of the same order of magnitude, and only deviates from the reference by a factor of about 1.35 for the largest structure. In addition, in Fig. S8 of the supplementary material, normalized gas-phase Raman and SERS spectra computed

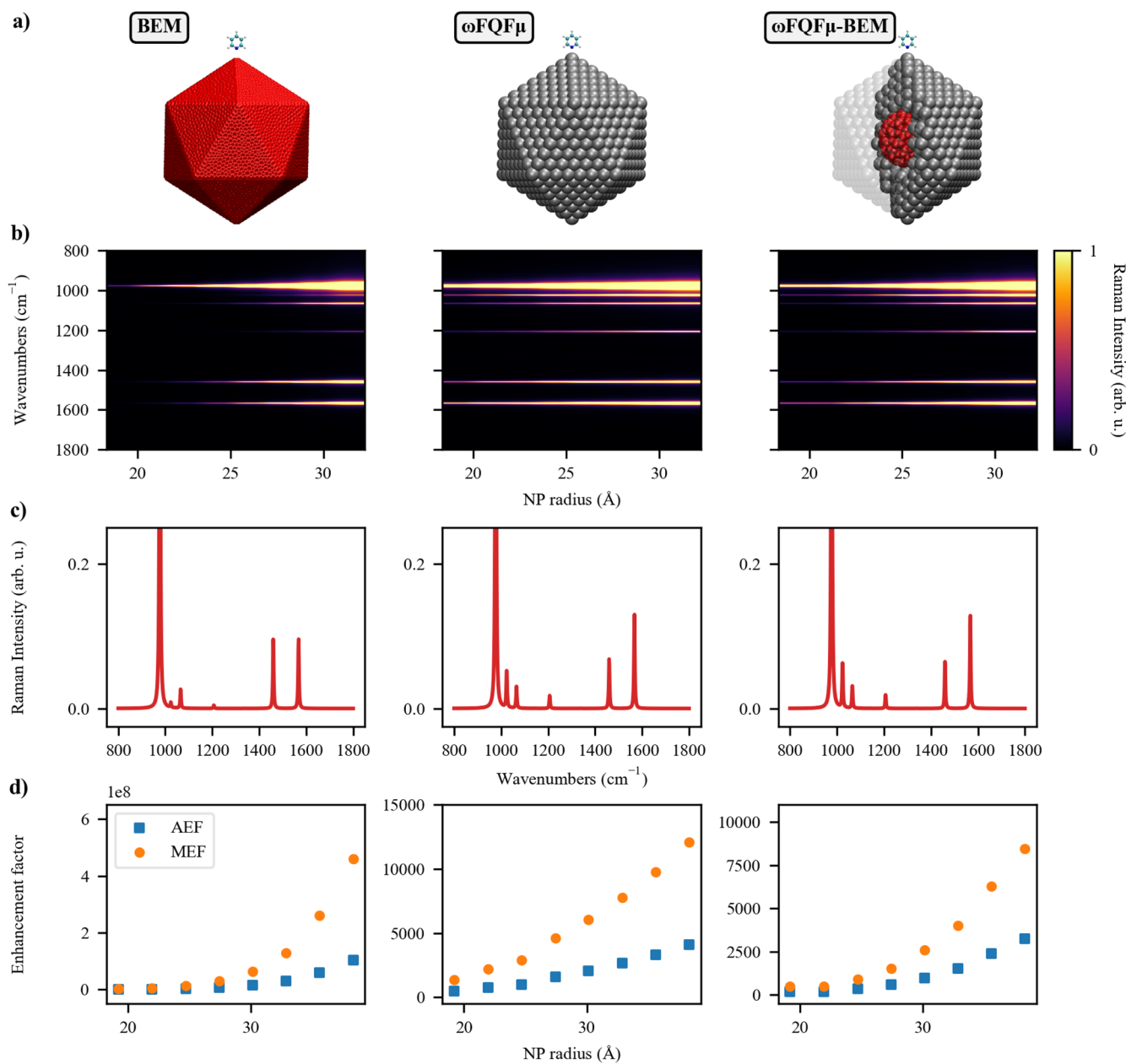


FIG. 5. Graphical depiction of pyridine adsorbed on Ag I_h systems described at the full-BEM (left), full- ω FQF μ (center), and ω FQF μ -BEM (right) levels. (b) Normalized pyridine SERS spectra as a function of the NP radius. (c) Normalized SERS of pyridine adsorbed on the largest NP. (d) AEF and MEF as a function of the NP radius. BEM response is described with the BB dielectric function, and ω FQF μ -BEM I_h systems are characterized by $d = 5.76 \text{ \AA}$.

22 January 2025 11:20:58

at PRF are reported for the largest nanoparticle studied using each formalism.

It is worth remarking that the QM/BEM trends arising from Fig. 5 can be substantially affected by varying the dielectric functions (J & C and Palik). These results are reported in Sec. S2.3 of the [supplementary material](#) and show that J & C permittivity yields

a complete modification of the spectral response for the largest NP (see Figs. S9 and S12 of the [supplementary material](#)), also affecting computed AEF and MEF values, further magnifying the quantitative discrepancies compared to the fully atomistic ω FQF μ description. Conversely, the QM/ ω FQF μ -BEM spectra remain consistent regardless of the chosen parameters but are crucially affected

by a variation in the BEM- ω FQF μ distance d . In fact, by setting $d = 2.88 \text{ \AA}$, inconsistent trends in both AEF and MEF are reported as the system size increases (see Figs. S11–S13 of the [supplementary material](#)). This behavior completely aligns with our findings from the study on ρ^{error} of spherical ω FQF μ -BEM NPs (see Sec. IV A).

To remove any arbitrariness in selecting the minimum NP-pyridine distance for the full-BEM systems, we have performed distance-dependent studies of AEF and MEF for pyridine adsorbed on the tip of icosahedral nanoparticles with a 3 nm radius. These calculations were performed at the full-BEM, full- ω FQF μ , and ω FQF μ -BEM (characterized by the BB dielectric function and $d = 5.76 \text{ \AA}$) levels, as shown in Fig. S14 in the [supplementary material](#). The results reveal a monotonic decrease in both descriptors for all three models, supporting the validity of our full-BEM calculations. In addition, the decay trends for full- ω FQF μ and ω FQF μ -BEM show a one-to-one correspondence, while the full-BEM studies exhibit a smoother decay with distance, further corroborating the robustness of the ω FQF μ -BEM approach.

We conclude this section by remarking on the enhanced computational efficiency of the QM/ ω FQF μ -BEM method as compared to the fully atomistic ω FQF μ description (see Table S7 of the [supplementary material](#) for the numerical % speed-up). Notably, the computational saving is particularly evident for the largest systems (radius $> 3 \text{ nm}$), for which, as previously discussed, an improved quantitative and qualitative description of the SERS response is also obtained. These findings underscore the potential of ω FQF μ -BEM for its application to large systems, where atomistic details at their surface play a major role in their plasmonic features, offering a substantial reduction in computational cost, up to 58%.

V. CONCLUSIONS

This work has presented a novel multiscale implicit-atomistic approach (ω FQF μ -BEM) to investigate the plasmonic response of metal NPs. ω FQF μ -BEM combines a spherical implicit continuum core embedded within an atomistically defined shell, preserving the essential plasmonic response at the NP surface. The method is theoretically constructed by integrating the fully atomistic ω FQF μ and implicit BEM methodologies for plasmonics and constitutes the first attempt to merge atomistic and continuum descriptions for the study of plasmonic substrates in the context of classical electrodynamics. To validate the ω FQF μ -BEM model, we have initially demonstrated its capacity to reproduce the absorption cross section of spherical Ag nanoparticles, taking the fully atomistic ω FQF μ method as a reference. In particular, we have presented a comprehensive analysis of the different factors influencing ω FQF μ -BEM response: the thickness of the atomistic shell, BEM- ω FQF μ distance, BEM dielectric function, and discretization of the continuum core. Our in-depth analysis suggests that the best results at the implicit continuum-atomistic ω FQF μ -BEM level for Ag NPs are obtained by setting the BEM- ω FQF μ distance to twice the nearest neighbor distance and using the Brendel-Bormann dielectric function while keeping the outer shells described atomistically.

The coupling of ω FQF μ -BEM to a QM region has been presented, giving rise to the QM/ ω FQF μ -BEM approach, which is able to describe molecular plasmonics, i.e., how plasmons affect the

molecular electronic structure and the resulting spectral signals. To showcase the potentialities of the method, QM/ ω FQF μ -BEM has been challenged to reproduce the SERS response of pyridine adsorbed on the tip of Ag Ih NPs. The quality of the method has been assessed by an in-depth comparison with fully atomistic QM/ ω FQF μ (reference) and fully implicit QM/BEM spectra. Our results show that, while QM/BEM outcomes strongly differ, QM/ ω FQF μ -BEM can reproduce QM/ ω FQF μ SERS spectra, specifically for the largest NP sizes. More in detail, an almost perfect agreement of normalized Raman intensities for the largest system is observed, along with a similar qualitative and quantitative outcome for AEF and MEF descriptors with increasing NP radius. As a result of this work, two main points may be highlighted: (i) an implicit description of the NP structure yields substantial discrepancies in simulated SERS spectra as compared to an atomistic description and should be generally avoided; and (ii) it is crucial to describe at a full atomistic level the NP surface, while the core can be safely treated by an implicit description. Finally, the enhanced computational efficiency observed for the largest QM/ ω FQF μ -BEM structures yields a computational saving of more than half compared to QM/ ω FQF μ . Therefore, large, complex-shaped systems can be afforded. This originates from a substantial reduction of the computational effort required to solve the linear system in Eq. (14), whose dimension is strongly reduced by replacing the core atoms with a continuum description. In addition, memory-related issues are mitigated. To end the presentation, it is worth mentioning that both BEM and ω FQF μ models are formulated in the quasistatic regime, i.e., retardation effects are discarded. Therefore, they appropriately treat systems of dimension significantly smaller than that of the incident wavelength. In addition, in ω FQF μ -BEM, the ω FQF μ and BEM layers interact via electrostatic forces, i.e., charge transfer is inhibited. The above two limitations of the approach will deserve careful investigation in future communications.

SUPPLEMENTARY MATERIAL

See the [supplementary material](#) for details on ω FQF μ -BEM equations. Geometrical parameters, PRFs, ρ^{error} , and computational speed-ups. Defined volume for ρ^{error} calculations. Further results on classical and QM/classical responses as a function of core-to-shell distance, dielectric function, and BEM core discretization for spherical and Ih core-shell systems. Graphical representation of pyridine's normal modes.

ACKNOWLEDGMENTS

The authors acknowledge Professor Stefano Corni (University of Padova) for the fruitful discussions. We gratefully acknowledge the Center for High-Performance Computing (CHPC) at SNS for providing the computational infrastructure. This work has received funding from the European Research Council (ERC) under the European Union's Horizon 2020 research and innovation program (Grant Agreement No. 818064).

AUTHOR DECLARATIONS

Conflict of Interest

The authors have no conflicts to disclose.

Author Contributions

Pablo Grobas Illobre: Data curation (lead); Formal analysis (lead); Investigation (lead); Methodology (equal); Software (lead); Validation (lead); Visualization (lead); Writing – original draft (lead).
Piero Lafiosca: Software (supporting). **Luca Bonatti:** Methodology (equal); Software (supporting). **Tommaso Giovannini:** Conceptualization (equal); Formal analysis (equal); Investigation (equal); Methodology (equal); Writing – original draft (equal); Writing – review & editing (equal). **Chiara Cappelli:** Conceptualization (equal); Funding acquisition (lead); Project administration (lead); Resources (lead); Supervision (lead); Writing – review & editing (equal).

DATA AVAILABILITY

The data that support the findings of this study are available from the corresponding author upon reasonable request.

REFERENCES

- ¹V. Giannini, A. I. Fernández-Domínguez, S. C. Heck, and S. A. Maier, *Chem. Rev.* **111**, 3888 (2011).
- ²S. A. Maier, *Plasmonics: Fundamentals and Applications* (Springer Science & Business Media, 2007).
- ³T. W. Odom and G. C. Schatz, “Introduction to plasmonics,” *Chem. Rev.* **111**, 3667 (2011).
- ⁴K. L. Kelly, E. Coronado, L. L. Zhao, and G. C. Schatz, “The optical properties of metal nanoparticles: The influence of size, shape, and dielectric environment,” *J. Phys. Chem. B* **107**, 668 (2003).
- ⁵E. Coccia, J. Fregoni, C. Guido, M. Marsili, S. Pipolo, and S. Corni, *J. Chem. Phys.* **153**, 200901 (2020).
- ⁶K. A. Willets and R. P. Van Duyne, *Annu. Rev. Phys. Chem.* **58**, 267 (2007).
- ⁷R. Zhang, Y. Zhang, Z. Dong, S. Jiang, C. Zhang, L. Chen, L. Zhang, Y. Liao, J. Aizpurua, Y. e. Luo *et al.*, *Nature* **498**, 82 (2013).
- ⁸S. Jiang, Y. Zhang, R. Zhang, C. Hu, M. Liao, Y. Luo, J. Yang, Z. Dong, and J. Hou, *Nat. Nanotechnol.* **10**, 865 (2015).
- ⁹N. Chiang, X. Chen, G. Goubert, D. V. Chulhai, X. Chen, E. A. Pozzi, N. Jiang, M. C. Hersam, T. Seideman, L. Jensen, and R. P. Van Duyne, *Nano Lett.* **16**, 7774 (2016).
- ¹⁰J. Langer, D. Jimenez de Aberasturi, J. Aizpurua, R. A. Alvarez-Puebla, B. Augué, J. J. Baumberg, G. C. Bazan, S. E. Bell, A. Boisen, A. G. Brolo *et al.*, *ACS Nano* **14**, 28 (2019).
- ¹¹P. Lafiosca, L. Nicoli, L. Bonatti, T. Giovannini, S. Corni, and C. Cappelli, *J. Chem. Theory Comput.* **19**, 3616 (2023).
- ¹²L. Zhao, L. Jensen, and G. C. Schatz, *J. Am. Chem. Soc.* **128**, 2911 (2006).
- ¹³L. Jensen, C. M. Aikens, and G. C. Schatz, *Chem. Soc. Rev.* **37**, 1061 (2008).
- ¹⁴S. M. Morton and L. Jensen, *J. Am. Chem. Soc.* **131**, 4090 (2009).
- ¹⁵S. M. Morton, D. W. Silverstein, and L. Jensen, *Chem. Rev.* **111**, 3962 (2011).
- ¹⁶A. Sanchez-Gonzalez, S. Corni, and B. Mennucci, *J. Phys. Chem. C* **115**, 5450 (2011).
- ¹⁷S. M. Morton and L. Jensen, *J. Chem. Phys.* **133**, 074103 (2010).
- ¹⁸S. M. Morton and L. Jensen, *J. Chem. Phys.* **135**, 134103 (2011).
- ¹⁹G. Mie, *Ann. Phys.* **330**, 377 (1908).
- ²⁰A. Tafove, S. C. Hagness, and M. Piket-May, *Computational Electromagnetism: The Finite-Difference Time-Domain Method* (Elsevier, Amsterdam, The Netherlands, 2005).
- ²¹F. J. García de Abajo and A. Howie, *Phys. Rev. B* **65**, 115418 (2002).
- ²²V. Myroshnychenko, E. Carbó-Argibay, I. Pastoriza-Santos, J. Pérez-Juste, L. M. Liz-Marzán, and F. J. García de Abajo, *Adv. Mater.* **20**, 4288 (2008).
- ²³B. Mennucci and S. Corni, *Nat. Rev. Chem.* **3**, 315 (2019).
- ²⁴L. Bonatti, G. Gil, T. Giovannini, S. Corni, and C. Cappelli, *Front. Chem.* **8**, 340 (2020).
- ²⁵L. L. Jensen and L. Jensen, *J. Phys. Chem. C* **112**, 15697 (2008).
- ²⁶L. L. Jensen and L. Jensen, *J. Phys. Chem. C* **113**, 15182 (2009).
- ²⁷V. I. Zakomirnyi, Z. Rinkevicius, G. V. Baryshnikov, L. K. Sørensen, and H. Ågren, *J. Phys. Chem. C* **123**, 28867 (2019).
- ²⁸V. I. Zakomirnyi, I. L. Rasskazov, L. K. Sørensen, P. S. Carney, Z. Rinkevicius, and H. Ågren, *Phys. Chem. Chem. Phys.* **22**, 13467 (2020).
- ²⁹J. L. Payton, S. M. Morton, J. E. Moore, and L. Jensen, *J. Chem. Phys.* **136**, 214103 (2012).
- ³⁰Z. Pei, Y. Mao, Y. Shao, and W. Liang, *J. Chem. Phys.* **157**, 164110 (2022).
- ³¹T. Giovannini, M. Rosa, S. Corni, and C. Cappelli, *Nanoscale* **11**, 6004 (2019).
- ³²T. Giovannini, L. Bonatti, M. Polini, and C. Cappelli, *J. Phys. Chem. Lett.* **11**, 7595 (2020).
- ³³P. Lafiosca, T. Giovannini, M. Benzi, and C. Cappelli, *J. Phys. Chem. C* **125**, 23848 (2021).
- ³⁴L. Bonatti, L. Nicoli, T. Giovannini, and C. Cappelli, *Nanoscale Adv.* **4**, 2294 (2022).
- ³⁵T. Giovannini, L. Bonatti, P. Lafiosca, L. Nicoli, M. Castagnola, P. G. Illobre, S. Corni, and C. Cappelli, *ACS Photonics* **9**, 3025 (2022).
- ³⁶S. Zanotto, L. Bonatti, M. F. Pantano, V. Mišekis, G. Speranza, T. Giovannini, C. Coletti, C. Cappelli, A. Tredicucci, and A. Toncelli, *ACS Photonics* **10**, 394 (2023).
- ³⁷L. Nicoli, P. Lafiosca, P. Grobas Illobre, L. Bonatti, T. Giovannini, and C. Cappelli, *Front. Photonics* **4**, 1199598 (2023).
- ³⁸P. Lafiosca, L. Nicoli, S. Pipolo, S. Corni, T. Giovannini, and C. Cappelli, *J. Phys. Chem. C* **128**, 17513 (2024).
- ³⁹L. Nicoli, S. Sodamico, P. Lafiosca, T. Giovannini, and C. Cappelli, *ACS Phys. Chem. Au* **4**, 669 (2024).
- ⁴⁰S. Corni and J. Tomasi, *J. Chem. Phys.* **114**, 3739 (2001).
- ⁴¹S. Corni and J. Tomasi, *Chem. Phys. Lett.* **342**, 135 (2001).
- ⁴²S. Corni and J. Tomasi, *J. Chem. Phys.* **116**, 1156 (2002).
- ⁴³S. Corni and J. Tomasi, *Chem. Phys. Lett.* **365**, 552 (2002).
- ⁴⁴S. Corni and J. Tomasi, *Surface-Enhanced Raman Scattering* (Springer, 2006), pp. 105–123.
- ⁴⁵M. Romanelli, G. Dall’Osto, and S. Corni, *J. Chem. Phys.* **155**, 214304 (2021).
- ⁴⁶C. V. Coane, M. Romanelli, G. Dall’Osto, R. Di Felice, and S. Corni, *Commun. Chem.* **7**, 32 (2024).
- ⁴⁷U. Hohenester and A. Trügler, *Comput. Phys. Commun.* **183**, 370 (2012).
- ⁴⁸M. E. Casida, *Recent Advances in Density Functional Methods: (Part I)* (World Scientific, 1995), pp. 155–192.
- ⁴⁹M. G. Albrecht and J. A. Creighton, *J. Am. Chem. Soc.* **99**, 5215 (1977).
- ⁵⁰D. L. Jeanmaire and R. P. Van Duyne, *J. Electroanal. Chem. Interfacial Electrochem.* **84**, 1 (1977).
- ⁵¹A. Campion and P. Kambhampati, *Chem. Soc. Rev.* **27**, 241 (1998).
- ⁵²C. E. Talley, J. B. Jackson, C. Oubre, N. K. Grady, C. W. Hollars, S. M. Lane, T. R. Huser, P. J. Nordlander, and N. J. Halas, *Nano Lett.* **5**(8), 1569 (2005).
- ⁵³R. Alvarez-Puebla, L. M. Liz-Marzán, and F. J. García de Abajo, *J. Phys. Chem. Lett.* **1**, 2428 (2010).
- ⁵⁴E. Le Ru and P. Etchegoin, *Principles of Surface-Enhanced Raman Spectroscopy: And Related Plasmonic Effects* (Elsevier, 2008).
- ⁵⁵B. Sharma, R. R. Frontiera, A.-I. Henry, E. Ringe, and R. P. Van Duyne, *Mater. Today* **15**, 16 (2012).
- ⁵⁶X. X. Han, R. S. Rodriguez, C. L. Haynes, Y. Ozaki, and B. Zhao, *Nat. Rev. Methods Primers* **1**, 87 (2022).
- ⁵⁷J. T. Golab, J. R. Sprague, K. T. Carron, G. C. Schatz, and R. P. Van Duyne, *J. Chem. Phys.* **88**, 7942 (1988).
- ⁵⁸H. Lai, F. Xu, Y. Zhang, and L. Wang, *J. Mater. Chem. B* **6**, 4008 (2018).
- ⁵⁹H. Zhang, S. Duan, P. M. Radjenovic, Z.-Q. Tian, and J.-F. Li, *Acc. Chem. Res.* **53**, 729 (2020).
- ⁶⁰H.-S. Su, H.-S. Feng, X. Wu, J.-J. Sun, and B. Ren, *Nanoscale* **13**(33), 13962 (2021).
- ⁶¹X. Zhao, S. Campbell, G. Q. Wallace, A. Claing, C. G. Bazuin, and J.-F. Masson, *ACS Sens.* **5**, 2155 (2020).

- ⁶²L. Fang, X.-T. Pan, K. Liu, D. Jiang, D. Ye, L.-N. Ji, K. Wang, and X. Xia, *ACS Appl. Mater. Interfaces* **15**, 20677 (2023).
- ⁶³L. Troncoso-Afonso, G. A. Vinnacombe-Willson, C. García-Astrain, and L. M. Liz-Marzán, *Chem. Soc. Rev.* **53**, 5118 (2024).
- ⁶⁴J. Perumal, Y. Wang, A. B. E. Attia, U. S. Dinish, and M. Olivo, *Nanoscale* **13**, 553 (2021).
- ⁶⁵R. Taheri-Ledari, F. Ganjali, S. Zarei-Shokat, R. Dimmohammadi, F. R. Asl, A. Emami, Z. Mojtabapour, Z. Rashvandi, A. Kashtiaray, F. Jalali, and A. Maleki, *Nanoscale Adv.* **5**, 6768 (2023).
- ⁶⁶A. Pinchuk, G. v. Plessen, and U. Kreibig, *J. Phys. D: Appl. Phys.* **37**, 3133 (2004).
- ⁶⁷A. Pinchuk, U. Kreibig, and A. Hilger, *Surf. Sci.* **557**, 269 (2004).
- ⁶⁸B. Balamurugan and T. Maruyama, *Appl. Phys. Lett.* **87**, 143105 (2005).
- ⁶⁹T. Giovannini, A. Puglisi, M. Ambrosetti, and C. Cappelli, *J. Chem. Theory Comput.* **15**, 2233 (2019).
- ⁷⁰A. Mayer, *Phys. Rev. B* **75**, 045407 (2007).
- ⁷¹R. Fuchs, *Phys. Rev. B* **11**, 1732 (1975).
- ⁷²J. Tomasi, B. Mennucci, and R. Cammi, *Chem. Rev.* **105**, 2999 (2005).
- ⁷³S. Vukovic, S. Corni, and B. Mennucci, *J. Phys. Chem. C* **113**, 121 (2009).
- ⁷⁴P. Grobas Illobre, P. Lafiosca, T. Guidone, F. Mazza, T. Giovannini, and C. Cappelli, *Nanoscale Adv.* **6**, 3410 (2024).
- ⁷⁵T. Helgaker, P. Jørgensen, and J. Olsen, “Molecular integral evaluation,” in *Molecular Electronic-Structure Theory* (John Wiley & Sons, Ltd., 2000), Chap. 9, pp. 336–432.
- ⁷⁶A. Warshel and M. Levitt, *J. Mol. Biol.* **103**, 227 (1976).
- ⁷⁷H. Lin and D. G. Truhlar, *Theor. Chem. Acc.* **117**, 185 (2007).
- ⁷⁸H. M. Senn and W. Thiel, *Angew. Chem., Int. Ed.* **48**, 1198 (2009).
- ⁷⁹C. A. Guido, M. Rosa, R. Cammi, and S. Corni, *J. Chem. Phys.* **152**, 174114 (2020).
- ⁸⁰S. Corni, S. Pipolo, and R. Cammi, *J. Phys. Chem. A* **119**, 5405 (2015).
- ⁸¹E. Baerends *et al.*, ADF (version 2020.x), Theoretical Chemistry, Vrije Universiteit, Amsterdam, The Netherlands, 2020, <http://www.scm.com>.
- ⁸²L. Nicoli, T. Giovannini, and C. Cappelli, *J. Chem. Phys.* **157**, 214101 (2022).
- ⁸³P. Norman, K. Ruud, and T. Saue, *Principles and Practices of Molecular Properties: Theory, Modeling, and Simulations* (John Wiley & Sons, 2018).
- ⁸⁴T. Giovannini, F. Egidi, and C. Cappelli, *Phys. Chem. Chem. Phys.* **22**, 22864 (2020).
- ⁸⁵L. Jensen, J. Autschbach, and G. C. Schatz, *J. Chem. Phys.* **122**, 224115 (2005).
- ⁸⁶J. L. Payton, S. M. Morton, J. E. Moore, and L. Jensen, *Acc. Chem. Res.* **47**, 88 (2014).
- ⁸⁷G. Placzek, in *Handbuch der Radiologie*, edited by G. Marx (Akademische Verlagsgesellschaft, Leipzig, 1934).
- ⁸⁸G. Placzek and E. Teller, *Z. Phys.* **81**, 209 (1933).
- ⁸⁹L. Jensen, L. Zhao, J. Autschbach, and G. Schatz, *J. Chem. Phys.* **123**, 174110 (2005).
- ⁹⁰A. H. Larsen, J. J. Mortensen, J. Blomqvist, I. E. Castelli, R. Christensen, M. Dulak, J. Friis, M. N. Groves, B. Hammer, C. Hargus, E. D. Hermès, P. C. Jennings, P. B. Jensen, J. Kermode, J. R. Kitchin, E. L. Kolsbjerg, J. Kubal, K. Kaasbjerg, S. Lysgaard, J. B. Maronsson, T. Maxson, T. Olsen, L. Pastewka, A. Peterson, C. Rosengaard, J. Schiøtz, O. Schütt, M. Strange, K. S. Thygesen, T. Vegge, L. Vilhelmsen, M. Walter, Z. Zeng, and K. W. Jacobsen, *J. Phys.: Condens. Matter* **29**, 273002 (2017).
- ⁹¹C. Geuzaine and J.-F. Remacle, *Int. J. Numer. Methods Eng.* **79**, 1309 (2009).
- ⁹²E. D. Palik, *Handbook of Optical Constants of Solids* (Elsevier, 1997).
- ⁹³A. D. Rakić, A. B. Djurišić, J. M. Elazar, and M. L. Majewski, *Appl. Opt.* **37**, 5271 (1998).
- ⁹⁴P. B. Johnson and R.-W. Christy, *Phys. Rev. B* **6**, 4370 (1972).
- ⁹⁵S. Van Gisbergen, J. Snijders, and E. Baerends, *J. Chem. Phys.* **103**, 9347 (1995).
- ⁹⁶S. Van Gisbergen, J. Snijders, and E. Baerends, *Comput. Phys. Commun.* **118**, 119 (1999).
- ⁹⁷L. Fan and T. Ziegler, *J. Chem. Phys.* **96**, 9005 (1992).
- ⁹⁸L. Fan and T. Ziegler, *J. Phys. Chem.* **96**, 6937 (1992).
- ⁹⁹S. Van Gisbergen, J. Snijders, and E. Baerends, *Chem. Phys. Lett.* **259**, 599 (1996).
- ¹⁰⁰T.-H. Park and P. Nordlander, *Chem. Phys. Lett.* **472**, 228 (2009).
- ¹⁰¹R. Bardhan, S. Mukherjee, N. A. Mirin, S. D. Levit, P. Nordlander, and N. J. Halas, *J. Phys. Chem. C* **114**, 7378 (2010).
- ¹⁰²N. J. Halas, S. Lal, W.-S. Chang, S. Link, and P. Nordlander, *Chem. Rev.* **111**, 3913 (2011).
- ¹⁰³E. Prodan, C. Radloff, N. J. Halas, and P. Nordlander, *Science* **302**, 419 (2003).
- ¹⁰⁴P. Nordlander, C. Oubre, E. Prodan, K. Li, and M. I. Stockman, *Nano Lett.* **4**, 899 (2004).
- ¹⁰⁵V. Kulkarni, E. Prodan, and P. Nordlander, *Nano Lett.* **13**, 5873 (2013).
- ¹⁰⁶D.-C. Marinica, J. Aizpurua, and A. G. Borisov, *Opt. Express* **24**, 23941 (2016).
- ¹⁰⁷B. T. Thole, *Chem. Phys.* **59**, 341 (1981).

Chapter 5

Summary, conclusions, and future perspectives

During my Ph.D., I focused on developing classical methodologies to efficiently model the optical response of metal NPs, with a particular emphasis on capturing the atomistic details influencing their plasmonic properties. My work began in the context of the ω FQ model, which was originally proposed to evaluate the plasmonic features of sodium NPs,^{90,92} and later extended to the study of graphene-based systems.^{26,61,91,95} However, ω FQ is restricted to the description of intraband transitions contributing to the optical response, as it exclusively relies on the Drude model to account for charge redistribution between atoms. To overcome this limitation, in [Paper I] we developed the ω FQF μ model, expanding the ω FQ approach by incorporating the description of interband contributions for Ag and Au systems. Initially, these models were applied to analyze homogeneous metallic systems. Then, in [Paper II] we generalized the ω FQF μ framework to model the plasmonic behavior of any type of metal alloy, successfully validating this approach through the investigation of bimetallic Ag-Au NPs.

In addition, my research explored the modeling of surface-enhanced molecular properties through the development of multiscale QM/Classical methodologies. In [Paper III], we introduced a QM/ ω FQF μ formalism to evaluate Surface-enhanced fluorescence of chromophores positioned near metallic surfaces, revealing how subtle atomistic variations can profoundly impact fluorescence signals. Next, in [Paper IV] we developed the ω FQF μ -BEM model, which offers a mixed atomistic-implicit representation of metals. In this framework, metal NPs are modeled as an implicit BEM core integrated within an atomistic ω FQF μ shell. We also proposed a QM/ ω FQF μ -BEM coupling to efficiently investigate the SERS spectra of molecules physisorbed onto metallic NPs. This approach allowed us to capture the atomistic details that shape localized surface plasmons affecting the SERS response, while significantly improving the computational efficiency of our simulations.

The methodologies presented in this dissertation lay the foundation for future theoretical developments. In particular, the protocols described in [Paper I] and [Paper II] establish the basis for additional ω FQ(F μ) parametrizations to model the optical

response of metallic systems beyond Na, Ag, and Au, as well as their potential alloys. Moreover, the QM/Classical methodologies proposed in [Paper III] and [Paper IV] can be extended to evaluate additional surface-enhanced phenomena. Some examples include Surface-Enhanced Raman Optical Activity (SEROA),^{162–164} Surface-Enhanced Infrared Absorption (SEIRA),^{170,200,201} and Plasmon-Mediated Electronic Energy Transfer.^{9,29,62,158,159}

Finally, the improved computational performance of the models developed in this thesis paves the way for more extensive comparisons with realistic, large-scale problems. Specifically, applying our formalisms to the analysis of experimental data would significantly facilitate the interpretation of the results, while also enabling the *in silico* design of novel experiments. Notably, the QM/ ω FQF μ -BEM approach shows great potential for modeling tip-enhanced spectroscopies.^{9,29,41,43,158,159,195,202} In this context, tip-enhanced properties can be effectively investigated by positioning a QM molecule between an atomistically defined ω FQF μ tip and an implicit BEM plate. This hybrid setup would effectively address the difficulties associated with tip-base theoretical studies through purely implicit simulations, which often require *ad-hoc* refinements to solve modeling issues.^{60,62} Our mixed atomistic-implicit framework would overcome these challenges, providing an excellent balance between chemical accuracy and computational efficiency.

Acknowledgments

Starting a Ph.D. in the middle of a global pandemic, what could go wrong? As it turns out, quite a bit! These past four years have been anything but ordinary. It's been a rollercoaster of challenges, uncertainties, and doubts, but also one filled with achievements, important lessons, and personal growth. The day-to-day obstacles of such a journey are often daunting, as any Ph.D. student would agree. Yet, I've been fortunate to meet fellow travelers who made the road smoother during the toughest moments. This section is dedicated to all of you.

First of all, I would like to express my sincere gratitude to my supervisors, Prof. Chiara Cappelli and Dr. Tommaso Giovannini. Their guidance, both scientific and personal, has been a cornerstone of my Ph.D.. They not only provided support and expertise that allowed me to contribute to existing research lines but also gave me the freedom to explore my own ideas, a privilege I truly value.

I would also like to extend my gratitude to all my co-authors and colleagues from the EmbedLab group. I am particularly grateful to the ω -room members: Luca N., Piero, and Luca B., with whom I shared an office and collaborated for most of my Ph.D.. I also wish to thank other group members who accompanied me during this period: Frank, Chiara, Sulejman (and his wife Emina), Matteo, Sveva, and Sara. A special thanks to Sara for her personal advice during our many coffee break conversations. Additionally, I wish the best to the newcomers to the group and other members I overlapped with briefly: Marco, Francesco, Giovanni, Pietro, Emanuele, and Gioia.

Beyond my academic circle, I thank my entire family for their constant support throughout these years. I am especially grateful to my Mom, Dad, and Grandparents for their encouragement and care. I would also like to extend my gratitude to my friends from A Coruña. Though we usually meet only during my summer and Christmas visits, I deeply value the moments shared with David, Emilio, Lois, Jochy, Carla, and Nerea, and with my Bachelor's friends from "Cenas Química." Additionally, I would like to thank my Spanish-speaking friends in Pisa from the "Se habla Español" group, as well as my other Italian and international fellows, for their companionship and support.

My final words are dedicated to **Eva**, my girlfriend and life partner. Being by your side during these years has given me strength I didn't even know I needed, while helping me become a better person each day. For this and so much more, I want to finish this journey with a promise: to continue growing and improving together. We started our story five years ago, and I look forward to all the chapters yet to come.

Agradecementos

Comezar un Ph.D. no medio dunha pandemia mundial, que podería saír mal? Resulta que bastante! Estes últimos catro anos foron calquera cousa menos ordinarios. Foi unha montaña rusa de retos, incertezas e dúbidas, pero tamén unha chea de logros, leccións importantes e crecemento persoal. Os obstáculos do día a día nesta viaxe adoitan ser esgotadores, como calquera doutorando admitiría. Con todo, tiven a sorte de atopar compañeiros de viaxe que fixeron o camiño máis levadeiro nos momentos máis duros. Esta sección está dedicada a todos vós.

Gustaríaime empezar expresando a miña sincera gratitud aos meus supervisores, a Prof. Chiara Cappelli e o Dr. Tommaso Giovannini. A súa orientación, científica e persoal, foi fundamental durante o meu Ph.D.. Non só me proporcionaron apoio e experiencia para contribuír ás liñas de investigación existentes, senón que tamén me deron a liberdade de explorar as miñas propias ideas, un privilexio que aprecio profundamente.

Tamén quero expresar a miña gratitud a todos os meus coautores e colegas do grupo EmbedLab. En especial, aos membros da ω -room: Luca N., Piero e Luca B., cos que compartín oficina e colaborei durante boa parte do meu Ph.D.. Ademáis, quero dar as grazas aos outros membros do grupo que me acompañaron: Frank, Chiara, Sulejman (e a súa esposa Emina), Matteo, Sveva e Sara. Un especial agradecemento a Sara polos seus consellos persoais nas pausas do café. Por último, deséolle o mellor aos recén chegados e cos que só coincidín brevemente: Marco, Francesco, Giovanni, Pietro, Emanuele e Gioia.

Máis alá do meu círculo académico, quero dar as grazas á miña familia polo seu apoio constante durante estes anos. Estou especialmente agradecido á miña nai, ao meu pai e aos meus avós polos seus ánimos e coidados. Tamén quero expresar a miña gratitud aos meus amigos de A Coruña. Aínda que só nos vemos nas miñas visitas de verán e Nadal, valoro profundamente os momentos compartidos con David, Emilio, Lois, Jochy, Carla e Nerea, e cos meus amigos da carreira de “Cenas Química.” Ademáis, quero dar as grazas aos meus amigos hispanofalantes en Pisa do grupo “Se habla Español,” así como aos meus outros compañeiros italianos e internacionais, pola súa compañía e apoio.

As miñas palabras finais están dedicadas a **Eva**, a miña moza e compañeira de vida. Estar ao teu carón durante estes anos deume unha之力 que nin sequera eu sabía que necesitaba, mentres me axudabas a ser mellor persoa cada día. Por isto e por moito máis, quero rematar esta etapa cunha promesa: continuar medrando e mellorando xuntos. Comezamos a nosa historia hai cinco anos, e espero con ansia todos os capítulos que nos quedan por escribir.

Bibliography

- [1] Maier, S. A. *Plasmonics: fundamentals and applications.* Springer Science & Business Media, **2007**.
- [2] Novotny, L. and Hecht, B. *Principles of Nano-Optics.* Cambridge University Press, 2 edition, **2012**.
- [3] Pelton, M. and Bryant, G. W. *Introduction to metal-nanoparticle plasmonics,* volume 5. John Wiley & Sons, **2013**.
- [4] Trügler, A. *Optical Properties of Metallic Nanoparticles.* Springer International Publishing, **2016**.
- [5] Moskovits, M. *J. Chem. Phys.*, 69(9):4159–4161, **11 1978**. ISSN 0021-9606.
- [6] Anker, J. N., Hall, W. P., Lyandres, O., Shah, N. C., Zhao, J. and Van Duyne, R. P. *Nat. Mater.*, 7(6):442–453, **Jun 2008**. ISSN 1476-4660.
- [7] de Aberasturi, D. J., Serrano-Montes, A. B. and Liz-Marzán, L. M. *Adv. Opt. Mater.*, 3(5):602–617, **2015**.
- [8] Kim, M. J., Jung, D. H., Lee, C. Y., Hong, S., Heo, J. H. and Lee, J. H. *Small Struct.*, 4(9):2300047, **2023**.
- [9] Hang, Y., Wang, A. and Wu, N. *Chem. Soc. Rev.*, 53:2932–2971, **2024**.
- [10] Huang, J., Zhu, Y., Liu, C., Zhao, Y., Liu, Z., Hedhili, M. N., Fratalocchi, A. and Han, Y. *Small*, 11(39):5214–5221, **2015**.
- [11] Gong, C. and Leite, M. S. *ACS Photonics*, 3(4):507–513, **2016**.
- [12] Cao, M., Liu, Q., Chen, M., Chen, L., Yang, D., Hu, H., He, L., Zhang, G. and Zhang, Q. *ACS Omega*, 3(12):18623–18629, **2018**.
- [13] Ma, J., Liu, X., Wang, R., Zhang, J., Jiang, P., Wang, Y. and Tu, G. *ACS Appl. Nano Mater.*, 3(11):10885–10894, **2020**.
- [14] Awada, C., Dab, C., Grimaldi, M. G., Alshoaibi, A. and Ruffino, F. *Sci. Rep.*, 11(1):4714, **Feb 2021**.

-
- [15] Ju, L., Geng, B., Horng, J., Girit, C., Martin, M., Hao, Z., Bechtel, H. A., Liang, X., Zettl, A., Shen, Y. R. and Wang, F. *Nat. Nanotechnol.*, 6(10):630–634, **Oct 2011**. ISSN 1748-3395.
- [16] Grigorenko, A. N., Polini, M. and Novoselov, K. S. *Nat. Photon.*, 6:749 – 758, **2012**.
- [17] Low, T. and Avouris, P. *ACS Nano*, 8 2:1086–101, **2014**.
- [18] García de Abajo, F. J. *ACS Photonics*, 1(3):135–152, **2014**.
- [19] Cox, J. D., Silveiro, I. and García de Abajo, F. J. *ACS Nano*, 10(2):1995–2003, **2016**.
- [20] Ni, G. X., McLeod, A. S., Sun, Z., Wang, L., Xiong, L., Post, K. W., Sunku, S. S., Jiang, B.-Y., Hone, J., Dean, C. R., Fogler, M. M. and Basov, D. N. *Nature*, 557(7706):530–533, **May 2018**.
- [21] Wang, Y., Ou, J. Z., Chrimes, A. F., Carey, B. J., Daeneke, T., Alsaif, M. M. Y. A., Mortazavi, M., Zhuiykov, S., Medhekar, N., Bhaskaran, M., Friend, J. R., Strano, M. S. and Kalantar-Zadeh, K. *Nano Lett.*, 15(2):883–890, **2015**.
- [22] Krasnok, A., Lepeshov, S. and Alú, A. *Opt. Express*, 26(12):15972–15994, **Jun 2018**.
- [23] Hu, Y., Zhang, B. Y., Haque, F., Ren, G. and Ou, J. Z. *Mater. Horiz.*, 9:2288–2324, **2022**.
- [24] Santiago, E. Y., Besteiro, L. V., Kong, X.-T., Correa-Duarte, M. A., Wang, Z. and Govorov, A. O. *ACS Photonics*, 7(10):2807–2824, **2020**.
- [25] Wy, Y., Jung, H., Hong, J. W. and Han, S. W. *Acc. Chem. Res.*, 55(6):831–843, **2022**.
- [26] Bonatti, L., Nicoli, L., Giovannini, T. and Cappelli, C. *Nanoscale Adv.*, 4(10):2294–2302, **2022**.
- [27] Urbieto, M., Barbry, M., Zhang, Y., Koval, P., Sánchez-Portal, D., Zabala, N. and Aizpurua, J. *ACS Nano*, 12(1):585–595, **2018**.
- [28] Rosławska, A., Neuman, T. c. v., Doppagne, B., Borisov, A. G., Romeo, M., Scheurer, F., Aizpurua, J. and Schull, G. *Phys. Rev. X*, 12:011012, **Jan 2022**.
- [29] Hung, T.-C., Godinez-Loyola, Y., Steinbrecher, M., Kiraly, B., Khajetoorians, A. A., Doltsinis, N. L., Strassert, C. A. and Wegner, D. *J. Am. Chem. Soc.*, 146(13):8858–8864, **2024**.
- [30] Ding, S.-Y., You, E.-M., Tian, Z.-Q. and Moskovits, M. *Chem. Soc. Rev.*, 46(13):4042–4076, **2017**.

-
- [31] Langer, J., Jimenez de Aberasturi, D., Aizpurua, J., Alvarez-Puebla, R. A., Au-guié, B., Baumberg, J. J., Bazan, G. C., Bell, S. E., Boisen, A., Brolo, A. G. *et al.* *ACS Nano*, 14(1):28–117, **2019**.
- [32] Kelly, K. L., Coronado, E., Zhao, L. L. and Schatz, G. C. *The Journal of Physical Chemistry B*, 107(3):668–677, **2003**.
- [33] Liz-Marzán, L. M. *Langmuir*, 22(1):32–41, **2006**.
- [34] Sharifi, M., Attar, F., Saboury, A. A., Akhtari, K., Hooshmand, N., Hasan, A., El-Sayed, M. A. and Falahati, M. *J. Control. Release*, 311-312:170–189, **2019**. ISSN 0168-3659.
- [35] Lal, S., Grady, N. K., Kundu, J., Levin, C. S., Lassiter, J. B., Halas, N. J. and Halas, N. J. *Chem. Soc. Rev.*, 37 5:898–911, **2008**.
- [36] Xu, J., Zhang, Y.-J., Yin, H., Zhong, H.-L., Su, M., Tian, Z.-Q. and Li, J.-F. *Adv. Opt. Mater.*, 6(4):1701069, **2018**.
- [37] Lai, H., Xu, F., Zhang, Y. and Wang, L. *J. Mater. Chem. B*, 6(24):4008–4028, **2018**.
- [38] Yaraki, M. T. and Tan, Y. N. *Chem. Asian J.*, 15(20):3180–3208, **2020**.
- [39] Chiang, N., Jiang, N., Chulhai, D. V., Pozzi, E. A., Hersam, M. C., Jensen, L., Seideman, T. and Van Duyne, R. P. *Nano Lett.*, 15(6):4114–4120, **2015**.
- [40] Verma, P. *Chem. Rev.*, 117(9):6447–6466, **2017**.
- [41] Lee, H., Lee, D. Y., Kang, M. G., Koo, Y., Kim, T. and Park, K.-D. *Nanophotonics*, 9(10):3089–3110, **2020**.
- [42] Rosławska, A., Kaiser, K., Romeo, M., Devaux, E., Scheurer, F., Berciaud, S., Neuman, T. and Schull, G. *Nat. Nanotechnol.*, 19(6):738–743, **Jun 2024**. ISSN 1748-3395.
- [43] Höppener, C., Aizpurua, J., Chen, H., Gräfe, S., Jorio, A., Kupfer, S., Zhang, Z. and Deckert, V. *Nat. Rev. Methods Primers*, 4(1):47, **Jul 2024**. ISSN 2662-8449.
- [44] Angioni, A., Corni, S. and Mennucci, B. *Phys. Chem. Chem. Phys.*, 15:3294–3303, **2013**.
- [45] Reineck, P., Gómez, D., Ng, S. H., Karg, M., Bell, T., Mulvaney, P. and Bach, U. *ACS Nano*, 7(8):6636–6648, **2013**.
- [46] Fu, B., Flynn, J. D., Isaacoff, B. P., Rowland, D. J. and Biteen, J. S. *J. Phys. Chem. C*, 119(33):19350–19358, **2015**.
- [47] Wang, H., Pu, Y., Shan, B. and Li, M. *Inorg. Chem.*, 58(18):12457–12466, **2019**.

-
- [48] Trinh, Q. T., Van, T. L., Phan, T. T. N., Ong, K. P., Kosslick, H., Amaniampong, P. N., Sullivan, M. B., Chu, H.-S., An, H., Nguyen, T., Zhang, J., Zhang, J., Huyen, P. T. and Nguyen, N.-T. *J. Alloys Compd.*, **2024**.
- [49] Barcaro, G., Sementa, L., Fortunelli, A. and Stener, M. *J. Phys. Chem. C*, 118(48):28101–28108, **2014**.
- [50] Barcaro, G., Sementa, L., Fortunelli, A. and Stener, M. *Phys. Chem. Chem. Phys.*, 17(42):27952–27967, **2015**.
- [51] Marchesin, F., Koval, P., Barbry, M., Aizpurua, J. and Sánchez-Portal, D. *ACS Photonics*, 3(2):269–277, **2016**.
- [52] Varas, A., García-González, P., Feist, J., García-Vidal, F. and Rubio, A. *Nanophotonics*, 5(3):409–426, **2016**.
- [53] Sinha-Roy, R., Garcia-Gonzalez, P., Weissker, H.-C., Rabilloud, F. and Fernandez-Dominguez, A. I. *ACS Photonics*, 4(6):1484–1493, **2017**.
- [54] Asadi-Aghbolaghi, N., Rüger, R., Jamshidi, Z. and Visscher, L. *J. Phys. Chem. C*, 124(14):7946–7955, **2020**.
- [55] Danielis, N., Vega, L., Fronzoni, G., Stener, M., Bruix, A. and Neyman, K. M. *J. Phys. Chem. C*, 125(31):17372–17384, **2021**.
- [56] Müller, M. M., Perdana, N., Rockstuhl, C. and Holzer, C. *J. Chem. Phys.*, 156(9):094103, **03 2022**. ISSN 0021-9606.
- [57] Domenis, N., Grobas Illobre, P., Marsili, M., Stener, M., Toffoli, D. and Coccia, E. *Mol.*, 28(15), **2023**. ISSN 1420-3049.
- [58] Sanchez-Gonzalez, A., Corni, S. and Mennucci, B. *J. Phys. Chem. C*, 115(13):5450–5460, **2011**.
- [59] Payton, J. L., Morton, S. M., Moore, J. E. and Jensen, L. *Acc. Chem. Res.*, 47(1):88–99, **2014**.
- [60] Romanelli, M., Dall’Osto, G. and Corni, S. *J. Chem. Phys.*, 155(21):214304, **2021**.
- [61] Lafiosca, P., Nicoli, L., Bonatti, L., Giovannini, T., Corni, S. and Cappelli, C. *J. Chem. Theory Comput.*, 19(12):3616–3633, **2023**.
- [62] Coane, C. V., Romanelli, M., Dall’Osto, G., Di Felice, R. and Corni, S. *Commun. Chem.*, 7(1):32, **Feb 2024**. ISSN 2399-3669.
- [63] Grzelczak, M., Pérez-Juste, J., Mulvaney, P. and Liz-Marzáñ, L. M. *Chem. Soc. Rev.*, 37(9):1783–1791, **2008**.
- [64] Sau, T. K. and Rogach, A. L. *Adv. Mater.*, 22(16):1781–1804, **2010**.

-
- [65] De Marchi, S., Núñez-Sánchez, S., Bodelón, G., Pérez-Juste, J. and Pastoriza-Santos, I. *Nanoscale*, 12:23424–23443, **2020**.
- [66] Zheng, J., Cheng, X., Zhang, H., Bai, X., Ai, R., Shao, L. and Wang, J. *Chem. Rev.*, 121(21):13342–13453, **2021**.
- [67] Sen, S., Karan, N. S. and Pradhan, N. *Chem. Mat.*, 36(14):6696–6719, **2024**.
- [68] Chaudhary, M. and Weissker, H.-C. *Nat. Commun.*, 15(1):9225, **Oct 2024**.
- [69] García de Abajo, F. J. and Howie, A. *Phys. Rev. B*, 65:115418, **Mar 2002**.
- [70] Corni, S. and Tomasi, J. *J. Chem. Phys.*, 114(8):3739–3751, **2001**.
- [71] Halas, N. J., Lal, S., Chang, W.-S., Link, S. and Nordlander, P. *Chem. Rev.*, 111(6):3913–3961, **2011**.
- [72] Duan, H., Fernández-Domínguez, A. I., Bosman, M., Maier, S. A. and Yang, J. K. W. *Nano Lett.*, 12(3):1683–1689, **2012**.
- [73] Mie, G. *Ann. Phys.-Berlin*, 330(3):377–445, **1908**.
- [74] Draine, B. T. and Flatau, P. J. *J. Opt. Soc. Am. A*, 11(4):1491–1499, **1994**.
- [75] Hao, F., Nehl, C. L., Hafner, J. H. and Nordlander, P. *Nano Lett.*, 7(3):729–732, **2007**.
- [76] Taflove, A., Hagness, S. C. and Piket-May, M. *Computational electromagnetics: the finite-difference time-domain method*. Elsevier Amsterdam, The Netherlands, **2005**.
- [77] Shuford, K. L., Ratner, M. A., Gray, S. K. and Schatz, G. C. *Appl. Phys. B*, 84(1):11–18, **Jul 2006**.
- [78] Jensen, L. L. and Jensen, L. *J. Phys. Chem. C*, 112(40):15697–15703, **2008**.
- [79] Jensen, L. L. and Jensen, L. *J. Phys. Chem. C*, 113(34):15182–15190, **2009**.
- [80] Morton, S. M. and Jensen, L. *J. Chem. Phys.*, 133(7):074103, **2010**.
- [81] Morton, S. M. and Jensen, L. *J. Chem. Phys.*, 135(13):134103, **2011**.
- [82] Payton, J. L., Morton, S. M., Moore, J. E. and Jensen, L. *J. Chem. Phys.*, 136(21):214103, **2012**.
- [83] Chen, X., Moore, J. E., Zekarias, M. and Jensen, L. *Nat. Commun.*, 6:8921, **2015**.
- [84] Zakomirnyi, V. I., Rinkevicius, Z., Baryshnikov, G. V., Sørensen, L. K. and Ågren, H. *J. Phys. Chem. C*, 123(47):28867–28880, **2019**.

-
- [85] Zakomirnyi, V. I., Rasskazov, I. L., Sørensen, L. K., Carney, P. S., Rinkevicius, Z. and Ågren, H. *Phys. Chem. Chem. Phys.*, 22(24):13467–13473, **2020**.
- [86] Becca, J. C., Chen, X. and Jensen, L. *J. Chem. Phys.*, 154(22):224705, **2021**.
- [87] Sørensen, L. K., Utyushev, A. D., Zakomirnyi, V. I. and Ågren, H. *Phys. Chem. Chem. Phys.*, 23:173–185, **2021**.
- [88] Ye, H., Becca, J. C. and Jensen, L. *J. Chem. Phys.*, 160 1, **2024**.
- [89] Sørensen, L. K., Gerasimov, V. S., Karpov, S. V. and Ågren, H. *Phys. Chem. Chem. Phys.*, 26:24209–24245, **2024**.
- [90] Giovannini, T., Rosa, M., Corni, S. and Cappelli, C. *Nanoscale*, 11(13):6004–6015, **2019**.
- [91] Giovannini, T., Bonatti, L., Polini, M. and Cappelli, C. *J. Phys. Chem. Lett.*, 11(18):7595–7602, **2020**.
- [92] Bonatti, L., Gil, G., Giovannini, T., Corni, S. and Cappelli, C. *Front. Chem.*, 8:340, **2020**.
- [93] Lafiosca, P., Giovannini, T., Benzi, M. and Cappelli, C. *J. Phys. Chem. C*, 125(43):23848–23863, **2021**.
- [94] Lafiosca, P., Giovannini, T., Benzi, M. and Cappelli, C. *J. Phys. Chem. C*, 127:6115 – 6115, **2023**.
- [95] Zanotto, S., Bonatti, L., Pantano, M. F., Mišekis, V., Speranza, G., Giovannini, T., Coletti, C., Cappelli, C., Tredicucci, A. and Toncelli, A. *ACS Photonics*, 10(2):394–400, **2023**.
- [96] Lafiosca, P., Nicoli, L., Pipolo, S., Corni, S., Giovannini, T. and Cappelli, C. *J. Phys. Chem. C*, 128(41):17513–17525, **2024**.
- [97] Nicoli, L., Sodomaco, S., Lafiosca, P., Giovannini, T. and Cappelli, C. *ACS Phys. Chem. Au.*, 0(0):null, **0**.
- [98] Zhang, X., Li, X., Zhang, D., Su, N., Yang, W. and Everitt, H. *Nat. Commun.*, 8:14542, **02 2017**.
- [99] Savage, K. J., Hawkeye, M. M., Esteban, R., Borisov, A. G., Aizpurua, J. and Baumberg, J. J. *Nature*, 491(7425):574—577, **November 2012**. ISSN 0028-0836.
- [100] Scholl, J. A., García-Etxarri, A., Koh, A. L. and Dionne, J. A. *Nano Lett.*, 13(2):564–569, **2013**.
- [101] Tan, S. F., Wu, L., Yang, J. K., Bai, P., Bosman, M. and Nijhuis, C. A. *Science*, 343(6178):1496–1499, **2014**.

-
- [102] Esteban, R., Zugarramurdi, A., Zhang, P., Nordlander, P., García-Vidal, F. J., Borisov, A. G. and Aizpurua, J. *Faraday Discuss.*, 178:151–183, **2015**.
- [103] Zhu, W., Esteban, R., Borisov, A. G., Baumberg, J. J., Nordlander, P., Lezec, H. J., Aizpurua, J. and Crozier, K. B. *Nature Commun.*, 7(1):11495, **Jun 2016**. ISSN 2041-1723.
- [104] Campos, A., Troc, N., Cottancin, E., Pellarin, M., Weissker, H.-C., Lermé, J., Kociak, M. and Hillenkamp, M. *Nat. Phys.*, 15(3):275–280, **Mar 2019**. ISSN 1745-2481.
- [105] Esteban, R., Borisov, A. G., Nordlander, P. and Aizpurua, J. *Nat. Commun.*, 3(1):825, **May 2012**. ISSN 2041-1723.
- [106] Hohenester, U. *Phys. Rev. B*, 91:205436, **May 2015**.
- [107] Fuchs, R. *Phys. Rev. B*, 11:1732–1740, **Feb 1975**.
- [108] Miertuš, S., Scrocco, E. and Tomasi, J. *Chem. Phys.*, 55(1):117–129, **1981**. ISSN 0301-0104.
- [109] Cammi, R. and Tomasi, J. *J. Comput. Chem.*, 16(12):1449–1458, **1995**.
- [110] Cancès, E., Mennucci, B. and Tomasi, J. *J. Chem. Phys.*, 107(8):3032–3041, **1997**.
- [111] Corni, S. and Tomasi, J. *J. Chem. Phys.*, 116(3):1156–1164, **2002**.
- [112] Corni, S. and Tomasi, J. *Chem. Phys. Lett.*, 365(5-6):552–553, **2002**.
- [113] Corni, S. and Tomasi, J. *J. Chem. Phys.*, 117(15):7266–7278, **2002**.
- [114] Corni, S. and Tomasi, J. *J. Chem. Phys.*, 118(14):6481–6494, **2003**.
- [115] Andreussi, O., Corni, S., Mennucci, B. and Tomasi, J. *J. Chem. Phys.*, 121(20):10190–10202, **2004**.
- [116] Tomasi, J., Mennucci, B. and Cammi, R. *Chem. Rev.*, 105(8):2999–3094, **2005**.
- [117] Corni, S. and Tomasi, J. In *Surface-Enhanced Raman Scattering*, pages 105–123. Springer, **2006**.
- [118] Caricato, M., Andreussi, O. and Corni, S. *J. Phys. Chem. B*, 110(33):16652–16659, **2006**.
- [119] Pérez-González, O., Zabala, N., Borisov, A., Halas, N., Nordlander, P. and Aizpurua, J. *Nano Lett.*, 10(8):3090–3095, **2010**.
- [120] Koppens, F. H. L., Chang, D. E. and García de Abajo, F. J. *Nano Lett.*, 11(8):3370–3377, **2011**.

-
- [121] Hohenester, U. and Trügler, A. *Comput. Phys. Commun.*, 183(2):370–381, **2012**. ISSN 0010-4655.
- [122] Hohenester, U. *Comput. Phys. Commun.*, 185(3):1177–1187, **2014**. ISSN 0010-4655.
- [123] Mennucci, B. and Corni, S. *Nat. Rev. Chem.*, 3(5):315–330, **2019**.
- [124] Marcheselli, J., Chateau, D., Lerouge, F., Baldeck, P., Andraud, C., Parola, S., Baroni, S., Corni, S., Garavelli, M. and Rivalta, I. *J. Chem. Theory Comput.*, 16(6):3807–3815, **2020**.
- [125] Dall’Osto, G., Gil, G., Pipolo, S. and Corni, S. *J. Chem. Phys.*, 153(18):184114, **11** **2020**. ISSN 0021-9606.
- [126] Vukovic, S., Corni, S. and Mennucci, B. *J. Phys. Chem. C*, 113(1):121–133, **2009**.
- [127] Rakić, A. D., Djurišić, A. B., Elazar, J. M. and Majewski, M. L. *Appl. Opt.*, 37(22):5271–5283, **Aug 1998**.
- [128] Zhao, L., Jensen, L. and Schatz, G. C. *J. Am. Chem. Soc.*, 128(9):2911–2919, **2006**.
- [129] Jensen, L., Aikens, C. M. and Schatz, G. C. *Chem. Soc. Rev.*, 37(5):1061–1073, **2008**.
- [130] Morton, S. M. and Jensen, L. *J. Am. Chem. Soc.*, 131(11):4090–4098, **2009**.
- [131] Morton, S. M., Silverstein, D. W. and Jensen, L. *Chem. Rev.*, 111(6):3962–3994, **2011**.
- [132] Bade, W. L. *J. Chem. Phys.*, 27(6):1280–1284, **12** **1957**. ISSN 0021-9606.
- [133] Rick, S. W., Stuart, S. J. and Berne, B. J. *J. Chem. Phys.*, 101(7):6141–6156, **10** **1994**. ISSN 0021-9606.
- [134] Rick, S. W., Stuart, S. J., Bader, J. S. and Berne, B. *J. Mol. Liq.*, 65:31–40, **1995**.
- [135] Rick, S. W. and Berne, B. J. *J. Am. Chem. Soc.*, 118(3):672–679, **1996**.
- [136] Helgaker, T., Jørgensen, P. and Olsen, J. *Molecular Integral Evaluation*, chapter 9, pages 336–432. John Wiley & Sons, Ltd, **2000**. ISBN 9781119019572.
- [137] Fleischmann, M., Hendra, P. J. and McQuillan, A. J. *Chem. Phys. Lett.*, 26(2):163–166, **1974**.
- [138] Jeanmaire, D. L. and Van Duyne, R. P. *J. Electroanal. Chem. Interf. Electrochem.*, 84(1):1–20, **1977**.
- [139] Albrecht, M. G. and Creighton, J. A. *J. Am. Chem. Soc.*, 99(15):5215–5217, **1977**.

-
- [140] Smith, E. and Dent, G. *Introduction, Basic Theory and Principles*, chapter 1, pages 1–20. John Wiley & Sons, Ltd, **2019**. ISBN 9781119440598.
- [141] Nie, S. and Emory, S. R. *Science*, 275(5303):1102–1106, **1997**.
- [142] Campion, A. and Kambhampati, P. *Chem. Soc. Rev.*, 27(4):241–250, **1998**.
- [143] Jarvis, R. M. and Goodacre, R. *Anal. Chem.*, 76(1):40–47, **2004**.
- [144] Alvarez-Puebla, R., Liz-Marzán, L. M. and García de Abajo, F. J. *J. Phys. Chem. Lett.*, 1(16):2428–2434, **2010**.
- [145] Sharma, B., Frontiera, R. R., Henry, A.-L., Ringe, E. and Van Duyne, R. P. *Mater. Today*, 15(1):16–25, **2012**. ISSN 1369-7021.
- [146] Wang, Y., Wang, Y., Wang, W., Sun, K. and Chen, L. *ACS Appl. Mater.*, 8(41):28105–28115, **2016**.
- [147] Han, X. X., Rodriguez, R. S., Haynes, C. L., Ozaki, Y. and Zhao, B. *Nat. Rev. Methods Primers*, 1(1):1–17, **2022**.
- [148] Le Ru, E. C. and Auguié, B. *ACS Nano*, 18(14):9773–9783, **2024**.
- [149] Ma, H., Pan, S.-Q., Wang, W.-L., Yue, X., Xi, X.-H., Yan, S., Wu, D.-Y., Wang, X., Liu, G. and Ren, B. *ACS Nano*, 18(22):14000–14019, **2024**.
- [150] Chance, R. R., Prock, A. and Silbey, R. *Molecular Fluorescence and Energy Transfer Near Interfaces*, pages 1–65. John Wiley & Sons, Ltd, **1978**. ISBN 9780470142561.
- [151] Garoff, S., Weitz, D. A., Alvarez, M. S. and Gersten, J. I. *J. Chem. Phys.*, 81(11):5189–5200, **12 1984**. ISSN 0021-9606.
- [152] Yuan, H., Khatua, S., Zijlstra, P., Yorulmaz, M. and Orrit, M. *Angew. Chem. Int. Ed.*, 52(4):1217–1221, **2013**.
- [153] Li, J.-F., Li, C.-Y. and Aroca, R. F. *Chem. Soc. Rev.*, 46:3962–3979, **2017**.
- [154] Catingan, S. D. and Moores, A. *ACS Appl. Nano Mater.*, **2024**.
- [155] Andrew, P. and Barnes, W. L. *Science*, 306(5698):1002–1005, **2004**.
- [156] Reil, F., Hohenester, U., Krenn, J. R. and Leitner, A. *Nano Lett.*, 8(12):4128–4133, **2008**.
- [157] Atwater, H. A. and Polman, A. *Nat. Mater.*, 9(3):205–213, **Mar 2010**. ISSN 1476-4660.
- [158] Cao, S., Rosławska, A., Doppagne, B., Romeo, M., Féron, M., Chérioux, F., Bulou, H., Scheurer, F. and Schull, G. *Nat. Chem.*, 13(8):766–770, **Aug 2021**. ISSN 1755-4349.

-
- [159] Kong, F.-F., Tian, X.-J., Zhang, Y., Zhang, Y., Chen, G., Yu, Y.-J., Jing, S.-H., Gao, H.-Y., Luo, Y., Yang, J.-L., Dong, Z.-C. and Hou, J. G. *Nat. Nanotechnol.*, 17(7):729–736, **Jul 2022**. ISSN 1748-3395.
- [160] Janesko, B. G. and Scuseria, G. E. *J. Chem. Phys.*, 125(12):124704, **09 2006**. ISSN 0021-9606.
- [161] Abdali, S. and Blanch, E. W. *Chem. Soc. Rev.*, 37:980–992, **2008**.
- [162] Chulhai, D. V. and Jensen, L. *J. Phys. Chem. A*, 118 39:9069–79, **2014**.
- [163] Hu, L., Xi, F., Qv, L. and Fang, Y. *ACS Omega*, 3(1):1170–1177, **2018**.
- [164] Lee, S. G., Kwak, S. H., Son, W. K., Kim, S., Nam, K. T., Lee, H.-Y. and Jeong, D. H. *Anal. Chem.*, **2024**.
- [165] Linic, S., Christopher, P. and Ingram, D. B. *Nat. Mater.*, 10(12):911–921, **Dec 2011**. ISSN 1476-4660.
- [166] Mukherjee, S., Libisch, F., Large, N., Neumann, O., Brown, L. V., Cheng, J., Lassiter, J. B., Carter, E. A., Nordlander, P. and Halas, N. J. *Nano Lett.*, 13(1):240–247, **2013**.
- [167] Böckmann, H., Liu, S., Mielke, J., Gawinkowski, S., Waluk, J., Grill, L., Wolf, M. and Kumagai, T. *Nano Lett.*, 16(2):1034–1041, **2016**.
- [168] Kazuma, E., Jung, J., Ueba, H., Trenary, M. and Kim, Y. *Science*, 360(6388):521–526, **2018**.
- [169] Gellé, A., Jin, T., de la Garza, L., Price, G. D., Besteiro, L. V. and Moores, A. *Chem. Rev.*, 120(2):986–1041, **2020**.
- [170] Kozuch, J., Ataka, K. and Heberle, J. *Nat. Rev. Methods Primers*, 3(1):70, **Sep 2023**. ISSN 2662-8449.
- [171] Arcisauskaite, V., Kongsted, J., Hansen, T. and Mikkelsen, K. V. *Chem. Phys. Lett.*, 470(4-6):285–288, **2009**.
- [172] Casida, M. E. In *Recent Advances In Density Functional Methods: (Part I)*, pages 155–192. World Scientific, **1995**.
- [173] Norman, P., Ruud, K. and Saue, T. *Principles and practices of molecular properties: Theory, modeling, and simulations*. John Wiley & Sons, **2018**.
- [174] Le Ru, E. C., Blackie, E., Meyer, M. and Etchegoin, P. G. *J. Phys. Chem. C*, 111(37):13794–13803, **2007**.
- [175] LeRu, E. and Etchegoin, P. Principles of Surface Enhanced Raman Spectroscopy Elsevier, **2009**.

-
- [176] Zhang, X., Young, M. A., Lyandres, O. and Van Duyne, R. P. *J. Am. Chem. Soc.*, 127(12):4484–4489, **2005**.
- [177] Talley, C. E., Jackson, J. B., Oubre, C., Grady, N. K., Hollars, C. W., Lane, S. M., Huser, T. R., Nordlander, P. J. and Halas, N. J. *Nano Lett.*, 5 8:1569–74, **2005**.
- [178] Willets, K. A. and Van Duyne, R. P. *Annu. Rev. Phys. Chem.*, 58:267–297, **2007**.
- [179] Le Ru, E. and Etchegoin, P. *Principles of Surface-Enhanced Raman Spectroscopy: and related plasmonic effects*. Elsevier, **2008**.
- [180] Huh, Y. S., Chung, A. J. and Erickson, D. *Microfluid. Nanofluidics*, 6(3):285–297, **2009**.
- [181] Hartman, T., Wondergem, C. S., Kumar, N., van den Berg, A. and Weekhuysen, B. M. *J. Phys. Chem. Lett.*, 7(8):1570–1584, **2016**.
- [182] Cialla-May, D., Zheng, X.-S., Weber, K. and Popp, J. *Chem. Soc. Rev.*, 46:3945–3961, **2017**.
- [183] Zong, C., Xu, M., Xu, L.-J., Wei, T., Ma, X., Zheng, X.-S., Hu, R. and Ren, B. *Chem. Rev.*, 118(10):4946–4980, **2018**.
- [184] Corni, S. and Tomasi, J. *Chem. Phys. Lett.*, 342(1-2):135–140, **2001**.
- [185] Chulhai, D. V., Chen, X. and Jensen, L. *J. Phys. Chem. C*, 120(37):20833–20842, **2016**.
- [186] Hu, Z., Chulhai, D. V. and Jensen, L. *J. Chem. Theory Comput.*, 12(12):5968–5978, **2016**.
- [187] Placzek, G. and Teller, E. *Z. Phys.*, 81(3-4):209–258, **1933**.
- [188] Placzek, G. *Ed. G. Marx, Akademische Verlagsgesellschaft, Leipzig*, **1934**.
- [189] Jensen, L., Zhao, L., Autschbach, J. and Schatz, G. *J. Chem. Phys.*, 123(17):174110, **2005**.
- [190] Drexhage, K. H., Kuhn, H. and Schäfer, F. P. *Berichte der Bunsengesellschaft für physikalische Chemie*, 72(2):329–329, **1968**.
- [191] Fothergill, S. M., Joyce, C. and Xie, F. *Nanoscale*, 10:20914–20929, **2018**.
- [192] Jung, Y., Kim, J., Kim, N. H. and Kim, H. G. *ACS Appl. Nano Mater.*, 6(2):976–985, **2023**.
- [193] Campu, A., Muresan, I., Craciun, A.-M., Vulpoi, A., Cainap, S., Astilean, S. and Focsan, M. *ACS Appl. Mater. Interfaces*, 15(48):55925–55937, **2023**.
- [194] Lamberti, V., Dolci, M. and Zijlstra, P. *ACS Nano*, 18(7):5805–5813, **2024**.

-
- [195] Yang, B., Chen, G., Ghafoor, A., Zhang, Y., Zhang, Y., Zhang, Y., Luo, Y., Yang, J., Sandoghdar, V., Aizpurua, J., Dong, Z. and Hou, J. G. *Nat. Photon.*, 14(11):693–699, **August 2020**. ISSN 1749-4893.
- [196] Lin, J.-S., Tian, X.-D., Li, G., Zhang, F.-L., Wang, Y. and Li, J.-F. *Chem. Soc. Rev.*, 51:9445–9468, **2022**.
- [197] Mei, Z. and Tang, L. *Anal. Chem.*, 89(1):633–639, **2017**.
- [198] Murphy, C. J., Chang, H.-H., Falagan-Lotsch, P., Gole, M. T., Hofmann, D. M., Hoang, K. N. L., McClain, S. M., Meyer, S. M., Turner, J. G., Unnikrishnan, M., Wu, M., Zhang, X. and Zhang, Y. *Acc. Chem. Res.*, 52(8):2124–2135, **2019**.
- [199] Li, Y., Yang, X., Hou, F., Chen, D., Liu, Y., Yu, D., Ming, D., Yang, Y. and Huang, H. *ACS Appl. Mater. Interfaces*, 13(48):57058–57066, **2021**.
- [200] Dong, L., Yang, X., Zhang, C., Cerjan, B., Zhou, L., Tseng, M. L., Zhang, Y., Alabastri, A., Nordlander, P. and Halas, N. J. *Nano Lett.*, 17(9):5768–5774, **2017**.
- [201] Wang, J., Xie, Z., Zhu, Y., Zeng, P., He, S., Wang, J., Wei, H. and Yu, C. *Trends Environ. Anal. Chem.*, 41:e00226, **2024**. ISSN 2214-1588.
- [202] Peeters, W., Toyouchi, S., Fujita, Y., Wolf, M., Fortuni, B., Fron, E., Inose, T., Hofkens, J., Endo, T., Miyata, Y. and Uji-i, H. *ACS Omega*, 8(41):38386–38393, **2023**.